

Dissipative Structures and Oscillations in Active Emulsions

Alexander Martin Bergmann

Vollständiger Abdruck der von der TUM School of Natural Sciences der Technischen Universität München zur Erlangung eines
Doktors der Naturwissenschaften (Dr. rer. Nat.)
genehmigten Dissertation.

Vorsitz: Prof. Dr. Cathleen Zeymer

Prüfer*innen der Dissertation:

1. Prof. Dr. Job Boekhoven
2. Prof. Dr. Kerstin Göpfrich
3. Prof. Dr. Henrike Niederholtmeyer

Die Dissertation wurde am 11.10.2023 bei der Technischen Universität München eingereicht und durch die TUM School of Natural Sciences am 15.11.2023 angenommen.

“What I cannot create, I do not understand.”

R. Feynman

I. Abstract

Dissipative structures are ubiquitous in living organisms. Their formation and properties are governed by catalytical reaction cycles and rely on the continuous consumption of energy to maintain a non-equilibrium state.

Inspired by life's constant avoidance of equilibrium and the resulting dynamic properties, synthetic systems have been designed to mimic these properties. One of these systems is chemically regulated droplets, *i.e.*, active droplets. The properties of these droplets are governed by fluxes of droplet material, which are, in turn, regulated through chemical reactions. Although exciting properties like the suppression of Ostwald ripening, control over size and number, or even self-division of such droplets have been predicted by numerical calculations, experimental evidence has been lacking. To unravel such active properties, active coacervate-based droplets have been developed, which are also considered a model system for actively regulated membraneless organelles in living cells. However, despite tremendous progress in coupling the formation of such droplets to chemical reactions, it has been challenging to observe active behaviors due to limitations in the microscopic analysis and keeping such systems in a non-equilibrium steady state.

The observation of dynamic behaviors for active droplets is often limited due to the short timescale of their kinetics. In general, the formation of active coacervate-based droplets is often too fast to be observed, and the analysis of all or individual droplets is complicated with a conventional microscopic setup. We show how to study droplets from their formation until their dissolution, both individually and collectively. This is achieved by encapsulating the reaction cycle into micrometer-sized water-in-oil droplets, effectively generating microreactors through the implementation of droplet-based microfluidics. Our findings at the collective level emphasized the role of fuel concentration in dictating active droplet formation and properties. At the individual level, our observations revealed that active droplets grow through fusion, decay simultaneously, and their shrinkage rate scales with their initial volume.

We then demonstrate how to achieve a non-equilibrium steady state through continuous fueling of these microreactors. Under steady-state conditions, active droplets could undergo a morphological transition into spherical shells of liquid droplet material as well as oscillating cycles of nucleation, growth, fusion, and shrinkage. These dynamic behaviors are consequences of reaction-diffusion gradients occurring within the active droplets. The formation of spherical shells results from the destabilization of the active droplet's core due to product depletion. The oscillatory behavior stems from the system's attempt to regulate the size and number of active droplets, which is counteracted by gravitationally induced fusion.

Finally, a general guideline on the synthesis and macroscopic to microscopic analysis of chemically fueled supramolecular materials is presented.

In conclusion, this work unraveled the dynamic behaviors of chemically fueled active droplet systems. We envision that similar mechanisms are involved in the regulation of membraneless organelles, controlling their morphology, size, and number. Furthermore, this work could be a stepping stone in unraveling further dynamic behaviors, such as the spontaneous self-division of active droplets, corroborating their role as protocell models in the emergence of life.

II. Zusammenfassung

Dissipative Strukturen sind allgegenwärtig in lebenden Organismen. Ihre Bildung und Eigenschaften werden von katalytischen Reaktionszyklen gesteuert und beruhen auf dem kontinuierlichen Verbrauch von Energie, um einen Nichtgleichgewichtszustand aufrechtzuerhalten.

Inspiziert von der fortlaufenden Vermeidung des Gleichgewichts und den sich daraus ergebenden dynamischen Eigenschaften in der Natur wurden synthetische Systeme entwickelt, um diese Eigenschaften nachzubilden. Eines dieser Systeme sind chemisch regulierte Tropfen, auch als aktive Tropfen bekannt. Die Eigenschaften dieser Tropfen werden durch Strömungen von Tropfenmaterials gesteuert, die wiederum durch chemische Reaktionen reguliert werden. Numerische Berechnungen sagen besondere Eigenschaften wie die Unterdrückung von Ostwald-Reifung, die Kontrolle über Größe und Anzahl oder sogar die Selbstteilung dieser Tropfen voraus. Experimentelle Beweise für diese Eigenschaften stehen jedoch noch aus. Um diese aktiven Eigenschaften zu belegen, wurden auf Koazervaten basierende aktive Tropfen entwickelt, die als Modellsystem für aktiv regulierte membranlose Organelle in lebenden Zellen dienen. Trotz erheblicher Fortschritte bei der Verknüpfung der Tropfenbildung mit chemischen Reaktionen stellte es sich als schwierig heraus, aktive Verhaltensweisen zu beobachten. Die Einschränkungen liegen sowohl in der mikroskopischen Analyse als auch in der Aufrechterhaltung eines stationären Nichtgleichgewichtszustandes.

Die Beobachtung der dynamischen Eigenschaften von aktiven Tropfen ist oft durch die kurzen Zeitskalen ihrer Reaktionskinetik eingeschränkt. Die Bildung von Tropfen ist oft zu schnell, um direkt beobachtet zu werden, und die Analyse von Einzeltropfen oder der gesamten Tropfenpopulation gestaltet sich schwierig mit herkömmlichen mikroskopischen Methoden. Wir zeigen, wie Tropfen von ihrer Bildung bis zu ihrer Auflösung, sowohl einzeln als auch kollektiv, umfassend analysiert werden können. Dies wurde erreicht, indem der Reaktionszyklus in mikrometergroßen Wasser-in-Öl-Tropfen eingekapselt wird, wodurch effektiv Mikroreaktoren entstehen. Unsere Untersuchungen auf kollektiver Ebene verdeutlichten den Einfluss der Treibstoffkonzentration auf die Eigenschaften der aktiven Tropfen. Auf individueller Ebene stellten wir fest, dass aktive Tropfen durch Fusion mit anderen Tropfen wachsen, sich gleichzeitig auflösen und ihre Schrumpfrate proportional zum anfänglichen Volumen ist. Anschließend zeigen wir, wie ein stationärer Nichtgleichgewichtszustand in diesen Mikroreaktoren erreicht werden kann, indem eine konstante Treibstoffkonzentration aufrechterhalten wird. In diesem stationären Zustand konnten aktive Tropfen einen morphologischen Übergang zu sphärischen Schalen aus flüssigem Tropfenmaterial sowie oszillierende Zyklen aus Nukleation, Wachstum, Fusion und Zerfall durchlaufen. Diese dynamischen Verhaltensweisen resultieren aus Reaktions-Diffusionsgradienten innerhalb der

aktiven Tropfen. Die Bildung sphärischer Schalen beruht auf der Destabilisierung des Kerns eines aktiven Tropfens durch eine reduzierte Produktkonzentration. Die Oszillationen ergeben sich aus dem Versuch des Systems, die Größe und Anzahl der aktiven Tropfen zu regulieren, was durch die Schwerkraft induzierte Fusion der Tropfen verhindert wird.

Abschließend präsentieren wir eine allgemeine Anleitung zur Synthese und Charakterisierung chemisch angetriebener supramolekularer Materialien auf makroskopischer und mikroskopischer Ebene.

Zusammenfassend hat diese Arbeit die dynamischen Verhaltensweisen chemisch angetriebener aktiver Emulsionen aufgedeckt. Wir denken, dass ähnliche Mechanismen bei der Regulation membranloser Organellen beteiligt sind, um deren Morphologie, Größe und Anzahl zu kontrollieren. Darüber hinaus könnte diese Arbeit als Ausgangspunkt dienen, um weitere dynamische Verhaltensweisen aufzudecken, wie beispielsweise die spontane Selbstteilung aktiver Tröpfchen. Dies würde die Bedeutung von aktiven Tropfen als Protozellmodell bei der Entstehung des Lebens untermauern.

III. Abbreviations

ATP	adenosine triphosphate
ADP	adenosine diphosphate
AMP	adenosine monophosphate
A, C, G, T, U	adenine, cytosine, guanine, thymine, uracil
CSTR	continuously stirred tank reactor
DBC	dibenzoyl-L-cysteine
DIC	<i>N,N'</i> -diisopropylcarbodiimide
DNA	deoxyribonucleic acid
DMS	dimethyl sulfate
e.g.	<i>exempli gratia</i> , for example
FADH₂	flavin adenine dinucleotide hydroquinone form
FFT	fast Fourier transform
GTP	guanosine triphosphate
GDP	guanosine diphosphate
i.e.	<i>id est</i> , that is
LLPS	liquid-liquid phase separation
MLOs	membraneless organelles
NADH	nicotinamide adenine dinucleotide reduced form
NESS	non-equilibrium steady state
P_i	inorganic phosphate
PDI	perylene diimide
pSS	polystyrene sulfonate
RNA	ribonucleic acid
SUV	small unilamellar vesicles
tRNA	transfer ribonucleic acid
UV	ultraviolet

IV. Table of Contents

I. Abstract	I
II. Zusammenfassung	III
III. Abbreviations	V
IV. Table of Contents	VI
1. Dissipative Structures	- 1 -
1.1 Life Away from Equilibrium	- 1 -
1.1.1 The Role of Molecules with High Chemical Potential	- 2 -
1.1.2 Utilizing Phosphate Anhydrides to Induce Structure Formation or Force Generation	- 3 -
1.1.3 Utilizing Phosphate Anhydrides to Regulate Membraneless Organelles	- 4 -
1.2 Chemically Fueled Systems	- 8 -
1.2.1 In Equilibrium Self-Assembly.....	- 8 -
1.2.2 Chemically Fueled Non-Equilibrium Self-Assembly	- 8 -
1.2.3 Active Droplets	- 11 -
1.2.4 Conclusion.....	- 17 -
1.3 Non-equilibrium Steady State.....	- 19 -
1.3.1 Continuous Fueling with Waste Accumulation.....	- 19 -
1.3.2 Continuous Fueling and Waste Removal	- 23 -
1.3.3 Conclusion.....	- 26 -
2. LLPS in a Confinement	- 27 -
2.1 Dynamics of Phase Transitions in a Confinement.....	- 27 -
2.2 Reversible LLPS in a Confinement	- 28 -
2.3 Conclusion.....	- 30 -
3. Aim of the Thesis	- 31 -
4. Evolution and Single-Droplet Analysis of Fuel-Driven Compartments by Droplet-Based Microfluidics	- 32 -
5. Liquid Spherical Shells are a Non-Equilibrium Steady State	- 63 -

6. Oscillations in Active Emulsions	- 120 -
6.1 Experimental Setup	- 120 -
6.2 Continuous Nucleation, Growth, Fusion, and Shrinkage of Active Droplets.....	- 121 -
6.3 Oscillations Result from the Interplay of Size-Control and Fusion	- 123 -
6.4 Control and Limitations of the Oscillations	- 125 -
6.5 Conclusion.....	- 128 -
7. Synthesis and Characterization of Chemically Fueled Supramolecular Materials Driven by Carbodiimide-Based Fuels.....	- 129 -
8. Conclusion and Outlook.....	- 166 -
9. Materials and Methods.....	- 168 -
10. Further Publications	- 170 -
11. Acknowledgments	- 172 -
12. References	- 174 -

1. Dissipative Structures

Self-assembling systems exist at all scales in nature, and the study of the underlying processes is particularly motivated by life itself. The process of self-assembly can be divided into two main kinds: static and dynamic. Static assemblies reside in a local or global equilibrium and do not require energy to be maintained—this has been the predominant focus of research. However, life is dynamic. In dynamic self-assembly, structure or pattern formation is intricately linked to the continuous consumption of energy.¹ In the following, I will delve into the significance of energy consumption for living organisms, explain how these underlying principles can be applied in the design of dissipative systems, and outline strategies to keep these systems far from equilibrium to observe the elusive dynamic properties so closely associated with life.

1.1 Life Away from Equilibrium

The question “What is life?” has intrigued researchers for centuries.² Due to its complexity, there is no general definition of life that everyone agrees on.³ However, certain properties are considered to be lifelike and essential to life as we know it. Briefly, these are compartmentalization to organize and regulate complex biochemical reactions, growth and division to replicate and increase in number to ensure persistency, information processing to store, maintain and evolve existing properties, adaptability to respond to changes in the environment, and energy transduction to keep living systems away from equilibrium.⁴ One can argue about which of these properties is essential for the most minimalistic form of life imaginable, but in my opinion, energy transduction is always a part of it. However, why is it important for life to harvest energy and keep itself away from equilibrium?

While at first glance, it seems abundant and a “waste” of energy for life to depend on the constant harvesting of energy to maintain its integrity, a closer look reveals that life would be physically impossible without it. Some go so far as “equilibrium is death, non-equilibrium is life”.⁵ While not everything that is out-of-equilibrium can already be considered life, it is one of the most essential characteristics, and everything that is in equilibrium is definitely not alive anymore. As stated by Erwin Schrödinger: “It is by avoiding the rapid decay into the inert state of ‘equilibrium’ that an organism appears so enigmatic”.² This avoidance of the equilibrium is so important because no observable changes occur at thermodynamic equilibrium. This means there can be no directed motion or the performance of any work. Life avoids reaching equilibrium by metabolism, the constant harvesting of energy from other energetic sources e.g., through the conversion of chemicals or light. However, recreating something like a

1. Dissipative Structures

metabolism on a molecular level is not as easy as just throwing “food” on a plate. To operate biochemical reaction networks in cells, energy must be converted and stored in a usable form. This is done primarily by transferring energy to small molecules to obtain energy-rich molecules such as ATP, NADH, FADH₂, and GTP.^{4,6} A complex machinery of proteins is required to achieve this transfer, but once obtained, these molecules can be used not only to drive other reactions, but also to create order in the form of assembling structures or even to fuel motion.

1.1.1 The Role of Molecules with High Chemical Potential

Phosphate anhydrides such as ATP or GTP are widely used in cells to drive otherwise unfavorable processes and reactions. Their main functions are derived from the energetic downhill cleavage of their phosphate anhydride bonds. In the case of the conversion of ATP to ADP and P_i, this bond cleavage contains a Gibbs free energy of approximately -28 to -34 kJ/mol.⁷ However, despite their high chemical potential, these molecules are kinetically stabilized under physiological conditions by the highly negatively charged phosphate groups. These negative charges repel electron-rich nucleophilic molecules such as hydroxide ions, which would otherwise readily attack the electrophilic center of the phosphate anhydride bonds.⁸ Such uncontrolled bond cleavage would result in the loss of stored energy. In order for these bonds to be cleaved and the stored energy to be used for its intended purpose, catalysis is required. In cells, enzymes use Mg²⁺ and the interaction of various amino acid side chains to minimize the activation barrier for the hydrolysis of ATP (Figure 1).^{6,9} The actual transfer of energy occurs in the form of phosphorylation or nucleotidylation or through a conformational change in the target molecule or enzyme.⁸ Nucleotidyl transfer is the key driving force in the biosynthesis of proteins, RNA and DNA. While in protein synthesis aminoacyl-AMPs are generated by aminoacyl-tRNA synthetases to transfer the activated amino acid to tRNAs,¹⁰ RNA and DNA polymerases directly transfer XMP or dXMP groups respectively from XTP or dXTP (X = A, G, C, and U/T).⁶ Phosphoryl transfer is used, for example, to activate glucose in the first step of glucose metabolism, but it also traps glucose inside cells as glucose-6-P.¹¹ The addition of the negative charges from the phosphate group prevents glucose from crossing the cell membrane.¹²

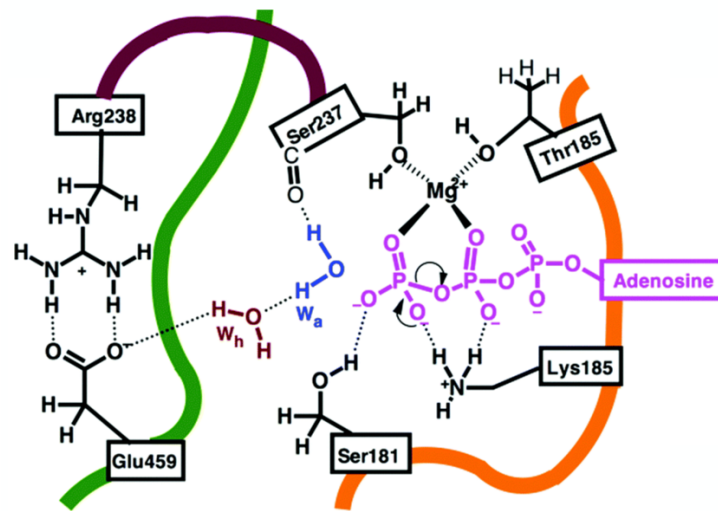


Figure 1: Catalyzed ATP hydrolysis in myosin. A representation of the catalytic active site of myosin is shown, demonstrating how ATP is coordinated and activated for hydrolysis through interactions with various amino acid residues as well as Mg^{2+} . Reprinted with permission from [9]. Copyright © 2016, Royal Society of Chemistry.

1.1.2 Utilizing Phosphate Anhydrides to Induce Structure Formation or Force Generation

As the example of glucose shows, activation of molecules is not only useful for the purpose of biosynthesis, but it can also change the properties of molecules and thus their interaction with other molecules or themselves. Changing the interaction of molecules with rather small and reversible changes at the molecular level shows a lot of versatility in structure formation. If we look at proteins, reversible activation or deactivation by post-translational modification can be easily introduced and removed to change their properties or organization, allowing the formation and degradation of larger structures or the performance of functions without the need for the synthesis or degradation of the protein.¹³ Very prominent examples that are driven by the hydrolysis of phosphate anhydrides to perform work or reversibly build larger structures are the formation of filaments such as actin or microtubules and the force generation or movement of motor proteins such as myosin or kinesin along these filaments. These processes are involved in muscle contraction as well as in the transport of cell organelles or other cargoes within the cell.^{14,15} The Binding of ATP to actin or GTP to tubulin monomers increases their self-assembly affinity and induces polymerization into filaments. However, in the assembled filament state, both ATP and GTP are catalytically hydrolyzed to ADP and GDP, respectively, which destabilizes the respective filaments and induces their disassembly.^{16,17} In muscle cells, the motor protein myosin converts the energy stored in ATP into a force to contract the muscle. Again, the binding and hydrolysis of ATP control the affinity of myosin to the actin filament, but unlike actin and microtubules, the ADP-bound myosin is tightly bound to actin (Figure 2A). The

subsequent release of ADP and phosphate induces a conformational change in the myosin structure, resulting in a power stroke that pulls the actin and myosin filaments in opposite directions (Figure 2B). The binding of ATP induces myosin detachment (Figure 2C), and myosin catalytically hydrolyzes ATP to ADP, inducing a recovery stroke that restores the initial conformation of myosin (Figure 2D). ADP-bound myosin then reattaches to actin, and the cycle begins again, with the combination of multiple power strokes resulting in muscle contraction.^{15,18,19}

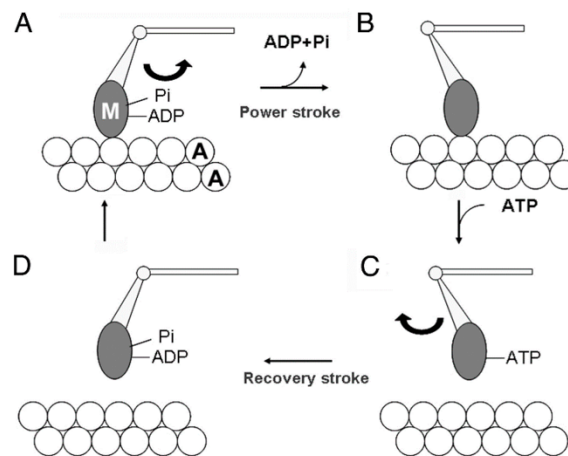


Figure 2: ATP-powered Myosin movement. **A)** Myosin (M) is bound to actin (A) in the ADP-bound state. **B)** The release of ADP and phosphate (Pi) results in a power stroke, leaving M bound to A in the postpower stroke configuration. **C)** The binding of ATP results in the release of ATP-bound M. **D)** The subsequent myosin-catalyzed hydrolysis of ATP results in a recovery stroke. The reformed ADP-bound M reattaches to A to repeat the cycle. Reprinted with permission from [19]. Copyright © 2008, the National Academy of Sciences of the USA.

1.1.3 Utilizing Phosphate Anhydrides to Regulate Membraneless Organelles

The generation of force and directional motion are among the most prominent examples of non-equilibrium processes that occur in life. However, many other processes are also coupled to non-equilibrium reactions. Recently, increasing attention has been paid to membraneless organelles (MLOs) such as stress granules, centrosomes, nucleoli, or P granules (Figure 3). These organelles are primarily formed through liquid-liquid phase separation and can be described as liquid-like droplets within cells. They lack a surrounding membrane, and their formation is induced by multivalent interactions of macromolecules such as proteins and RNA.

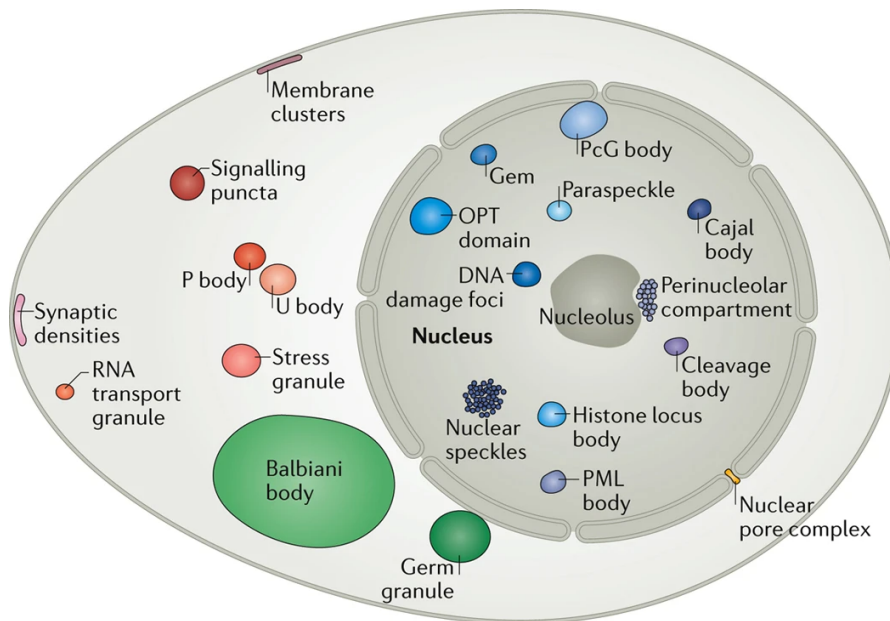


Figure 3: Schematic of MLOs in eukaryotic cells. MLOs are present in the nucleus, cytoplasm, and membranes, but not all are present in every cell type. Adapted with permission from [20]. Copyright © 2017, Springer Nature Limited.

It is becoming increasingly evident that these MLOs contribute to the cellular organization by concentrating specific biomolecules within them, thereby participating in the spatiotemporal control of cellular processes.^{20,21} In addition, these droplets are relatively easy to form and dissolve, allowing rapid responses to external stimuli. For example, stress granules form rapidly in the cytoplasm of cells in response to stress conditions such as heat, viral infection, oxidative stress, or UV irradiation.^{22,23} The most established pathway for their formation is the ATP-dependent phosphorylation of eIF2 α , which leads to the release of RNA and its subsequent phase-separation with other proteins to form stress granules.²⁴ Although this pathway is ATP-dependent, the energy from phosphorylation is not directly used to induce stress granule formation. However, other pathways, such as energy starvation, have also been reported.^{25,26} It has been proposed that the resulting depletion of ATP alone is sufficient to induce stress granule formation. The reduced ATP levels decrease the phosphorylation level of key proteins of stress granules, and the increase in attractive interactions due to the loss of negatively charged phosphate groups leads to the formation of stress granules.^{27,28} P granules are another example of such membraneless organelles regulated by phosphorylation and dephosphorylation. Similar to stress granules, phosphorylation of the highly enriched MEG protein in P granules leads to their dissolution, whereas its dephosphorylation induces the formation of P granules.²⁹

1. Dissipative Structures

In addition to controlling the formation and dissolution of these MLOs, it is important for cells to be able to control their properties, such as their liquid nature. Over time, MLOs are prone to lose their liquid-like properties and form gel-like or solid-like aggregates, a process known as maturation.³⁰ These changes in their properties can inhibit their function and are associated with diseases such as Alzheimer’s disease or amyotrophic lateral sclerosis.³¹⁻³³ Recent studies suggest that ATP-dependent enzymatic activity keeps MLOs in a non-equilibrium state, preventing maturation and maintaining liquidity (Figure 4).³⁴⁻³⁶

Furthermore, because MLOs are liquid, they are prone to coarsening by fusion or Ostwald ripening, ultimately forming a single MLO. However, there are instances where it is essential to control both the size and number of MLOs. While multiple coexisting MLOs are not stable under equilibrium conditions, it has been predicted that maintaining MLOs away from equilibrium can achieve stable coexisting MLOs.^{27,37}

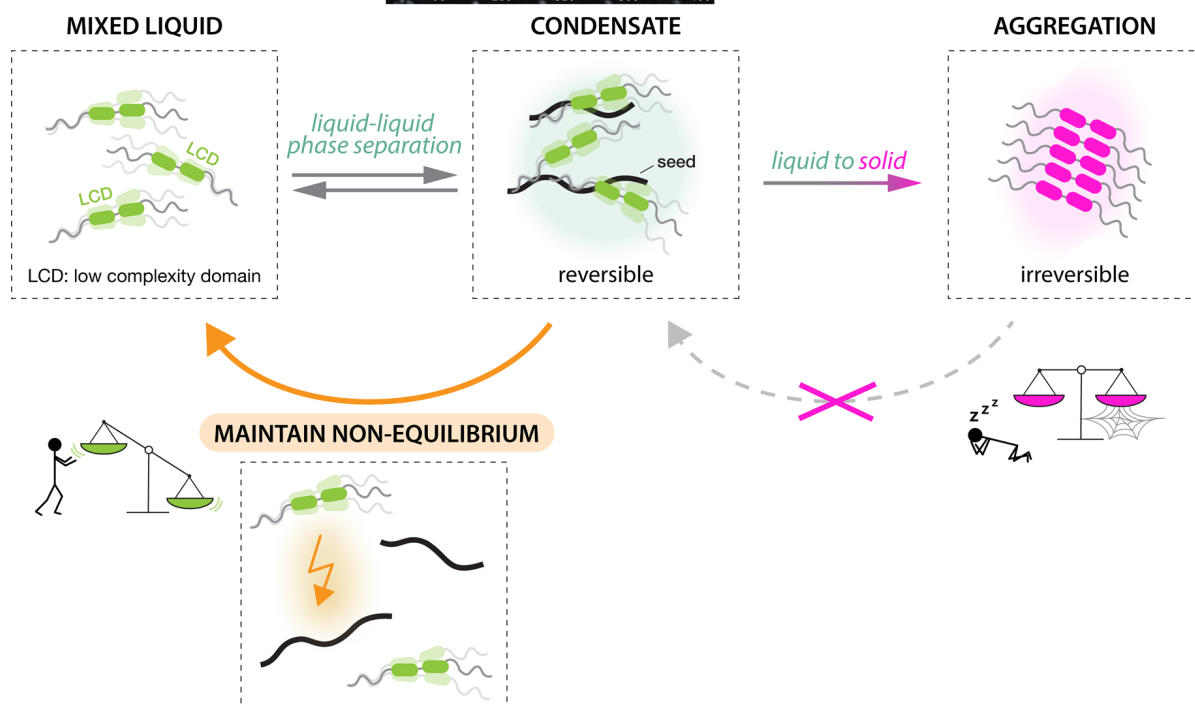


Figure 4: Liquid-liquid phase separation maintained away from equilibrium. Energy input maintains condensates away from equilibrium, preventing the potentially detrimental solidification. Adapted with permission from [36]. Copyright © 2020, the Authors.

While liquid-liquid phase separation in equilibrium is well understood, the mechanisms and dynamics of liquid-liquid phase separating in systems away from equilibrium are not.³⁷ Although experimental and theoretical work has made tremendous progress in recent years in understanding which cellular components are involved in the LLPS of MLOs and how this can be controlled by chemical reactions, the complexity of biological systems often hinders the full unraveling of their underlying regulatory mechanisms and the experimental confirmation of

1. Dissipative Structures

theoretical predictions. Therefore, model systems that capture the dynamics are needed to further enhance the understanding and verification of theoretical predictions regarding the behavior and properties of LLPS away from equilibrium.¹ In the following chapter, I will explain strategies for the design of chemically fueled systems and how chemical reactions can be used to regulate active droplets.

1.2 Chemically Fueled Systems

Inspired by nature and the unique properties and control that arise from driving systems away from equilibrium, significant efforts have been devoted to designing non-equilibrium systems that mimic some of these properties. Although cellular components have been successfully used to reproduce certain dynamic properties, synthetic systems are typically less complex and offer the advantage of complete customizability, thus enabling a wider range of applications as well as a deeper understanding of the fundamental mechanisms.

In order to design systems that mimic the properties of non-equilibrium systems observed in nature, it is essential to first understand how self-assembly generally works and how it can be coupled to chemical reactions that drive these assemblies away from equilibrium. In this chapter, I will explain the general principles of molecular self-assembly and how the molecular properties can be coupled to chemical reactions to form transient assemblies. From here, I will use active droplets as an example to further illustrate how chemical reactions can control the presence of assemblies, their properties, and, thus, their unique active behaviors.

1.2.1 In Equilibrium Self-Assembly

Molecular self-assembly refers to the spontaneous formation of larger, more complex structures driven and controlled by non-covalent interactions between the constituent molecules (building blocks). These interactions include hydrogen bonding, electrostatic interactions, van der Waals interactions, and the hydrophobic effect. In general, the propensity of molecules to self-assemble is determined by the interplay of attractive and repulsive interactions. When the attractive forces dominate, these molecules start to interact with each other in a way that minimizes their energy until they reach a stable local or global thermodynamic equilibrium. In this equilibrium state, systems can still exchange material with their surroundings, but, on average, there is no net flow of energy or matter.¹ These organized structures include fibers, tubes, vesicles, or DNA-based assemblies, among many others. However, these equilibrium assemblies are static, whereas biological systems rely on dynamic and adaptive assemblies. The unique properties of biological assemblies include spatiotemporal control, rapid adaptation to external stimuli, reorganization, directed motion, or upkeep of gradients. These properties depend on the constant flow of energy and matter and are driven by catalytic reaction cycles.^{13,38,39}

1.2.2 Chemically Fueled Non-Equilibrium Self-Assembly

Inspired by the use of molecules such as ATP in living systems, synthetic catalytic reaction cycles have been developed, which are coupled to self-assembly processes. In these reaction

1. Dissipative Structures

cycles, a catalyst (precursor) is activated by reacting with a reagent with a high chemical potential (fuel, Figure 5A, B). This activated catalyst (product) has a higher affinity to assemble and can form complex structures. However, the product is not thermodynamically stable and will eventually be deactivated, reverting it to the original catalyst. This deactivation can occur spontaneously by the solvent (e.g., hydrolysis by water⁴⁰) or by an additionally supplied reagent (e.g., H₂O₂ as an oxidizing agent⁴¹).⁴² This interplay of simultaneous activation and deactivation of the catalyst results in a finite lifetime of the assembling product, giving rise to dynamic features in the assemblies that depend on the presence of fuel and its catalytic conversion into a waste product (Figure 5C). Notably, in these fuel-driven cycles of activation and deactivation, it is essential that these reactions are practically irreversible and are not each other's microscopic reverse.⁴³ In addition, to achieve assembly formation, the assembly process must be fast relative to the kinetics of the reactions.⁴⁴ For example, if the deactivation reaction is extremely fast compared to the diffusivity of the product or the assembly kinetics, no assemblies will form despite the consumption of fuel. Another issue can arise if the disassembly kinetics of the system are very slow. In such cases, assemblies will form in the presence of fuel but may dissolve with a delay or not at all once the product is deactivated. Consequently, the assemblies become metastable or even kinetically trapped.⁴⁵

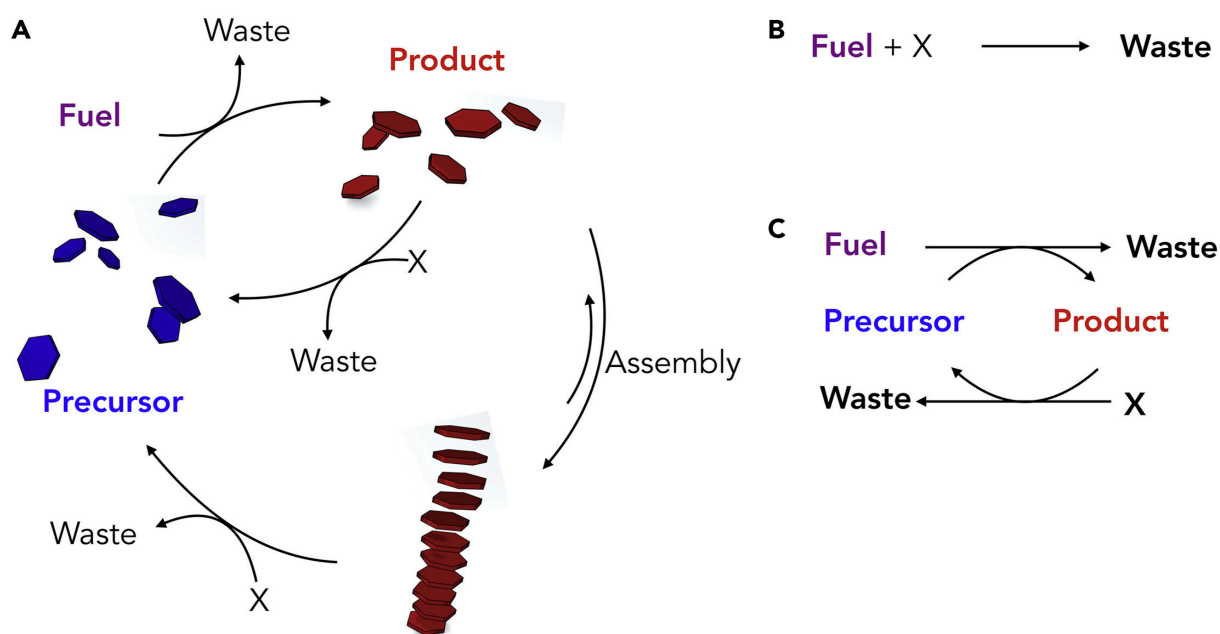


Figure 5: Reaction cycle for chemically fueled self-assembling systems. A) Schematic representation of a chemically fueled reaction cycle that leads to the formation assemblies. **B)** Energy is obtained by the net conversion of fuel to waste through a reaction with an additional species in solution (X). **C)** The conversion of fuel to waste is catalyzed by the formation of a transient product. Reprinted with permission from [39]. Copyright © 2019, Elsevier Inc.

1. Dissipative Structures

A common strategy employed to achieve chemically fueled self-assembly is comparable to the function of phosphorylation and dephosphorylation in cellular assemblies, *i.e.*, by introducing or abolishing charges that alter the affinity of building blocks for each other or their target. In one of the first examples, Van Esch and coworkers established a chemically fueled self-assembling system for the transient formation of fibers (Figure 6).⁴⁰ In their system, the precursor, *N,N'*-dibenzoyl-L-cysteine (DBC), did not assemble due to the electrostatic repulsion of the deprotonated carboxyl groups. However, the negative charges could be eliminated by esterifying the carboxyl groups with the fuel dimethyl sulfate (DMS), and the reduced repulsive interactions enabled self-assembly into fibers, ultimately leading to the formation of a hydrogel. However, the high pH not only increased the repulsive interactions of the precursor but also led to the gradual hydrolysis of the product back to the initial precursor DBC. This, in turn, induced the spontaneous disassembly of the fibers. The interplay of activation and deactivation resulted in alternating growth and collapse of the fibers reminiscent of the dynamic instability observed for microtubules.

While such designs provide control over the presence of assemblies, they do not inherently ensure the aforementioned properties of non-equilibrium assemblies.

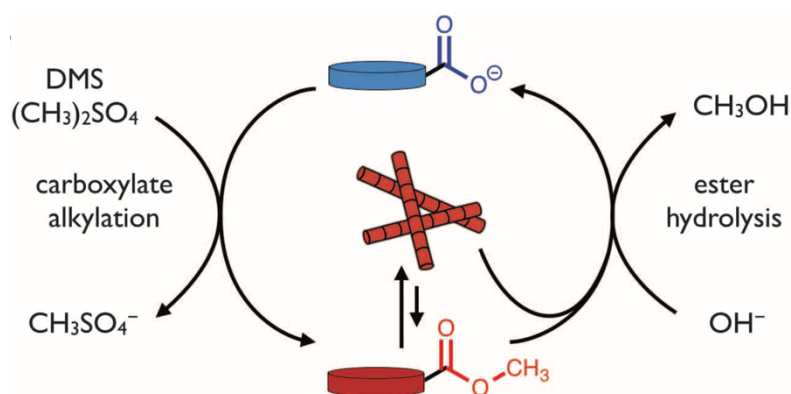


Figure 6: Fuel-driven self-assembly of DBC. The carboxylic acid of the precursor DBC (blue) is activated by alkylation with DMS to form methyl esters. The resulting activated products (red) self-assemble into fibers. The methyl esters can be spontaneously hydrolyzed back to the initial precursor in both the assembled and unassembled state. Adapted with permission from [40]. Copyright © 2015, American Association for the Advancement of Science.

Establishing transient assemblies represents the first step in mimicking life-like behaviors because it ensures that the activation and deactivation reactions influence the assembly formation, enabling both recycling of the building blocks as well as quick responses to external stimuli. However, to achieve further dynamic properties that are not possible to achieve in equilibrium systems, these assemblies must also induce feedback on the reaction cycle or their own formation. For example, the dynamic instability of rapid formation and collapse observed for microtubules cannot occur in systems forming fibers or tubular structures under

equilibrium conditions. In the case of microtubules, feedback manifests as accelerated deactivation within the assemblies, creating a kinetic asymmetry in the reaction cycle.¹⁷ This asymmetry in the energy consumption pathway is necessary to ensure that the energy transfer influences not only the presence of assemblies but also the assemblies themselves. In a fuel-driven self-assembling system where assembly processes are not influenced by the resulting assembly, the reaction cycle only influences the presence of the high-energy product concentration, but the assembly of the product is dictated by the relative thermodynamic stability of the unassembled and assembled product.¹³ However, to introduce asymmetry into a fuel-driven system and dictate its properties, it is not always necessary for the reaction rate constants to be different,¹⁷ as is the case for microtubule or molecular machines.¹³ Instead, asymmetry can be achieved if reaction fluxes are different in space or depend on local composition.⁴⁶

1.2.3 Active Droplets

Active droplets that show such asymmetry have been described in a theoretical framework.^{46,47} In these active droplets, phase separation is coupled to a fuel-driven reaction cycle in which the activation and deactivation reactions of the building blocks are spatially separated (Figure 7A). Numerical calculations for active droplets predict dynamic behaviors such as suppression of Ostwald ripening, the control of droplet number and size or self-division (Figure 7B).^{48,49} These behaviors result from continuous fluxes between the droplet and the dilute phase, driven by chemical reactions.

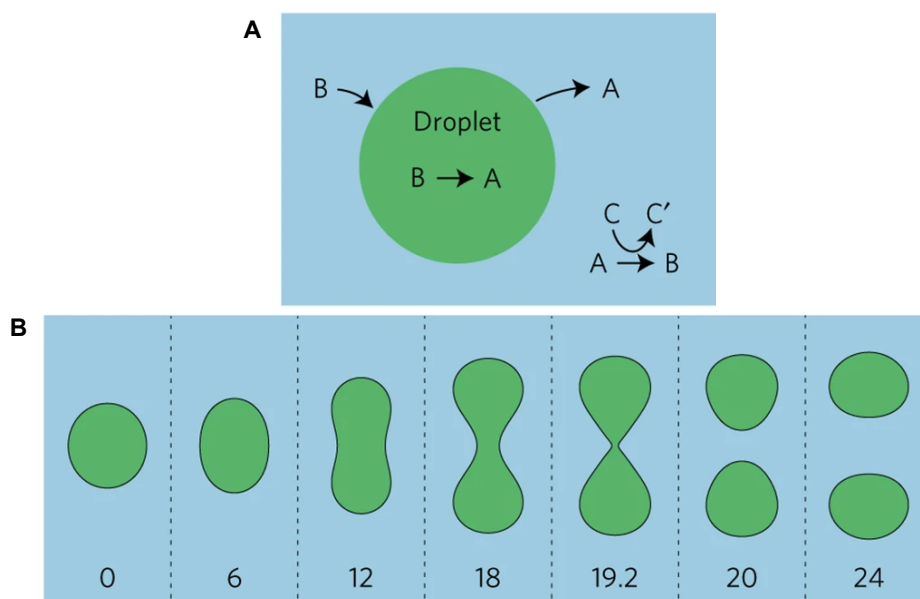


Figure 7: Self-division of chemically active droplets. A) Simple model of an active droplet. A soluble component A is converted into a droplet material B at the expense of a chemical fuel C. The droplet material B phase-separates and spontaneously converts back to component A. **B)** Sequence of shapes

1. Dissipative Structures

of a dividing droplet resulting from numerical calculations of chemically active droplets. Adapted with permission from [49]. Copyright © 2016, Springer Nature Limited.

The importance of these reactions and their spatial separation to induce fluxes becomes evident when compared to passive droplets, *i.e.*, phase separation is not coupled to chemical reactions and droplets with symmetric reactions. Considering a single droplet, passive droplets exchange material with their surroundings, but this exchange is balanced and does not result in a net influx or efflux of material (Figure 8A). However, coupling droplet formation to a catalytic reaction cycle alone does not induce fluxes either. If the activation and deactivation reactions occur equally outside and inside the droplets, and the concentration of activated molecules is kept constant, the resulting droplets behave similarly to passive droplets. In this case, the thermodynamic tendencies of the activated and deactivated molecules to phase-separate determine the presence of droplets. Both molecules exchange between the droplets and the surrounding phase, but their exchange is in equilibrium, and neither exhibits a net flux (Figure 8B). Therefore, the chemical reactions regulate the presence of droplets but not the properties of the resulting droplets. When the activation and deactivation reactions do not occur equally in both phases, the imbalance of the reactions induces net fluxes of molecules from the surrounding phase into the droplets and from the droplets into the surrounding phase (Figure 8C). Considering two coexisting phases—a droplet of phase-separated material in a dilute phase—there are two possible ways to separate the chemical reactions. Activation of the building blocks can occur in the dilute phase, while the deactivation occurs in the droplet phase, or vice versa. Theoretical studies have demonstrated that unique behaviors can emerge in such active systems where i) a chemical modification alters the affinities for the phases, ii) a driven reaction is involved in the step of chemical modification, and iii) the reaction dynamics differ inside and outside the droplets.³⁷ However, it should be noted that these active emulsions are governed by diffusive fluxes, and self-propulsion does not play a role as it does in the more traditional view of motile active matter.^{46,50}

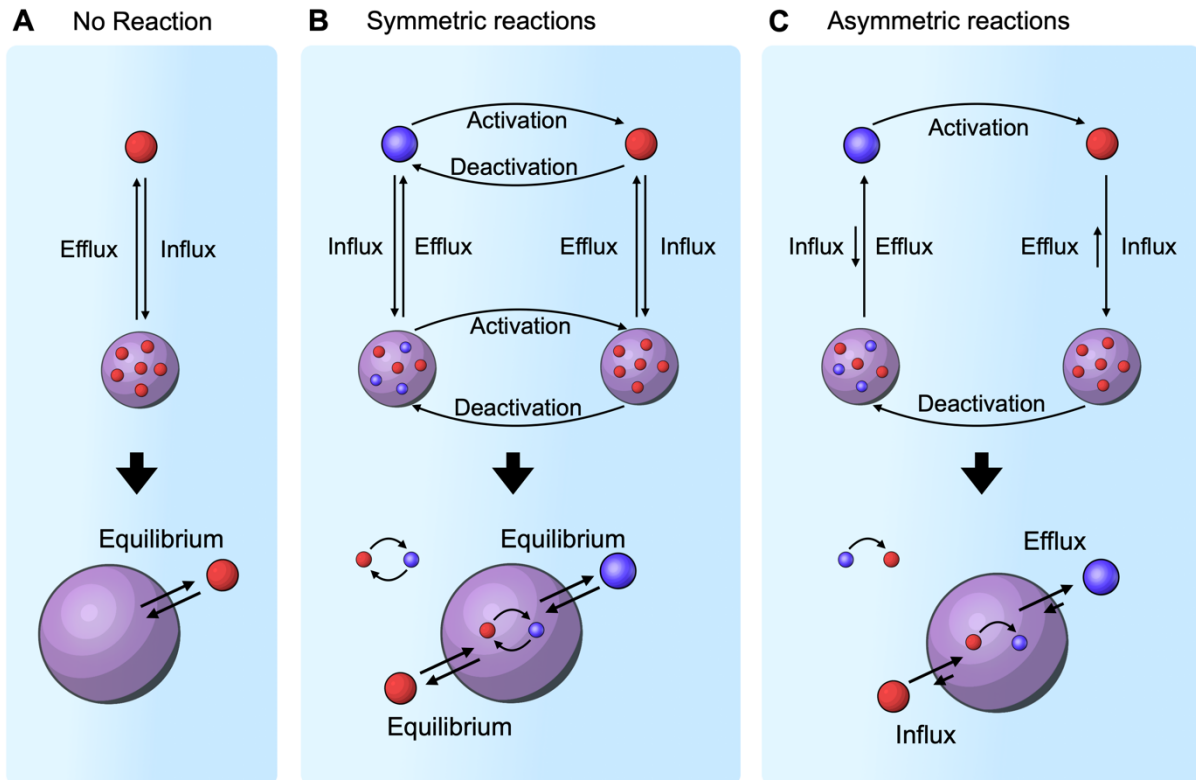


Figure 8: Liquid-liquid phase separation in equilibrium and driven by chemical reactions. A) Phase separation is not coupled to a reaction. The phase-separating droplets are in equilibrium with the surrounding dilute phase. **B)** Phase separation is coupled to a chemical reaction, but both the activation and deactivation proceed equally in the droplet as well as the dilute phase. **C)** Phase separation is coupled to a chemical reaction, but activation occurs only in the dilute phase, and deactivation occurs only in the droplet phase.

1.2.2.1 Internally Maintained Droplets

Theoretical studies⁴⁸ on a phase-separated system in which activation occurs within the droplets while deactivation occurs outside of the droplets reveal a net influx of precursor from the dilute phase into the droplets and a net efflux of product from the droplets into the dilute phase (Figure 9). The influx of precursor is driven by the depletion of precursor within the droplets through the fuel-driven conversion of precursor to product, whereas the efflux of product from the droplet is driven by the depletion of product in the dilute phase due to its degradation back to the precursor. In such autocatalytic droplets—droplets that produce their own building blocks—the activation rate scales with the droplet’s volume. Consequently, the influx of precursor also scales with the droplet’s volume, whereas the efflux of product is only slightly dependent on the droplet’s size.^{46,48} Although these droplets exhibit fluxes, they behave relatively similarly to passive droplets. In other words, in a system with a single droplet, the size of the droplet under steady-state conditions is determined by the number of available building blocks, and droplets do not have a stable size. They continue to grow as long as new

building blocks are supplied. In a system with multiple droplets, droplets exhibit Ostwald ripening, where large droplets grow at the expense of smaller ones. However, these droplets coarsen even faster than passive droplets due to the constant outflow of droplet material. Interestingly, similar behavior has been observed for a system in which both activation and deactivation occur outside of the droplets.⁵¹

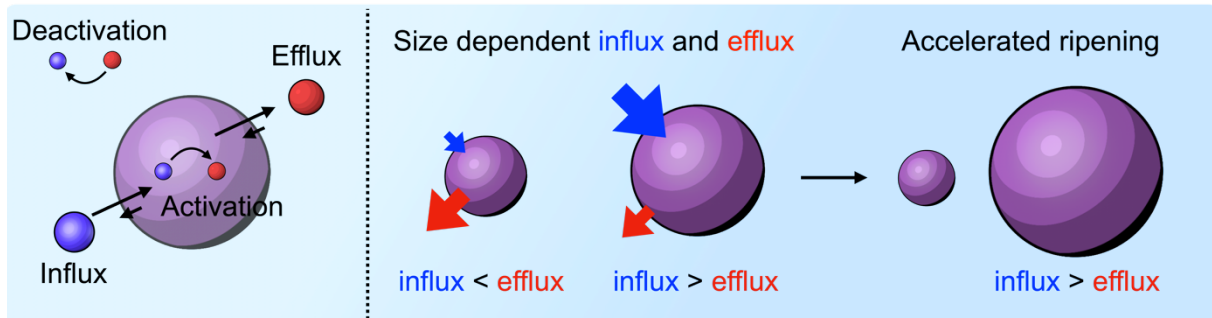


Figure 9: Internally maintained droplets. Schematic representation of active droplets in which deactivation is localized outside of the droplets and activation is localized inside of the droplets. Inspired by [52].

1.2.3.2 Externally Maintained Droplets

The second possibility for spatial separation of the activation and deactivation reaction in a system of two coexisting phases is the localization of the activation in the dilute phase and the deactivation inside the droplets (Figure 10). In a system where the product strongly prefers phase separation into droplets, while the precursor has a low affinity for partitioning into the phase-separated droplets, a constant net influx of product into the droplets and efflux of the precursor from the droplets into the dilute phase can be archived. In this case, the fluxes are driven by the oversaturation of the product in the dilute phase, a result of the activation reaction, as well as the oversaturation of the precursor in the droplet phase, a result of the deactivation reaction. In such a system, droplets do not follow the behavior of passive droplets, *i.e.*, they do not grow infinitely. For first-order reaction kinetics, the influx of droplet material depends on the diffusion of the product from the dilute phase into the droplets, and it is limited by the surface area. Meanwhile, the efflux of droplet material scales with the volume due to an increasing deactivation rate with an increasing total amount of product in a single droplet. Consequently, this leads to a faster increase in efflux compared to the influx of droplet material as the droplets grow larger, limiting the growth of the droplets and giving them a stable size. A droplet that is bigger than its stable size will shrink, while a droplet that is below its stable size will grow. In a system with multiple coexisting droplets, this leads to the resistance of Ostwald ripening and, ultimately, to the evolution of all droplets to the same size, enabling control over the number of droplets.³⁷ The coexistence of multiple droplets is thermodynamically unfavored

due to an increased surface area compared to a single large droplet. Therefore, such behavior is only possible for a system that is sustained in a non-equilibrium steady state (NESS).^{46,48,53} This concept is relevant in cellular biology, where various membraneless organelles are actively regulated using mechanisms such as enzyme-mediated phosphorylation and dephosphorylation of proteins.^{29,54,55} The spatial separation of these regulating enzymes is thought to enable the control over phase separation, a model referred to as the enrichment-inhibition model.²⁷

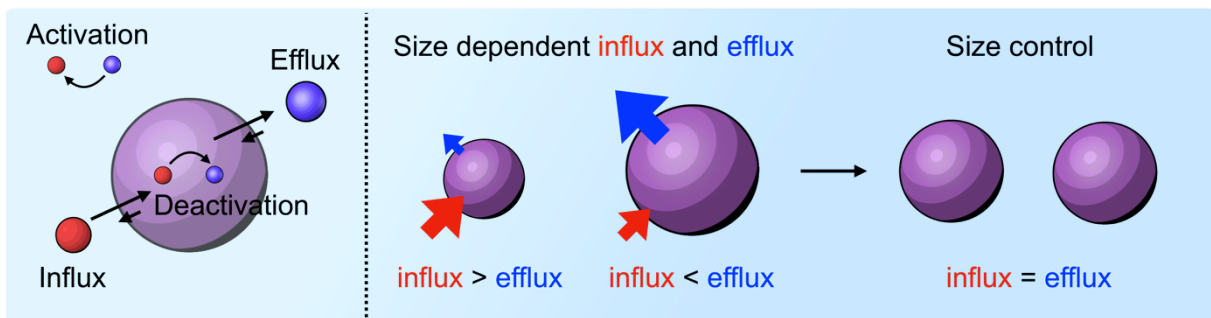


Figure 10: Externally maintained droplets. Schematic representation of active droplets in which activation is localized outside of the droplets and deactivation is localized inside of the droplets. Inspired by [52].

1.2.3.3 Fuel-driven Coacervate-based Droplets

A synthetic system that fulfills the criteria for chemically fueled active droplets in which the building blocks are activated outside and deactivated inside was developed by Donau *et al.*⁵⁶ In this system, phase separation is based on the concept of complex coacervation, *i.e.*, associative phase separation of two oppositely charged polyanions. Driven by attractive interactions like ion-ion pairing, π - π -stacking, and cation- π interactions, and an entropic gain through the release of counterions,⁵⁷⁻⁵⁹ phase-separation into polymer-rich liquid droplets and a polymer-poor dilute phase can be achieved. In contrast to phase-separation observed for oil in water, these droplets retain a high water content⁶⁰ that is responsible for their liquid nature.⁶¹ In the design of the active droplets, the affinity of a zwitterionic peptide to polyanionic ribonucleic acid (RNA) is increased through the conversion of its C-terminal aspartic acid into the corresponding anhydride by a carbodiimide-based fuel. The activation through anhydride formation and the resulting affinity increase to the RNA leads to the formation of coacervate-based droplets. However, the anhydride is unstable and spontaneously hydrolyzes back to the precursor which constitutes the deactivation. The high partitioning of the anhydride into the droplets and their high water content result in the predominant localization of the deactivation reaction inside of the droplets. The poorer partitioning of the precursor and the fuel into the droplets results in a diffusive precursor flux from the droplets to the dilute phase and its predominant reactivation therein. In combination, the predominant activation outside and

1. Dissipative Structures

deactivation inside of the droplets leads to a flux of product from the dilute phase into the droplet phase and a flux of the precursor from the droplet into the dilute phase, resulting in a system in which the chemical reactions should govern the properties of the phase-separated droplets. Indeed, the authors of the initial study demonstrated that the evolution of the droplets is tightly correlated to fuel-driven activation and spontaneous deactivation. The addition of fuel turns the sample turbid due to the formation of micrometer-sized droplets, as evidenced by microscopy. The turbidity is also tightly correlated to the concentration of the activated building blocks, *i.e.*, they increased and decreased simultaneously. After the fuel was consumed and the activated building blocks were hydrolyzed, the droplets dissolved. Interestingly, the droplets did not simply shrink in size upon dissolution, but they initially formed hollow shells, referred to as vacuoles. It was hypothesized that towards the end of the cycle, the deactivation in the core leads to an efflux of precursor and RNA, leading to vacuolization. Furthermore, these vacuoles did not dissolve evenly. Instead, the remaining shell ripped apart into droplet fragments that survived for tens of seconds before they dissolved, potentially showing a very primitive behavior of asymmetric division.⁵⁶ Although this system of active droplets already shows some interesting features, the behaviors predicted by theory, like suppression of Ostwald ripening and control of droplet size, are overshadowed by the constantly changing activation and deactivation rates resulting from the addition of batches of fuel to the system. To observe these behaviors, the system would have to be kept in a non-equilibrium steady state by maintaining a constant fuel concentration, which is experimentally difficult to achieve.

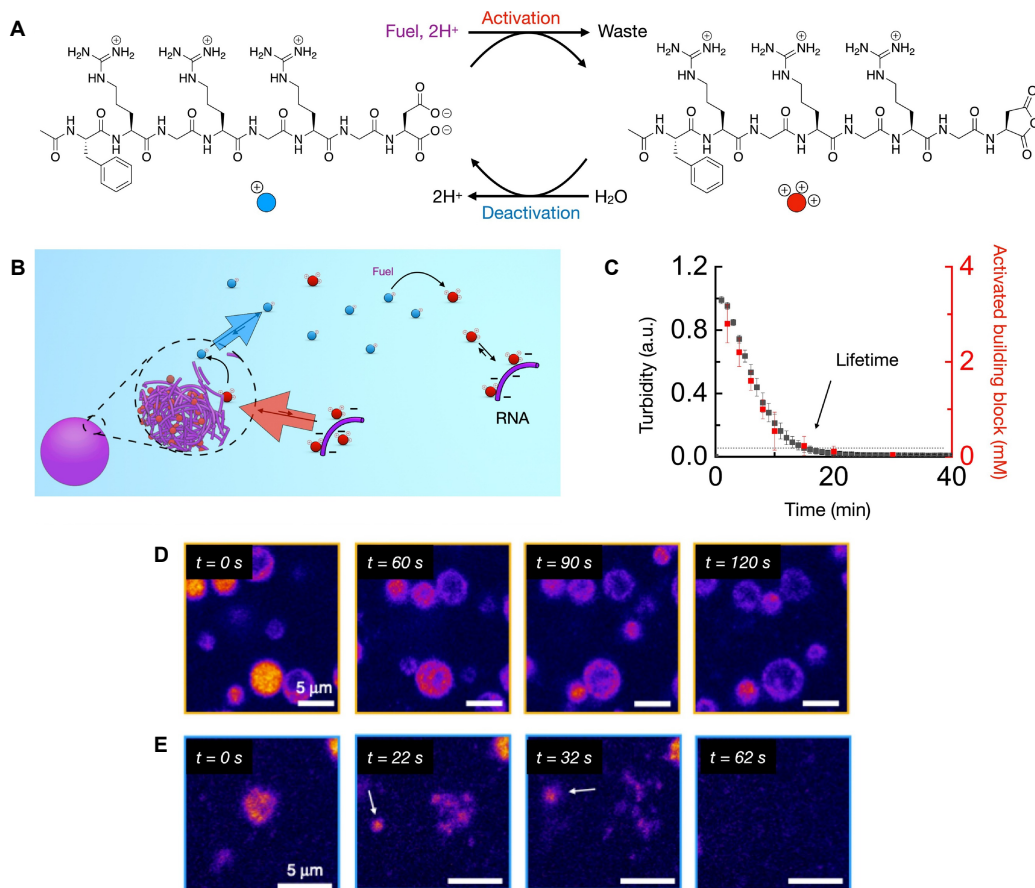


Figure 11: Externally maintained coacervate-based droplets. **A)** Fuel-driven activation of the precursor leads to the formation of the +3 charged product. Spontaneous deactivation of the product through hydrolysis recovers the precursor. **B)** Fuel-driven activation in the dilute phase leads to an increased affinity for RNA and results in the formation of coacervate-based droplets. **C)** The presence of coacervate-based droplets, as evident by turbidity measurements, is closely related to the amount of activated building blocks. **D)** Coacervate-based droplets form vacuoles upon dissolution. **E)** Collapsing vacuoles fragment. Adapted with permission from [56]. Copyright © 2020, The Author(s).

1.2.4 Conclusion

The construction of chemically fueled self-assembling systems requires understanding the underlying mechanisms of self-assembly and how to couple them to reactions that can drive these systems away from equilibrium. This coupling enables the formation of transient assemblies, which are important for life to respond rapidly to external stimuli and recycle valuable building blocks otherwise trapped in their thermodynamically stable assembled state. However, under non-equilibrium steady-state conditions, fuel-driven assemblies do not necessarily have different properties than their in-equilibrium counterparts if the assembly process is only influenced by the relative thermodynamic stability of the assembled and unassembled components. To observe active properties that emerge from the continuous consumption of energy, the assembled state needs to exert feedback on the energy

1. Dissipative Structures

consumption pathway. Theoretical studies have proposed that feedback mechanisms, such as the spatial separation of the activation and deactivation reactions in active droplets, can lead to intriguing active properties like the resistance of Ostwald ripening or even control over the droplet size and number. Such mechanisms might already be at play in regulating membraneless organelles in cells, but these mechanisms have yet to be experimentally verified. Although systems have been developed with the necessary prerequisites to observe such behaviors, demonstrating their maintenance away from equilibrium and the emergence of these behaviors remains a challenge. In the upcoming chapter, I will discuss various methods to achieve steady states in chemically fueled systems, the unique properties that can arise from these non-equilibrium steady states, and the advantages and disadvantages associated with these different strategies.

1.3 Non-equilibrium Steady State

Most chemically fueled self-assembling systems discussed so far have been studied in closed systems, *i.e.*, systems driven by the batch addition of fuel and allowed to settle toward equilibrium. In batch fueling, the total fuel amount is determined by the initial addition, and as fuel is continuously converted to waste, the fuel concentration steadily declines until it is fully consumed. While batch fueling can indeed drive a system out of equilibrium, it struggles to sustain a non-equilibrium steady state due to the fluctuating reaction rates caused by the decreasing fuel concentration.

However, life-like systems typically do not operate through batch-wise addition of fuel but remain away from equilibrium by continuously consuming fuel. Achieving such non-equilibrium steady states presents experimental challenges, including maintaining constant fuel concentrations and managing waste accumulation. In the following section, I will explore different approaches to maintain chemically fueled self-assembling systems away from equilibrium and will elucidate the resulting non-equilibrium behaviors.

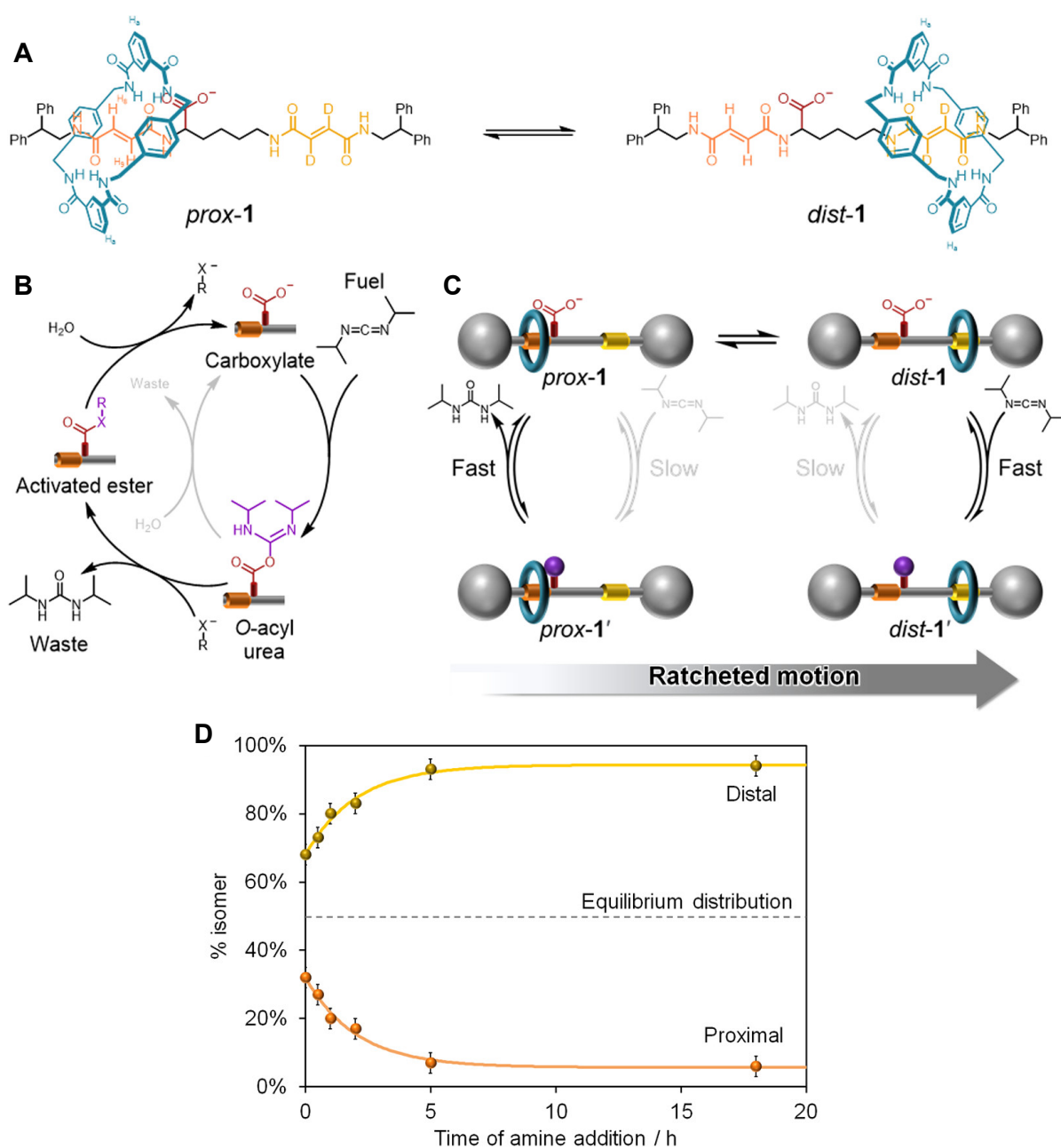
1.3.1 Continuous Fueling with Waste Accumulation

One of the simplest ways to transition from batch to more continuous fueling is the repetitive addition of batches of fuel. This results in the oscillation of the fuel concentration between the time intervals of addition. For sufficiently slow kinetics and short time intervals, only small deviations in the fuel and active product levels can be achieved. Since this does not represent an actual steady state, it is also called a pseudo-steady state.⁵¹ An example of such a steady state has been shown by Tena-Solsona *et al.*, in which primitive carboxylic acids were driven out-of-equilibrium with a carbodiimide to form an oil-in-water emulsion. Under batch fueling, the formed oil droplets showed accelerated ripening compared to classical Ostwald ripening, which could be further accelerated by keeping the system out of equilibrium in a pseudo-steady state.⁵¹

Another way of continuous fueling is the addition of a high excess of fuel in comparison to the catalytic species, which can establish a steady state. Even though the fuel level is continuously diminished in such a case, the change in the fuel level is small enough to be neglected, and steady levels of the activated species can be achieved.^{62,63} However, due to the necessary high excess of fuel, no varying steady-state levels can be achieved through the variation of the fuel level. Borsley *et al.* have reported an example of such a pseudo-steady state. In their system, the macrocycle distribution in a rotaxane-based information ratchet can be driven away from equilibrium using a carbodiimide fuel (Figure 12). Here, a carboxylate group that efficiently catalyzes the hydration of the carbodiimide was placed non-equidistant between the

1. Dissipative Structures

two macrocycle binding sites (Figure 12A). This design exhibits double kinetic gating (Figure 12B and C). Firstly, while the macrocycle resides on the binding site proximal to the carboxylic acid, the steric hindrance slows down the reaction of the fuel with the carboxylic acid, which would present a barrier for the macrocycle movement. Hydrogen bonding between the macrocycle and the activated carboxylic acid barrier accelerates hydrolysis and removes the barrier. Both effects reinforce each other and lead to a doubly kinetically gated ratchet that shows a 1:18 directionality that can be maintained away from equilibrium in a pseudo-steady state.⁶⁴



1. Dissipative Structures

Figure 12: Fuel-driven doubly kinetically gated ratchet in a NESS. A) The two states of the rotaxane-based information ratchet: In *prox-1*, the macrocycle resides on the binding site closest to the carboxylic acid barrier, and in *dist-1*, it resides on the binding site away from the carboxylic acid. **B)** The catalytic reaction cycle of fuel-to-waste conversion: The activation of the carboxylic acid by the fuel diisopropylcarbodiimide and the subsequent attack of a nucleophile acts as a steric barrier to the macrocycle movement. The activated ester is spontaneously hydrolyzed back to the initial carboxylic acid, completing the cycle. **C)** Hydrolysis of the activated ester and removal of the barrier are faster than the reactivation in the *prox-1* state. In the *dist-1* state, the activation of the carboxylic acid to form the barrier is faster than the hydrolysis of the activated ester. **D)** The isomer distribution can be frozen through quenching with an amine. The supply of excess fuel to the system keeps the distribution away from equilibrium in a non-equilibrium steady state. Adapted with permission from [64]. Copyright © 2021, American Chemical Society.

To add fuel continuously, syringe pumps can be utilized. By continuously stirring and adding small volumes of highly concentrated fuel stocks, steady levels of fuel and activated product can be achieved. Moreover, adjusting the inflow provides control over the fuel level within a broad range of steady states. In systems where the waste does not interfere with self-assembly kinetics, these non-equilibrium steady states can be sustained for extended periods of time, only ceasing when factors like dilution of the reaction solution or side reactions inhibit the system.⁴¹ However, in many systems, the waste cannot be neglected. Upon reaching a certain concentration, it can lead to poisoning or fatigue of the systems.⁶⁵⁻⁶⁸ However, the continuous supply of fuel alone is also not sufficient to maintain activated species out-of-equilibrium because the system can only be driven away from equilibrium as long as the fuel-to-waste ratio itself is away from equilibrium.⁴³

An example of such a system was shown by the group of Fletcher,⁶⁶ who developed a system in which a micelle-forming component **3** induces feedback on the reaction cycle through both the catalysis of its own formation from **1** and **2** and its breakdown into components **4** and **5** (Figure 13A). The initial precursor **1** of the micelle-forming component is regenerated from the breakdown product **4** through the use of H_2O_2 as the chemical fuel. Under steady-state conditions, they observed oscillations in the micelle population, which could be explained by five different stages of the reaction cycle (Figure 13B). In the first stage, the micellar component forms slowly, limited by the soluble amount of **2** diffusing from an oil reservoir into the aqueous phase. However, once micelles are formed, they catalyze their own formation by solubilizing component **2**, resulting in an exponential increase in micelles. This growth continues until the chemically fueled recovery of **1** from the breakdown product **4** becomes rate-limiting. This results in the dominating breakdown of the micellar component **3** through the reaction with **2**, and further release of **2** upon dissolution of the micelles accelerates the destruction of additional micelles. Upon complete depletion of **3**, any excess of solubilized **2** returns to the oil reservoir, restoring the original conditions of the system and enabling the next oscillation. These oscillations can be sustained for several days, and their frequency and amplitude can

1. Dissipative Structures

be tuned by varying the supply rate of the chemical fuel (Figure 13C). However, the accumulation of the waste product **5** leads to an increase in the frequency and amplitude of the oscillations (Figure 13D). Although the waste does not significantly interfere with the system on short timescales, it shows the importance of preventing the alteration of assemblies as well as the dampening or increase of the driven reaction caused by the accumulation of waste.

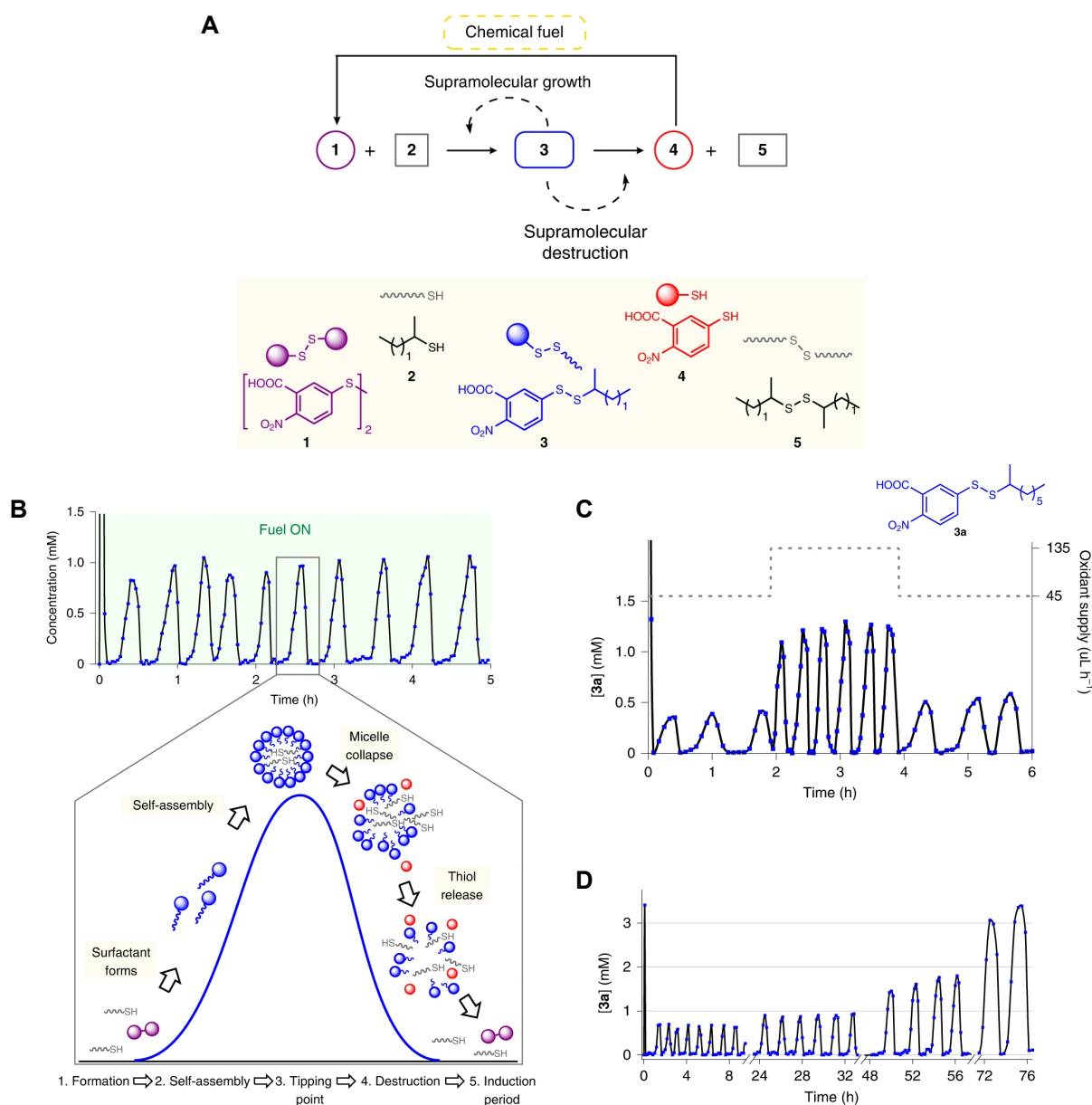


Figure 13: Autonomously oscillating supramolecular self-replicator. A) Schematic overview of the reaction cycle and its components that catalyze their own formation and breakdown. **B)** Oscillations in the concentration of **3** and schematic summary of the five stages of an oscillation. **C)** The frequency and amplitude of the oscillations are dependent on the continuous supply of the chemical fuel (oxidant). **D)** Oscillations can be sustained for several days, but the frequency and amplitude increase due to the

accumulation of waste **5**. Adapted with permission from [66]. Copyright © 2022, the Author(s), under exclusive license to Springer Nature Limited.

1.3.2 Continuous Fueling and Waste Removal

1.3.2.1 Continuously Stirred Tank Reactor

While the continuous addition of fuel to a system can be achieved as easily as pipetting it to the reaction solution, the selective removal of waste is more challenging. However, it is also possible to maintain a system in a non-equilibrium steady state while waste is removed non-selectively by employing a continuously stirred tank reactor (CSTR).

In such a setup, the fuel is added continuously through a syringe pump, but additionally, a part of the total reaction solution is removed continuously to prevent waste accumulation. Since waste removal in such a setup lacks selectivity, it leads to a depletion of the precursor and the product. Consequently, it is necessary to continuously replenish the precursor and other essential components. Although the entire reaction solution will eventually be replaced, this approach allows the maintenance of both fuel and product concentrations, thereby keeping the assemblies away from equilibrium.

Schnitter *et al.* used a CSTR setup to maintain *N*-Boc-protected aspartic acid away from equilibrium by the continuous addition of a carbodiimide (Figure 14A).⁶⁹ The activation of the precursor leads to the formation of the activated anhydride, which assembles into crystals. By continuously adding fuel and precursor while removing waste, both the anhydride and the assemblies could be kept in a steady state, as evidenced by a steady scattering rate and constant anhydride concentration (Figure 14B-E). Interestingly, their system exhibits different behaviors under steady-state conditions depending on the previous state of the system (Figure 14D-E). If the system is kept in a non-equilibrium steady state in the metastable zone of the phase diagram, whether there were already crystals or no assemblies in the system determines the formation of new assemblies (Figure 14F). With this approach, they created a bistable system capable of storing volatile memory under non-equilibrium steady-state conditions.

1. Dissipative Structures

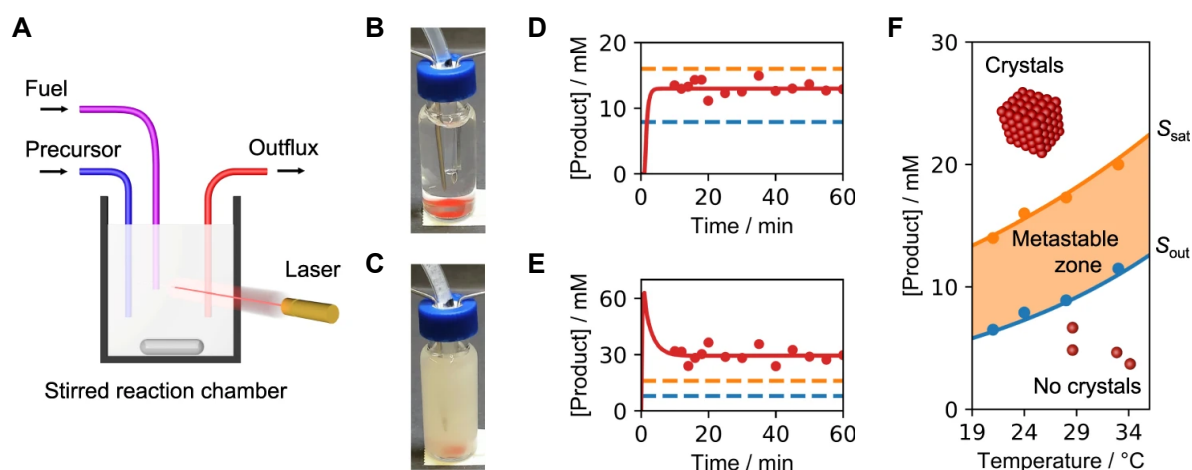


Figure 14: Bistability in a chemically fueled self-assembling system in a CSTR. **A)** Schematic representation of the CSTR setup. **B-C)** Representative photographs of the reaction solution with the same in and outflux of materials, but to C) an initial fuel spike was added, leading to the formation of assemblies. **D)** Product concentration measured by HPLC for B), where the system was started without assemblies. **E)** Product concentration measured by HPLC for C), where the system was started with an initial spike in the product concentration to induce assembly formation. **F)** Phase diagram of crystal formation. In the metastable zone, both crystals and no crystals can be present. Adapted with permission from [69]. Copyright © 2022, The Author(s).

1.3.2.2 Selective Diffusive Exchange

In a CSTR, it is possible to keep the system in various non-equilibrium steady states, but the continuous non-selective removal of waste comes with the cost of losing the oftentimes very precious precursors or other essential components of the system, which have to be continuously supplied together with the fuel. To transition to a non-equilibrium steady state in which the precursor is recycled by the system, it is therefore important to introduce selective removal of waste. One way of selective removal of the waste is to use the size difference of the waste in comparison to the precursor. Oftentimes, the fuel and waste molecules are rather small in comparison to the precursors, which often consist of several amino acids. The group of Hermans established a system to achieve non-equilibrium steady states using this size difference.⁶⁵ The reported system consists of a symmetric peptide derivative of perylene diimide (PDI) that contains the consensus peptide sequence for protein kinase A. This precursor can be phosphorylated twice by the kinase under the consumption of ATP. The resulting double phosphorylated p2-PDI species promoted the growth of the initially small PDI aggregates into bigger structures. The addition of a second enzyme λ -protein phosphatase, that catalyzes the dephosphorylation of p2-PDI to PDI, led to the disassembly of the larger aggregates, achieving an ATP-driven cycle. However, if the cycle was run by the batch wise addition of ATP, they were not able to refuel the system after it relaxed to its initial state. This was due to the accumulation of the waste ADP and phosphate (Pi). Especially Pi is a potent

1. Dissipative Structures

inhibitor for the enzyme λ -protein phosphatase and prevents, therefore, the further dephosphorylation of the activated p2-PDI and prevents disassembly. Using the size difference between ATP/ADP and PDI/p2-PDI as well as the enzymes, they could recover the system by dialyzing it against fresh buffer with a molecular weight cutoff of 2 kDa. To achieve a NESS, they clamped a dialysis cassette between two flow chambers which they could continuously flush with fresh ATP solution (Figure 15A and B). Through the dialysis membrane, ADP was continuously removed from the system, and ATP was continuously supplied and maintained at the concentrations applied in the flow chambers. With this setup, they could maintain the system in a non-equilibrium steady state as long as they kept the influx of ATP constant. Furthermore, they could also show that they can keep the system at interchangeable steady states depending on the conditions applied in the flow chambers (Figure 15C).

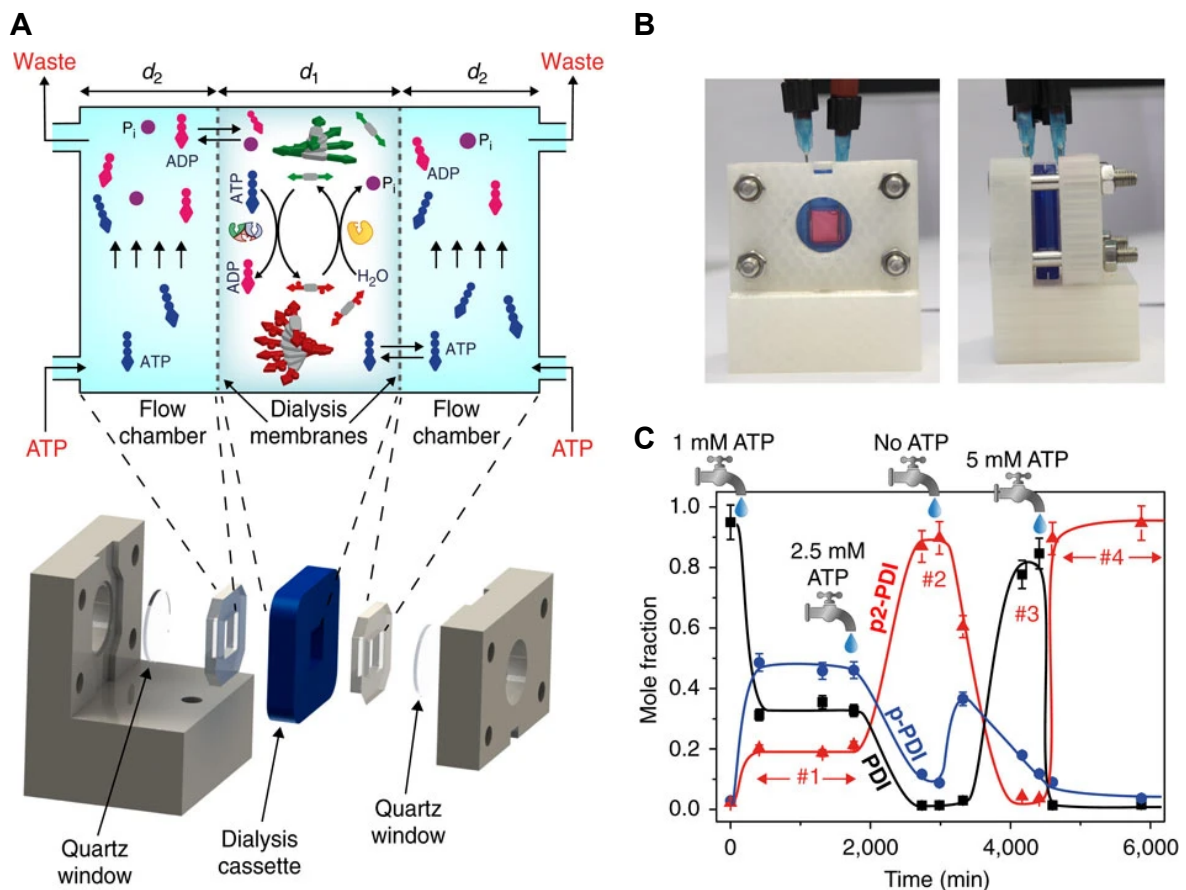


Figure 15: NESS through selective diffusive exchange of ATP and ADP in a flow chamber. A) Overview of the flow chamber setup and its construction. **B)** Photograph of the flow chamber setup. **C)** Concentrations of different reaction components in response to different supplied concentrations of ATP. Steady-state concentrations can be adjusted depending on the amount of ATP supplied. Adapted with permission from [65]. Copyright © 2017, The Author(s).

1.3.3 Conclusion

Batch fueling is the most common approach to drive chemically fueled systems away from equilibrium. It is easy to achieve experimentally and effectively demonstrates the fuel dependency and reversibility of the system. However, to investigate non-equilibrium behaviors beyond the transient formation of assemblies, it is often necessary to maintain systems in a NESS. Various methods have been developed to achieve a NESS, but most of them are highly specific to individual systems. Repetitive or excessive fuel addition suffers from waste accumulation, which usually leads to the poisoning of the system. In this regard, waste removal poses a significant challenge. While unselective removal of waste is relatively easy and universally achievable with CSTR, it limits the analysis of the assembly behavior due to the continuous exchange of all components of the system. Selective waste removal combined with continuous fuel addition approaches a true NESS but requires a tailored experimental setup for each system, and examples remain scarce.

To further explore and study the behaviors of chemically fueled systems resulting from their non-equilibrium nature, it is crucial to improve and broaden the applicability of NESS setups for different chemically fueled systems. These setups should be easy to implement while minimally intrusive to allow the undisturbed observation of emerging behaviors.

2. LLPS in a Confinement

In the previous chapters, I discussed how life-like non-equilibrium behaviors can be achieved in chemically fueled systems. However, not only designing such reaction networks or sustaining them away from equilibrium is challenging but also the observation and characterization of the resulting behaviors pose significant experimental problems.

Analyzing self-assembling systems is inherently complex, requiring a diverse range of analytical methods to gain a comprehensive understanding. Microscopic analysis presents challenges in observing the formation, dissolution, or dynamics of assemblies. In bulk setups, tracking small assemblies over time is hindered by their movement in and out of the imaging plane and their tendency to settle on the bottom of the observation chambers, significantly affecting their behavior. Moreover, assembly formation is often rapid, making it difficult to capture its dynamics unless the system is immediately imaged after sample preparation.

To address these issues, self-assembling systems have been enclosed within micrometer-sized confinements, such as vesicles or water-in-oil emulsions. In the following, I will explore various confinement-based approaches for analyzing liquid-liquid phase separating systems, which enhance microscopic analysis.

2.1 Dynamics of Phase Transitions in a Confinement

While the dynamics of LLPS play a crucial role in living organisms, our understanding of the mechanisms and dynamics involved in the formation, growth, and dissolution of structures like membraneless organelles remains limited.^{70,71} This can, in part, be attributed to the lack of suitable tools for monitoring dynamic events such as spinodal decomposition, nucleation and growth, coarsening, and dissolution of condensates. Droplet-based microfluidics offers a distinct advantage in this regard, as it facilitates rapid on-chip mixing of reagents, followed by both fast and extended analysis of the reaction mixture. This enables researchers to explore not only the thermodynamic properties of phase-separating systems but also to delve into their dynamic behaviors.⁷²

Linsenmeier *et al.* reported a microfluidic chip design capable of encapsulating components undergoing phase separation into microfluidic droplets. This setup allows for immediate microscopic analysis of the reaction mixture, enabling the observation of both the formation and growth of synthetic MLOs (Figure 16).⁷⁰ They observed that the volume of phase-separated material as well as their nucleation rate scaled linearly with the volume of the corresponding microfluidic droplet. This linear scaling of the nucleation rate is consistent with rare nucleation events from which they concluded that the formation of their synthetic MLOs

2. LLPS in a Confinement

followed a nucleation and growth mechanism. Furthermore, the coarsening of the synthetic MLOs was also influenced by the confinement. Due to the small size of the microfluidic droplets, the synthetic MLOs sedimented, leading to an increase in collision events compared to what would be expected for Brownian motion-driven collisions. However, in the presence of a hydrogel network within the microfluidic droplets, these collision events could be prevented, effectively halting the coarsening of the synthetic MLOs. This emphasizes the significance of the cytoskeleton in preventing MLO coalescence within cells.

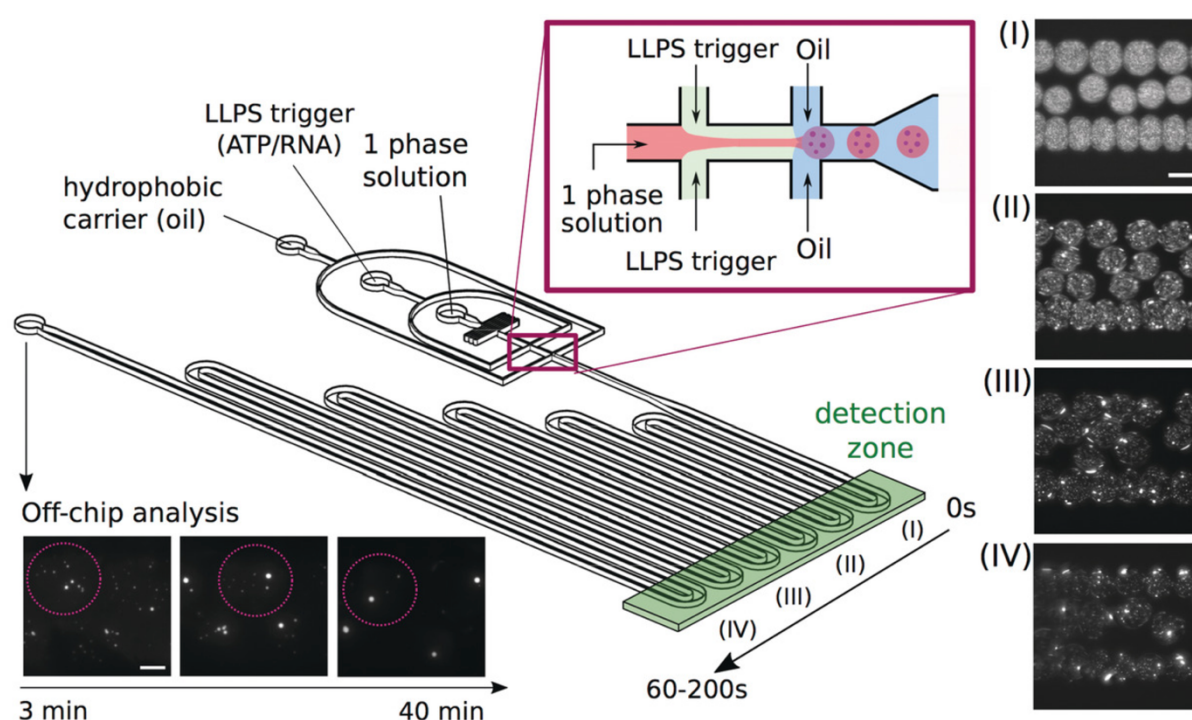


Figure 16: Droplet-based microfluidics to analyze dynamics of formation and growth of synthetic membraneless organelles. Schematic representation of the used microfluidic device. Two aqueous phases can be injected and encapsulated into microfluidic droplets by a carrier oil. The microfluidic droplets can be analyzed in the detection zone through image acquisition. Representative images of detection zones (I-IV) are shown, and microfluidic droplets can be further analyzed off-chip. Reprinted with permission from [70]. Copyright © 2019, Wiley-VCH Verlag.

2.2 Reversible LLPS in a Confinement

The immediate analysis of microfluidic droplets following the encapsulation of phase-separating components represents a promising approach for studying the dynamics of LLPS. However, this method typically requires the induction of phase separation through mixing of the initial components. Reversible phase separation requires the consecutive injection of reagents, which is possible but technically more challenging to achieve. Semi-permeable vesicles have also been used to encapsulate and study LLPS. One notable advantage of this approach is the ability to induce and dissolve phase separation reversibly by altering the

aqueous environment surrounding these vesicles. For example, the group of Dora Tang demonstrated the reversible formation and dissolution of coacervate-based droplets within lipid vesicles depending on the reversible protonation of polylysine.⁷³ At a pH above the pKa of lysin, the amino group is deprotonated, and polylysine cannot form complex coacervates with ATP due to the lack of attractive electrostatic interactions. However, reversible phase separation is induced upon protonation by decreasing the pH in the aqueous solution surrounding the vesicles. Interestingly, they could not only control the formation of coacervate-based droplets inside the vesicles but also induce an otherwise dormant enzymatic reaction inside the vesicles upon coacervation. Their system presents a synthetic model for reversible membraneless compartmentalization in biological systems that can control enzymatic activity. In another approach, the induction of LLPS in vesicles produced by droplet-based microfluidics was demonstrated.^{74,75} The group of Dekker presented a setup to produce SUVs with droplet-based microfluidics that consecutively enabled the induction of coacervation.⁷⁴ Initially, only polylysine was encapsulated inside the liposomes. Through embedding protein nanopores into the lipid bilayer, they were able to induce coacervation inside of the liposomes through the addition of ATP to the surrounding solution. Upon diffusion of ATP into the liposomes, coacervation between polylysine and ATP was induced. In an alternative approach, they were able to encapsulate all coacervation components into the liposomes and trigger coacervation consecutively through a change in pH in the external solution that also altered the pH inside of the liposomes without the need for pores in the lipid bilayer (Figure 17A).⁷⁶ Using the liposomes as a cell mimic, they further investigated the interactions of the coacervate-based droplets with the membrane of the liposomes (Figure 17B). For unmodified liposomes, they observed the homogenous nucleation of coacervate-based droplets throughout the liposomes, followed by their 3D diffusion throughout the liposome interior. The introduction of polyanionic lipids resulted in the initial homogenous nucleation of coacervate-based droplets throughout the liposomes, but after maturation, they preferentially localized and moved alongside the membrane. The lack of any morphological change to the coacervate-based droplets upon localization at the membrane was explained by the low strength of the coacervate-membrane interactions. The introduction of hydrophobic cholesterol-tagged RNA molecules into the membrane increased the interaction strength, resulting in the predominant nucleation of coacervates at the membrane and their consecutive wetting of the membrane.

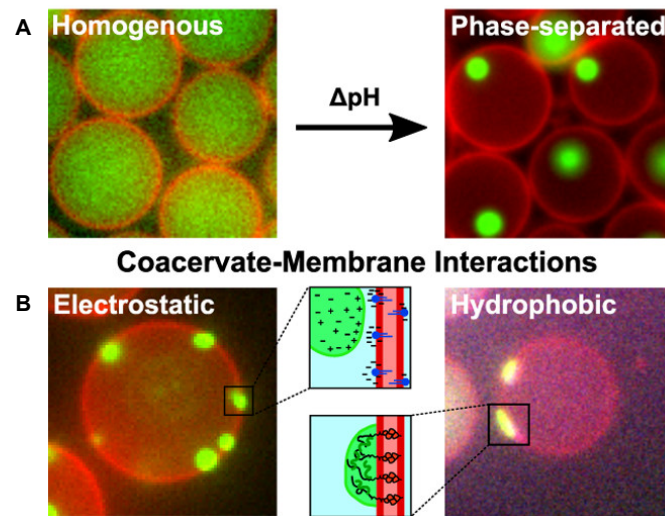


Figure 17: Reversible LLPS and membrane interaction in a confinement. A) A change in pH of the surrounding solution triggers LLPS inside the liposomes. **B)** In dependence on the membrane properties, coacervates reside at the surface of the liposomes (electrostatic) or even lose their regular spherical shape due to wetting (hydrophobic). Reprinted with permission from [76]. Copyright © 2022, American Chemical Society.

2.3 Conclusion

Droplet-based microfluidics has emerged as a valuable tool in analyzing LLPS systems. It allows improved analysis of dynamic behaviors like the formation of phase-separated droplets through rapid mixing or reversible induction of LLPS and immediate imaging of the samples. Furthermore, the encapsulation into cell-sized confinements can help to elucidate the influence of confinements on LLPS in cells. Until now, these approaches were mainly used to analyze the dynamics of passive droplets, but similar techniques should be applicable to study chemically fueled droplets. These droplets can undergo significant changes during their lifetime because their dynamics are closely linked to their reaction kinetics. This complexity makes it challenging to analyze their behaviors without the ability to track individual droplets over extended periods. The advantages of droplet-based microfluidics hold the potential to provide crucial insights into out-of-equilibrium behaviors that arise from continuous activation and deactivation in LLPS systems.

3. Aim of the Thesis

This thesis aimed to study non-equilibrium behaviors in chemically fueled active systems. Such behaviors are governed by the continuous consumption of energy that drives the system away from equilibrium. In Chapter 1, I discussed the unique properties that are accessible by driving systems away from equilibrium and why life would be impossible under equilibrium conditions. Inspired by life's constant avoidance of equilibrium and the resulting unique properties, artificial systems have been designed to mimic these properties. One of these systems is chemically regulated droplets, *i.e.*, active droplets. The properties of these droplets are governed by fluxes of droplet material, which are, in turn, regulated through chemical reactions. Although exciting properties like the suppression of Ostwald ripening, control over size and number, or even self-division of such droplets have been predicted by numerical calculations, experimental evidence has been lacking. To unravel these active properties, active coacervate-based droplets have been developed, which are also a model system for actively regulated membraneless organelles in living cells. However, despite tremendous progress in coupling the formation of such droplets to chemical reactions, it has been challenging to observe active behaviors due to limitations in the microscopic analysis as well as keeping such systems in a non-equilibrium steady state.

The first aim of this thesis was to study the dynamics of active coacervate-based droplets over their entire lifetime. The observation of dynamic behaviors for active droplets is often limited due to the short timescale of their kinetics. In general, the formation of active coacervate-based droplets is often too fast to be observed, and the analysis of all or individual droplets is complicated with a conventional microscopic setup. As described in Chapter 4, we were able to study droplets from their formation until their dissolution, both individually as well as collectively, through the encapsulation of the reaction cycle into micrometer-sized water-in-oil droplets using droplet-based microfluidics.

The second aim of this thesis was to sustain these active droplets in a non-equilibrium steady state to study the emergence of active behaviors. In Chapters 5 and 6, we show how to achieve a non-equilibrium steady state through continuous fueling of microreactors. Here, we observed that active droplets can undergo a morphological transition due to size-dependent gradients as well as oscillating cycles of nucleation, growth, fusion, and shrinkage.

The last aim of this thesis was to give a general guideline on the analysis of chemically fueled assemblies. In Chapter 7, we explain the synthesis and macroscopic to microscopic analysis of self-assembling systems and emphasize the need of different approaches on the example of chemically fueled crystals and fibers.

4. Evolution and Single-Droplet Analysis of Fuel-Driven Compartments by Droplet-Based Microfluidics

Abstract.

Membraneless organelles are formed via liquid-liquid phase separation, which is actively regulated through chemical reactions. Active droplets based on complex coacervation offer a valuable model to investigate such chemically regulated membraneless organelles, shedding light on their active regulatory mechanisms. Next to the formation, the dynamics in active droplets are also intertwined with the governing chemical reactions. However, the dynamics of active droplets are difficult to capture, and their analysis is often limited due to the short timescales of their kinetics. A promising way to improve the analysis of such systems is their encapsulation into micrometer-sized confinements. In this work, we used the benefits of confinement by encapsulating active droplets into water-in-oil droplets using droplet-based microfluidics. This approach enabled us to study the formation, the total volume evolution, and the behavior of individual active droplets. We discovered that not only the formation of active droplets is dictated by the fuel concentration but also their properties. Furthermore, we observed that active droplets predominantly grow through fusion, their decay starts simultaneously independent of their volume, and their decay rate scales with their initial volume. This approach will help to uncover new properties of active droplets by improving and simplifying the analysis of their dynamic properties.

This work has been published:

Title: Evolution and Single-Droplet Analysis of Fuel-Driven Compartments by Droplet-Based Microfluidics

Authors: Alexander M. Bergmann, Carsten Donau, Fabian Späth, Kevin Jahnke, Kerstin Göpfrich, Job Boekhoven

First published: 03. June 2022

Journal: *Angew. Chem. Int. Ed.*, **2022**, 61, e202203928

Publisher: Wiley-VCH GmbH

DOI: 10.1002/anie.202203928

Reprinted with permission from Wiley-VCH. Copyright © 2022 The Authors. Angewandte Chemie International Edition published by Wiley-VCH GmbH.

This section states the individual work of each author in the publication above. J. Boekhoven and A. M. Bergmann designed the experiments with inputs from all authors. A. M. Bergmann, C. Donau and F. Späth carried out the experiments. K. Göpfrich, K. Jahnke and A. M. Bergmann fabricated the microfluidic chips and designed the experimental setup. J. Boekhoven, A. M. Bergmann wrote the manuscript with inputs from all authors.



Protocells Hot Paper

How to cite: *Angew. Chem. Int. Ed.* **2022**, *61*, e202203928

International Edition: doi.org/10.1002/anie.202203928

German Edition: doi.org/10.1002/ange.202203928

Evolution and Single-Droplet Analysis of Fuel-Driven Compartments by Droplet-Based Microfluidics

Alexander M. Bergmann, Carsten Donau, Fabian Späth, Kevin Jahnke, Kerstin Göpfrich,* and Job Boekhoven*

Abstract: Active droplets are a great model for membraneless organelles. However, the analysis of these systems remains challenging and is often limited due to the short timescales of their kinetics. We used droplet-based microfluidics to encapsulate a fuel-driven cycle that drives phase separation into coacervate-based droplets to overcome this challenge. This approach enables the analysis of every coacervate-based droplet in the reaction container throughout its lifetime. We discovered that the fuel concentration dictates the formation of the coacervate-based droplets and their properties. We observed that coacervate-based droplets grow through fusion, decay simultaneously independent of their volume, and shrinkage rate scales with their initial volume. This method helps to further understand the regulation of membraneless organelles, and we believe the analysis of individual coacervate-based droplets enables future selection- or evolution-based studies.

Liquid-liquid phase separation (LLPS) as an underlying mechanism for forming membraneless organelles is attracting increasing attention due to its role in regulating intracellular processes. It is involved in the promotion^[1] and suppression^[2] of gene transcription, signal transduction,^[3] or stress response.^[4] These organelles have regulatory properties, but their formation and dissolution are also regulated through chemical reactions such as methylation^[5] or phosphorylation.^[6] There is increasing evidence that mis-

regulation of these organelles leads to diseases like amyotrophic lateral sclerosis.^[7] To better study the regulation of the formation and dissolution of these membraneless organelles, artificial LLPS systems have been developed. Reversible LLPS based on the principle of complex coacervation has been achieved through changes in pH,^[8] temperature,^[9] salt concentration, or in response to UV light.^[10] In these cases, the formation and dissolution of coacervate-based droplets are regulated by changes in their environment, shifting the system from one equilibrium position to another. Another approach is to regulate the formation and dissolution of these coacervate-based droplets by chemical reactions, as it is also observed for membraneless organelles in cells. This can be done through reversible phosphorylation^[11] or methylation^[12] with enzymes or entirely artificial through reversible anhydride formation with carbodiimides.^[13] Regulation by chemical reactions also opens a pathway for new emergent properties of these coacervate-based droplets. It has been predicted that life-like behavior like size control or self-division is possible for these active droplets.^[14]

However, microscopy analysis of active coacervate-based droplets has been limited. This limitation is partly because only a small fraction of the total reaction solution can be imaged. On the one hand, this leads to a bias depending on which part of the solution is imaged, e.g., imaging close or far away from the top or bottom coverslip can change the average size of the observed coacervate-based droplets. On the other hand, droplets cannot be tracked over their entire lifetime. Instead, a snapshot of some of the droplets is obtained. Finally, the time of mixing and imaging is relatively slow, as droplets can already form and grow in the first tens of seconds after mixing. These limitations are challenging for further developing active droplets and studying their behavior within a population.

Microfluidic technology is emerging as an essential tool in the analysis of LLPS systems,^[15] and especially droplet-based microfluidic techniques are valuable to overcome these limitations for the analysis of LLPS systems. It has been used to encapsulate coacervate-based droplets into cell-sized compartments like stabilized water-in-oil droplets^[9b,16] and lipid vesicles.^[8,17] This enables high-throughput screening of coacervate-based droplets regarding their phase transition behavior^[18] or viscosity,^[19] and the measurement of partitioning coefficients of different molecules or the influence of coacervate-based droplets on reaction rates.^[20] Encapsulation into liposomes is an efficient way of studying pH-responsive coacervate-based droplets,

[*] A. M. Bergmann, C. Donau, F. Späth, J. Boekhoven
Department of Chemistry, Technical University of Munich
Lichtenbergstrasse 4, 85748 Garching (Germany)
E-mail: job.boekhoven@tum.de

K. Jahnke, K. Göpfrich
Biophysical Engineering Group, Max Planck Institute for Medical
Research
Jahnstraße 29, 69120 Heidelberg (Germany)
E-mail: kerstin.goepfrich@mr.mpg.de

K. Jahnke, K. Göpfrich
Department of Physics and Astronomy, Heidelberg University
69120 Heidelberg (Germany)

© 2022 The Authors. *Angewandte Chemie International Edition* published by Wiley-VCH GmbH. This is an open access article under the terms of the Creative Commons Attribution License, which permits use, distribution and reproduction in any medium, provided the original work is properly cited.

i.e., understanding coacervate-membrane interactions^[8b] and the activation of dormant enzymatic reactions by the formation of coacervate-based droplets.^[8a] Less attention has been paid to studying dynamic properties like nucleation^[16,21] or dissolution of active coacervate-based droplets. In particular, fuel-driven, active droplets are an exciting target for these analyses as their properties are highly dynamic and switch from nucleation, growth, and collapse through dissolution and self-division in minutes.

Therefore, this work aims to introduce a method that allows us to analyze the behavior of every fuel-driven active droplet formed throughout its lifetime in an experiment. Thus, we use a microfluidic setup to analyze a fuel-driven LLPS system in a confined volume. This allows simultaneous analysis of every droplet in the reaction volume immediately after the start of the reaction cycle and tracking and analysis of the behavior of individual droplets from their nucleation to dissolution.

In this work, we use a fuel-driven reaction cycle coupled with the formation of coacervate-based droplets that we recently introduced.^[13] The system consists of a precursor peptide Ac-F(RG)₃D-OH and either the polyanion polystyrene sulfonate (pSS) or polyuridylic acid (pU). The aspartic acid moiety of the peptide precursor can be activated to its corresponding anhydride through the reaction with 1-ethyl-3-(3-dimethylaminopropyl) carbodiimide (EDC) as the fuel (Figure 1a). The activated peptide (i.e., the anhydride)

rapidly hydrolyzes back to the initial precursor peptide. The constant fuel-driven activation and deactivation continue until all fuel is depleted. Thus, the addition of fuel results in a population of droplets regulated by the reaction kinetics of activation and deactivation when the reaction is coupled to droplet formation. To do so, the peptide was designed such that activation leads to the negation of two negative charges and converts the overall charge of the peptide from +1 to +3. In its activated state, the affinity of the peptide for the polyanion increases, and, when sufficient peptide has been activated, phase separation through complex coacervation can occur (Figure 1b). However, in the droplet, the peptide can be deactivated through hydrolysis, after which it leaves the droplet. Thus, the droplets are governed by constant in- and out-flux of droplet materials which is regulated through the kinetics of activation and deactivation. Coacervate-based droplets are thus present in the system as long as a sufficient product concentration can be maintained through fuel consumption.

To better capture this dynamic behavior by microscopy, we introduced a droplet-generating microfluidic platform suitable for fuel-driven self-assembling systems (Figure 1c). The precursor and EDC solutions are injected via two different inlets in the design. Due to the laminar flow in the microfluidic device, no significant mixing happens before the encapsulation into the microfluidic droplets.^[22] Surfactant-stabilized microfluidic water-in-perfluorinated oil drop-

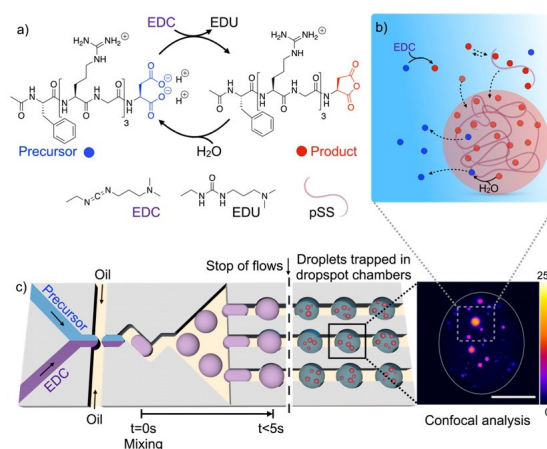


Figure 1. Schematic representation of the reaction cycle and the microfluidic setup. a) Reaction cycle of the precursor Ac-F(RG)₃D-OH with EDC. EDC converts the +1 charged precursor to the +3 charged anhydride product. The product can then hydrolyze back to the precursor. This cycle continues until EDC is depleted. b) Formation and dissolution of coacervates in a confined volume depending on the reaction cycle. The product (red) forms coacervates with polystyrene sulfonate (pSS). Once the product is hydrolyzed back to the precursor (blue), the coacervates dissolve. c) Schematic representation of the microfluidic chip that is used for microfluidic droplet formation and trapping of these droplets in droplet chambers. EDC and precursor solutions are supplied from two different channels and are mixed right after the formation of the microfluidic droplets. Upon stopping the flow, the microfluidic droplets are trapped in the droplet chambers. In these chambers, the microfluidic droplets are imaged via confocal time-lapse imaging by excitation of sulforhodamine B for coacervate-based droplets with pSS or Cy3-A15 for coacervate-based droplets with pU at 552 nm. The pseudocolor-coded confocal image represents a maximum z-projection of a z-stack throughout one microfluidic droplet. The grey value scale from 0 to 255 is given next to the image. The grey line represents the periphery of the microfluidic droplet. The scale bar represents 20 μm .

lets of equal size are produced at a T-junction. The two fuel and precursor phases are homogenized directly after their encapsulation in the microfluidic droplet through convective mixing, which is considered the starting time of the fuel-driven reaction cycle. In the following seconds, the microfluidic droplets pass through an array of so-called dropspot chambers, which hold the microfluidic droplets in place once the flow of all inlets is stopped.^[23] To control the flow rates, we use a pressure controller instead of syringe pumps to ensure an almost immediate flow stop. Once the microfluidic droplets are entrapped in one of the dropspot chambers, they are imaged via confocal microscopy in an XYZ time series. Due to the minimal microfluidic droplet volume of 33 pL, it is possible to image the entire reaction volume via z-stack imaging with a time resolution as short as 5 seconds per z-stack (time-resolution is limited by the image acquisition time of the microscope).

In other words, we can track the emergence, evolution, and decay of each coacervate-based droplet in the microfluidic droplet at an interval down to 5 seconds. We first analyzed whether the droplets formed in bulk and microfluidic droplets behaved similarly. To create the pU-based droplets in the microfluidic device, we combined the peptide stream with the fuel stream in a 1:1 ratio such that a 33 ± 4 pL microfluidic droplet contained 23 mM peptide, 4.1 mM pU, and 25 mM fuel to form coacervate-based droplets and 0.1 μ M Cy3-tagged A15 hybridized to pU to visualize them by confocal microscopy (Figure S1a–d, Figure S2a–d). The microfluidic droplet was captured less than 5 seconds after its creation and analyzed by confocal microscopy through sequential Z-stack imaging (17.4 seconds per stack). Similar to experiments in bulk, in the first minutes, the droplets grew predominantly through fusion (Figure 2a, Movie S1, Figure S3b). Around 10 minutes into the cycle, the droplets started to form vacuoles, after which the droplets decayed and divided into smaller droplets (Figure S3c and d). Excitingly, because of the rapid mixing and imaging in microfluidics, we could, for the first time, see the nucleation of the droplets (Figure 2a, Figure S3a). We counted the number and measured the volume of each coacervate-based droplet throughout the reaction cycle. The average droplet volume increased steadily in the first minutes due to the fusion-induced growth (Figures 2b and c). After 10 minutes, it suddenly collapses due to droplet decay. Notably, the evolution of the average droplet volume and the total droplet volume was similar in microfluidic confinement and in bulk-generated droplets.

We only observed significantly dissimilar behavior if we used coacervate-based droplets with pSS as the polyanion and if they reached diameters greater than a few micrometers. For example, when 10 mM peptide, 5 mM pSS, and 10 mM EDC were used, the diameter was relatively large, and we found that the droplet size of the coacervate-based droplets grew faster in the confinement of microfluidic droplets than in bulk. (Figure S4a and b). We also observed that in these cases, almost all of the coacervate-based droplets were lying at the bottom of the microfluidic droplet (Figure S4c and d). These observations can be explained by gravitationally induced fusion which has been reported

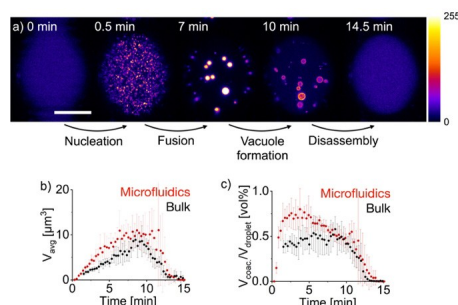


Figure 2. Comparison of the behavior of coacervate-based droplets in the bulk and the microfluidic setup. Conditions are 23 mM Ac-F(RG)₃D-OH, 4.1 mM pU, 0.1 μ M Cy3-A15 and 200 mM MES at pH 5.3 with 25 mM EDC. a) Representative images over one cycle of coacervate assembly and disassembly in a 33 pL water droplet entrapped in a microfluidic dropspot chamber. Images are recorded by excitation of Cy3-A15 at 552 nm. The pseudocolor-coded confocal image represents a maximum z-projection of a z-stack throughout one microfluidic droplet. The grey value scale from 0 to 255 is given next to the image. The scale bar represents 20 μ m. b, c) Comparison of the average and the total volume of pU droplets between the microfluidic and the bulk setup. The total volume is given as volume percent, defined as the total volume of coacervate-based droplets divided by the volume of the microfluidic droplet or the imaged volume for the bulk setup. Error bars represent the standard deviation of 5 independent experiments.

previously in confined volumes,^[16] i.e., due to the small volume of their container, droplets settle and fuse at the increased local concentration at the bottom of their microfluidic container. This effect is less pronounced for pU coacervates, most likely, because pU coacervates are less dense than pSS coacervates (Figure S5a and b).

Due to the fast mixing and imaging possible, we observed, for the first time, the nucleation and growth of the coacervate-based droplets (Figure 3a, Supporting Information Movie 2). The fluorescence was homogeneously distributed directly after the microfluidic droplet was created and captured in the device, but it coarsened with time. Within tens of seconds, droplets distinguishable from background fluorescence were detected. We define that time, i.e., when droplets with a diameter larger than 400 nm were detected, as the nucleation time. This definition is likely an overestimation of the actual nucleation due to the limited ability of light-based microscopy to detect smaller particles. We analyzed the influence of the fuel, the peptide precursor, and the pSS concentration on the nucleation time. We observed that more coacervate-based droplets were formed for higher EDC concentrations at lower nucleation times (Figure 3b and c, Figure S6g), i.e., the nucleation time decreases from 0.67 ± 0.08 min for 10 mM EDC to 0.23 ± 0.02 min for 30 mM EDC. We explain the observation because the anhydride concentration rises more rapidly and thus crosses the critical concentration for binodal or even spinodal decomposition.^[24] To verify this explanation, we used a previously written kinetic model. Briefly, the kinetic

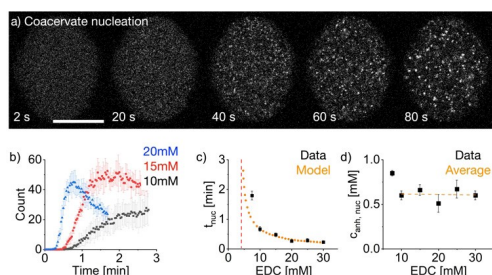


Figure 3. Analysis of coacervate-based droplet formation. All experiments are performed with conditions of 8 mM Ac-F(RG)₃D-OH, 5 mM pSS, 0.1 μ M sulforhodamine B, and 200 mM MES at pH 5.3 with varying fuel concentrations. a) Representative images of coacervates' initial formation and growth when 20 mM of EDC is added. Images are recorded by excitation of sulforhodamine B at 552 nm. The images show one z-plane in the middle of a microfluidic droplet. The scale bar represents 20 μ m. b) Number of coacervate-based droplets depending on the amount of EDC added. Coacervate-based droplets are counted in one z-plane in the middle of a microfluidic droplet over the first 3 min after the start of the reaction cycle. Error bars represent the standard deviation of at least 9 measurements from 3 independent experiments. c) The time the first coacervate-based droplet could be detected (t_{nuc}) is shown as a function of the amount of EDC added. Error bars represent the standard deviation of at least 9 measurements from 3 independent experiments. The orange dotted line represents the nucleation times calculated by the kinetic model depending on the EDC concentration. The red line represents the EDC concentration below which no fuel-driven nucleation of coacervate-based droplets is possible according to the kinetic model. d) Anhydride concentration for different EDC concentrations at the time of nucleation. The kinetic model calculates anhydride concentrations. The orange dotted line represents the average anhydride concentration needed to nucleate coacervate-based droplets. Error bars are calculated from the standard deviation of the nucleation times.

model calculates the concentration of all reagents of the reaction cycle for every second in the experiments through a set of differential equations. The model assumes a homogeneous solution, i.e., it does not consider the droplet material's phase separation. We can extract the kinetic model's kinetics of activation and deactivation, i.e., the activation constant k_1 and the deactivation constant k_4 (Supporting Information). Indeed, when we correlate the nucleation times with the anhydride concentrations predicted by the kinetic model, we find that nucleation occurred at an anhydride concentration of 0.61 mM, independent of the amount of fuel added (Figure 3d). Using this concentration, we can predict the dependence of the nucleation time on the fuel concentration with the kinetic model (Figure 3c), giving us a minimum concentration of 4.7 mM EDC needed to induce coacervation. Additionally, we found that with increasing precursor concentration, the nucleation time decreases (Figure S6a). The kinetics of the reaction cycle can also explain this observation since the activation reaction is a second-order reaction and therefore scales both with the fuel and the precursor concentration. However, suppose we correlate the nucleation time again to the predicted anhydride concentrations. In that case, we observe

that the anhydride concentration needed for nucleation decreases with increasing precursor concentrations (Figure S6b and h). We explain this because the precursor already has a particular affinity to the polyanion. Therefore, an increased precursor concentration reduces the amount of anhydride needed to induce coacervation. In contrast, increasing the pSS concentration increased the nucleation time because the amount of anhydride needed to induce coacervation scales with the pSS concentration (Figure S6d, e, and i).

There are different methods to determine the total volume of the separated phase, like centrifugation^[13a] or confocal microscopy.^[25] Centrifugation requires sample volumes of several 100 μ L for accurate determination. In contrast, confocal microscopy suffers from an inhomogeneous distribution of the coacervate-based droplets, especially in the z-direction throughout the sample. Through encapsulation into microfluidic droplets, the inhomogeneous distribution in the z-direction can be overcome, but time-resolved measurements remain challenging.^[8,16] With the microfluidic setup presented, it is possible to determine the total volume of the phase-separated droplets, as a function of time, from their nucleation until their dissolution. First, we compared the total volumes measured by centrifugation to those measured in the microfluidic setup. To avoid errors due to the time-dependence of the total volume in fuel-driven LLPS systems, we used a static LLPS-system. Specifically, we used Ac-F(RG)₃N-NH₂, i.e., a mimic of our active product that is permanently 3+ because its carboxylates are amidated. We confirmed that the total volumes measured with our microfluidic setup matched the total volumes measured through established methods (Figure S7a and b).

Next, we used the active droplets and tested how the fuel, the peptide precursor, and the pSS concentration influenced the maximum total volume of the coacervate-based phase. The amount of fuel added determined the total volume of coacervate-based droplets (Figure 4a). However, quantitative analysis showed that the total volume only increased until an EDC concentration of about 20–25 mM, after which it, surprisingly, leveled off (Figure 4b and c, Figure S8a). The complete conversion of the precursor cannot explain the decline in the anhydride (Figure S6g), and centrifugation of the non-fuel-driven LLPS system with different pseudo-anhydride to precursor ratios confirmed that upon reaching a specific precursor conversion, the total volume of coacervate-based droplets is not increasing further (Figure S8d). Moreover, we observed that the time coacervate-based droplets remained non-spherical after fusion increased with higher EDC concentrations (Figure 4e, Figure S9a and b). Both observations can be explained by increased viscosity of the droplet phase with increasing fuel, i.e., a denser phase would imply a smaller volume and slower droplet fusion. FRAP experiments on the diffusivity of NBD-labeled precursor confirmed that the diffusivity inside the coacervate-based droplets decreased with increasing EDC (Figure 4d, Figure S10a–d). To verify that the decrease in diffusivity results from the peptide product and is not induced directly by the EDC itself, we performed

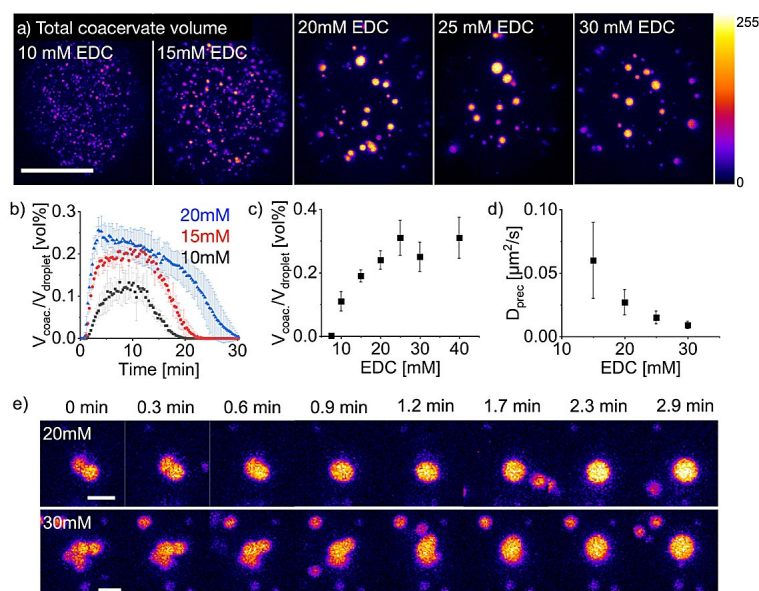


Figure 4. Analysis of the total volume of coacervate-based droplets and their viscosity. All conditions are 8 mM Ac-F(RG)₃D-OH, 5 mM pSS, and 200 mM MES at pH 5.3 with varying fuel concentrations. a) Images of the coacervation cycle showing the maximum amount of coacervate volume at different EDC concentrations. Images are recorded by excitation of sulforhodamine B at 552 nm. The pseudocolor-coded confocal images represent a maximum z-projection of a z-stack throughout one microfluidic droplet. The grey value scale is given next to the images. The scale bar represents 20 µm. b) Analysis of the total volume of coacervate-based droplets over the entire reaction cycle. The total volume is given as volume percent, defined as the total volume of coacervate-based droplets divided by the total volume of the microfluidic droplet. Error bars represent the standard deviation of 3 experiments. c) Maximum total volume of coacervate-based droplets as a function of the EDC concentration. Error bars represent the standard deviation of 3 experiments. d) The diffusivity of NBD-labeled product inside of coacervate-based droplets. Error bars represent the standard deviation of 9 experiments. e) Time series of droplet fusion. Fusion is drastically slower at increased EDC concentrations. The depicted time represents the time of the fusion event and not the actual time in the reaction cycle. Images are recorded by excitation of sulforhodamine B at 552 nm. The scale bar represents 2 µm.

similar FRAP experiments on the non-dynamic coacervate-based droplets with the static Ac-F(RG)₃N-NH₂ as peptide (Figure S8c). We observe the same behavior for the dye sulforhodamine B (Figure S8b). Those experiments confirmed that diffusivity decreases by increasing the peptide to precursor ratio until no more liquid droplets are formed. Instead, a more solid-like precipitate is observed. We hypothesize that from around 25 mM EDC, no further polyanion is recruited into the coacervate-based droplets upon further increasing the fuel concentration. Further increasing the fuel, and thus the amount of anhydride leads to replacing precursor with anhydride molecules in the coacervate-based droplets. The higher affinity of anhydride for pSS leads to a denser packing of the coacervate-based droplets and hence a stagnation in the total volume increase. For verification, we conducted fluorescence partitioning experiments with non-dynamic droplets using Ac-F(RG)₃N-NH₂ as a model peptide for the anhydride. For non-dynamic coacervate-based droplets, we observed that the pSS recruitment into the droplets only increased up to 2 mM of the model anhydride and leveled off afterward (Figure S11a).

In contrast, the precursor recruited into the coacervate-based droplets decreased with increasing model anhydride concentrations (Figure S11b). We observed similar total peptide amounts recruiting into the coacervate-based droplets for the fuel-driven system for 20 mM and 30 mM EDC (Figure S11c). These experiments conclude that the anhydride to precursor ratio in the droplets increased. Thus, more fuel leads to more droplet material, but it also leads to a denser packing of the droplet material.

A significant advantage of our experimental setup is that each coacervate-based droplet can be followed throughout its lifetime. In perspective, droplets prepared in larger containers are impossible to track due to Brownian motion in and out of the imaging area. Thus, we tracked the emergence, motion, fusion, and decay of an entire population of coacervate-based droplets for the first time. We used automated particle-tracking^[26] and manually optimized the trajectory linking and tracing. In the first 1.5 min, despite the small volume of the microfluidic droplet, it was impossible to reliably track individual coacervate-based droplets because of their small size and fast movement.

From there on, we could identify 39 coacervate-based droplets, and we tracked their motion, fusion events, and decay pathways (Figure 5a and b, Supporting Information Movie 3). From the collective data, we observed several new behaviors. First, we found that coacervate-based droplets fused more frequently than we expected, i.e., all 39 droplets fused more than once until only three droplets remained at 12.6 minutes. We color-coded these three droplets and the droplets they originated from before fusion events cyan, orange and green. The droplets fused 19 (orange), 13 (cyan), and 3 (green) times, respectively. We found that coacervate-based droplets did not move far between fusion events. In other words, the last three droplets were roughly in the center of all of their original droplets. This confirms there is no convective flow inside the microfluidic droplet, and the coacervates move exclusively by Brownian motion.

The droplets' tracking data allowed us to follow the "life" of every individual droplet, which offered insights into the behaviors of a droplet on an individual level. For example, the individual volume of every coacervate is tracked (Figure 5c). In that plot, we color-coded the data points based on the color-coding of the last three droplets (cyan, orange, and green). To make the plot comprehensible, we only show 12 droplets. When a track remains horizontal, the droplet neither grows nor shrinks, while a sudden increase in the track represents a fusion event. From these tracks, we can conclude that between 2 to 10 minutes, the droplet size is relatively stable, i.e., they do not grow or shrink.

The primary mechanism of growth in this timeframe is fusion. Coalescence has been reported as the primary mechanism for droplet growth.^[16] It is in line with recent findings that coacervate-based droplets do not undergo major Ostwald ripening, or ripening can even be suppressed.^[27] Then, after 10 minutes, all three remaining droplets start to shrink following an exponential decay until the droplet size falls below the detection limit of the tracking software. In the decay profile of the droplets, we found another new behavior. The rate of the decay of the droplets scales with the droplet volume. The greater the volume, the faster the droplets decay. This first-order decay seems to suggest that the pseudo-first-order of the volume loss per unit of time, i.e., the slope of these lines, is the same for each of the three remaining droplets (Figure S12a and b), which indicates that the hydrolysis of the anhydride is the rate-determining step for the droplet decay and not the disassembly of the precursor molecules. Additionally, the exponential volume decay can be captured well using only the kinetic model's anhydride hydrolysis constant (k_d). The calculated volume decay slightly overestimates the measured volume decay, most likely due to a residual activation that is still happening in the system (Figure S12b). The correlation between the anhydride hydrolysis and the loss of droplet material was strong even at high EDC concentrations, where droplets become more viscous (Figure S13a). We explain this observation because the reduced diffusivity at high EDC concentrations is not constant throughout the reaction cycle but tends to increase again at the end of the cycle.

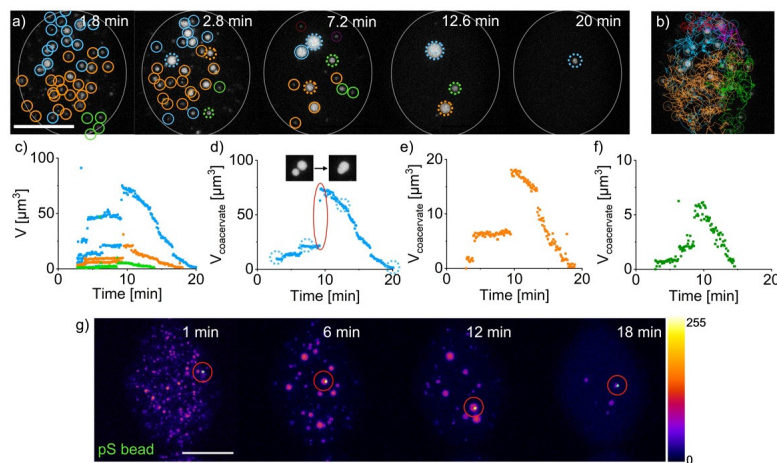


Figure 5. Tracking of coacervate-based droplets in a microfluidic droplet. a) A z-projection image time series. All droplets that fuse are assigned to the same population and marked with the same color. A solid grey circle marks the periphery of the microfluidic droplet. The dotted circles mark the coacervate-based droplet that is tracked under (d)–(f). b) The combined pathways of every droplet of the different populations. c) Volumes of every coacervate-based droplet of the different populations detected in the microfluidic droplet. d)–f) The volume of one coacervate-based droplet the population picked at 2.8 min and followed until its dissolution. A fusion event is highlighted. g) The same experiment as above, but with a blue-fluorescent pS bead. The bead incorporates into a coacervate-based droplet and remains incorporated until its dissolution. The grey value scale is shown next to the images. All scale bars represent 20 μm . All conditions are 10 mM Ac-F(RG)₃D-OH, 5 mM pSS and 0.1 μM sulforhodamine B in 200 mM MES at pH 5.3.

Therefore, coacervate-based droplets get more liquid towards the end of the reaction cycle when the amount of activated species is reduced, and no diffusion limitation is observed for the dissolution of the coacervate-based droplets. The decrease in the viscosity and, therefore, the increase in the diffusivity throughout the cycle can be observed by a reduction in the fusion time from 1.5 min at the start of the reaction cycle to less than 0.3 min right before the dissolution of the coacervate-based droplets occurs (Figure S13b). The close resemblance of volume decay and anhydride decay emphasizes that our coacervate-based droplets are dynamic. The identical shrinkage rate constant also leads to a longer lifetime the bigger the coacervate-based droplets are, as they can maintain a sufficient size for a more extended period.

We can also analyze the average likelihood of fusion for coacervate-based droplets depending on the EDC concentration (Figures S14a and b). Here, we observe that the fusion rate scales with the EDC concentration in the first minutes. We explain this trend by faster growth in the average volume of the coacervate-based droplets and the resulting higher likelihood of fusion. For fuel concentrations above 20 mM EDC the fusion rate declines significantly after 5 minutes. In comparison, experiments with fuel concentrations below 20 mM EDC show a more homogeneous fusion rate throughout the reaction cycle. For high EDC concentrations, the rapid decrease in the number of coacervate-based droplets and their decreased mobility due to their bigger average size leads to a decreased likelihood of droplet fusion.

When we followed the life of a single droplet, we found that it underwent three major fusion events between 3 and 12 minutes (Figure 5d). Each of the three fusion events was characterized by a jump in its volume which further corroborates the growth-through-fusion hypothesis. This fusion behavior was observed for most droplets (Figures 5e and f). This setup makes it possible to analyze the collective behavior of coacervate-based droplets and each droplet's individual "life". Furthermore, we believe that tracking individual coacervates opens the possibility of future selection or evolution-based studies. This could, for example, be achieved by introducing one enzyme-coated micrometer-sized particle per reaction chamber that is incorporated into the coacervate-based droplets. To demonstrate this feature, we introduced a single polystyrene bead (pS bead) into the microfluidic droplets (Figure 5g). A coacervate-based droplet takes up this unfunctionalized pS bead and remains in the droplet until dissolution. The unfunctionalized pS beads do not affect the behavior of the coacervate-based droplet. If the surface of this bead were catalytically active, its activity would only alter the behavior of this single droplet, giving it a potential advantage or disadvantage over others.

We successfully imaged the entire life-cycle of fuel-driven active droplets enabled by a microfluidic system for droplet formation and analysis. With the method, we found four new behaviors in our active droplets. The droplets nucleate rapidly, but the kinetics of the reaction cycle can tune the nucleation time, i.e., the nucleation time directly

follows the rate of anhydride formation. The droplets grow because of fusion, they fuse frequently, and their frequency of fusion at the beginning of the reaction cycle scales with the fuel concentration. However, the droplet's density increases with an increasing amount of fuel added, making the fusion process slower. The droplets decay at roughly the same timepoint, the shrinkage rate constant is independent of their volume and is equal to the hydrolysis rate constant of the activated species.

The advantages of studying our droplets in microfluidics combined with a dropspot chamber can be used with other active systems. We anticipate that the method will be applied to study other chemically fueled systems in more detail. We also anticipate that this setup will be handy for evolution-based experiments where droplets will compete for scarce resources and the future observation of self-dividing or self-reproducing droplets systems.

Acknowledgements

The BoekhovenLab is grateful for support from the TUM Innovation Network—RISE funded through the Excellence Strategy. J.B. and K.G. are grateful for funding from the Max Planck School Matter to Life supported by the German Federal Ministry of Education and Research (BMBF) in collaboration with the Max Planck Society. K.G. received funding from the Deutsche Forschungsgemeinschaft (DFG, German Research Foundation) under Germany's Excellence Strategy via the Excellence Cluster 3D Matter Made to Order (EXC-2082/1–390761711) and the Max Planck Society. K.J. thanks the Carl Zeiss and the Joachim Herz Foundation for financial support. Open Access funding enabled and organized by Projekt DEAL.

Conflict of Interest

The authors declare no conflict of interest.

Data Availability Statement

The data that support the findings of this study are available from the corresponding author upon request.

Keywords: Artificial Organelles · Droplet-Based Microfluidics · Nonequilibrium Processes · Phase Transitions

- [1] K. M. Harlen, L. S. Churchman, *Nat. Rev. Mol. Cell Biol.* **2017**, *18*, 263–273.
- [2] A. G. Larson, D. Elnatan, M. M. Keenen, M. J. Trnka, J. B. Johnston, A. L. Burlingame, D. A. Agard, S. Redding, G. J. Narlikar, *Nature* **2017**, *547*, 236–240.
- [3] X. Su, J. A. Ditlev, E. Hui, W. Xing, S. Banjade, J. Okrut, D. S. King, J. Taunton, M. K. Rosen, R. D. Vale, *Science* **2016**, *352*, 595–599.
- [4] a) P. Anderson, N. Kedersha, *Curr. Biol.* **2009**, *19*, R397–R398; b) J. R. Buchan, R. Parker, *Mol. Cell* **2009**, *36*, 932–941.

- [5] S. Qamar, G. Wang, S. J. Randle, F. S. Ruggeri, J. A. Varela, J. Q. Lin, E. C. Phillips, A. Miyashita, D. Williams, F. Ströhl, W. Meadows, R. Ferry, V. J. Dardov, G. G. Tartaglia, L. A. Farrer, G. S. Kaminski Schierle, C. F. Kaminski, C. E. Holt, P. E. Fraser, G. Schmitt-Ulms, D. Klenerman, T. Knowles, M. Vendruscolo, P. St George-Hyslop, *Cell* **2018**, *173*, 720–734, e715.
- [6] a) A. K. Rai, J.-X. Chen, M. Selbach, L. Pelkmans, *Nature* **2018**, *559*, 211–216; b) J. T. Wang, J. Smith, B. C. Chen, H. Schmidt, D. Rasoloson, A. Paix, B. G. Lambrus, D. Calidas, E. Betzig, G. Seydoux, *eLife* **2014**, *3*, e04591.
- [7] a) A. E. Conicella, G. H. Zerze, J. Mittal, N. L. Fawzi, *Structure* **2016**, *24*, 1537–1549; b) A. Patel, Hyun O. Lee, L. Jawerth, S. Maharana, M. Jahnke, Marco Y. Hein, S. Stoyanov, J. Mahamid, S. Saha, Titus M. Franzmann, A. Pozniakowski, I. Poser, N. Maghelli, Loïc A. Royer, M. Weigert, Eugene W. Myers, S. Grill, D. Drechsel, Anthony A. Hyman, S. Alberti, *Cell* **2015**, *162*, 1066–1077.
- [8] a) C. Love, J. Steinkuhler, D. T. Gonzales, N. Yandrapalli, T. Robinson, R. Dimova, T. D. Tang, *Angew. Chem. Int. Ed.* **2020**, *59*, 5950–5957; *Angew. Chem.* **2020**, *132*, 6006–6013; b) S. Deshpande, F. Brandenburg, A. Lau, M. G. F. Last, W. K. Spoelstra, L. Reese, S. Wunnava, M. Dogterom, C. Dekker, *Nat. Commun.* **2019**, *10*, 1800.
- [9] a) W. M. Aumiller, Jr., F. Pir Cakmak, B. W. Davis, C. D. Keating, *Langmuir* **2016**, *32*, 10042–10053; b) Q. H. Zhao, F. H. Cao, Z. H. Luo, W. T. S. Huck, N. N. Deng, *Angew. Chem. Int. Ed.* **2022**, *61*, e202117500; *Angew. Chem.* **2022**, *134*, e202117500.
- [10] N. Martin, L. Tian, D. Spencer, A. Coutable-Pennarun, J. L. R. Anderson, S. Mann, *Angew. Chem. Int. Ed.* **2019**, *58*, 14594–14598; *Angew. Chem.* **2019**, *131*, 14736–14740.
- [11] W. M. Aumiller, Jr., C. D. Keating, *Nat. Chem.* **2016**, *8*, 129–137.
- [12] T. J. Nott, E. Petsalaki, P. Farber, D. Jervis, E. Fussner, A. Plochowitz, T. D. Craggs, D. P. Bazett-Jones, T. Pawson, J. D. Forman-Kay, A. J. Baldwin, *Mol. Cell* **2015**, *57*, 936–947.
- [13] a) C. Donau, F. Späth, M. Sosson, B. A. K. Kriebisch, F. Schnitter, M. Tena-Solsona, H. S. Kang, E. Salibi, M. Sattler, H. Mutschler, J. Boekhoven, *Nat. Commun.* **2020**, *11*, 5167; b) F. Späth, C. Donau, A. M. Bergmann, M. Kränzlein, C. V. Synatschke, B. Rieger, J. Boekhoven, *J. Am. Chem. Soc.* **2021**, *143*, 4782–4789.
- [14] a) D. Zwicker, R. Seyboldt, C. A. Weber, A. A. Hyman, F. Jülicher, *Nat. Phys.* **2016**, *13*, 408–413; b) C. A. Weber, D. Zwicker, F. Jülicher, C. F. Lee, *Rep. Prog. Phys.* **2019**, *82*, 064601.
- [15] M. Linsenmeier, M. R. G. Kopp, S. Stavrakis, A. de Mello, P. Arosio, *Biochim. Biophys. Acta Mol. Cell Res.* **2021**, *1868*, 118823.
- [16] M. Linsenmeier, M. R. G. Kopp, F. Grigolato, L. Emmanouilidis, D. Liu, D. Zurcher, M. Hondele, K. Weis, U. Capasso Palmiero, P. Arosio, *Angew. Chem. Int. Ed.* **2019**, *58*, 14489–14494; *Angew. Chem.* **2019**, *131*, 14631–14636.
- [17] a) M. Sobrinos-Sanguino, S. Zorrilla, C. D. Keating, B. Monterroso, G. Rivas, *Chem. Commun.* **2017**, *53*, 4775–4778; b) N. N. Deng, W. T. S. Huck, *Angew. Chem. Int. Ed.* **2017**, *56*, 9736–9740; *Angew. Chem.* **2017**, *129*, 9868–9872.
- [18] a) B. J. Bleier, S. L. Anna, L. M. Walker, *J. Phys. Chem. B* **2018**, *122*, 4067–4076; b) J.-u. Shim, G. Cristobal, D. R. Link, T. Thorsen, Y. Jia, K. Piattelli, S. Fraden, *J. Am. Chem. Soc.* **2007**, *129*, 8825–8835; c) A. Bremer, T. Mittag, M. Heymann, *Lab Chip* **2020**, *20*, 4225–4234; d) M. R. G. Kopp, M. Linsenmeier, B. Hettich, S. Prantl, S. Stavrakis, J. C. Leroux, P. Arosio, *Anal. Chem.* **2020**, *92*, 5803–5812.
- [19] N. Taylor, S. Elbaum-Garfinkle, N. Vaidya, H. Zhang, H. A. Stone, C. P. Brangwynne, *Soft Matter* **2016**, *12*, 9142–9150.
- [20] T. Beneyton, C. Love, M. Girault, T.-Y. D. Tang, J.-C. Baret, *ChemSystemsChem* **2020**, *2*, e2000022.
- [21] R. Cochereau, D. Renard, C. Nous, A. Boire, *J. Colloid Interface Sci.* **2020**, *580*, 709–719.
- [22] a) P. J. A. Kenis, R. F. Ismagilov, G. M. Whitesides, *Science* **1999**, *285*, 83–85; b) B. Zhao, J. S. Moore, D. J. Beebe, *Science* **2001**, *291*, 1023–1026.
- [23] a) C. H. Schmitz, A. C. Rowat, S. Koster, D. A. Weitz, *Lab Chip* **2009**, *9*, 44–49; b) J. F. Edd, K. J. Humphry, D. Irimia, D. A. Weitz, *Lab Chip* **2009**, *9*, 1859–1865.
- [24] a) K. K. Nakashima, M. A. Vibhute, E. Spruijt, *Front. Mol. Biosci.* **2019**, *6*, 21; b) J. Heckel, F. Batti, R. T. Mathers, A. Walther, *Soft Matter* **2021**, *17*, 5401–5409; c) J. W. Cahn, *J. Chem. Phys.* **1965**, *42*, 93–99.
- [25] W. Peebles, M. K. Rosen, *Nat. Chem. Biol.* **2021**, *17*, 693–702.
- [26] J. Y. Tinevez, N. Perry, J. Schindelin, G. M. Hoopes, G. D. Reynolds, E. Laplantine, S. Y. Bednarek, S. L. Shorte, K. W. Eliceiri, *Methods* **2017**, *115*, 80–90.
- [27] K. K. Nakashima, M. H. I. van Haren, A. A. M. Andre, I. Robu, E. Spruijt, *Nat. Commun.* **2021**, *12*, 3819.

Manuscript received: March 16, 2022

Accepted manuscript online: June 3, 2022

Version of record online: June 24, 2022



Supporting Information

**Evolution and Single-Droplet Analysis of Fuel-Driven Compartments
by Droplet-Based Microfluidics**

A. M. Bergmann, C. Donau, F. Späth, K. Jahnke, K. Göpfrich, J. Boekhoven**

Experimental Section

Materials. All solvents were purchased in analytical grade from Sigma Aldrich and used without further purification. N,N-Dimethyl formamide (DMF) was purchased from Sigma-Aldrich in peptide synthesis grade. Fmoc-R(Pbf)-OH, Fmoc-D(OtBu)-OH, Ac-F-OH, Fmoc-G-OH and Fmoc-N(Trt)-OH, N,N'-Diisopropylcarbodiimide (DIC), Ethyl cyano(hydroxyimino)acetate (Oxyma, Nova-biochem®), Wang resins (100- 200 mesh, 0.4-0.8 mmol/g), Rink Amide resins (100- 200 mesh, 0.4-0.8 mmol/g), 4-(Dimethylamino)-pyridine (DMAP), Trifluoroacetic acid (TFA, 99%), Piperidine (99%), Triisopropylsilane (TIPS), N,N-Diisopropylethylamine (DIPEA), 4-Chloro-7-nitrobenzofurazan (NBD-Cl, 98%), styrene sulfonate sodium salt 2-(Dodecylthiocarbonothioylthio)-2-methylpropionic acid (98%), 4,4'-Azobis(4-cyanovaleric acid (ACPA, ≥98%), tris(2-carboxyethyl) phosphine (TCEP), sodium borohydride (NaBH₄), Polystyrene sulfonate (pSS, 75kDa, 18wt% in water), polyuridylic acid potassium salt (pU), 1-ethyl-3-(3-dimethylaminopropyl)carbodiimide (EDC), sulforhodamine 101, 4-morpholineethanesulfonic acid (MES) buffer and Sylgard 184 silicon elastomere were all purchased from Sigma-Aldrich and used without any further purification unless indicated otherwise. The peptide Ac-F(RG)₃D-OH was purchased from CASLO Aps. Nuclease-free water was freshly prepared by filtration (DURAN) of MQ-water. Cy3-A15 was purchased from biomers.net GmbH. 2w% 008-Fluorosurfactant in HFE7500 was purchased from RAN Biotechnologies. Sulfo-Cyanine5-maleimide(1-(6-((2-(2,5-dioxo-2,5-dihydro-1H-pyrrol-1-yl)ethyl)amino)-6-oxohexyl)-3,3-di-methyl-2-((1E,3E)-5-((E)-1,3,3-trimethyl-5-sulfonatoindolin-2-ylidene)penta-1,3-dien-1-yl)-3H-indol-1-ium-5-sulfonate) was purchased from Lumiprobe.

Peptide synthesis and purification. The peptides Ac-F(RG)₃N-NH₂ and NBD-G(RG)₃D-OH were synthesized via solid-phase synthesis on a CEM Liberty microwave-assisted peptide synthesizer, purified by reversed-phase HPLC and characterized by electrospray ionization mass spectrometry (ESI-MS) as well as analytical HPLC as previously described.^[1]

Synthesis of Cy5-pSS. Poly(styrene sulfonate) homopolymer was synthesized via RAFT polymerization. For this purpose, styrene sulfonate sodium salt was polymerized in MQ-water at 75°C with 0.01 eq. 2-(Dodecylthiocarbonothioylthio)-2-methylpropionic acid (98%) and 0.002 eq. of 4,4'-Azobis(4-cyanovaleric acid (ACPA, ≥98%) for 5 hours. The solution was purged before with Argon for 20 minutes to remove air. The crude solution was purified by dialysis against MQ-water in 12-14 kDa MWCO dialysis tubings (Spectra/Por® 4, 29 mm diameter) for two days. The product was dried by lyophilization. The CTA-terminated poly(styrene sulfonate) (440 mg) was solubilized in 15 mL MQ-water, 15 mL of a freshly prepared 1M NaBH₄ solution were added dropwise and the mixture was then

stirred for 3.5 hours at room temperature. The crude solution was dialyzed against MQ-water for 2 days in 12-14 kDa MWCO dialysis tubings (Spectra/Por® 4, 29 mm diameter) and lyophilized. The resulting product was then reacted with 150 eq. of tris(2-carboxyethyl) phosphine (TCEP) at room temperature in DMF for 24 hours. 20 eq. of Sulfo-Cyanine5-maleimide(1-(6-((2-(2,5-dioxo-2,5-dihydro-1H-pyrrol-1-yl)ethyl)amino)-6-oxohexyl)-3,3-dimethyl-2-((1E,3E)-5-((E)-1,3,3-trimethyl-5-sulfonatoindolin-2-ylidene)penta-1,3-dien-1-yl)-3H-indol-1-ium-5-sulfonate) were added to an aliquot of this solution together with a catalytic amount of ethylenediamine and stirred at 50 °C for 24 hours. The crude product was purified by dialysis in a 2000 MWCO Slide-A-Lyzer Dialysis Cassette® (ThermoFisher Scientific) against MQ-water for 2 days and finally lyophilized.

Standard sample preparation. Stock solutions of Ac-F(RG)₃-D-OH (300 mM), pU (41 mM, according to monomer units), pSS (41 mM, according to monomer units) and MES (650 mM) were prepared by dissolving the respective amount of each component in MQ water and adjusting the pH to 5.3 by addition of a 5 M sodium hydroxide solution. Stock solutions for NBD-G(RG)₃-D-OH, Ac-F(RG)₃-N-NH₂, sulforhodamine B, Cy3-A15 and Cy5-pSS were also prepared in MQ water but without pH adjustment. All stocks were filtrated with a syringe filter (PTFE, 0.2µm pore size). Samples with the desired concentrations of each component were prepared from these stock solutions. For the preparation of non-fuel-driven coacervate-based droplets, the added concentration of the pseudo anhydride Ac-F(RG)₃-N-NH₂ is subtracted from the precursor Ac-F(RG)₃-D-OH to keep the total peptide concentration constant. Stock solutions for EDC were prepared freshly before each experiment by dissolving the respective amount in MQ water.

Microfluidic chip production. Microfluidic PDMS (Polydimethylsiloxane, Sylgard 184, Dow Corning)-based devices were designed with QCAD-pro (RibbonSoft GmbH) and fabricated using photo- and soft-lithography^[2] as previously described.^[3]

Microfluidic droplet formation. Surfactant-stabilized water in oil droplets was produced using 2% 008-FluoroSurfactant in 3M Novec7500 as the oil phase, EDC in MQ water as one of the water phases and Ac-F(RG)₃-D-OH, PSS/pU and sulforhodamine B in MES buffer at pH 5.3 as the second water phase. Both water phases contained the doubled concentrations of the respective components and were mixed in a 1 to 1 ratio to yield the desired concentrations inside the microfluidic droplets. Both aqueous phases and the oil phase were injected into the microfluidic PDMS-based device through polytetrafluoroethylene (PTFE) tubes (0.4-0.9 mm, Bola, Germany) using a flow control system (ELVEFLOW Pressure Controller OB1 MK3). Typically, pressures of 610 mbar for the water phases and 810 mbar for the oil phase were used to produce stable water in oil droplets with a diameter of 40 µm.

Confocal fluorescence microscopy. To analyze the coacervate in a microfluidic droplet a lightning SP8 confocal microscope (Leica) with a 63x water immersion objective was used. Coacervates were stained with the fluorophore sulforhodamine B which was excited at 552 nm and detected from 565-700 nm with a HyD detector. The pinhole was set to 1 Airy unit. To analyze the evolution of coacervates in the entire microfluidic droplet, time series imaging of a single microfluidic droplet was acquired in z-stacks with 2 μm between z-planes (20 z-planes in total). All experiments that imaged the entire microfluidic droplet were acquired with a resolution of 600 x 600 pixels at 3.3x zoom and 400x scan speed (bidirectional scan) which results in a time resolution of 17.4 s/stack. To get a better time resolution for the tracking of the coacervates inside of the microfluidic droplet, the scan speed was increased to 1800x which results in a time resolution of 5.4 s/stack. To analyze the nucleation of coacervates, one z-plane of four microfluidic droplets was imaged simultaneously over time. All experiments that imaged the nucleation of coacervates were acquired with a resolution of 1334 x 1334 pixels at 1.43x zoom and 400x scan speed (bidirectional scan) which results in a time resolution of 1.4 s/frame.

Fluorescence recovery after photobleaching. The diffusivity inside of coacervates was calculated from fluorescence recovery after photobleaching experiments. Measurements were performed in a microscopy well plate chamber (IBIDI, μ -slide Angiogenesis Glass Bottom). Coacervates were stained with sulforhodamine B or NBD-G(RG)₃D-OH, an NBD labeled fluorescent version of the precursor peptide Ac-F(RG)₃D-OH, which was excited at 488 nm and detected from 565-635 nm with a PMT detector. FRAP experiments were performed on coacervates that were close to the glass at the bottom of the imaging chamber to have coacervates of sufficient size and to minimize their movement during image acquisition. Images were acquired at a resolution of 135x135 pixels, 400x scan speed (bidirectional scan) and 15x zoom. A spot size of 1 μm in diameter was chosen for bleaching and is kept constant for all experiments. Recovery data were normalized through double normalization with the following equation:^[4]

$$F(t) = \frac{(T_0 - B_0)(I_t - B_t)}{(T_t - B_t)(I_0 - B_0)}$$

Here $F(t)$ represents the normalized fluorescence intensity which is calculated from the average intensity of 3 ROIs. I_t represents the average intensity of the bleached ROI, T_t represents the average intensity of an unbleached ROI within the bleached coacervate and B_t represents the average intensity of a ROI without any coacervates. The fluorescence recovery $F(t)$ is then given by the equation^[5]

$$F(t) = F_{\infty} \exp \left[-\frac{2}{1 + \left(\frac{8tD}{a^2} \right)} \right]$$

with F_{∞} representing the fluorescence at full recovery, a representing the bleached area and D representing the translational diffusion coefficient of the fluorescent probe.^[5]

Image analysis. The z-stack image-series obtained by confocal microscopy are converted into maximum z-projections using Fiji ImageJ. One threshold was determined with the “moments”^[6] algorithm for each different set of imaging parameters to separate the fluorescence of the coacervate-based droplets from the background fluorescence. The “watershed” plugin is used to separate detected non-spherical particles resulting from overlapping fluorescence of two or more coacervate-based droplets. The preinstalled “analyze particles” package of Fiji ImageJ is used to determine the number and area of the coacervate-based droplets. The volume is calculated from the area of coacervate-based droplets under the assumption that they are perfectly spherical.

Tracking of coacervates. Tracking of coacervate-based droplets was done with the imageJ plugin TrackMate.^[7] The parameters used for tracking of every coacervate were LoG detector with an estimated diameter of 3.2 μm , a threshold of 0.09 and LAP Tracker with a frame to frame linking of 5 μm , gap closing of 5 μm and 2 frames, and segment merging of 15 μm . The parameters used for volume tracking were LoG detector with an estimated diameter of 4.5 μm , a threshold of 0.1 and LAP Tracker with a frame to frame linking of 5 μm , gap closing of 5 μm and 2 frames, and segment merging of 5 μm . Subsequently, the tracks were inspected and corrected manually. The estimated blob diameter for volume tracking was increased to more accurately display the diameter of the bigger coacervate-based droplets while a lower estimated blob diameter gave better results for the path tracking of small coacervate-based droplets.

Centrifugation. For centrifugation samples of 200 μl were prepared as described previously. To improve the contrast between coacervate- and dilute-phase, 15 μM of sulforhodamine B was added to each sample. The samples were incubated for 15 min and then centrifuged for another 15 min at 13.5k rpm. The volumes of the coacervate phases were determined by comparison with samples of known sulforhodamine volumes.

Fluorescence spectroscopy. Fluorescence spectroscopy was performed on a Jasco spectrofluorimeter (Jasco FP-8300, SpectraManager software 2.13) with external temperature control (Jasco MCB-100). To determine the amount of NBD-labeled peptide in the dilute phase of fuel-driven coacervate-based droplets, 150 μl samples of 8 mM Ac-F(RG)₃D-OH, 5 mM pSS, and 1 μM NBD-G(RG)₃D-OH in 200 mM MES buffer at pH 5.3 were prepared. As a

control, samples of the same conditions without NBD-G(RG)₃D-OH were prepared. EDC is added to the samples and after 4 min they were centrifuged for 5 min at 20,412 g. 100 µl of the clear supernatant solution is carefully removed with a pipette. To account for the dependence of the fluorescence of dyes on their environment, 1 µM of NBD-G(RG)₃D-OH is added to the control samples after centrifugation. The samples were excited at 467 nm and the fluorescence intensity at 526 nm in comparison to the corresponding control sample gave the remaining amount of NBD-G(RG)₃D-OH in the dilute phase. To determine the amount of NBD-labeled precursor and Cy5-labeled pSS in the dilute phase of non-fuel-driven coacervate-based droplets, 150 µl samples with 8 mM peptide as a combination of Ac-F(RG)₃D-OH and Ac-F(RG)₃D-NH₂, 5 mM pSS, and 1 µM NBD-G(RG)₃D-OH or 1 µM Cy5-pSS in 200 mM MES buffer at pH 5.3 were prepared. As a control, samples of the same conditions without the fluorophore were prepared. To induce coacervation, pSS is added at last to the samples and after 10 min they were centrifuged for 15 min at 20,412 g. 100 µl of the supernatant solution is carefully removed with a pipette and added to a centrifugal tube containing 1 µl of an aqueous solution of NaCl (4 M) to dissolve residual turbidity. Similar to the fuel-driven system, the respective fluorophore is added to the control samples after centrifugation. The samples with NBD-G(RG)₃D-OH were excited at 467 nm and the fluorescence intensity at 526 nm in comparison to the corresponding control sample gave the remaining amount of peptide in the dilute phase. The samples with Cy5-pSS were excited at 630 nm and the fluorescence intensity at 653 nm in comparison to the corresponding control samples gave the remaining amount of pSS in the dilute phase.

Kinetic model. We used a kinetic model written in MATLAB to predict the evolution of the anhydride concentration over time. The rate constants were determined by fitting the model to peptide anhydride, EDC, and precursor concentrations measured by analytical HPLC. More details can be found in our previous work.^[1] The following rate constants were used

$$k_0 = 7.50 \cdot 10^{-5} \text{ s}^{-1}$$

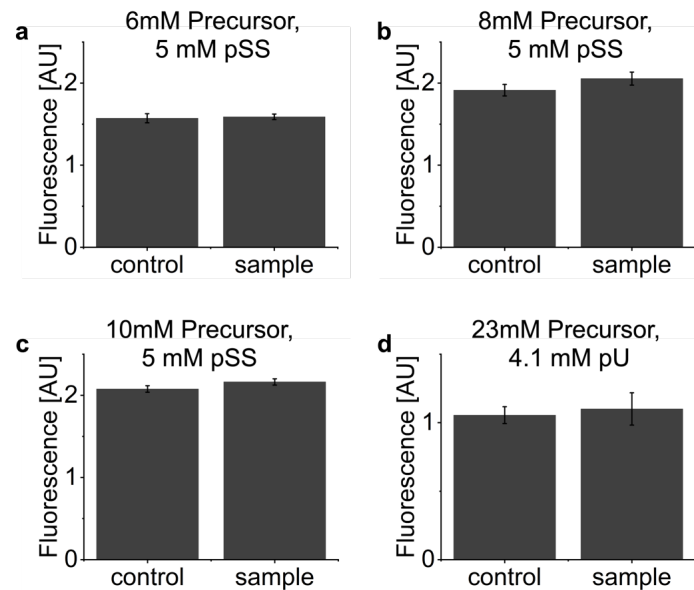
$$k_1 = 1.80 \cdot 10^{-1} \text{ M}^{-1} \text{ s}^{-1}$$

$$k_2 = 5.40 \cdot 10^{-1} \text{ s}^{-1}$$

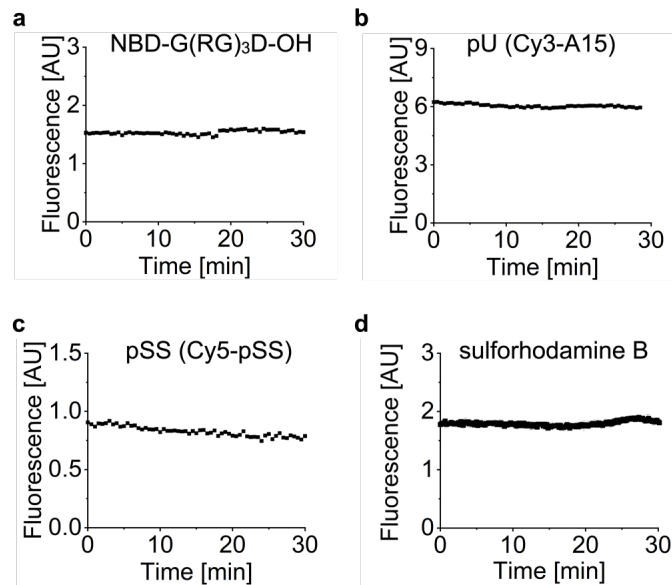
$$k_3 = 2.16 \cdot 10^{-1} \text{ s}^{-1}$$

$$k_4 = 0.85 \cdot 10^{-2} \text{ s}^{-1} \text{ [1a]}$$

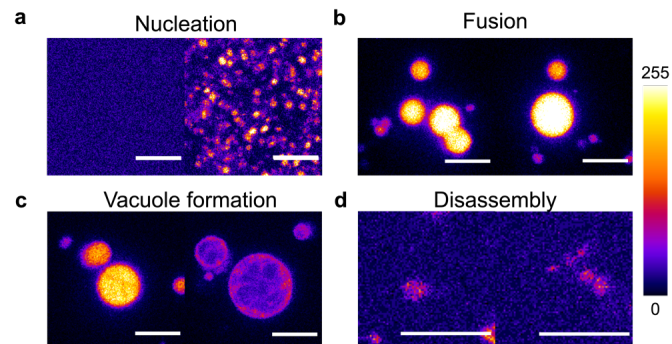
Supporting Figures



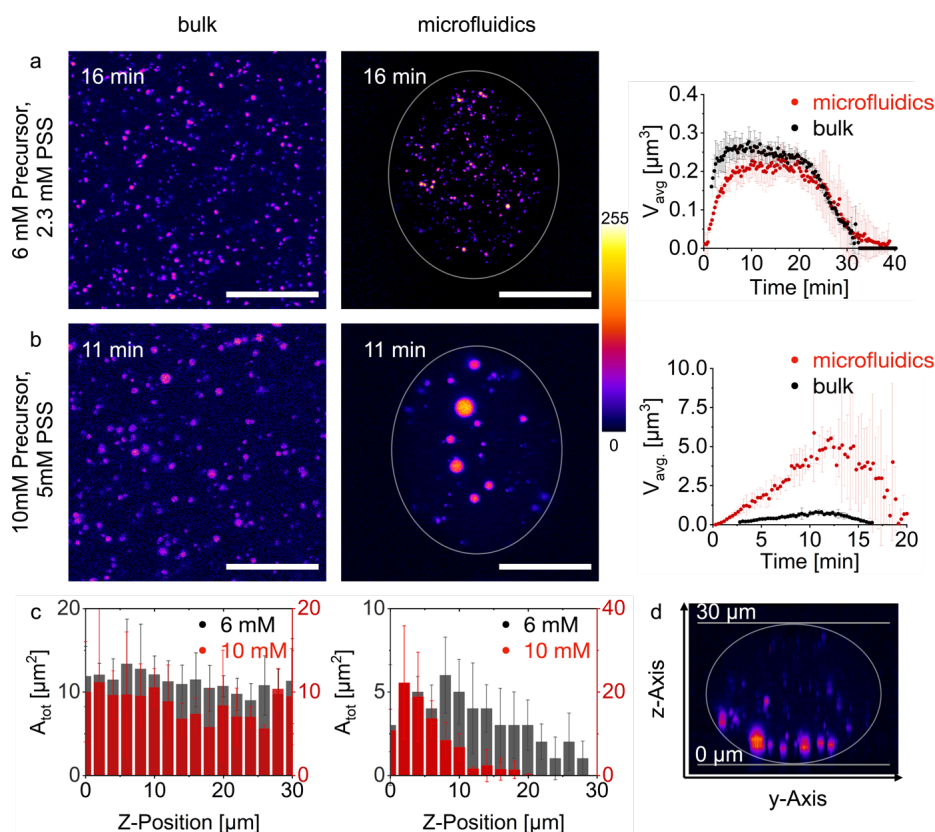
Supporting figure 1. Verification of droplet composition. a-d Average fluorescence of $0.1 \mu\text{M}$ sulforhodamine B for pSS and $0.1 \mu\text{M}$ Cy3-A15 for pU measured inside of the microfluidic droplets. For the samples, precursor, pSS/pU, MES and sulforhodamine B/Cy3-A15 were prepared with double the concentration as indicated and were then mixed in the microfluidic device with water in a 1:1 ratio and encapsulated into microfluidic droplets. For the control, a sample with the indicated concentrations of precursor, pSS/pU, MES and sulforhodamine B/Cy3-A15 were encapsulated into microfluidic droplets without mixing with water. The fluorescence is compared to verify correct mixing ratios. Error bars represent the standard deviation from triplicate measurements.



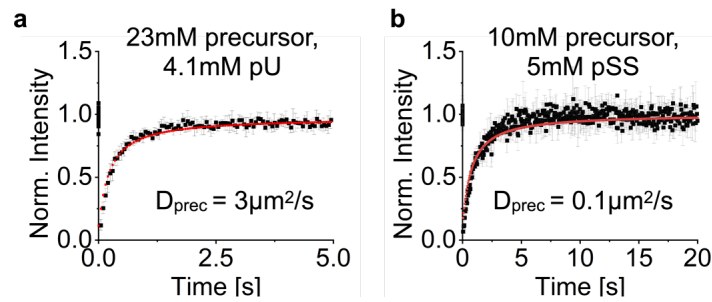
Supporting figure 2. Concentration stability of the fluorescent components of coacervate-based droplets. **a** Fluorescence of 1 μM NBD-G(RG)₃D-OH was measured over time inside of a microfluidic droplet. Conditions are 10 mM Ac-F(RG)₃D-OH, 5 mM pSS, 200 mM MES at pH 5.3. **b** Fluorescence of 0.1 μM Cy3-A15 was measured over time inside of a microfluidic droplet. Conditions are 23 mM Ac-F(RG)₃D-OH, 4.1 mM pU, 200 mM MES at pH 5.3. **c** Fluorescence of 1 μM Cy5-pSS was measured over time inside of a microfluidic droplet. Conditions are 10 mM Ac-F(RG)₃D-OH, 5 mM pSS, 200 mM MES at pH 5.3. **d** Fluorescence of 0.1 μM sulforhodamine B was measured over time inside of a microfluidic droplet. Conditions are 10 mM Ac-F(RG)₃D-OH, 5 mM pSS, 200 mM MES at pH 5.3.



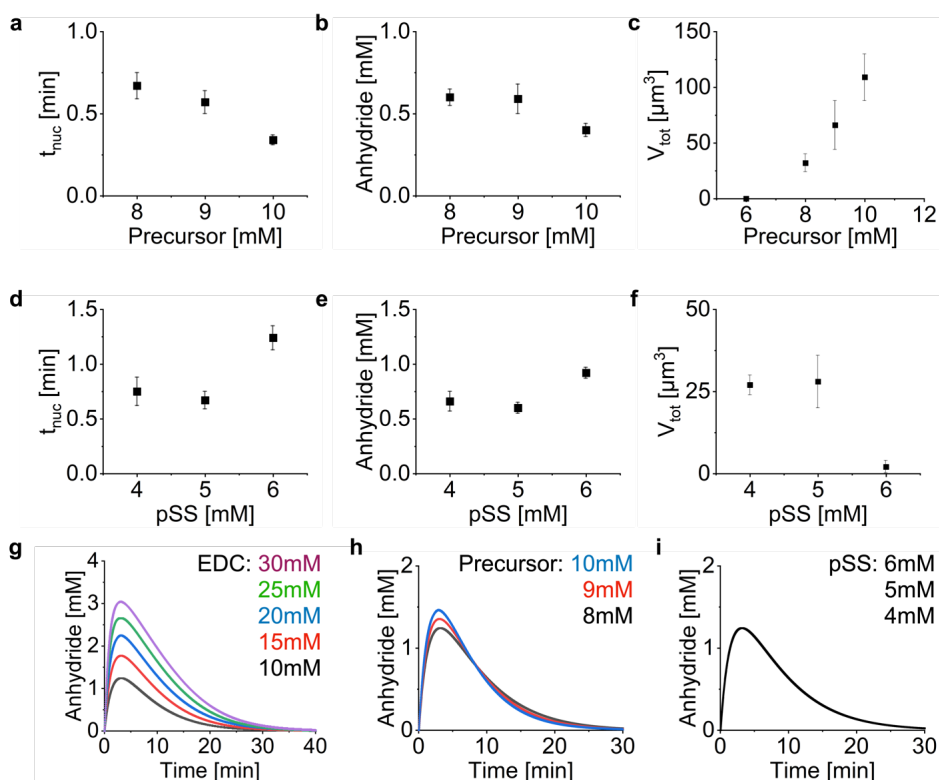
Supporting figure 3. Different behaviors of coacervate-based droplets. Conditions are 23 mM Ac-F(RG)₃D-OH, 4.1 mM pU, 200 mM MES at pH 5.3 with 25 mM EDC. The scale bar represents 5 μ m. The pseudocolor-coded confocal image represents a maximum z-projection of a z-stack throughout one microfluidic droplet. The grey value scale from 0 to 255 is given next to the images. **a** Formation of coacervate-based droplets after the addition of EDC. **b** Fusion of coacervate-based droplets with each other and the recovery of a spherical shape after fusion. **c** Coacervate-based droplets form vacuoles during their decay. **d** The dissolution of coacervate-based droplets leads to the formation of small daughter droplets.



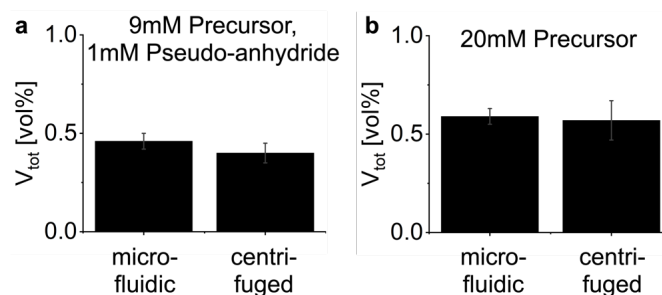
Supporting figure 4. Fusion of coacervates is influenced by the confinement. **a** A comparison of the z-projection of coacervate-based droplets imaged in the bulk and imaged in the confinement of a microfluidic droplet. Both images are taken 16 min after the addition of 10 mM EDC. The pseudocolor-coded confocal image represents a maximum z-projection of a z-stack throughout one microfluidic droplet. The grey value scale from 0 to 255 is given next to the images. The scale bar represents 20 μm . A comparison of the quantitative analysis of both techniques shows that the average volume of the coacervate-based droplets is the same. **b** A comparison of the z-projection of coacervate-based droplets imaged in the bulk and imaged in the confinement of a microfluidic droplet. Both images are taken 11 min after the addition of 10 mM EDC. The scale bar represents 20 μm . A comparison of the quantitative analysis of both techniques shows that the average volume of the coacervate-based droplets in the microfluidic droplets is significantly bigger than the respective average volume in the bulk setup. **c** In the bulk setup the total area of imaged coacervate-based droplets is similar within a range of 30 μm in the direction of the z-position. In the microfluidic setup the total area of imaged coacervate-based droplets is only similar over a range of 30 μm in the z-direction for conditions under which coacervate-based droplets with an average volume of less than 0.3 μm^3 (6 mM precursor) are formed. For conditions with coacervate-based droplets of sizes up to 5-6 μm^3 the total area of imaged coacervate-based droplets is significantly higher towards the bottom of the microfluidic droplet. **d** z-y-projection of a microfluidic droplet containing 10 mM precursor and 5 mM pSS 11 min after EDC addition. Most coacervate-based droplets sit at the bottom of the microfluidic droplet.



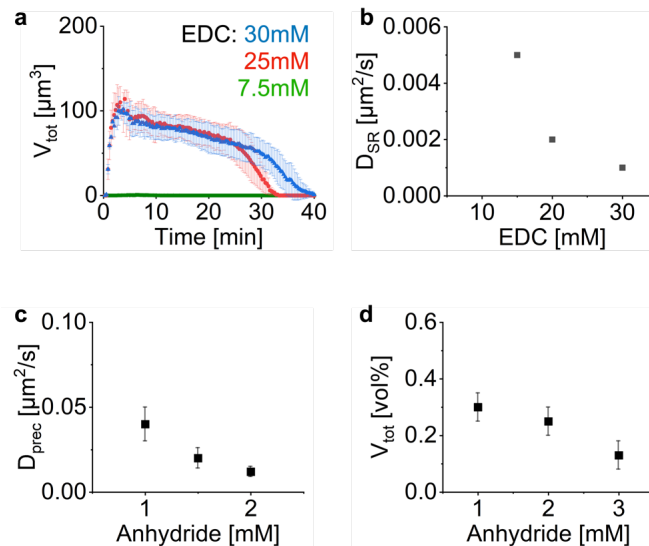
Supporting figure 5. Comparison of the precursor diffusivity inside pU- and pSS- based droplets. **a** Fluorescence recovery after photobleaching of NBD-G(RG)₃D-OH in pU-based droplets. **b** Fluorescence recovery after photobleaching of NBD-G(RG)₃D-OH in pSS-based droplets. The red solid line represents the fit of the fluorescence recovery. Error bars represent standard deviation from 3 measurements.



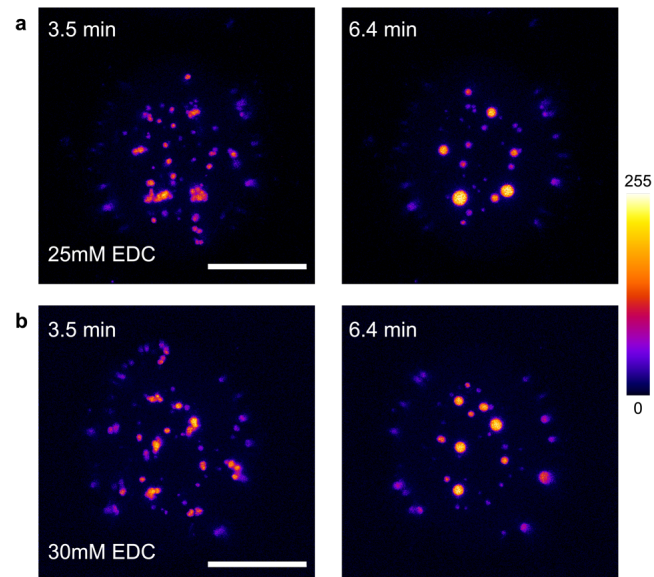
Supporting figure 6. Analysis of the nucleation time and the total volume of coacervate-based droplets. Standard conditions in these experiments are 8 mM Ac-F(RG)₃D-OH, 5 mM pSS, 10 mM EDC, 0.1 μ M sulforhodamine B in 200 mM MES at pH 5.3 with a variation in the concentration of the respective component. **a** Dependency of the nucleation time on the precursor concentration. **b** The anhydride concentration at the timepoint of nucleation dependent on the precursor concentration. Anhydride concentration is determined with the kinetic model at the time of nucleation. **c** Dependence of the total volume of coacervate-based droplets on the precursor concentration. **d** Dependence of the nucleation time on the pSS concentration. **e** The anhydride concentration at the timepoint of nucleation dependent on the pSS concentration. Anhydride concentration is determined with the kinetic model at the time of nucleation. **f** Dependence of the total volume of coacervate-based droplets on the pSS concentration. **g** Anhydride concentration for different initial EDC concentrations calculated with the kinetic model. **h** Anhydride concentration for different initial precursor concentrations calculated with the kinetic model. **i** Anhydride concentration for different initial pSS concentrations calculated with the kinetic model. Note that pSS is not part of the kinetic model.



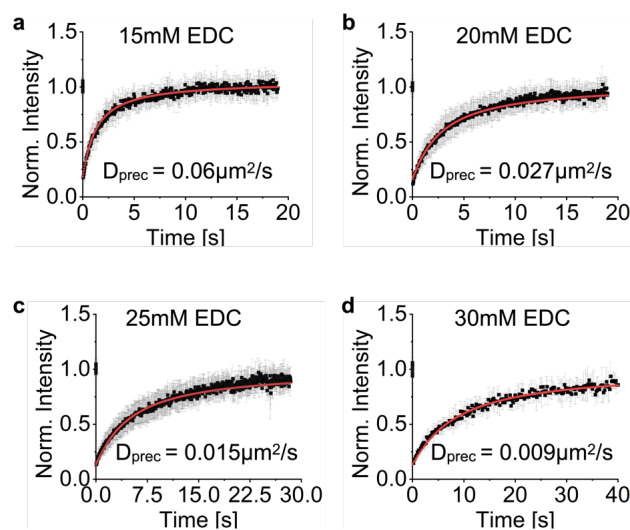
Supporting figure 7. Comparison of the total volume of coacervate-based droplets measured by centrifugation and in the microfluidic setup. The total volume of non-fuel-driven coacervate-based droplets is measured by centrifugation and by confocal microscopy in the microfluidic setup. **a** 9mM of the precursor $\text{Ac-F(RG)}_3\text{D-OH}$ and 1mM of the pseudo-anhydride $\text{Ac-F(RG)}_3\text{N-NH}_2$ with 5 mM pSS in 200 mM MES at pH 5.3 were used to mimic the maximum anhydride level of the fuel-driven system with the conditions 10 mM $\text{Ac-F(RG)}_3\text{D-OH}$, 5 mM pSS, 10 mM EDC in 200 mM MES at pH 5.3. Error bars represent the standard deviation of 3 experiments. **b** 20 mM $\text{Ac-F(RG)}_3\text{D-OH}$ with 5 mM pSS in 200 mM MES at pH 5.3 were used as a second non-fuel-driven system. Under these conditions, coacervation takes place without the need for anhydride formation. Error bars represent the standard deviation of 3 experiments.



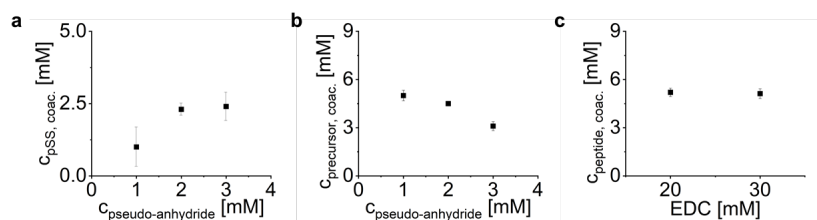
Supporting figure 8. Analysis of the total volume and viscosity of coacervate-based droplets. Standard conditions in these experiments are 8 mM Ac-F(RG)₃D-OH, 5 mM pSS in 200 mM MES at pH 5.3 with a variation in the concentration of the respective component. **a** Analysis of the total volume of coacervate-based droplets over the entire reaction cycle depending on the fuel concentration. The total volume is given as volume percent defined as the total volume of coacervate-based droplets divided by the total volume of the microfluidic droplet. Error bars represent the standard deviation of 3 experiments. **b** The diffusivity of sulforhodamine B inside of coacervate-based droplets depending on the fuel concentration. The diffusivity is determined by FRAP experiments with 0.1 μM sulforhodamine B. **c** The diffusivity of NBD-G(RG)₃D-OH inside of coacervate-based droplets depending on the concentration of the pseudo anhydride Ac-F(RG)₃N-NH₂. The diffusivity is determined by FRAP experiments with 1 μM NBD-G(RG)₃D-OH. **d** Dependency of the total volume of coacervate-based droplets on the concentration of the pseudo-anhydride Ac-F(RG)₃N-NH₂. The volume of the coacervate-based droplets is determined by centrifugation. Error bars represent the standard deviation of 3 experiments.



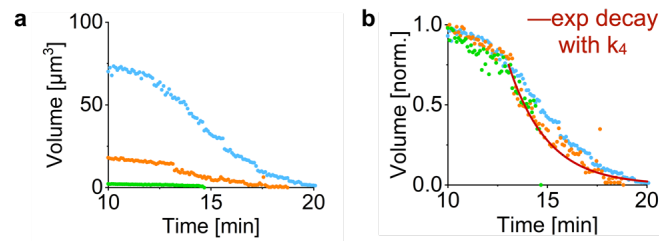
Supporting figure 9. Agglomerate formation. Standard conditions in these experiments are 8 mM Ac-F(RG)₃D-OH, 5 mM pSS, 0.1 μ M sulforhodamine B in 200 mM MES at pH 5.3 with the respective EDC concentration. **a-b** Coacervate-based droplets initially form agglomerate-like structures after fusion. After several minutes the spherical shape is restored. Images are z-projections at the given time point. Scale bars represent 20 μ m.



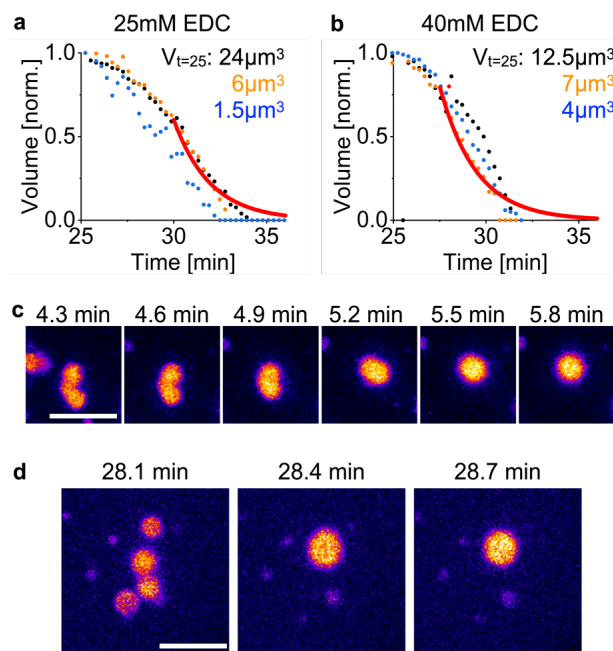
Supporting figure 10. Comparison of precursor diffusivity inside pSS-based droplets depending on the EDC concentration. For all experiments, 8 mM Ac-F(RG)₃D-OH, 5 mM pSS, and 1 μM NBD-G(RG)₃D-OH in 200 mM MES at pH 5.3 was used. **a-d** Fluorescence recovery after photobleaching of NBD-G(RG)₃D-OH in coacervate-based droplets depending on the fuel concentration. The red solid line represents the fit of the fluorescence recovery. Error bars represent standard deviation from 9 measurements.



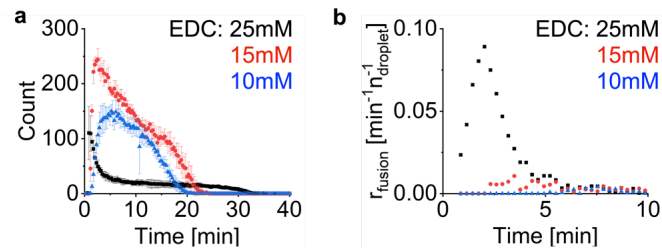
Supporting figure 11. Fluorescence partitioning of precursor, pSS, and the total amount of peptide in coacervate-based droplets. **a** Fluorescence partitioning of 1 μM Cy-5 pSS in non-fuel-driven coacervate-based droplets depending on the concentration of pseudo-anhydride. The amount of pSS that is missing in the supernatant after centrifugation is regarded as the amount of pSS that partitioned into the coacervate-based droplets. Combined concentrations of Ac-F(RG)₃D-OH and Ac-F(RG)₃N-NH₂ are 8 mM with 5 mM pSS in 200 mM MES at pH 5.3. Error bars represent standard deviations from 3 measurements. **b** Fluorescence partitioning of 1 μM NBD-G(RG)₃D-OH in non-fuel-driven coacervate-based droplets depending on the concentration of pseudo-anhydride. The amount of precursor that is missing in the supernatant after centrifugation is regarded as the amount of precursor that partitioned into the coacervate-based droplets. In the non-fuel-driven case NBD-G(RG)₃D-OH is only a measure for the precursor since no activation to the anhydride is possible. Combined concentrations of Ac-F(RG)₃D-OH and Ac-F(RG)₃N-NH₂ are 8 mM with 5mM pSS in 200 mM MES at pH 5.3. Error bars represent standard deviations from 3 measurements. **c** Fluorescence partitioning of 1 μM NBD-G(RG)₃D-OH in fuel-driven coacervate-based droplets depending on the concentration of EDC. The amount of peptide that is missing in the supernatant after centrifugation is regarded as the amount of peptide that partitioned into the coacervate-based droplets. In the fuel-driven case, NBD-G(RG)₃D-OH is considered as a measure for both the precursor as well as the anhydride since it is able to form the anhydride itself. Combined concentrations of Ac-F(RG)₃D-OH and Ac-F(RG)₃N-NH₂ are 8 mM with 5mM pSS in 200 mM MES at pH 5.3. Error bars represent standard deviation from 3 measurements.



Supporting figure 12. Comparison of the volume decay. **a** Volume decay profile of the blue, orange, and green droplets from figures 5a and c. **b** Normalization of the volume decay shows that all three droplets decay with a similar rate constant. The red solid line represents an exponential decay using the hydrolysis constant k_4 from the kinetic model as the constant k for exponential volume decay with the formula $y = V_0 e^{-kt}$.



Supporting figure 13. Comparison of the volume decay for high fuel concentrations. For all experiments 8 mM Ac-F(RG)₃D-OH, 5 mM pSS and 0.1 μM sulforhodamine B in 200 mM MES at pH 5.3 were used. **a,b** Normalization of the volume decay for three droplets of different starting volumes shows that all three droplets decay with a similar rate constant. The red solid line represents an exponential decay using the hydrolysis constant k_4 from the kinetic model as the constant k for exponential volume decay with the formula $y = V_0 e^{-kt}$. The coacervate-based droplets were fueled with the indicated amount. **c** Time series of a fusion early in the reaction cycle with a high ratio of activated to deactivated species present. The scale bar represents 5 μm . **d** Time series of a fusion event late in the reaction cycle with a low ratio of activated to deactivated species present. The scale bar represents 5 μm . **c** and **d** show coacervate-based droplets from the same experiment in which they were fueled with 40 mM EDC.



Supporting figure 14. Comparison of the droplet number and the average droplet fusion rate.

For all experiments 8 mM Ac-F(RG)₃D-OH, 5 mM pSS and 0.1 μM sulforhodamine B in 200 mM MES at pH 5.3 were used with varying EDC concentrations. **a** The number of coacervate-based droplets that were detected at each time point during the reaction cycle above a radius threshold of 400 nm. **b**. The average likelihood of every coacervate-based droplet to undergo a fusion event. The rate of fusion is defined as the decline in droplet number in comparison to the previously measured data point. Fusion rates are only calculated after the maximum number of coacervate-based droplets has been reached and until the average size of coacervate-based droplets declines. The decline in the average size is used as an indicator for the start of droplet dissolution. The fusion rates are plotted with a rolling average of $n=5$.

References

- [1] a) F. Spath, C. Donau, A. M. Bergmann, M. Kranzlein, C. V. Synatschke, B. Rieger, J. Boekhoven, *J Am Chem Soc* **2021**, *143*, 4782-4789; b) F. Schnitter, A. M. Bergmann, B. Winkeljann, J. Rodon Fores, O. Lieleg, J. Boekhoven, *Nat Protoc* **2021**, *16*, 3901-3932.
- [2] D. C. Duffy, J. C. McDonald, O. J. A. Schueller, G. M. Whitesides, *Analytical Chemistry* **1998**, *70*, 4974-4984.
- [3] a) M. Weiss, J. P. Frohnmayer, L. T. Benk, B. Haller, J. W. Janiesch, T. Heitkamp, M. Borsch, R. B. Lira, R. Dimova, R. Lipowsky, E. Bodenschatz, J. C. Baret, T. Vidakovic-Koch, K. Sundmacher, I. Platzman, J. P. Spatz, *Nat Mater* **2018**, *17*, 89-96; b) T. W. Hofmann, S. Hanselmann, J. W. Janiesch, A. Rademacher, C. H. Bohm, *Lab Chip* **2012**, *12*, 916-922.
- [4] C. Wu, C. D. Allis, *Chromatin and Chromatin Remodeling Enzymes, Part A*, Elsevier Science, **2004**.
- [5] A. B. Kayitmazer, H. B. Bohidar, K. W. Mattison, A. Bose, J. Sarkar, A. Hashidzume, P. S. Russo, W. Jaeger, P. L. Dubin, *Soft Matter* **2007**, *3*, 1064-1076.
- [6] W.-H. Tsai, *Computer Vision, Graphics, and Image Processing* **1985**, *29*, 377-393.
- [7] J. Y. Tinevez, N. Perry, J. Schindelin, G. M. Hoopes, G. D. Reynolds, E. Laplantine, S. Y. Bednarek, S. L. Shorte, K. W. Eliceiri, *Methods* **2017**, *115*, 80-90.

5. Liquid Spherical Shells are a Non-Equilibrium Steady State

Abstract.

In Chapter 1, I explained how the spatial separation of activation and deactivation can lead to unique dynamic behaviors in active droplets. However, the behaviors observed in Chapter 4 are primarily influenced by either the activation or deactivation reaction, rather than arising from their simultaneous interplay. This results from the used batch-fueling approach, leading to continually shifting reaction rates—resulting in the activation reaction dominating during the initial stages and the deactivation reaction dominating later in the droplets' lifecycle. The emergence of active dynamic behaviors is thus overshadowed by these continually changing rate ratios. To overcome this issue, active droplets have to be maintained with a balance between activation and deactivation rates, establishing a non-equilibrium steady state. In this work, we encapsulate active droplets into water-in-oil microreactors and continuously fuel them to maintain them in a non-equilibrium steady state. We observe that active droplets show size-dependent instabilities, which result in the formation of active spherical shells composed of liquid droplet material. Under equilibrium conditions, the formation of such shells is thermodynamically unfavored due to their increased surface area. We verify that the mechanism is related to gradients of short-lived droplet material, demonstrating the capability of chemical gradients to regulate the morphology of active droplets.

This work is under review (passed reviewer revision, ongoing editorial revision):

Title: Liquid spherical shells are a non-equilibrium steady state

Authors: Alexander M. Bergmann, Jonathan Bauermann, Giacomo Bartolucci, Carsten Donau, Michele Stasi, Anna-Lena Holtmannspötter, Frank Jülicher, Christoph A. Weber, and Job Boekhoven

First published: 28. April 2023

Journal: *Nature Communications (Under Review)*

Publisher: Research Square

DOI: 10.21203/rs.3.rs-2642406/v1

Reprinted with permission from Research Square. Copyright © 2023, the Authors.

This section states the individual work of each author in the publication above. J. Boekhoven and C. Weber designed the project. J. Boekhoven, C. Weber, and F. Jülicher supervised the project. A. M. Bergmann and C. Donau designed the experiments. A. M. Bergmann, C. Donau, M. Stasi, and A. Holtmannspätter performed the experiments. A. M. Bergmann, C. Donau, and M. Stasi analyzed the data. J. Bauermann and G. Bartolucci performed the theoretical calculations. J. Boekhoven, C. Weber, A. M. Bergmann, J. Bauermann, G. Bartolucci, and C. Donau wrote and edited the manuscript.



Preprints are preliminary reports that have not undergone peer review.
They should not be considered conclusive, used to inform clinical practice,
or referenced by the media as validated information.

Liquid spherical shells are a non-equilibrium steady state

Job Boekhoven (✉ job.boekhoven@tum.de)

Technical University Munich <https://orcid.org/0000-0002-9126-2430>

Alexander Bergmann

Technical University Munich

Jonathan Bauermann

Max Planck Institute for the Physics of Complex Systems <https://orcid.org/0000-0002-0301-7655>

Giacomo Bartolucci

Max Planck Institute for the Physics of Complex Systems

Carsten Donau

Technical University Munich

Michele Stasi

Technical University Munich

Anna-Lena Holtmannspötter

Technical University Munich

Frank Jülicher

Max Planck Institute for the Physics of Complex Systems <https://orcid.org/0000-0003-4731-9185>

Christoph Weber

University of Augsburg <https://orcid.org/0000-0001-6279-0405>

Physical Sciences - Article

Keywords: liquid-liquid phase separation, dissipative structures, chemically fueled droplets

Posted Date: April 28th, 2023

DOI: <https://doi.org/10.21203/rs.3.rs-2642406/v1>

License: © ⓘ This work is licensed under a Creative Commons Attribution 4.0 International License.

[Read Full License](#)

Abstract

Liquid-liquid phase separation is the process in which two immiscible liquids demix. This spontaneous phenomenon yields spherical droplets that eventually coarsen to one large, stable droplet governed by the principle of minimal free energy. In chemically fueled phase separation, the formation of phase-separating molecules is coupled to a fuel-driven, non-equilibrium reaction cycle.¹ It thus yields dissipative structures sustained by a continuous fuel conversion.² Such dissipative structures are ubiquitous in biology³ but are poorly understood as they are governed by non-equilibrium thermodynamics.⁴ Here, we bridge the gap between passive, close-to-equilibrium, and active, dissipative structures with chemically fueled phase separation. We observe that spherical, active droplets can transition into a new morphology—a liquid, spherical shell of droplet material. A spherical shell is highly unstable at equilibrium, and this dissipative structure can be sustained only by continuous conversion of chemical energy. We demonstrate that the mechanism is related to gradients of shortlived droplet material. We characterize how far out of equilibrium the spherical shell state is and the chemical power necessary to sustain it. Our work suggests new avenues for assembling complex stable morphologies, which might already be exploited to form membraneless organelles by cells.

Introduction

Spontaneous structure formation through self-assembly and phase separation is essential in biology and engineering.⁵ These structures form through free energy minimization, leading to in- or close-to-equilibrium morphologies. Typical examples are structures formed by amphiphiles,⁶⁻⁸ nanoparticles,⁹ liquid crystals,¹⁰ peptides,¹¹⁻¹³ and the demixing of immiscible liquids,¹⁴ which find application in healthcare,¹⁵ optoelectronics,¹⁶ and others. In contrast, dissipative structures can only form when a system is forcefully kept from reaching a free energy minimum by a continuous energy supply.^{2,17-19} Active droplets exemplify a dissipative structure since their maintenance requires a continuous supply of free energy and matter.^{1,20-25} These structures are ubiquitous in biology³ but remain poorly understood⁴, and synthetic models are rare.²⁶ In contrast, in- or close-to-equilibrium droplets are well-understood.²⁷⁻³² Such droplets form via phase separation in mixtures of immiscible liquids. They tend towards a spherical shape, corresponding to minimal interfacial surface energy. Minimizing this energy also drives coarsening through fusion and Ostwald ripening, yielding a single droplet (Fig. 1A).

Active droplets are a new class of dissipative structures whose properties are governed by chemical reactions and diffusive fluxes. Theoretical studies on these structures show exciting behaviors that result from their non-equilibrium nature, which includes inhibiting Ostwald ripening and thereby controlling their size^{33,34} and spontaneous self-division.^{35,36} These behaviors require a non-equilibrium steady state which has been hard to achieve under experimental conditions.^{37,38} Synthetic analogs are scarce to test these exciting behaviors, and methods to continuously fuel these droplets do not exist.

In this work, we describe how continuously fueled phase separation yields a new dissipative structure: a thin, spherical shell of phase-separated liquid (Fig. 1B). This is intriguing since the additional interface and, thus, the larger surface area compared to volume makes such spherical shells thermodynamically unstable. The energy supply to sustain the thermodynamically unstable state comes from continuously converting fuel to waste, leading to diffusive fluxes that stabilize the spherical shell. We show that this non-equilibrium spherical shell state forms due to an instability of the active droplet's core and that the shell interfaces act as a pump for fuel-activated chemical components.

Results and discussion

Fuel-driven complex coacervation. In our chemically fueled droplets, DIC (N,N'-diisopropylcarbodiimide) is the high energy molecule (fuel) that reacts with the C-terminal aspartic acid of a peptide (Ac-F(RG)₃D-OH, precursor, Fig. 2A). It converts the precursor into its corresponding cyclic anhydride (product, Fig. 2A). That product has a half-life of 58 seconds ($k_{\text{deact.}} = 0.012 \pm 0.009 \text{ s}^{-1}$, Extended Data Fig. 1A-C, Table S5) before it is deactivated through hydrolysis. Upon activation, the peptide turns from zwitterionic to cationic with an overall charge of +3 ($k_{\text{act.}} = 0.17 \pm 0.008 \text{ M}^{-1} \text{ s}^{-1}$, Extended Data Fig. 1A-C, Table S5). In their short lifetime, the cationic, activated peptide can bind a polyanion (pSS, 400 monomer repeat units, 75kDa). The non-activated, zwitterionic precursor interacts weakly with the polyanion pSS ($K_{\text{D, prec.}}$ of $104.5 \pm 11.4 \text{ } \mu\text{M}$, Extended Data Fig. 1D-F). In contrast, the product interacts strongly with pSS ($K_{\text{D, prod.}}$ of $2.4 \pm 1.2 \text{ } \mu\text{M}$, Extended Data Fig. 1D-F and supplementary discussion 1). Thus, chemical fuel creates a population of short-lived activated building blocks that can interact with polyanions and phase separate into complex coacervate droplets.

Size-dependent spherical shell formation upon dissolution. When we fueled a solution of 22 mM peptide and 12 mM pSS (the concentration is expressed in repeat units) in 200 mM MES buffer with a batch of 20 mM fuel, we found that the sample turned turbid (Extended Data Fig. 2A) due to the formation of micron-sized coacervate-based droplets as evidenced by confocal microscopy (Fig. 2B). These droplets fused, and, when the emulsion has depleted most of its fuel, the droplets decayed—a clear solution without droplets was obtained (Extended Data Fig. 2A). In the dissolution process, after around 7 minutes, when the fuel ran low, we found that the droplets transitioned from a homogenous droplet to a spherical shell (Fig. 2B, Movie S1), a process referred to as vacuolization³⁹⁻⁴¹ which is also reminiscent of bubbly phase separation in active fluids⁴². Moreover, we found that the larger the droplet, the sooner the droplet became unstable and formed a spherical shell (Fig. 2C and D).

If the solution was fueled with only 10 mM DIC, the droplets stayed smaller and did not form spherical shells during their dissolution (Extended Data Fig. 2B-C, Movie S2). Vacuole formation has previously been shown as a dissolution pathway of coacervate-based droplets^{20,43,44}. In our case, we hypothesize that these spherical shells form because when fuel runs low, the influx of new droplet material decreases and the deactivation of the peptide in the core outcompetes the influx of new material. Thus, gradients of product material could form within the droplet, leading to the dissolution of the droplet's core. A larger

droplet would have a steeper gradient and thus dissolve sooner. This mechanism suggests that spherical shells could form and be sustained in steady state when fuel is provided continuously to very large droplets.

Continuously fueled active droplets in microreactors. Continuously fueling soft matter to yield sustained non-equilibrium steady states is challenging because these solutions cannot be stirred without affecting the assemblies. Moreover, waste accumulation often inhibits the self-assembling process.^{38,45} Therefore, we developed aqueous microreactors into which fuel continuously diffuses from a reservoir (Fig. 3A and B). We made these aqueous microreactors by preparing a stable emulsion of water droplets in a fluorinated oil phase. The water droplets (microreactors) contained the peptide, buffer, and polyanion, *i.e.*, all reagents except the fuel. The fluorinated oil contained the fuel, which diffused into the microreactors at the oil-water interface until a steady state of fuel and product was reached (Fig. 3A and Extended Data Fig. 3A-B). Excitingly, the waste of the reaction cycle (DIU) partitioned preferentially outside the microreactors and crystallized in the fluorinated oil phase (Extended Data Fig. 3A,C). For the experimental conditions of Fig. 2 (0.5 M DIC in the oil phase), a concentration of 8.4 mM DIC in the aqueous phase was measured (Extended Data Fig. 3D). Moreover, the concentration of fuel in the fluorinated oil controlled the fuel concentration inside the microreactor, too (Extended Data Fig. 3D). Thus, this new continuous fueling method allows us to continuously fuel microreactors at various steady states and simultaneously avoid the challenge of accumulating waste. Z-stacks of the microreactors can be acquired with a confocal microscope. When projected onto one plane, each coacervate droplet can be counted, and its volume measured (Fig. 3A). Finally, with our method, many microreactors of volumes ranging from thousands to millions of μm^3 are made in one experiment (Fig. 3G).

The size-dependent transition of active droplets into active spherical shells. Within seconds after preparing the microreactors, coacervate droplets nucleated and grew through fusion (Fig. 3A). After about 10 minutes, the total volume of all combined droplets within one microreactor reached its maximum. It stayed constant throughout the experiment, indicating a steady state in activation and deactivation was reached (Extended Data Fig. 3E-F, Movie S3). Within 30 minutes, all droplets fused until one large active droplet remained. We identified two possible behaviors of the active droplet: in small microreactors, the active droplet sunk to the bottom of the reactor, slightly wetted the reactor floor and remained stable for the entire observation time (Fig. 3A, Extended Data Figs. 4A and 5A-B, Movie S4).

In large microreactors, the active droplet was also larger. These droplets sunk and slightly wetted the reactor floor (Fig. 3B). However, after about 2 h, its core became unstable. Remarkably, the droplet transitioned and left behind a shell of droplet material homogenous in thickness (Fig. 3C) that was stable for several hours (Extended Data Fig. 5C-E, Movie S5). As the original droplet had wetted the floor, we did not obtain a spherical shell for batch-fueling experiments. Instead, we observed a half dome of phase-separated material (Fig. 3C). If we performed the same experiments with passive droplets, we did not observe the formation of any spherical shells (Extended Data Fig. 4B-G). We measured the product's diffusion coefficient within the active droplets and the active spherical shells, D_{prod} , by fluorescence recovery after photobleaching (FRAP) to be $0.03 \mu\text{m}^2/\text{sec}$ (Fig. 3E and Extended Data Fig. 6B,E, Table S4).

Additional FRAP experiments on the precursor, and the polyanion (Extended Data Fig. 6A,C,D,F), confirmed the shell was liquid and not in a dynamically arrested state⁴⁶ which was further corroborated when we exchanged the fluorinated oil with fluorinated oil without fuel. The spherical shell rapidly dissolved until all droplet material had decayed (Fig. 3E). When the oil was exchanged with DIC-loaded oil, droplets reappeared that fused. Still, due to extensive wetting of the newly formed active droplets, only a small fraction of the microreactors yielded spherical shells.

Next, we tested the permeability and partitioning of the shell by adding fluorescently labeled anionic molecules and nanoparticles: a U₁₅ RNA oligomer, dextran sulfate, carboxy-terminated polystyrene particles, and a DNA oligomer (ATCG)₈ (Fig. 3F). All partitioned well into the shell except for (ATCG)₈ which showed a lower fluorescence in the shell than in the dilute phase. Additionally, both U₁₅ and dextran sulfate showed similar fluorescence within the interior of the spherical shell compared to the dilute phase outside (Extended Data Fig. 7A-B), whereas (ATCG)₈ was excluded from the interior of the spherical shells (Extended Data Fig. 7C). This suggests that the shell acts as a permeable membrane to molecules that partition well, but not ones that hardly partition or large particles that do not leave the spherical shell.⁴⁷

We quantified the relationship between the reactor volume and droplet behavior. We first confirmed the volume of the droplet material scales linearly with the reactor volume (Fig. 3G and H). Simply put, a larger microreactor contains more precursor molecules and produces more product molecules. This dataset revealed that a shell could be expected when the microreactor was larger than roughly 30.000 μm^3 (Fig. 3H). This microreactor volume corresponds to a coacervate-based droplet volume of 150 μm^3 . In other words, shells were formed when the microreactor was sufficiently large to form coacervate-based droplets larger than 150 μm^3 corresponding to the threshold radius $r_{\text{unstable}} = 3.3 \mu\text{m}$ (Fig. 3I). Additionally, we found that the thickness of the spherical shells L_{shell} was relatively constant ($L_{\text{shell,exp.}} = 2.4 \pm 0.4 \mu\text{m}$) over an extensive range of total phase-separated material ($V_{\text{coacervate, shell}} = 150$ to 3000 μm^3).

The mechanism for spherical shell formation. Different mechanisms have been reported for forming morphologies similar to the spherical shells observed in this work. Stable shell-like morphologies at thermodynamic equilibrium have previously been reported due to the formation of multiphase compartmentalization.⁴⁸⁻⁵⁰ In these cases, a third coexisting phase in the droplet's core stabilizes the outer liquid shell-like phase. In our case, the transition into a spherical shell is not due to the formation of an additional coexisting dense phase in the core of the droplet but there is an additional dilute domain with a composition similar to the surrounding dilute phase, i.e., all the droplet-forming materials are depleted from the core (Extended Data Fig. 7D-E). This hypothesis is supported by the phase diagram associated to the corresponding mixture with the stabilized product, which does not exhibit three-phase coexistence (Extended Data Fig. 9A-B). Another possibility is the formation of vesicular structures due to surface-active building blocks supplied^{51,52} or formed in situ through, e.g., pH change⁵³ or charge mismatch⁴⁷. However, the formation of new surface-active building blocks can be excluded due to the absence of the spherical shell transition in the compositionally equivalent reactors containing droplets

with $r < r_{\text{unstable}}$ and the formation of stable passive droplets of similar compositions (Extended Data Fig. 4D-I). The transition of droplets into metastable shells has been reported as a transient state due to underlying reentrant phase transitions⁴³, degradation of the building blocks⁴⁴, dynamically arrested states due to a change in composition⁴⁶ or after deep temperature quenches⁵⁴, or by applying an electric field⁴¹. However, these mechanisms rely on changes in external factors or chemical composition, and the resulting non-equilibrium morphologies cannot be sustained in time. In contrast, spherical shells in our system are stationary, and their morphology can be sustained. Therefore, neither of these mechanisms explains the formation of our observed spherical shells.

To better understand the mechanism of the spherical shell formation, we measured the product's and fuel's partition coefficients in the coacervate-based droplets with a spin-down assay. We found that the fuel only weakly partitions inside the droplets ($K_{\text{fuel}} = 1.4 \pm 1.7$, Table S3, supplementary discussion 2). Thus, most of the fuel remains outside the droplets. In contrast, the product partitions strongly inside the droplets ($K_{\text{product}} = 3360 \pm 1645$, Table S2). We conclude that activation predominantly occurs outside, whereas deactivation occurs inside the droplets. The spatial separation of these reactions leads to a diffusion gradient of product that builds up from the outside of the droplet towards its core (Fig. 4A). In other words, the greater the radius of the active droplet, the more its core is depleted from the product. It thus destabilizes, leading to the core's instability and the transition into a spherical shell (Fig. 4B and Extended Data Fig. 7E, Movie S6).

Quantitative verification of the mechanism for spherical shell formation. To quantitatively verify that hypothesis, we developed a non-equilibrium, thermodynamics-based model that describes a droplet in the center of a spherical reactor with the fuel and waste concentrations maintained at the reactor's boundary. We used experimentally determined steady-state concentrations, rate constants, diffusion, and partitioning coefficients (Table S1-5). To provide a theory with minimal physiochemical ingredients, we do not describe the polyanion and the wetting of the spherical shell on the microreactor wall. We experimentally determined the concentrations of the three components in the phase diagram (see supplementary discussion 2), which was then fitted by a mean-field Flory Huggins model showing good agreement (Extended Data Fig. 9A-B).

We used our model to calculate the product's concentration profile from a droplet core to its boundary (Fig. 4C). We used a droplet with a 5 μm radius which is greater than r_{unstable} (Fig. 3I). The concentration decreases from 1200 mM at the droplet interface to 450 mM at the core, which is depleted of droplet material because of the deactivation. The core's concentration is far below the spinodal decomposition concentration. Thus, the droplet core cannot be stable, *i.e.*, a new domain more similar to the outside nucleates at the core and grows, leaving behind a spherical shell of droplet material (Fig. 4D). A droplet with a radius smaller than r_{unstable} has a core in which the product concentration remains above the spinodal decomposition concentration and is thus stable (Fig. 4E).-Strikingly, we found that the model predicted r_{unstable} to be 2 μm , *i.e.*, close to the experimentally determined 3.3 μm .

Further calculations created a diagram that predicts a droplet's behavior based on its microreactor size and fuel concentration (Fig. 4F). At low steady-state fuel concentrations, insufficient droplet material is activated to form a stable droplet. Above 5 mM of fuel, phase separation is observed, and a stable droplet or a spherical shell is found depending on the microreactor size. Surprisingly, large reactors produced stable droplets beyond a steady-state fuel concentration of 20 mM. We explain this because as the fuel concentration increases, its concentration inside the droplets increases. The resulting peptide re-activation inside the droplet weakens the concentration gradient of the product inside (Extended Data Fig. 10A). According to our model, the non-equilibrium steady states of an active spherical shell and an active droplet can coexist (blue-red shaded area). Some of these theoretical calculations could be experimentally verified. We changed the fluorinated oil's fuel concentration to tune the microreactors' fuel concentration between 0.4 and 16.8 mM (Fig. 4F, Extended Data Fig. 3D and 8) to find agreement with the predicted microreactor sizes for the formation of spherical shells, droplets, and the homogenous phase.

In line with the experiments, the model also predicted that the shell thickness (L) is relatively constant with varying reactor sizes, despite decreasing slightly towards bigger reactor volumes (Extended Data Fig. 10B-C). However, the absolute value is lower than measured ($L_{\text{theory}} \sim 0.3 - 0.6 \mu\text{m}$). Using the model, we calculated that L initially decreases rapidly with an increasing deactivation rate constant ($k_{\text{deact.}}$) but is then quite stable over a broad range of $k_{\text{deact.}}$. However, no droplets were found if the product is too short-lived (Fig. 4G). In contrast, increasing the product's diffusion constant made the shell thicker, *i.e.*, the activated product can diffuse further in its short lifetime leading to a weaker gradient. Yet, a too-fast diffusing product led to no droplets (Fig. 4H).

Free energy and chemical work to sustain spherical shells. Finally, we calculated the free energy and the chemical work needed to produce spherical shells (see supplementary methods I). The free energy difference between a spherical shell and a droplet of identical volume is reflected in the additional interface. For an assumed surface tension (γ) of $75 \mu\text{N/m}$, the additional free energy cost (F_{surface}) of a spherical shell with an inner radius (R_{in}) of $2 \mu\text{m}$ compared to a droplet equals 4 fJ . Based on the equilibrium constant of the acid-anhydride equilibrium,⁵⁵ we calculate a free energy difference between the precursor and the product of about $10 k_{\text{B}}T$. Combined with the steady-state concentration of the product, we calculated that the system is chemically away from equilibrium by 80 nJ ($F_{\text{act}} = 80 \text{ nJ}$). Therefore, the additional surface energy is negligible compared to the free energy needed for activating the precursor to the product to sustain the spherical shell. We calculated the number of chemical cycles to sustain the steady state to be $6 \cdot 10^4 / (\mu\text{m}^3 \cdot \text{s})$. Combined with the free energy difference of the cycle, the total free energy turned over per time and volume is $J_{\text{tot}} = 0.275 \text{ W/L}$. Simply put, this power is supplied to maintain the product population in the activated state. At 0.275 W/L , the power consumption is smaller but comparable to that of living cells at 1 W/L . One reason is that the concentration of fuel (ATP in cells) and the energy it liberates upon hydrolysis are in the same range as our synthetic system.⁵⁶ Interestingly, reminiscent morphologies of spherical shells have been observed in various cell types.^{39,57}

Nevertheless, what fraction of this power maintains the spherical shell morphology? The spherical shell results from activation dominating deactivation outside, while net deactivation is inside. This imbalance of chemical rates gives rise to a net diffusive influx of product and efflux of the precursor at the shell interfaces, J_{int} . The flux of the product multiplied by the activation energy of $10 k_{\text{B}}T$ corresponds to the power to keep the shell interface steady and prevent the relaxation to the active droplet or even the homogenous state. Thus, the imbalance of chemical rates between the two coexisting phases gives rise to an energy pump. We find that the power of this pump is about $J_{\text{int}} = 0.198 \text{ W/L}$ (see supplementary methods I). Compared to the supplied chemical power, this yields an efficiency, $J_{\text{int}}/J_{\text{tot}}$, of about 72%. The efficiency is lower than 100% because the deactivation outside and the re-activation inside the shell do not contribute to the flux through the interface.

Conclusions

Our new microreactors are a versatile method to fuel assemblies continuously. We used them to study spherical shells—a new dissipative structure that theory and experiment verified to originate from reaction-diffusion gradients. These reactors pave the way for elucidating other dissipative structures and new morphologies. Those can help elucidate biological structure formation and be applied as new microfabrication methods. Besides continuously fueling dissipative structures, we foresee that the new microreactors are essential to power chemically fueled molecular motors and machines.

Methods

Materials. All solvents were purchased in analytical grade from Sigma Aldrich and used without further purification. *N,N*-dimethyl formamide (DMF), Fmoc-R(Pbf)-OH, Fmoc-D(OtBu)-OH, Fmoc-G-OH, Fmoc-N(Trt)-OH, *N,N*-diisopropylcarbodiimide (DIC), ethyl cyano(hydroxyimino)acetate (Oxyma, Nova-biochem©), Wang resins (100- 200 mesh, 0.4-0.8 mmol/g), Rink Amide resins (100-200 mesh, 0.4-0.8 mmol/g), 4-(dimethylamino)-pyridine (DMAP), trifluoroacetic acid (TFA, 99%), piperidine (99%), triisopropylsilane (TIPS), *N,N'*-diisopropylethylamine (DIPEA), 4-chloro-7-nitrobenzofurazan (NBD-Cl, 98%), polystyrene sulfonate (pSS, 75kDa, 18wt% in water), sulforhodamine B, 4-morpholineethanesulfonic acid (MES) buffer, carboxylate-modified polystyrene beads (fluorescent yellow-green, 1 μm mean particle size), Cy3-labeled (ATCG)₈ were all purchased from Sigma-Aldrich and used without any further purification unless indicated otherwise. Peptides Ac-F(RG)₃D-OH and Ac-F(RG)₃N-NH₂ were purchased from CASLO Aps. Peptides NBD-G(RG)₃N-NH₂ and NBD-G(RG)₃D-OH were synthesized using a published procedure.²⁵ Cy5-pSS (710 kDa) was synthesized using a published procedure.⁵⁰ Cy3-U₁₅ was purchased from biomers.net GmbH. Cy3-dextran sulfate (40 kDa) was purchased from CD Bioparticles. 2w% 008-Fluorosurfactant in Novec 7500 was purchased from RAN Biotechnologies. Novec 7500 was purchased by lolitec.

Standard sample preparation. Stock solutions of Ac-F(RG)₃D-OH (precursor, 300 mM), pSS (41 mM, according to monomer units), and MES (650 mM) was prepared by dissolving the respective amount of

each component in MQ water and adjusting the pH to 5.3. Stock solutions for Ac-F(RG)₃N-NH₂ (product*), and the fluorescent dyes were also prepared in MQ water but without pH adjustment. All stocks were filtrated with a syringe filter (PTFE, 0.2 μm pore size). For active droplets fueled with a batch of fuel: 5-20 mM DIC (fuel) was added to a solution (20-500 μL) of precursor and pSS in 200 mM MES at pH 5.3, and the solution was mixed with a pipette. For active droplets fueled with excess fuel: 5 μL of DIC is added to a solution (20 μL) of 10 mM precursor and 5 mM pSS in 200 mM MES at pH 5.3. The sample is mixed with a pipette, and residual DIC above the solubility limit is left as a reservoir on top of the aqueous solution. For active droplets fueled continuously, a solution (5 μL) containing precursor and pSS in 200 mM MES at pH 5.3 was mixed with perfluorinated oil (Novec 7500, 50 μL) containing the fluorosurfactant and 0.025-1.5 M DIC. For passive droplets that are not fueled, pSS was added to a solution containing precursor and product* in 200 mM MES at pH 5.3, and the solution was mixed with a pipette.

Nuclear magnetic resonance spectroscopy (NMR). ¹H-NMR spectra were recorded with 16 or 64 scans at room temperature on Bruker AVHD 300, AVHD400, and AVHD500 spectrometers. Chemical shifts are reported in parts per million (ppm) relative to the signal of the deuterated solvent D₂O (δ = 4.7 ppm). All measurements were performed in triplicate (N=3) at 25 °C.

High-performance liquid chromatography (HPLC). High-pressure liquid chromatography was performed using analytical HPLC (ThermoFisher, Vanquish Duo UHPLC, and Thermofisher Dionex Ultimate 3000) with a Hypersil Gold C18 column (100 x 3 mm, 250 x 4.6 mm). Separation was performed using a linear gradient of acetonitrile (2 to 98%) and water with 0.1 % TFA, and the chromatogram was analyzed using detectors at 220 nm and 254 nm. The data was collected and analyzed with the Chromeleon 7 Chromatography Data System Software (Version 7.2 SR4). All measurements were performed in triplicate (N=3) at 25 °C.

Fluorescence spectroscopy. Fluorescence spectroscopy was performed on a Jasco spectrofluorimeter (Jasco FP-8300, SpectraManager software 2.13) with external temperature control (Jasco MCB-100). All experiments were performed in triplicate (N=3) at 25 °C.

Isothermal titration calorimetry (ITC). ITC experiments were performed with a MicroCal PEAQ-ITC from Malvern Pananalytical. All experiments were performed at 25 °C. The following conditions were used: pSS 75kDa (1 mM sulfonate units in MES 200 mM, pH 5.3) was titrated with the precursor (15 mM in 200 mM MES, pH 5.3): 25 injections, 1.5 μL/inj. pSS 75kDa (0.05 mM sulfonate unit in 200 mM MES, pH 5.3) was titrated with the product* (1.5 mM as charged units, 0.5 mM as molecular concentrations in 200 mM MES, pH 5.3): 25 injections, 1.5 μL/inj. All experiments were performed in triplicate (N=3). For each experiment, a control was performed by titrating the corresponding amount of peptide (precursor or product*) in 200 mM MES buffer (pH 5.3) without pSS. Data were fitted using a non-linear least squares algorithm provided with the PEAQ-ITC Analysis software.

Kinetic model. The concentration profiles of the precursor and its corresponding anhydride (product) were determined by HPLC, whereas NMR quantified fuel and waste. The resulting experimental data were fitted

to a custom program in Python 3 previously published by the group of Hartley and applied to similar systems.⁵⁸ Further information can be found in the supplementary information.

Method to continuously fuel active droplets. Surfactant-stabilized water in oil droplets was produced using 1 % 008-FluoroSurfactant in 3M HFE7500 as the oil phase. To form microreactors of varying size, 5 μL of a solution containing 10 mM precursor and 5 mM pSS in 200 mM MES at pH 5.3 were added to 50 μL of the oil phase in a 200 μL Eppendorf tube. Active droplets: For the preparation of active droplets, fuel was added to the oil phase before adding the sample containing the precursor and pSS. Snipping of the centrifugal tube resulted in the formation of microreactors with a random size distribution. The microreactors were imaged at the confocal microscope in untreated observation chambers⁵⁹ consisting of a 24 mm x 60 mm glass cover slide and a 16 mm x 16 mm glass cover slide that were separated by two slices of double-sided sticky tape and sealed with two-component glue.

Passive droplets: For the preparation of passive droplets, coacervation is induced right before the encapsulation into the microreactors by adding pSS as the last component. The microreactors were sealed and imaged in untreated observation chambers.

Dissolution and reinduction: To exchange the oil phase, 30 μL of a solution containing 10 mM precursor and 5 mM pSS in 200 mM MES at pH 5.3 were added to 300 μL of the oil phase containing the fuel in a 1 mL Eppendorf tube. After 2 h a sample was imaged in an observation chamber as a control for the formation of spherical shells. The residual microreactors in the Eppendorf tube were pipetted into 300 μL of perfluorinated oil containing no fuel. A sample of these microreactors was imaged in an observation chamber to confirm the dissolution of active droplets and shells. Again after 2 h, the residual microreactors in the oil containing no fuel were pipetted into 50 μL of perfluorinated oil containing 0.5 M DIC. A sample of these microreactors was imaged in an observation chamber.

Confocal fluorescence microscopy and droplet analysis. A lightning SP8 confocal microscope (Leica) with a 63x water immersion objective (1.2 NA) was used to analyze the coacervates in bulk and the microfluidic reactors (microreactors). Sulforhodamine B was added to track the coacervates via fluorescence if not indicated otherwise, and the dye was excited at 552 nm and imaged at 565-700 nm with a HyD detector. The pinhole was set to 1 Airy unit.

Coacervate-based droplets and coacervate-based spherical shells were analyzed with ImageJ (Fiji). For the analysis, images of coacervate-based droplets were thresholded with the moments thresholding algorithm, and a gaussian blur was applied. Subsequently, the images were analyzed with the analyze particle plugin in ImageJ. The used parameters were size = 5 μm^2 -infinity, circularity = 0-1, and all images were analyzed once with holes included and once without holes. The thickness of the coacervate-based spherical shells was determined by subtracting the vacuole's radius from the droplet's radius with holes. The volume of coacervate-based spherical shells was calculated assuming a spherical shape and considering the half-sphere shape due to wetting at the interface of the microreactor and the oil. The volume of coacervate-based droplets without vacuoles was calculated assuming a spherical droplet.

Fluorescence recovery after photobleaching (FRAP). The diffusivity of the molecules inside active droplets was measured via spot bleaching. Measurements were performed in microfluidic reactors. For

the recovery of the peptides, coacervate-based droplets were stained with NBD-G(RG)₃D-OH (fluorescent analog of precursor) or NBD-G(RG)₃N-NH₂ (fluorescent analog of product*) which was excited at 488 nm and imaged at 565-635 nm with a PMT detector. For the recovery of pSS, Cy5-pSS was excited at 638 and imaged at 648-720 nm with a PMT detector. A spot size of $r = 1 \mu\text{m}$ in radius was bleached in all experiments. Recovery data were normalized through double normalization⁶⁰ and fitted to a first-order exponential equation⁶¹ to obtain the diffusion coefficient as previously described²⁵.

Determination of the partitioning and concentration of molecules inside and outside the droplet phase.

We used a centrifugation assay to determine the amount of precursor, product*, and fuel in the dilute phase and inside passive droplets for the phase diagram. We measured their concentrations using HPLC, fluorescence spectroscopy, and NMR. The total droplet volume was determined by visually comparing the centrifuged droplet phase to size standards. Further information on the procedure can be found in the supplementary information.

Estimating the concentration of product and fuel in the microfluidic droplet. To validate whether the continuously fueled microreactors contain a steady-state level of product and fuel, we chose an indirect quantification method by HPLC for the product⁶², and quantification by NMR for the fuel and waste. We assumed that fuel diffusion from the surrounding oil phase into a microfluidic reactor ($r = 5\text{-}50 \mu\text{m}$) is fast and should be comparable to a two-phase system in a glass vial under vigorous stirring. We used perfluorinated oil without surfactant in these experiments to avoid stabilized emulsions. Further information on the procedure can be found in the supplementary information.

Theoretical model. In the theoretical model, we use an effective ternary mixture composed of a solvent component, precursor A, and product B. The influence of fuel, waste, and polyanion is accounted for implicitly. We determined the molecular interaction parameters of a ternary Flory-Huggins free energy density from experimentally measured equilibrium concentrations of the precursor and product. Furthermore, experimentally determined values of kinetic parameters, such as reaction rates and diffusivities, were used in linearized reaction-diffusion equations for obtaining spatial concentration profiles. We solved these kinetic equations by assuming local phase equilibria at a sharp interface in two spherically symmetric geometries. First, we considered an active droplet at the center. Once the concentrations at the core of this droplet lie within the spinodal regime of the phase diagram, the system is locally unstable. Therefore, we also solved a second geometry with a spherically symmetric shell of the dense phase that encloses a more dilute inner phase while surrounded by another dilute phase. Thus, two interfaces exist. Further information on the calculations can be found in the supplementary information.

Declarations

Acknowledgments

The BoekhovenLab is grateful for support from the TUM Innovation Network - RISE funded through the Excellence Strategy and the European Research Council (ERC starting grant 852187). This research was

conducted within the Max Planck School Matter to Life, supported by the German Federal Ministry of Education and Research (BMBF) in collaboration with the Max Planck Society. Funded by the Deutsche Forschungsgemeinschaft (DFG, German Research Foundation) under Germany's Excellence Strategy - EXC-2094 – 390783311. C. Weber acknowledges the European Research Council (ERC) under the European Union's Horizon 2020 research and innovation program (Fuelled Life, Grant Number 949021) for financial support.

Author contributions

J.Bo. and C.W. designed the project. J.Bo., C.W., and F.J. supervised the project. A.M.B. and C.D. designed the experiments. A.M.B., C.D., M.S., and A.H. performed the experiments. A.M.B., C.D., and M.S. analyzed the data. J.Ba. and G.B. performed the theoretical calculations. J.Bo., C.W., A.M.B., J.Ba., G.B., and C.D. wrote and edited the manuscript.

Data availability

The data supporting this study's findings are available from the corresponding authors upon reasonable request.

Competing interests

The authors declare no competing interests.

References

1. Donau, C. & Boekhoven, J. The chemistry of chemically fueled droplets. *Trends in Chemistry* **5**, 45-60 (2023). <https://doi.org/10.1016/j.trechm.2022.11.003>
2. Boekhoven, J., Hendriksen, W. E., Koper, G. J. M., Eelkema, R. & van Esch, J. H. Transient assembly of active materials fueled by a chemical reaction. *Science* **349**, 1075-1079 (2015). <https://doi.org/10.1126/science.aac6103>
3. Karsenti, E. Self-organization in cell biology: a brief history. *Nature Reviews Molecular Cell Biology* **9**, 255-262 (2008). <https://doi.org/10.1038/nrm2357>
4. Self-assembling life. *Nature Nanotechnology* **11**, 909-909 (2016). <https://doi.org/10.1038/nnano.2016.255>
5. Whitesides, G. M. & Grzybowski, B. Self-Assembly at All Scales. *Science* **295**, 2418-2421 (2002). <https://doi.org/10.1126/science.1070821>
6. Minkenberg, C. B. *et al.* Responsive wormlike micelles from dynamic covalent surfactants. *Langmuir* **28**, 13570-13576 (2012). <https://doi.org/10.1021/la302294r>
7. Hartgerink, J. D., Beniash, E. & Stupp, S. I. Self-Assembly and Mineralization of Peptide-Amphiphile Nanofibers. *Science* **294**, 1684-1688 (2001). <https://doi.org/10.1126/science.1063187>

8. Hill, J. P. *et al.* Self-Assembled Hexa-*peri*-hexabenzocoronene Graphitic Nanotube. *Science* **304**, 1481-1483 (2004). <https://doi.org/doi:10.1126/science.1097789>
9. Glotzer, S. C. & Solomon, M. J. Anisotropy of building blocks and their assembly into complex structures. *Nature Materials* **6**, 557-562 (2007). <https://doi.org/doi:10.1038/nmat1949>
10. Kato, T. Self-Assembly of Phase-Segregated Liquid Crystal Structures. *Science* **295**, 2414-2418 (2002). <https://doi.org/doi:10.1126/science.1070967-a>
11. Levin, A. *et al.* Biomimetic peptide self-assembly for functional materials. *Nature Reviews Chemistry* **4**, 615-634 (2020). <https://doi.org/doi:10.1038/s41570-020-0215-y>
12. Lampel, A. *et al.* Polymeric peptide pigments with sequence-encoded properties. *Science* **356**, 1064-1068 (2017). <https://doi.org/doi:10.1126/science.aal5005>
13. Silva, G. A. *et al.* Selective Differentiation of Neural Progenitor Cells by High-Epitope Density Nanofibers. *Science* **303**, 1352-1355 (2004). <https://doi.org/doi:10.1126/science.1093783>
14. Veis, A. A review of the early development of the thermodynamics of the complex coacervation phase separation. *Advances in Colloid and Interface Science* **167**, 2-11 (2011). [https://doi.org:https://doi.org/10.1016/j.cis.2011.01.007](https://doi.org/https://doi.org/10.1016/j.cis.2011.01.007)
15. Boekhoven, J. & Stupp, S. I. 25th Anniversary Article: Supramolecular Materials for Regenerative Medicine. *Advanced Materials* **26**, 1642-1659 (2014). [https://doi.org:https://doi.org/10.1002/adma.201304606](https://doi.org/https://doi.org/10.1002/adma.201304606)
16. Hirst, A. R., Escuder, B., Miravet, J. F. & Smith, D. K. High-tech applications of self-assembling supramolecular nanostructured gel-phase materials: from regenerative medicine to electronic devices. *Angewandte Chemie International Edition* **47**, 8002-8018 (2008). <https://doi.org/doi:10.1002/anie.200800022>
17. van Rossum, S. A. P., Tena-Solsona, M., van Esch, J. H., Eelkema, R. & Boekhoven, J. Dissipative out-of-equilibrium assembly of man-made supramolecular materials. *Chemical Society Reviews* **46**, 5519-5535 (2017). <https://doi.org/doi:10.1039/C7CS00246G>
18. Ragazzon, G. & Prins, L. J. Energy consumption in chemical fuel-driven self-assembly. *Nature Nanotechnology* **13**, 882-889 (2018). <https://doi.org/doi:10.1038/s41565-018-0250-8>
19. De, S. & Klajn, R. Dissipative Self-Assembly Driven by the Consumption of Chemical Fuels. *Advanced Materials* **30**, 1706750 (2018). [https://doi.org:https://doi.org/10.1002/adma.201706750](https://doi.org/https://doi.org/10.1002/adma.201706750)
20. Donau, C. *et al.* Active coacervate droplets as a model for membraneless organelles and protocells. *Nature Communications* **11**, 5167 (2020). <https://doi.org/doi:10.1038/s41467-020-18815-9>
21. Fanalista, F., Deshpande, S., Lau, A., Pawlik, G. & Dekker, C. FtsZ-Induced Shape Transformation of Coacervates. *Advanced Biosystems* **2** (2018). <https://doi.org/doi:10.1002/adbi.201800136>
22. Deng, J. & Walther, A. Programmable and Chemically Fueled DNA Coacervates by Transient Liquid-Liquid Phase Separation. *Chem* **6**, 3329-3343 (2020). <https://doi.org/doi:10.1016/j.chempr.2020.09.022>
23. Nakashima, K. K., Baaij, J. F. & Spruijt, E. Reversible generation of coacervate droplets in an enzymatic network. *Soft Matter* **14**, 361-367 (2018). <https://doi.org/doi:10.1039/C7SM01897E>

24. Aumiller, W. M., Jr. & Keating, C. D. Phosphorylation-mediated RNA/peptide complex coacervation as a model for intracellular liquid organelles. *Nature Chemistry* **8**, 129-137 (2016).
<https://doi.org/10.1038/nchem.2414>
25. Spath, F. *et al.* Molecular Design of Chemically Fueled Peptide-Polyelectrolyte Coacervate-Based Assemblies. *Journal of the American Chemical Society* **143**, 4782-4789 (2021).
<https://doi.org/10.1021/jacs.1c01148>
26. Das, K., Gabrielli, L. & Prins, L. J. Chemically Fueled Self-Assembly in Biology and Chemistry. *Angewandte Chemie International Edition* **60**, 20120-20143 (2021).
<https://doi.org/https://doi.org/10.1002/anie.202100274>
27. Koga, S., Williams, D. S., Perriman, A. W. & Mann, S. Peptide–nucleotide microdroplets as a step towards a membrane-free protocell model. *Nature Chemistry* **3**, 720-724 (2011).
<https://doi.org/10.1038/nchem.1110>
28. Drobot, B. *et al.* Compartmentalised RNA catalysis in membrane-free coacervate protocells. *Nature Communications* **9**, 3643 (2018). <https://doi.org/10.1038/s41467-018-06072-w>
29. Poudyal, R. R. *et al.* Template-directed RNA polymerization and enhanced ribozyme catalysis inside membraneless compartments formed by coacervates. *Nature Communications* **10**, 490 (2019).
<https://doi.org/10.1038/s41467-019-08353-4>
30. Gucht, J. v. d., Spruijt, E., Lemmers, M. & Cohen Stuart, M. A. Polyelectrolyte complexes: Bulk phases and colloidal systems. *Journal of Colloid and Interface Science* **361**, 407-422 (2011).
<https://doi.org/https://doi.org/10.1016/j.jcis.2011.05.080>
31. Abbas, M., Lipiński, W. P., Wang, J. & Spruijt, E. Peptide-based coacervates as biomimetic protocells. *Chemical Society Reviews* **50**, 3690-3705 (2021). <https://doi.org/10.1039/D0CS00307G>
32. Aumiller, W. M., Jr., Pir Cakmak, F., Davis, B. W. & Keating, C. D. RNA-Based Coacervates as a Model for Membraneless Organelles: Formation, Properties, and Interfacial Liposome Assembly. *Langmuir* **32**, 10042-10053 (2016). <https://doi.org/10.1021/acs.langmuir.6b02499>
33. Weber, C. A., Zwicker, D., Jülicher, F. & Lee, C. F. Physics of active emulsions. *Reports on Progress in Physics* **82**, 064601 (2019). <https://doi.org/10.1088/1361-6633/ab052b>
34. Wurtz, J. D. & Lee, C. F. Chemical-Reaction-Controlled Phase Separated Drops: Formation, Size Selection, and Coarsening. *Physical Review Letters* **120**, 078102 (2018).
<https://doi.org/10.1103/PhysRevLett.120.078102>
35. Zwicker, D., Seyboldt, R., Weber, C. A., Hyman, A. A. & Jülicher, F. Growth and division of active droplets provides a model for protocells. *Nature Physics* **13**, 408-413 (2017).
<https://doi.org/10.1038/nphys3984>
36. Seyboldt, R. & Jülicher, F. Role of hydrodynamic flows in chemically driven droplet division. *New Journal of Physics* **20**, 105010 (2018). <https://doi.org/10.1088/1367-2630/aae735>
37. Heinen, L. & Walther, A. Programmable dynamic steady states in ATP-driven nonequilibrium DNA systems. *Science Advances* **5**, eaaw0590 (2019). <https://doi.org/doi:10.1126/sciadv.aaw0590>

38. Sorrenti, A., Leira-Iglesias, J., Sato, A. & Hermans, T. M. Non-equilibrium steady states in supramolecular polymerization. *Nature Communications* **8**, 15899 (2017).
<https://doi.org/10.1038/ncomms15899>
39. Schmidt, H. B. & Rohatgi, R. In Vivo Formation of Vacuolated Multi-phase Compartments Lacking Membranes. *Cell Reports* **16**, 1228-1236 (2016). <https://doi.org/10.1016/j.celrep.2016.06.088>
40. Moreau, N. G., Martin, N., Gobbo, P., Tang, T. Y. D. & Mann, S. Spontaneous membrane-less multi-compartmentalization via aqueous two-phase separation in complex coacervate micro-droplets. *Chemical Communications* **56**, 12717-12720 (2020). <https://doi.org/10.1039/D0CC05399F>
41. Yin, Y. *et al.* Non-equilibrium behaviour in coacervate-based protocells under electric-field-induced excitation. *Nature Communications* **7**, 10658 (2016). <https://doi.org/10.1038/ncomms10658>
42. Tjhung, E., Nardini, C. & Cates, M. E. Cluster Phases and Bubbly Phase Separation in Active Fluids: Reversal of the Ostwald Process. *Physical Review X* **8**, 031080 (2018).
<https://doi.org/10.1103/PhysRevX.8.031080>
43. Banerjee, P. R., Milin, A. N., Moosa, M. M., Onuchic, P. L. & Deniz, A. A. Reentrant Phase Transition Drives Dynamic Substructure Formation in Ribonucleoprotein Droplets. *Angewandte Chemie International Edition* **56**, 11354-11359 (2017).
<https://doi.org/https://doi.org/10.1002/anie.201703191>
44. Saleh, O. A., Jeon, B.-j. & Liedl, T. Enzymatic degradation of liquid droplets of DNA is modulated near the phase boundary. *Proceedings of the National Academy of Sciences* **117**, 16160-16166 (2020).
<https://doi.org/doi:10.1073/pnas.2001654117>
45. Sharko, A., Livitz, D., De Piccoli, S., Bishop, K. J. M. & Hermans, T. M. Insights into Chemically Fueled Supramolecular Polymers. *Chemical Reviews* **122**, 11759-11777 (2022).
<https://doi.org/10.1021/acs.chemrev.1c00958>
46. Feric, M. *et al.* Mesoscale structure–function relationships in mitochondrial transcriptional condensates. *Proceedings of the National Academy of Sciences* **119**, e2207303119 (2022).
<https://doi.org/doi:10.1073/pnas.2207303119>
47. Alshareedah, I., Moosa, M. M., Raju, M., Potoyan, D. A. & Banerjee, P. R. Phase transition of RNA–protein complexes into ordered hollow condensates. *Proceedings of the National Academy of Sciences* **117**, 15650-15658 (2020). <https://doi.org/doi:10.1073/pnas.1922365117>
48. Yu, H. *et al.* HSP70 chaperones RNA-free TDP-43 into anisotropic intranuclear liquid spherical shells. *Science* **371**, eabb4309 (2021). <https://doi.org/doi:10.1126/science.abb4309>
49. Feric, M. *et al.* Coexisting Liquid Phases Underlie Nucleolar Subcompartments. *Cell* **165**, 1686-1697 (2016). <https://doi.org/10.1016/j.cell.2016.04.047>
50. Donau, C., Spath, F., Stasi, M., Bergmann, A. M. & Boekhoven, J. Phase Transitions in Chemically Fueled, Multiphase Complex Coacervate Droplets. *Angewandte Chemie International Edition* **61**, e202211905 (2022). <https://doi.org/10.1002/anie.202211905>
51. Taylor, N. *et al.* Biophysical characterization of organelle-based RNA/protein liquid phases using microfluidics. *Soft Matter* **12**, 9142-9150 (2016). <https://doi.org/10.1039/c6sm01087c>

52. Williams, D. S., Patil, A. J. & Mann, S. Spontaneous Structuration in Coacervate-Based Protocells by Polyoxometalate-Mediated Membrane Assembly. *Small* **10**, 1830-1840 (2014).
<https://doi.org/10.1002/sml.201303654>
53. Yin, Z., Tian, L., Patil, A. J., Li, M. & Mann, S. Spontaneous Membranization in a Silk-Based Coacervate Protocell Model. *Angewandte Chemie International Edition* **61**, e202202302 (2022).
<https://doi.org/10.1002/anie.202202302>
54. Erkamp, N. A. *et al.* Spatially non-uniform condensates emerge from dynamically arrested phase separation. *Nature Communications* **14**, 684 (2023). <https://doi.org/10.1038/s41467-023-36059-1>
55. Higuchi, T., Ebersson, L. & McRae, J. D. Acid anhydride-free acid equilibria in water in some substituted succinic acid systems and their interaction with aniline. *Journal of the American Chemical Society* **89**, 3001-3004 (1967). <https://doi.org/10.1021/ja00988a036>
56. Milo, R. & Phillips, R. *Cell biology by the numbers*. (Garland Science, 2015).
57. Brangwynne, C. P., Mitchison, T. J. & Hyman, A. A. Active liquid-like behavior of nucleoli determines their size and shape in *Xenopus laevis* oocytes. *Proceedings of the National Academy of Sciences* **108**, 4334-4339 (2011). <https://doi.org/10.1073/pnas.1017150108>
58. Jayalath, I. M., Wang, H., Mantel, G., Kariyawasam, L. S. & Hartley, C. S. Chemically Fueled Transient Geometry Changes in Diphenic Acids. *Organic Letters* **22**, 7567-7571 (2020).
<https://doi.org/10.1021/acs.orglett.0c02757>
59. Hofmann, T. W., Hänselmann, S., Janiesch, J.-W., Rademacher, A. & Böhm, C. H. J. Applying microdroplets as sensors for label-free detection of chemical reactions. *Lab on a Chip* **12**, 916-922 (2012). <https://doi.org/10.1039/C2LC20971C>
60. Wu, C. & Allis, C. D. *Chromatin and Chromatin Remodeling Enzymes, Part A*. (Elsevier, 2004).
61. Kayitmazer, A. B. *et al.* Mesophase separation and probe dynamics in protein–polyelectrolyte coacervates. *Soft Matter* **3**, 1064-1076 (2007).
62. Schnitter, F. & Boekhoven, J. A Method to Quench Carbodiimide-Fueled Self-Assembly. *ChemSystemsChem* **3** (2020). <https://doi.org/10.1002/syst.202000037>

Figures

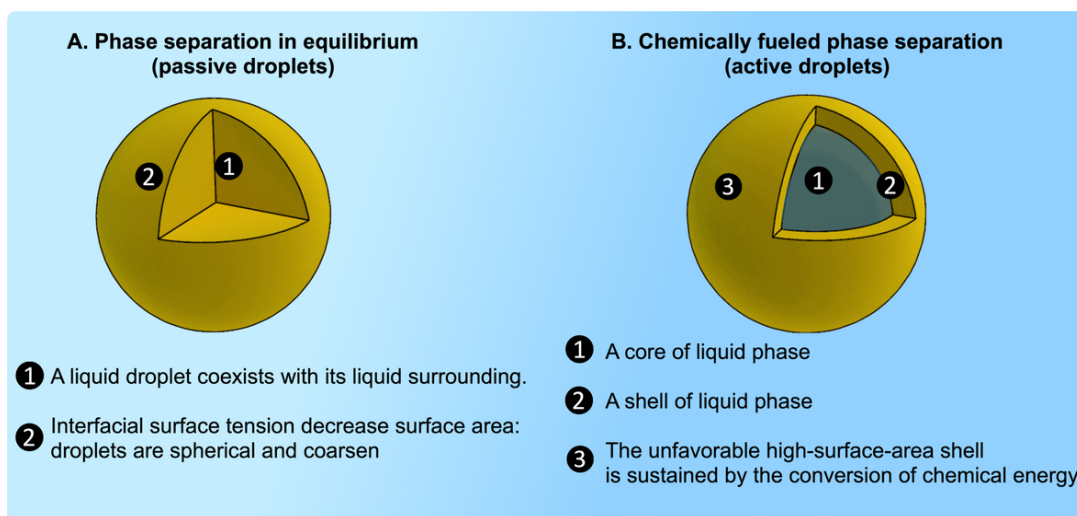


Figure 1

A. Phase separation close to thermodynamic equilibrium leads to spherical droplets. B. A new morphology is described in this work: a liquid, spherical shell.

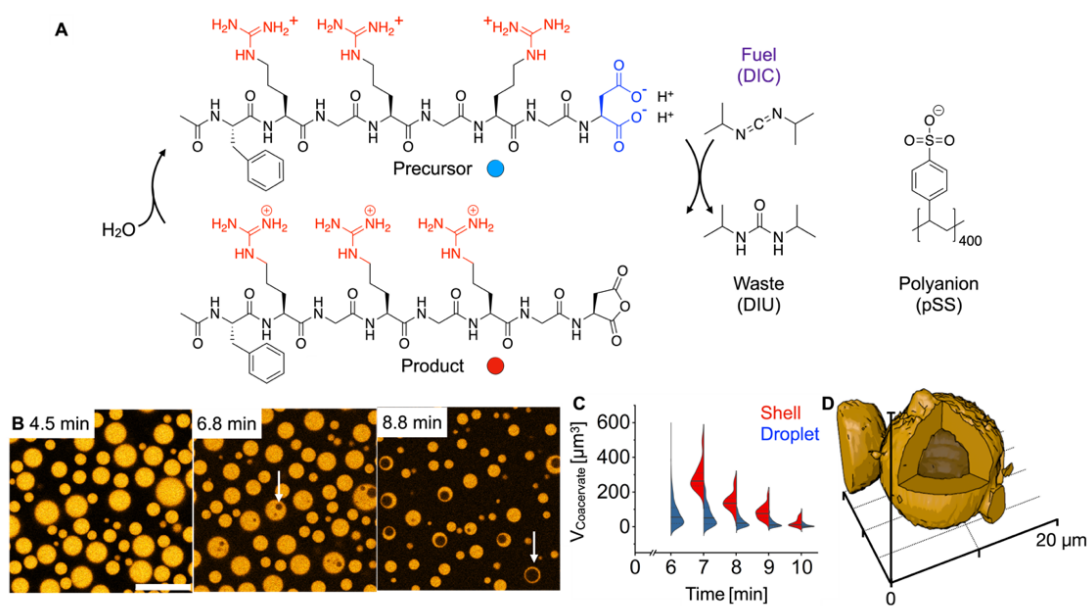


Figure 2

Chemically fueled droplets under batch-fueling. **A.** Chemical structures of the components that form chemically fueled droplets and liquid shells. **B.** Confocal microscopy of a solution of 22 mM precursor, 12 mM pSS, and 0.1 μM sulforhodamine B in 200 mM MES buffer at pH 5.3 fueled with 20 mM DIC. After 7 minutes, the active droplets became unstable and swelled to form a spherical shell (white arrows). Scale bar: 20 μm . **C.** The volume distribution of active droplets (blue) and active liquid shells (red) is shown over time. The solid line represents the median, and the dotted lines represent the upper and lower quartile. Larger active droplets formed spherical shells earlier than smaller active droplets. **D.** 3D reconstruction from confocal microscopy data shows the spherical nature of the shell. Conditions were 10 mM precursor, 5 mM pSS, and 0.1 μM sulforhodamine B in 200 mM MES buffer at pH 5.3 fueled with an excess of DIC (5 μL) on top of 20 μL of the sample. The diffusion of excess fuel into the sample leads to the formation of bigger droplets that are longer lived. The z-stack for the 3D reconstruction is imaged two hours after adding fuel.

5. Liquid Spherical Shells are a Non-Equilibrium Steady State

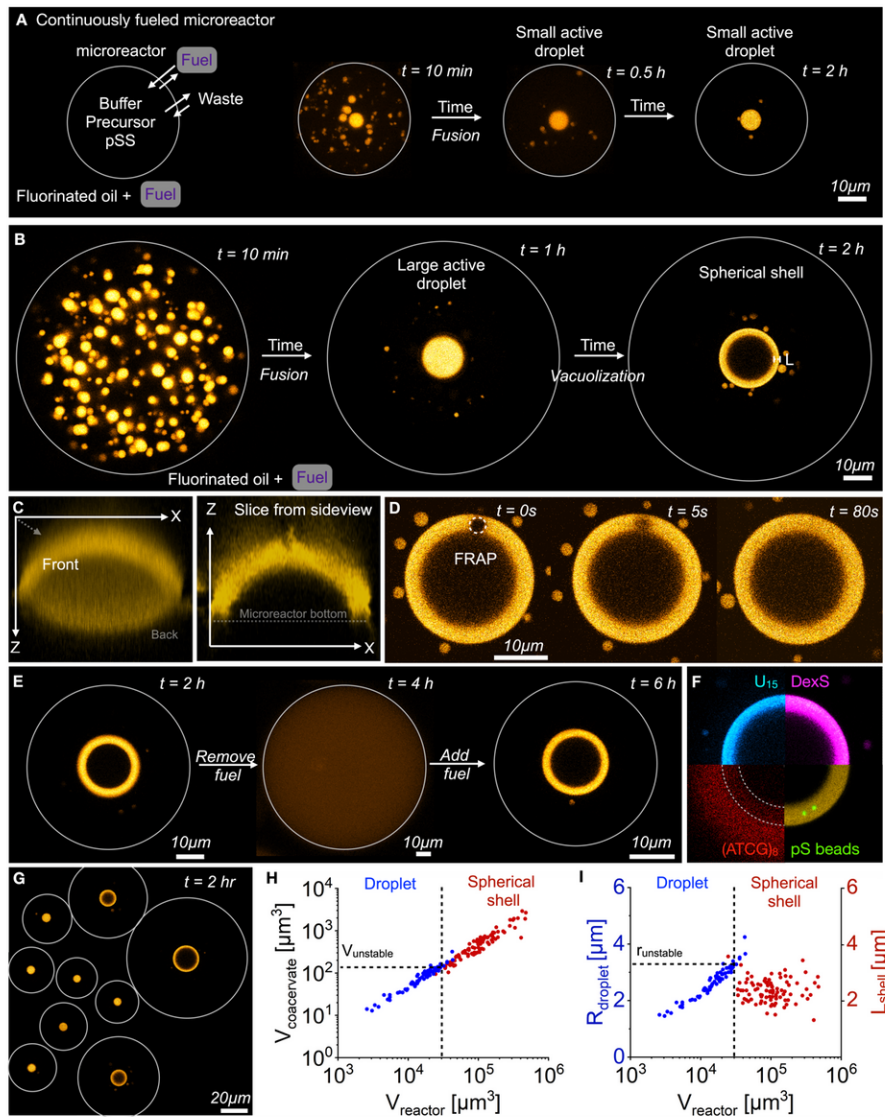


Figure 3

Spherical shells are a stable, non-equilibrium state. **A-B.** Experimental setup to form microreactors that continuously fuel active droplets. Surfactant-stabilized microfluidic droplets (microreactors, grey outline) containing 10 mM precursor, 5 mM pSS, and $0.1 \mu\text{M}$ sulforhodamine B in 200 mM MES buffer at pH 5.3 were embedded in a fluorinated oil which contained 0.5 M DIC (fuel) to sustain the microreactor at a fuel concentration of 8.4 mM. Time-lapsed micrographs of a small (**A**) and large (**B**) microreactor in a steady

state. The grey circle represents the size of the microreactor. The images for 10 min and 0.5 h in **A** and the image for 10 min in **B** are z-projections of the microreactor. All other images are from one Z-plane. **C**. A 3D projection of a spherical shell reconstructed from Z-stack imaging. The left image shows the projection of the average pixel intensity. The right image shows a slice in the XZ plane through the middle of the spherical shell. **D**. A FRAP study of the spherical shell demonstrates that the shell is liquid and dynamic. **E**. The microreactor was fueled with 0.5 M DIC in the oil phase. After the formation of spherical shells (2 h), the oil phase was replaced with oil containing no DIC. After a homogenous solution was obtained (4 h), the oil was replaced with 0.5 M DIC-containing oil. The grey circle represents the size of the microreactor. **F**. Partitioning of different fluorescently labeled molecules into the spherical shell. The dotted line represents the outlines of the spherical shell. **G**. A macroscopic view of multiple microreactors shows that large reactors formed spherical shells while small microreactors contained droplets. The center Z-plane of each of the individual droplets and shells is projected. The grey circle represents the size of the microfluidic reactor. **H**. The volume of the total coacervate material is shown for every individual microreactor that contained an active droplet (blue) or an active shell (red). Above a critical reactor volume, active droplets with a volume bigger than $V_{unstable}$ transformed into spherical shells. **I**. The radius of the active droplet (blue) and the shell thickness L of the active shell (red) for every individual microreactor, is shown. Spherical shells had a similar thickness L_{shell} , which was within the range of $r_{unstable}$

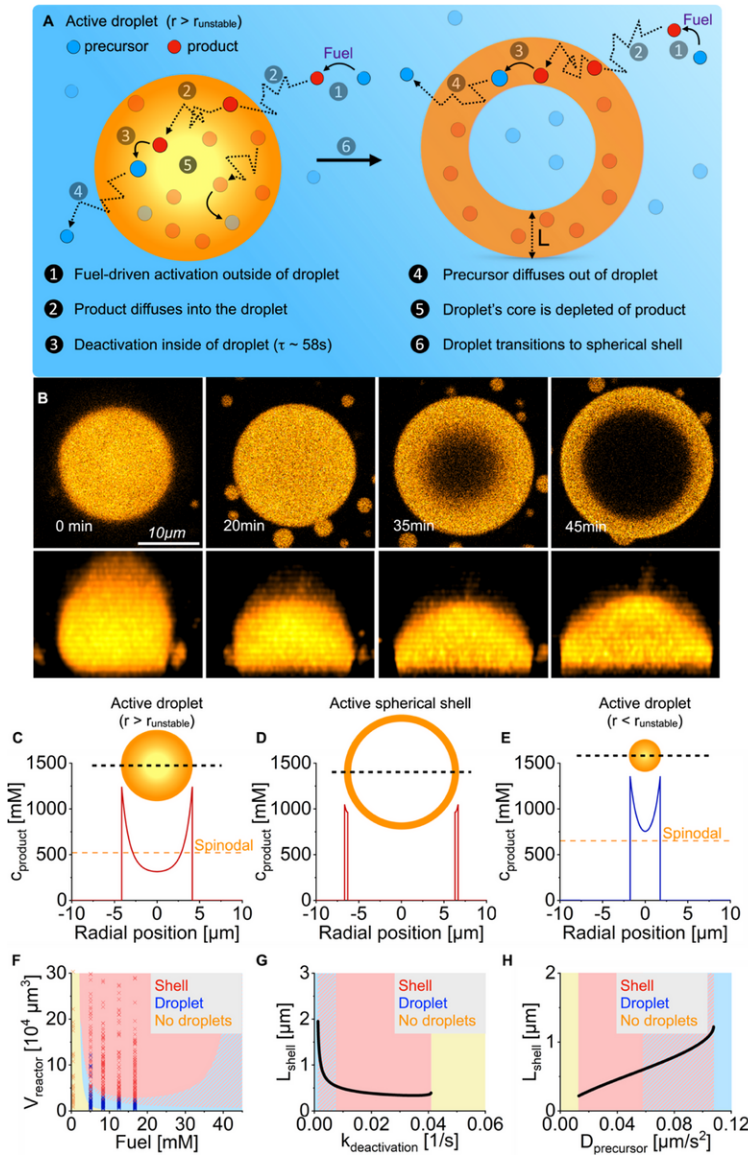


Figure 4

The mechanism of spherical shell formation. **A.** Schematic representation of the mechanism of spherical shell formation. **B.** Confocal micrograph timelapse series of an active droplet with a critical radius larger than $r_{unstable}$. Over 20 minutes, the droplet wetted the microreactor's bottom and transitioned into a spherical shell. The upper row of images shows the XY-plane close to the bottom of the reactor. The bottom row of images shows the XZ-projection. **C-E.** Concentration profiles of a large chemically fueled

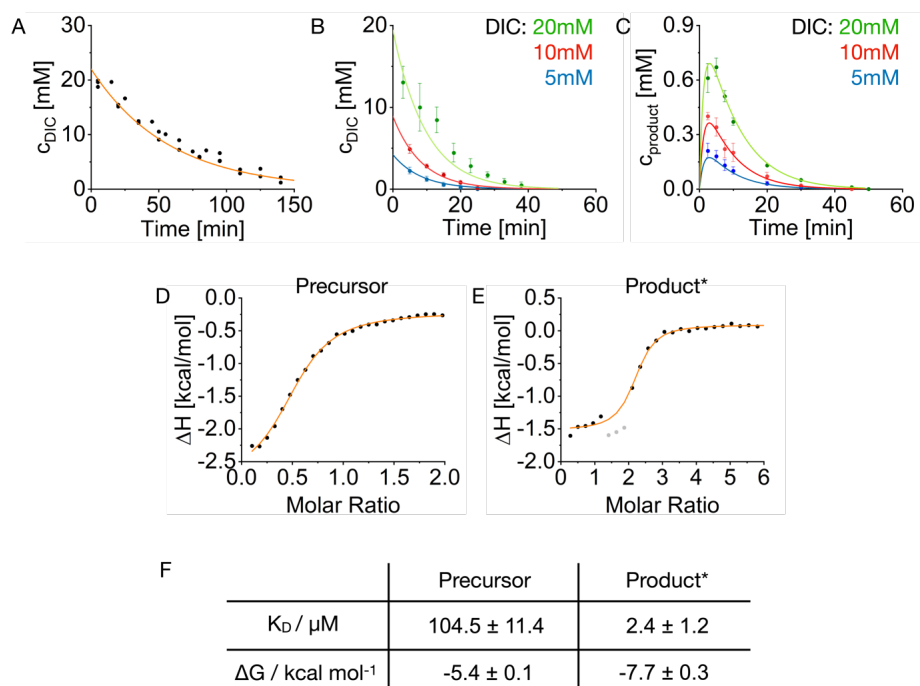
droplet with $r > r_{unstable}$ (**C**) before transitioning into a spherical shell, a spherical shell (**D**), and a small chemically fueled droplet with $r < r_{unstable}$ (**E**). The insets show a scheme of the droplet and spherical shell. **F**. The system's behavior as a function of steady-state concentration fuel and reactor volume. The shaded areas represent the stable state calculated by the model. The red-blue shaded area represents the coexistence of stable droplets and shells. The markers show the phase-separated state of the experimental data. **G-H**. The shell thickness L_{shell} for a microreactor with a radius of $25 \mu\text{m}$ as a function of varying deactivation rate constants (**G**) or precursor diffusion constants (**H**).

Supplementary Files

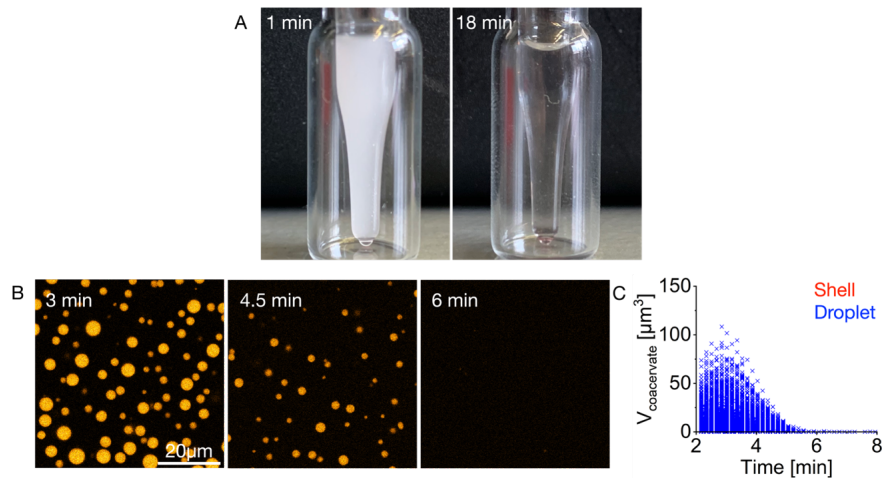
This is a list of supplementary files associated with this preprint. Click to download.

- [SINaturesubmission.pdf](#)
- [MovieS1batchsphericalshellformation.avi](#)
- [MovieS2nosphericalshells.avi](#)
- [MovieS3volumestability.avi](#)
- [MovieS4stableactivedroplet.avi](#)
- [MovieS5stableactiveshell.avi](#)
- [MovieS6sphericalshellformation.avi](#)
- [ExtendedDataFigures.docx](#)

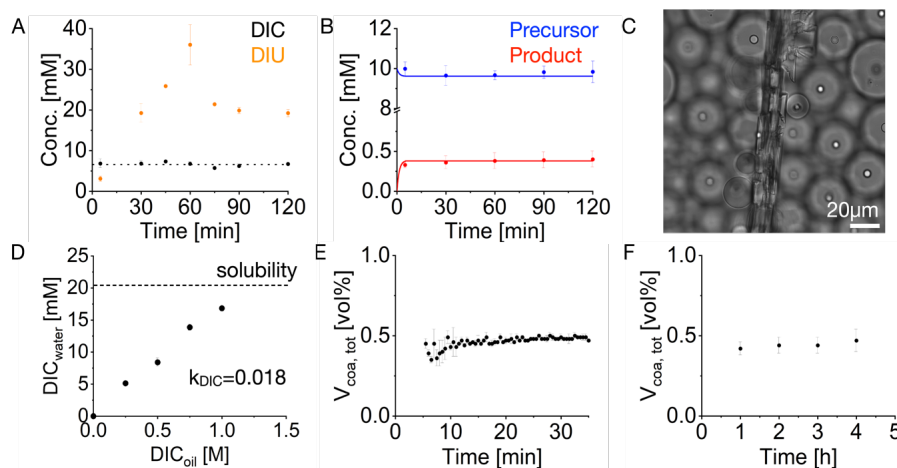
Extended Data Figures

**Extended Data Fig. 1. Determination of the reaction constants and binding affinities.**

A. Kinetics of 20 mM DIC hydration in 200 mM MES buffer at pH 5.3 measured by NMR. **B.** Kinetics of the DIC hydration catalyzed by the precursor. Conditions were 10 mM precursor and 200 mM MES at pH 5.3. Error bars represent the standard deviation of triplicate measurements ($N=3$). Solid lines represent the fits of the kinetic model. **C.** Formation of the product upon addition of DIC measured by HPLC. Conditions were 10 mM precursor and 200 mM MES at pH 5.3. Error bars represent the standard deviation of triplicate measurements ($N=3$). Solid lines represent the fits of the kinetic model. **D-F.** The change in enthalpy measured by ITC for the interaction between precursor (**D**) or product* (**E**) and pSS. Gray data points were not included in the fitting because they showed signs of coacervation. The solid lines represent the fit of the PEAQ-ITC Analysis software. **F.** Dissociation constant K_D and free energy ΔG of the interaction between precursor/product* and pSS.

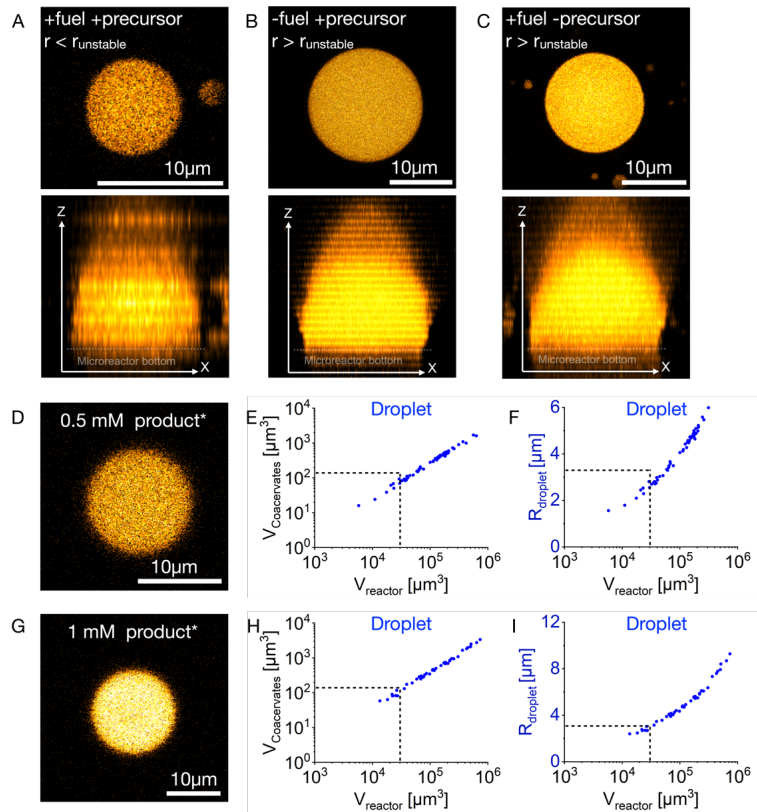


Extended Data Fig. 2. Batch fueling of active droplets. **A.** Images of an HPLC inlet containing a solution of 22 mM precursor, 12 mM pSS, and 0.1 μM sulforhodamine B in 200 mM MES buffer at pH 5.3 fueled with 20 mM DIC. After adding the fuel, the sample turned turbid (1 min), and a clear solution was obtained again after 18 min. **B.** Confocal microscopy of a solution from A with 0.1 μM sulforhodamine B and fueled with 10 mM DIC. The active droplets grew and fused initially, but their size stayed below the size of the active droplets fueled with 20 mM DIC (Fig. 1B,C). After around 4 min, they started to dissolve without forming spherical shells. Imaging was done in PVA-coated ibidi chambers. **C** The volume of each active droplet (blue) is plotted for each time point. No spherical shells (red) were observed. Experiments were performed in triplicate ($N=3$).



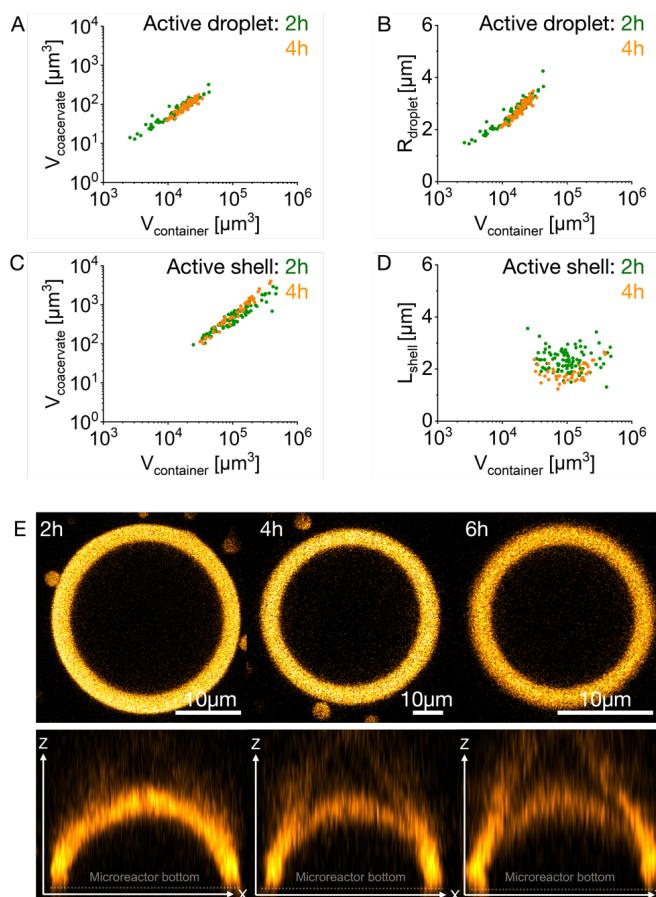
Extended Data Fig. 3. Total coacervate volumes and reactant concentrations in a steady state.

A. DIC (fuel) and DIU (waste) concentrations under steady-state conditions were determined by NMR. Conditions were 10 mM precursor and 200 mM MES at pH 5.3. To achieve a steady state, perfluorinated oil containing 0.5 M DIC was added to the aqueous phase. The dotted line represents the average DIC concentration of 6.6 mM. Error bars represent the standard deviation of triplicate measurements ($N=3$). **B.** Analytical HPLC determined average precursor and product concentrations under steady-state conditions. Conditions were 10 mM precursor and 200 mM MES at pH 5.3. To achieve a steady state, perfluorinated oil containing 0.5 M DIC was added to the aqueous phase. Error bars represent the standard deviation of triplicate measurements ($N=3$). Solid lines represent the steady-state concentration of DIC calculated by the kinetic model (see methods I.F and I.G) of 6.6 mM. **C.** A representative bright field image of a DIU crystal formed in the oil phase during a steady-state experiment. **D.** The dependency of the DIC concentration in the oil phase on the DIC concentration in the aqueous phase. The aqueous phase consisted of 200 mM MES at pH 5.3, and the oil phase of Novec 7500 perfluorinated oil. The dotted line represents the DIC concentration in the aqueous phase if an excess of pure DIC was added on top of the aqueous phase without the oil phase. The average partitioning coefficient of DIC between the aqueous phase and the oil phase was $k_{DIC} = 0.018$. Error bars represent the standard deviation of triplicate measurements ($N=3$). **E.** Total coacervate volume in one microfluidic reactor in the first 30 min after adding fuel. Conditions were 10 mM precursor, 5 mM pSS, and 200 mM MES at pH 5.3 with 0.5 M DIC. **F.** Average total coacervate volume of different microfluidic reactors over 4 h. Conditions were the same as in E. Error bars represent the standard deviation of at least 30 measurements spread over 3 independent experiments.

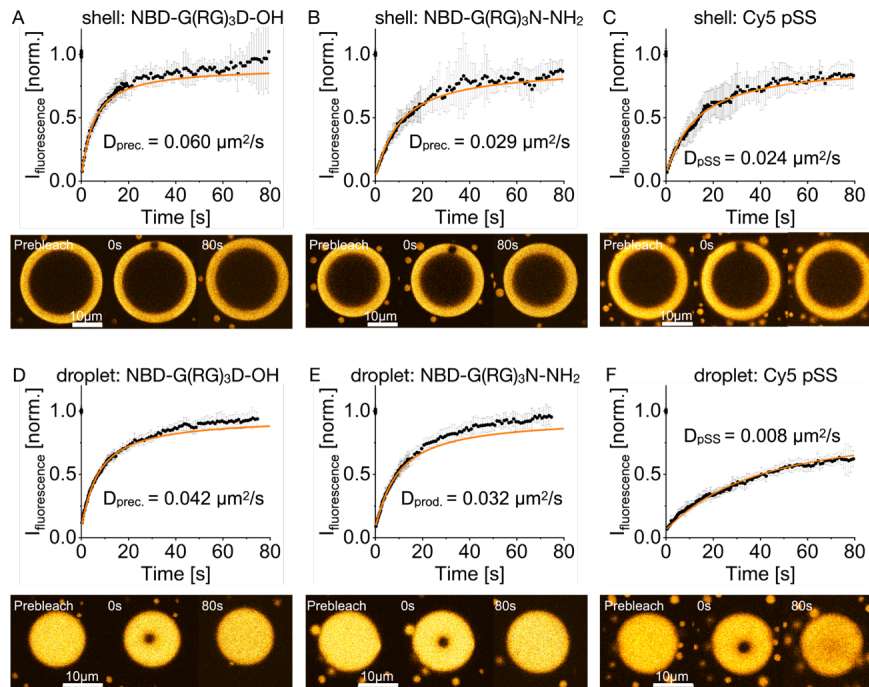


Extended Data Fig. 4. Wetting of active and passive droplets without transitioning into a shell.

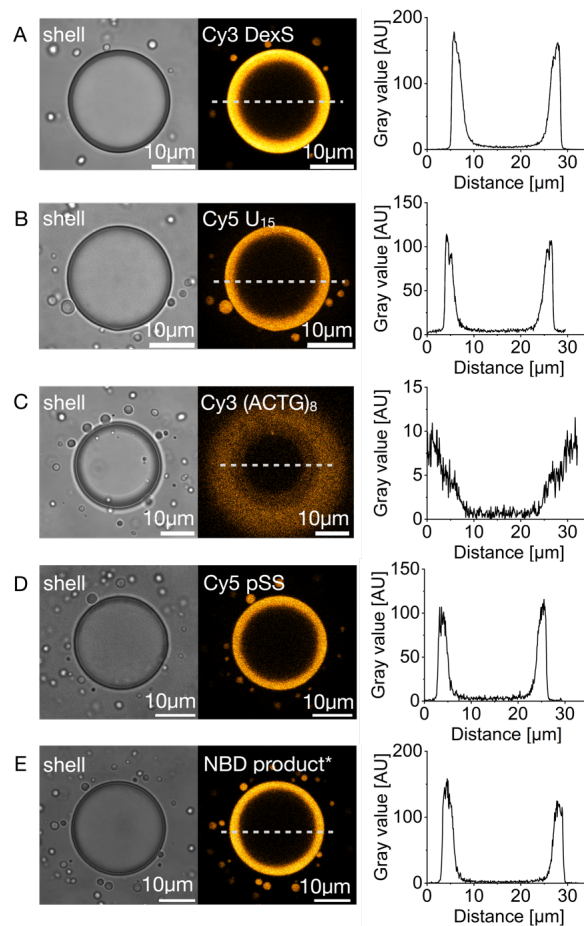
All experiments were performed in microfluidic reactors. 5 mM pSS, 200 mM MES at pH 5.3, and 0.1 μM sulforhodamine B as a dye were used. **A-C** The upper row of images shows the XY-plane at the center of the droplet to demonstrate that no spherical shell was formed. The bottom row of images shows the XZ-projection of the active/passive droplet to demonstrate the wetting at the bottom of the microreactor. **A.** A representative active droplet with $r < r_{\text{unstable}}$ is shown 6 h after adding fuel. In addition to the abovementioned conditions, the sample contained 10 mM precursor, and 0.5 M DIC was added to the oil phase to achieve a steady state. **B.** A representative passive droplet with $r > r_{\text{unstable}}$ is shown 6 h after the induction of droplet formation. Conditions were 9 mM precursor, 1 mM product* with no DIC in the oil phase. Additionally, 1 w% Krytox 157 FSH was added to the oil phase. **C.** A representative passive droplet with $r > r_{\text{shell}}$ is shown 6 days after the induction of droplet formation. These passive droplets consist only of product* and pSS without the precursor. Since the added fuel cannot react with the product*, these droplets are thus passive. Conditions were 0 mM precursor, 2 mM product* with 0.5 M DIC in the oil phase to achieve a steady state. **D-I.** Images were acquired 4 h after the induction of droplet formation. Dashed lines represent the container size, coacervate volume, and size upon which spherical shell formation was observed for active droplets. All experiments were performed in triplicate ($N=3$). **D-F.** Conditions were 9.5 mM precursor and 0.5 mM product*. **G-I.** Conditions were 9 mM precursor and 1 mM product*. To show that passive droplets do not transition into shells, a micrograph of a representative passive coacervate-based droplet (**D, G**), the volume of the total coacervate material (**E, H**) for every individual microreactor, and the radius (**F, I**) of the passive droplet in every individual microreactor is shown.



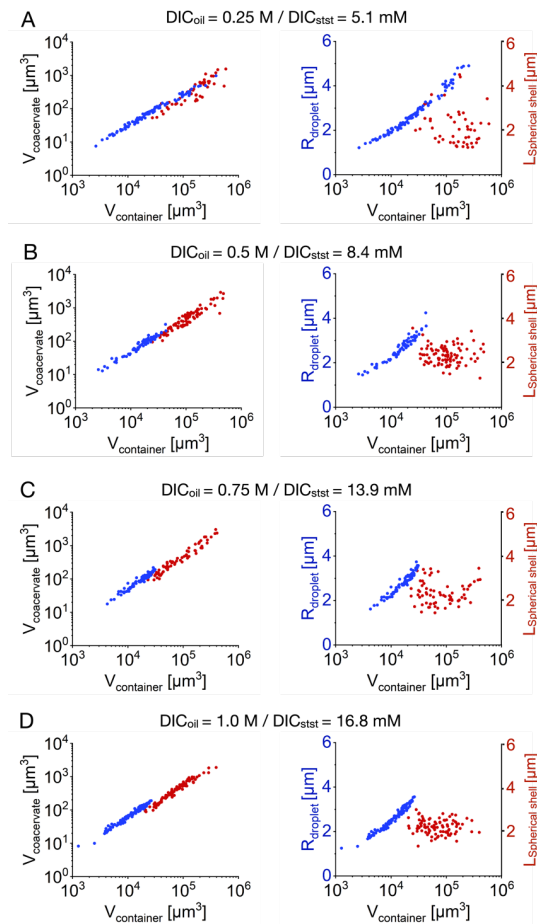
Extended Data Fig. 5. Stability of active spherical shells. All experiments were performed in microreactors. Conditions were 10 mM precursor, 5 mM pSS, and 200 mM MES at pH 5.3 with 0.1 μM sulforhodamine B. 0.5 M DIC was added to the oil phase to achieve a steady state. **A, C.** The volume of the total coacervate material 2 h and 4 h after the induction of coacervation is shown for every individual microreactor that contained an active droplet (**A**) or an active shell (**C**). The volume of active droplets and active shells, as well as the threshold upon which shells were formed, did not change between 2 h and 4 h. **B, D.** The radius of the active droplet (**B**) as well as the shell thickness L_{shell} of the active shell (**D**) in every individual microreactor is shown 2 h and 4 h after the induction of coacervation. The radius of active droplets and L_{shell} of active shells, and the threshold upon which shells are formed did not change between 2 h and 4 h. All experiments were performed in triplicate ($N=3$). **E.** A representative active shell 2 h, 4 h, and 6 h after the induction of coacervation. In the upper row, the XY-plane of an active shell is shown, and in the bottom row, the XZ-plane through the middle of the 3D projection of the respective active shell is shown.



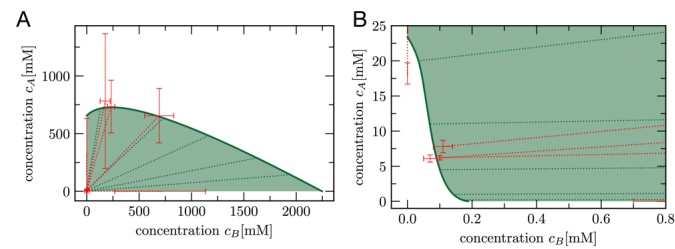
Extended Data Fig. 6. FRAP of active droplets and active spherical shells. All experiments were performed in microreactors. Conditions were 10 mM precursor, 5 mM pSS, and 200 mM MES at pH 5.3 with 1 μM of the respective dye. 0.5 M DIC was added to the oil phase to achieve a steady state. Error bars represent the standard deviation of 10 different measurements ($N=10$). The time series shows the fluorescence recovery of a representative active shell. **A-C.** FRAP of the labeled precursor (**A**), labeled product* (**B**), and labeled pSS (**C**) shells 3 h after the induction of coacervation. **D-F.** FRAP of the labeled precursor (**D**), the labeled product* (**E**), and of the labeled pSS (**F**) active droplets 1 h after the induction of coacervation. Active droplets were imaged before they transitioned into a spherical shell.



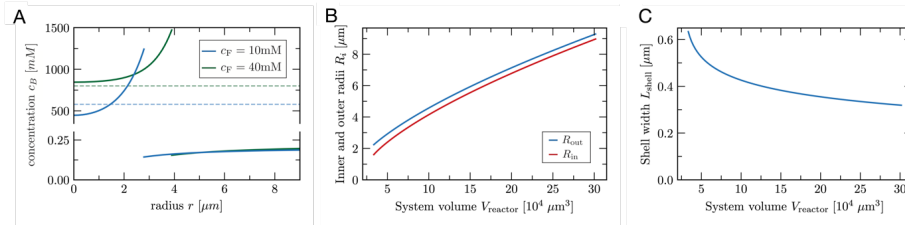
Extended Data Fig. 7. Partitioning of fluorescent molecules into the active spherical shells. Conditions were 10 mM precursor, 5 mM pSS, and 200 mM MES at pH 5.3 with 1 μM of the respective dye. 0.5 M DIC was added to the oil phase to achieve a steady state. Active spherical shells were imaged 3 h after the induction of coacervation. **A-E.** Bright-field image of an active shell containing Cy3 labeled dextran sulfate (Cy3 DexS, excitation at 552 nm, **A**), Cy5 labeled 15-mer of oligouridylic acid (Cy5 U_{15} , excitation at 638 nm, **B**) Cy3 labeled (ACTG) $_8$ (Cy3 (ACTG) $_8$, excitation at 552 nm, **C**), Cy5 labeled pSS (Cy5 pSS, excitation at 638 nm, **D**), and NBD labeled product* (excitation at 488 nm, **E**). The line profile of the fluorescence along the dotted line is shown.



Extended Data Fig. 8. Spherical shell formation with varying fuel concentrations. Conditions were 10 mM precursor, 5 mM pSS, and 200 mM MES at pH 5.3 with 0.1 μM sulforhodamine B. The indicated amount of DIC_{oil} was added to the oil phase to achieve a steady-state concentration of DIC_{stst} in the microfluidic reactors. After forming the spherical shells, active droplets and shells were measured at 0.5 h. **A-D.** Left: The volume of the total coacervate material is shown for every individual microreactor that contained an active droplet (blue) or an active shell (red). Right: The radius of the active droplet (blue) and the shell thickness L (red) of the active shell in every individual microreactor is shown. All experiments were performed in triplicate ($N=3$).



Extended Data Fig. 9. Phase diagram. A-B. Five independent measurements (red data points with error bars) of different phase equilibria were used to fit the binodal line (solid green line) where two phases can coexist. The two corresponding concentration measurements are connected by a red dotted line, while the green dotted lines show a representative selection of tie lines of the model.



Extended Data Fig. 10. Influence of different parameters on the spinodal instability at the droplet core and the shell width. A. Influence of fuel concentration on spinodal instability at the droplet's core. Radial concentration profiles for two different fuel concentrations are shown. For the lower fuel concentration (blue), the core of a droplet reaches the spinodal concentration (blue dashed). The stationary droplet is larger for the higher fuel concentration (green). However, the concentration at the core stays above the corresponding spinodal concentration (green dashed) due to weaker gradients resulting from a higher activation inside. For systems with high fuel concentrations, the precursor A gets activated and forms the product B inside the droplet. **B-C.** Influence of the system size on the shell width. Both interface radii increase as a function of system volume (**B**), but despite the 400 % increase of both radii, the distance between them $L_{\text{shell}} = R_{\text{out}} - R_{\text{in}}$ decreases only by 30 % (**C**).

Supporting Information for:

Title: Liquid spherical shells are a non-equilibrium steady state

Authors: Alexander M. Bergmann,^{1*} Jonathan Bauermann,^{2,3*} Giacomo Bartolucci,^{2,3*} Carsten Donau,^{1*} Michele Stasi,¹ Anna-Lena Holtmannspötter,¹ Frank Jülicher,^{2,3} Christoph A. Weber,^{4,*} Job Boekhoven^{1,*}

Affiliations:

¹School of Natural Sciences, Department of Chemistry, Technical University of Munich, Lichtenbergstrasse 4, 85748 Garching, Germany.

²Max Planck Institute for the Physics of Complex Systems, Nöthnitzer Strasse 38, 01187 Dresden, Germany.

³Center for Systems Biology Dresden, Pfotenhauerstrasse 108, 01307 Dresden, Germany.

⁴Faculty of Mathematics, Natural Sciences, and Materials Engineering: Institute of Physics, University of Augsburg, Universitätsstrasse 1, 86159 Augsburg, Germany.

*equal contribution

+corresponding author

Table of Contents

I. Supplementary Methods

- (A) Determination of rate constants of the chemical reaction cycle
- (B) Kinetic model
- (C) Determination of the partitioning and concentration of molecules inside and outside of the droplet phase
- (D) Determination of total droplet volumes
- (E) Estimating the concentration of product and fuel in the microfluidic droplet
- (F) Thermodynamic model for the experimental phase diagram
- (G) Sharp interface model for the kinetics of active droplets and active spherical shells
- (H) Parameter values used in numerical calculations
- (I) Calculations of free energies and free energy rates

II. Supplementary Discussion

III. Supplementary Tables

IV. Supplementary Figures

V. Supplementary Movies

VI. Supplementary References

I. Supplementary Methods

(A) Determination of rate constants of the chemical reaction cycle. The concentration profiles of the precursor and its corresponding anhydride (product) were determined by HPLC, whereas NMR quantified fuel and waste.

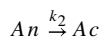
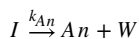
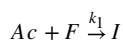
Due to the instability of the product, a quenching technique was used with an amine that converts the product into a quantifiable amide¹⁻³. To a solution (145 μL) of 10 mM precursor in 200 mM MES at pH 5.3 was added a solution (5 μL) of 5-20 mM DIC in acetonitrile in an HPLC vial. After each time point, 10 μL of the reaction mixture was added to 20 μL of an aqueous solution of ethylamine (400 mM). The resulting clear solution was then injected into the HPLC, and the concentration of the precursor and product was calculated from the resulting peak integrals.

Quantification of fuel and waste: 5-20 mM DIC was added to a solution (1 mL) of 200 mM MES at pH 5.3 and vortexed for 30 s to dissolve all DIC. The sample also contained 10 vol% D_2O and 80 mM acetonitrile (ACN) as a reference. 10 mM precursor was added to 500 μL of this solution. The solution was vortexed and added to an NMR tube. ^1H -NMR measurements were performed on a 300 MHz NMR every 5 min until no more DIC was detected. The concentrations of fuel and waste were then calculated from the peak integrals, which were compared with the acetonitrile reference. The chemical shifts of the compared signals were ^1H NMR (300 MHz, D_2O): ACN δ (ppm) = 2.07 (s, 3H, CH_3), DIC δ (ppm) = 1.22-1.23 (d, 12H, CH_3), DIU δ (ppm) = 1.09-1.10 (d, 12H, CH_3).

The obtained data from the HPLC and NMR experiments were then fitted via a kinetic model in python.

(B) Kinetic model.

The reaction cycle in a homogeneous system is described in a kinetic modeled according to the following mechanism:



Ac is the dicarboxylic acid, F is the fuel, I is the intermediate O-acylurea, W is the waste, and An is the anhydride.

The mechanism translates into the following set of differential equations:

$$\begin{cases} \frac{d[A_c]}{dt} = -k_1 \cdot [A_c] \cdot [F] + k_2 \cdot [A_n] + k_{Ac} \cdot [I] \\ \frac{d[F]}{dt} = -k_1 \cdot [A_c] \cdot [F] - k_0 \cdot [F] \\ \frac{d[W]}{dT} = +k_0 \cdot [F] + k_{Ac} \cdot [I] + k_{An} \cdot [I] \\ \frac{d[A_n]}{dt} = +k_{An} \cdot [I] - k_2 \cdot [A_n] \\ \frac{d[I]}{dt} = +k_1 \cdot [A_c] \cdot [F] - k_{An} \cdot [I] - k_{Ac} \cdot [I] \end{cases} \quad (1)$$

We then applied steady-state approximation to obtain:

$$\frac{d[I]}{dt} = +k_1 \cdot [A_c] \cdot [F] - k_{An} \cdot [I] - k_{Ac} \cdot [I] \approx 0 \Rightarrow [I] \approx \frac{k_1 \cdot [A_c] \cdot [F]}{k_{An} \cdot \left(\frac{k_{Ac}}{k_{An}} + 1\right)}$$

We called $\frac{k_{Ac}}{k_{An}} = K$ and used the relation above in the set of differential equations to obtain:

$$\begin{cases} \frac{d[A_c]}{dt} = -k_1 \cdot [A_c] \cdot [F] + k_2 \cdot [A_n] + \frac{K \cdot k_1 \cdot [A_c] \cdot [F]}{(K+1)} \\ \frac{d[F]}{dt} = -k_1 \cdot [A_c] \cdot [F] - k_0 \cdot [F] \\ \frac{d[W]}{dT} = +k_0 \cdot [F] + k_1 \cdot [A_c] \cdot [F] \\ \frac{d[A_n]}{dt} = +\frac{k_1 \cdot [A_c] \cdot [F]}{(K+1)} - k_2 \cdot [A_n] \end{cases} \quad (2)$$

Experimental data were fit to the equation system (2) using a custom program in Python 3 (kinmodel, <https://github.com/scotthartley/kinmodel>) previously published by the group of Hartley and applied to similar systems⁴. To calculate concentrations of precursor and product under continuous fueling, the change in fuel concentration was set to 0 ($\frac{d[F]}{dt}=0$).

(C) Determination of the partitioning and concentration of molecules inside and outside of the droplet phase. To determine the amount of precursor, product*, and fuel in the dilute phase and inside passive droplets for the phase diagram, we measured their concentrations using HPLC, fluorescence spectroscopy, and NMR.

For the precursor, we quantified the fraction of the precursor that remained in the dilute phase of passive droplets by HPLC. 5 mM pSS was added to a solution containing 10-x mM precursor and x mM product* (total peptide concentration = 10 mM) or 20 mM precursor (without product*) in 200 mM MES at pH 5.3. The turbid suspension ($V = 150 \mu\text{L}$) was vortexed, incubated for 5 min, and then centrifuged for another 15 min at $20,412 \times g$. 100 μL of the supernatant was removed and added into an HPLC inlet. 1 μL of NaCl (4 M) aqueous solution was added to dissolve residual turbidity. The resulting clear solution was injected into the HPLC and compared to a solution containing 10-x mM precursor or 20 mM precursor

without pSS to calculate the fraction of precursor that remained in the supernatant after droplet formation.

Product*: we quantified the fraction of product* as a measure for the anhydride product that remained in the dilute phase of passive droplets by fluorescence spectroscopy because its concentration in the supernatant could not be determined accurately via HPLC (peak overlap with the precursor, low fraction remaining in supernatant). Therefore, we used NBD-G(RG)₃N-NH₂ (fluorescent analog of product*), which partitions similarly into the droplet phase as product*⁵. To a solution of 10-x mM precursor and x mM product* (total peptide concentration = 10 mM) or 2 mM product* (without precursor) in 200 mM MES at pH 5.3 with 1 μM NBD-G(RG)₃N-NH₂ were added 5 mM pSS. The turbid suspension (V = 150 μL) was vortexed, incubated for 5 min, and then centrifuged for another 15 min at 20,412×g. 100 μL of the supernatant was removed and added into an Eppendorf tube. 1 μL of an aqueous solution of NaCl (4 M) was added to dissolve residual turbidity. The fluorescence of the sample was then measured on the fluorimeter (Excitation at 467 nm, emission at 526 nm). To account for the dependence of the fluorescence of dyes on their environment⁶, we prepared an identical sample without NBD-G(RG)₃N-NH₂. We added the supernatant (96 μL) to an Eppendorf tube containing 1 μL of an aqueous solution of NaCl (4 M). To the clear solution, we then added 1 μM NBD-G(RG)₃N-NH₂ (4 μL) as in the previous sample and measured its fluorescence intensity. The intensity ratio between these two samples was used as the fraction of the fluorescent molecules that remained in the supernatant.

Fuel: we quantified the fraction of fuel partitioned into the droplet phase of passive droplets using NMR. To avoid the reaction of precursor and fuel, passive droplets consisting only of product* and pSS were used. 10 mM DIC (1.55 μl) was added to a solution (1 mL) containing 2 mM product* and 5 mM pSS in 200 mM MES at pH 5.3. The solution was vortexed and incubated for 5 min. The sample was centrifuged for 5 min at 20,412×g and the supernatant was carefully removed. The residual coacervate phase (about 1 μL) was dissolved in a solution (50 μL) containing 400 mM NaCl, 560 mM borate buffer at pH 10, 80 mM ACN as standard, and 20 vol% D₂O. The high pH prevents further hydrolysis of DIC between sample preparation and measurement. the DIC concentration was determined by ¹H-NMR spectroscopy. Blank measurements without droplets were performed to account for residual DIC containing dilute phase on the walls of the sample containers after the removal of the supernatant. As a blank, 10 mM DIC was added to a solution (1 mL) containing 200 mM MES at pH 5.3. The blank solution without droplets was treated similarly to the solution with droplets. The sample was centrifuged for 5 min at 20,412×g and the supernatant was carefully removed. A solution (50 μL) containing 400 mM NaCl, 560 mM borate buffer at pH 10, 80 mM ACN as standard, and 20 vol% D₂O was added and the DIC concentration was determined by ¹H-NMR spectroscopy. The concentrations of fuel were then calculated from the peak

integrals which were compared with the acetonitrile reference and corrected by the blank. The chemical shifts of the compared signals were ^1H NMR (500 MHz, D_2O): ACN δ (ppm) = 2.07 (s, 3H, CH_3), DIC δ (ppm) = 1.22-1.23 (d, 12H, CH_3).

Combined with the total volumes of the droplet pellets (see method below), we calculated the partitioning of the individual molecules in passive droplets (Table S1-3). The resulting error bars of the concentration inside the droplets (c_{in}) and the partitioning coefficient (K) represent the accumulated standard deviation from the experiments measuring the fraction of molecules in the supernatant (c_{out}) and the total volumes of the coacervate pellets.

(D) Determination of total droplet volumes. To calculate the partitioning of the precursor, product*, and fuel in the droplet phase for the phase diagram, the total droplet volume was estimated via a centrifugation assay. For that, samples (200 μL) of passive droplets containing 10-x mM precursor and x mM product* (total peptide concentration = 10 mM), 20 mM precursor (without product), or 2 mM product* (without precursor) in 200 mM MES at pH 5.3 with 15 μM sulforhodamine B (for visualization) were prepared. After the addition of 5 mM pSS, the turbid suspensions were incubated for 5 min and then centrifuged for another 15 min at $20,412\times g$. The volume of the droplet pellets (0.4-2 μL) was then compared to size standards visually (Table S1-3).

(E) Estimating the concentration of product and fuel in the microreactors. To validate whether the continuously fueled microreactors contain a steady-state level of product and fuel, we chose an indirect quantification method by HPLC for the product, and quantification by NMR for the fuel. We assumed that the diffusion of fuel from the surrounding oil phase into a microfluidic reactor ($r= 5\text{-}50 \mu\text{m}$) is fast and should be comparable to a two-phase system in a glass vial under vigorous stirring. We used perfluorinated oil without surfactant in these experiments to avoid stabilized emulsions.

Product: 250 μL of an aqueous solution containing 10 mM precursor in 200 mM MES at pH 5.3 was added on top of perfluorinated oil (Novec 7500, 1 mL) in an HPLC vial. We started the reaction network by the addition of 0.5 M DIC into the oil phase and vigorously stirring the reaction mixture. To determine the concentration of the product, 10 μL of the aqueous phase was quenched with 20 μL of an aqueous solution of ethylamine (400 mM) every 30 min. The reaction between the amine and the product yields a stable amide that can be quantified^{1,2}. We correlated the resulting peak integrals of the amide to the product assuming that the absorption of the amide is equal to the absorption of the precursor (Fig. S1).

Fuel and waste in the steady state: 1.25 mL of 10 mM precursor in 200 mM MES at pH 5.3 were added to 5 mL of perfluorinated oil (Novec 7500) containing 0.5 M DIC. The mixture was vigorously stirred and samples of 25 μL were taken and quenched with 25 μL 640 mM borate

buffer at pH 10 with 20 vol% D₂O and 80 mM acetonitrile as a reference. The high pH inhibits the direct DIC hydration and the reaction of the precursor with DIC to ensure that the time until the sample is measured is not influencing the measured concentrations of fuel and waste. Samples are measured by ¹H-NMR spectroscopy. The concentrations of fuel and waste were then calculated from the peak integrals which were compared to the acetonitrile peak reference (Fig. S1). The chemical shifts of the compared signals were ¹H NMR (400 MHz, D₂O): ACN δ (ppm) = 2.07 (s, 3H, CH₃), DIC δ (ppm) = 1.22-1.23 (d, 12H, CH₃), DIU δ (ppm) = 1.09-1.10 (d, 12H, CH₃).

Variation of the fuel concentration in the microreactor: The concentration of fuel in the aqueous phase was measured for different fuel concentrations in the oil phase to determine the partitioning into the aqueous phase. 1 mL of 200 mM MES at pH 5.3 is added to 10 mL of perfluorinated oil (Novec 7500) containing 0.25 – 1.0 M DIC. The mixtures were vortexed for 20 s and after the phases have separated 250 μ l of the aqueous phase are added to 250 μ l of 640 mM borate buffer at pH 10 with 20 vol% D₂O and 80 mM acetonitrile as a reference. Samples were measured by ¹H-NMR spectroscopy. The concentrations of fuel were then calculated from the peak integrals which were compared to the acetonitrile peak reference (Fig. S4D). The chemical shifts of the compared signals were ¹H NMR (400 MHz, D₂O): ACN δ (ppm) = 2.07 (s, 3H, CH₃), DIC δ (ppm) = 1.22-1.23 (d, 12H, CH₃).

(F) Thermodynamic model for the experimental phase diagram

In the theoretical model, we use an effective ternary mixture where the influence of fuel, waste, and polyanion is accounted for in an implicit manner; details see section (P). The effective components of the ternary mixture are solvent, the precursor A , and the product B . For these components, equilibrium concentrations inside and outside were determined experimentally; see Table (1-2). To fit the corresponding experimental diagram, we use a Flory-Huggins free energy density given as ^{7,8}

$$f(c_A, c_B) = k_B T \left[\sum_{i=A,B,S} c_i \log(r_i c_i) + \sum_{ij=AB,AS,BS} \chi_{ij} r_i c_i r_j c_j \right], \quad (3)$$

where c_A and c_B denote the concentrations of components A and B , respectively. In Eq. (3), we have combined the molecular volumes ν_A , ν_B , and ν_S in the ratios introduced the molecular volume ratios $r_i = \nu_i/\nu_S$. The concentration of the solvent follows from the incompressibility of the mixture, $c_S = 1/\nu_S - r_A c_A - r_B c_B$. This free energy density depends on five parameters: the molecular volume ratios, r_A and r_B , and the interaction parameters, χ_{AB} , χ_{AS} , and χ_{AB} . We determine these five parameters by fitting experimental measurements of different phase equilibria. At phase equilibria, the chemical potentials $\mu_i = \partial f/\partial c_i$ of components A and B and the osmotic pressure $\Pi = -f + \sum_{i=A,B} c_i \mu_i$ are balanced between the phases. For the measurements, the product was stabilised against hydrolysis by mutating the C terminal aspartic acid for an asparagine. This chemical modification yields a peptide that has the same interaction propensities as the product but is stable, i.e., it does not convert to the precursor. Every measured point in the phase diagram gives three constraints

$$\mu_A(c_A^I, c_B^I) = \mu_A(c_A^{II}, c_B^{II}), \quad (4)$$

$$\mu_B(c_A^I, c_B^I) = \mu_B(c_A^{II}, c_B^{II}), \quad (5)$$

$$\Pi(c_A^I, c_B^I) = \Pi(c_A^{II}, c_B^{II}). \quad (6)$$

We obtained the five unknown parameters by simultaneously minimizing the deviations for the

resulting 13 conditions. The best fit was obtained for $r_A = 35.1$, $r_B = 19.4$, $\chi_{AB} = -0.18$, $\chi_{AS} = 0.78$, and $\chi_{BS} = 1.29$. In Ext. Data Fig. 9, we show the corresponding phase diagram together with the experimental measured concentration values. The last thermodynamic parameter needed for our model is the surface tension γ . Since γ is difficult to estimate within our experimental setup, we use the value $\gamma = 75 \mu\text{N m}^{-1}$ which is thousand times smaller than the air-water interfacial tension. Our value is in good agreement with surface tensions measured for similar coacervates⁹. Note that the used value is slightly larger than for biological condensates¹⁰.

(G) Sharp interface model for the kinetics of active droplets and active spherical shells

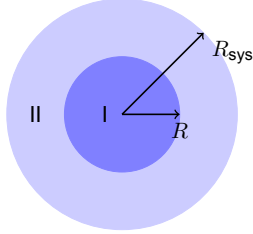
In general, diffusion is driven by spatial gradients of chemical potentials, while reactions minimize the difference in chemical potentials between products and reactants. For the following, we consider linearized kinetic equations, where diffusion is driven by spatial gradients of concentrations and the reaction



is driven by the differences in concentrations of the respective components. The resulting kinetic parameters in terms of diffusivities and rate coefficients are then determined via experimental measurements, see experimental section. Therefore, the dynamical equation for c_A and c_B read^{11,12}

$$\partial_t c_i^\alpha = D_i^\alpha \nabla^2 c_i^\alpha + k_i^\alpha c_j^\alpha - k_{ji}^\alpha c_i^\alpha. \quad (8)$$

In the case of spherical active droplets, there are two different domains with $\alpha = \text{I,II}$, where I denotes the dense phase of droplet and II denotes the dilute phase outside the droplet. For spherical symmetric active spherical shells, three different domains exist, $\alpha = \text{I,II,III}$, where I denotes the dilute phase within the core of the spherical shell, III labels the dense phase of the spherical shell, and II correspond to the dilute phase outside the spherical shell.



Sketch I. Geometry for active droplet.

We calculate the radial symmetric stationary profiles that solve Eq. (8) in the two different domains as a function of the radial coordinate r . At the droplet's core ($r = 0$), we impose no flux boundary conditions for the solution of domain I. Similarly, no flux boundary conditions are imposed at system boundary $r = R_{sys}$ for the solution in domain II. The two domains are coupled at the sharp interface at position $r = R$. Here, we impose concentration boundary conditions $c_A^\alpha(R) = a^\alpha$, $c_B^\alpha(R) = b^\alpha$. These concentrations are later determined self-consistently. For these boundary conditions, the stationary solutions for domain I read

$$c_A^I(r) = \frac{b^I - a^I \rho_k^I R \sinh(r/\lambda^I)}{\rho_D^I - \rho_k^I r \sinh(R/\lambda^I)} + \frac{a^I \rho_D^I - b^I}{\rho_D^I - \rho_k^I}, \quad (9)$$

$$c_B^I(r) = \rho_D^I \frac{b^I - a^I \rho_k^I R \sinh(r/\lambda^I)}{\rho_D^I - \rho_k^I r \sinh(R/\lambda^I)} + \rho_k^I \frac{a^I \rho_D^I - b^I}{\rho_D^I - \rho_k^I}, \quad (10)$$

while in domain II, the stationary solutions follow

$$c_A^{II}(r) = \frac{a^{II} k_{BA}^{II} - b^{II} k_{AB}^{II}}{k_{BA}^{II} - k_{AB}^{II} \rho_D^{II}} \frac{R}{r} \frac{\sinh(r/\lambda^{II}) + \Phi \cosh(r/\lambda^{II})}{\sinh(R/\lambda^{II}) + \Phi \cosh(R/\lambda^{II})} - \frac{a^{II} k_{BA}^{II} - b^{II} k_{AB}^{II} \rho_D^{II}}{k_{BA}^{II} - k_{AB}^{II} \rho_D^{II}}, \quad (11)$$

$$c_B^{II}(r) = \rho_D^{II} \frac{a^{II} k_{BA}^{II} - b^{II} k_{AB}^{II}}{k_{BA}^{II} - k_{AB}^{II} \rho_D^{II}} \frac{R}{r} \frac{\sinh(r/\lambda^{II}) + \Phi \cosh(r/\lambda^{II})}{\sinh(R/\lambda^{II}) + \Phi \cosh(R/\lambda^{II})} - \rho_k^{II} \frac{a^{II} k_{BA}^{II} - b^{II} k_{AB}^{II} \rho_D^{II}}{k_{BA}^{II} - k_{AB}^{II} \rho_D^{II}}. \quad (12)$$

We have made use of $\lambda^\alpha = \sqrt{D_A^\alpha D_B^\alpha / (D_A^\alpha k_{AB}^\alpha + D_B^\alpha k_{BA}^\alpha)}$, $\rho_D^\alpha = -D_A^\alpha / D_B^\alpha$, and $\rho_k^\alpha = k_{BA}^\alpha / k_{AB}^\alpha$, where $\alpha = I, II$ indicate the phases.

The coefficient $\Phi = -(\lambda^{II} R_{sys} \cosh[\lambda^{II} R_{sys}] - \sinh[\lambda^{II} R_{sys}]) / (\lambda^{II} R_{sys} \sinh[\lambda^{II} R_{sys}] - \cosh[\lambda^{II} R_{sys}])$ ensures the zero flux boundary condition at the system radius.

Finally, we have to determine the four interface concentrations a^I , a^{II} , b^I , b^{II} and the position of the interface R . For this, we need five constraints. Three of these constraints follow from the

assumption of a local equilibrium of phase separation ¹²

$$\mu_A(a^I, b^I) = \mu_A(a^{II}, b^{II}), \quad (13)$$

$$\mu_B(a^I, b^I) = \mu_B(a^{II}, b^{II}), \quad (14)$$

$$\Pi(a^I, b^I) = \Pi(a^{II}, b^{II}) - \frac{2\gamma}{R}. \quad (15)$$

Furthermore, the total of A and B have to be conserved in the system,

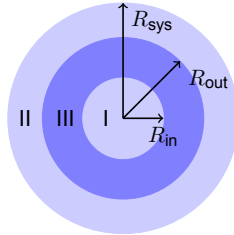
$$V_{\text{sys}} \bar{c}_{\text{tot}} = \frac{4}{3} \pi \left[(a^I + b^I) R^3 + (a^{II} + b^{II}) (R_{\text{sys}}^3 - R^3) \right], \quad (16)$$

where $c_{\text{tot}} = c_A + c_B$ is the conserved quantity associated to the chemical reaction in Eq. (7).

Finally, the conservation law at the interface in the stationary state requires

$$j_i^I(R) = j_i^{II}(R), \quad (17)$$

where $j_i^\alpha = -D_i^\alpha \partial_r c_i^\alpha$ is radial component of the material flux density. Note that the stationary solution implies that $j_A^\alpha(r) = -j_B^\alpha(r)$. Thus, the constraint Eq. (17) is fulfilled simultaneously for both components A and B , making the total number of independent constraints equal to five.



Sketch II. Geometry for active spherical shell.

(P2) Chemically active spherical shell

In the spherical shell state, the stationary concentration profiles in domain I and II have the same functional form as in the active droplet state. In addition, there is the shell domain III between domain I and domain II. Here, the stationary solutions of Eq. (8), with concentration boundary conditions on the interfaces left and right

$$c_A^{\text{III}}(r) = K_1 \frac{\sinh(r/\lambda^{\text{III}})}{r} + K_2 \frac{\cosh(r/\lambda^{\text{III}})}{r} + K_3 + \frac{K_4}{r}, \quad (18)$$

$$c_B^{\text{III}}(r) = \rho_D^{\text{III}} \left[K_1 \frac{\sinh(r/\lambda^{\text{III}})}{r} + K_2 \frac{\cosh(r/\lambda^{\text{III}})}{r} \right] + \rho_k^{\text{III}} \left[K_3 + \frac{K_4}{r} \right]. \quad (19)$$

Here, we have abbreviated

$$K_1 = \frac{\text{csch}[(R_{\text{out}} - R_{\text{in}})/\lambda^{\text{III}}]}{K_{BA}^{\text{III}} - \rho_D^{\text{III}} K_{AB}^{\text{III}}} \left[(b^{\text{III},\text{in}} K_{AB}^{\text{III}} - a^{\text{III},\text{in}} K_{BA}^{\text{III}}) R_{\text{in}} \cosh(R_{\text{out}}/\lambda^{\text{III}}) - (b^{\text{III},\text{out}} K_{AB}^{\text{III}} - a^{\text{III},\text{out}} K_{BA}^{\text{III}}) R_{\text{out}} \cosh(R_{\text{in}}/\lambda^{\text{III}}) \right], \quad (20)$$

$$K_2 = \frac{\text{csch}[(R_{\text{out}} - R_{\text{in}})/\lambda^{\text{III}}]}{K_{BA}^{\text{III}} - \rho_D^{\text{III}} K_{AB}^{\text{III}}} \left[(b^{\text{III},\text{out}} K_{AB}^{\text{III}} - a^{\text{III},\text{out}} K_{BA}^{\text{III}}) R_{\text{out}} \sinh(R_{\text{in}}/\lambda^{\text{III}}) - (b^{\text{III},\text{in}} K_{AB}^{\text{III}} - a^{\text{III},\text{in}} K_{BA}^{\text{III}}) R_{\text{in}} \sinh(R_{\text{out}}/\lambda^{\text{III}}) \right], \quad (21)$$

$$K_3 = \frac{(a^{\text{III},\text{out}} D_A^{\text{III}} + b^{\text{III},\text{out}} D_B^{\text{III}}) R_{\text{out}} - (a^{\text{III},\text{in}} D_A^{\text{III}} + b^{\text{III},\text{in}} D_B^{\text{III}}) R_{\text{in}}}{(D_A^{\text{III}} + D_B^{\text{III}} \rho_k^{\text{III}}) (R_{\text{out}} - R_{\text{in}})}, \quad (22)$$

$$K_4 = \frac{(a^{\text{III},\text{in}} - a^{\text{III},\text{out}}) D_A^{\text{III}} + (b^{\text{III},\text{in}} - b^{\text{III},\text{out}}) D_B^{\text{III}}}{(D_A^{\text{III}} + D_B^{\text{III}} \rho_k^{\text{III}}) (R_{\text{out}} - R_{\text{in}})} R_{\text{in}} R_{\text{out}}. \quad (23)$$

We introduced $\lambda^{\text{III}} = \sqrt{D_A^{\text{III}} D_B^{\text{III}} / (D_A^{\text{III}} k_{AB}^{\text{III}} + D_B^{\text{III}} k_{BA}^{\text{III}})}$, $\rho_D^{\text{III}} = -D_A^{\text{III}} / D_B^{\text{III}}$, and $\rho_k^{\text{III}} = k_{BA}^{\text{III}} / k_{AB}^{\text{III}}$, in analogy to phases I and II.

Finally, we have to determine the eight interface concentrations $a^{\text{I}}, a^{\text{III},\text{in}}, a^{\text{III},\text{out}}, a^{\text{II}}, b^{\text{I}}, b^{\text{III},\text{in}}, b^{\text{III},\text{out}}$, and b^{II} , and the two positions of the interfaces R_{in} and R_{out} . For this, we need ten constraints, three of which follow from the assumption of a local equilibrium of phase separation at R_{in}

$$\mu_A(a^{\text{I}}, b^{\text{I}}) = \mu_A(a^{\text{III},\text{in}}, b^{\text{III},\text{in}}), \quad (24)$$

$$\mu_B(a^{\text{I}}, b^{\text{I}}) = \mu_B(a^{\text{III},\text{in}}, b^{\text{III},\text{in}}), \quad (25)$$

$$\Pi(a^{\text{I}}, b^{\text{I}}) = \Pi(a^{\text{III},\text{in}}, b^{\text{III},\text{in}}) - \frac{2\gamma}{R_{\text{in}}}, \quad (26)$$

and three from local equilibrium of phase separation at R_{out}

$$\mu_A(a^{\text{III,out}}, b^{\text{III,out}}) = \mu_A(a^{\text{II}}, b^{\text{II}}), \quad (27)$$

$$\mu_B(a^{\text{III,out}}, b^{\text{III,out}}) = \mu_B(a^{\text{II}}, b^{\text{II}}), \quad (28)$$

$$\Pi(a^{\text{III,out}}, b^{\text{III,out}}) = \Pi(a^{\text{II}}, b^{\text{II}}) - \frac{2\gamma}{R_{\text{out}}}. \quad (29)$$

These six equations must be supplemented with a global conservation law

$$\bar{c}_{\text{tot}} V_{\text{sys}} = \int dV (c_A + c_B), \quad (30)$$

a local conservation law at R_{in} ,

$$j_i^{\text{I}}(R_{\text{in}}) = j_i^{\text{II}}(R_{\text{in}}), \quad (31)$$

and a local conservation law at R_{out} ,

$$j_i^{\text{II}}(R_{\text{out}}) = j_i^{\text{III}}(R_{\text{out}}). \quad (32)$$

In contrast to domains I and II, in domain III, $j_A \neq -j_B$, due to the $1/r$ term in the solution of the Laplace equation. Thus, the two flux equations have to be balanced for the components A and B at one interface, respectively. Due to the symmetry of the stationary solutions, one equality is automatically fulfilled at the second interface. Thus, we are left with three independent constraints coming from the local conservation laws at the interfaces Eqs. (31) and (32).

(H) Parameter values used in numerical calculations

If not indicated otherwise, we chose the parameters indicated in Table 6 for the numerical calculations. For the figures shown in this work, we fixed the following parameter values as stated in Table 7. To illustrate the dependency of the stationary profiles on the parameters, we show the concentration profiles in composition space for different settings of the ratio of $D_A^{\text{II}}/D_B^{\text{II}}$, the surface tension γ , and the ratio of the activation rates $k_{BA}^{\text{I}}/k_{BA}^{\text{II}}$ in Sup. Fig. 1.

(I) Calculations of free energies and free energy rates

We can estimate the free energy difference between a spherical shell stationary state and the corresponding homogeneous state with the same average concentrations

$$\bar{c}_i = \frac{1}{V_{\text{sys}}} \int dV c_i, \quad (33)$$

with $i = A, B$. In the following estimates, we will consider spherical shells at steady state corresponding to $R_{\text{sys}} = 35 \mu\text{m}$. We start from the concentrations in the coexisting phases, c_i^+ and c_i^- , corresponding to the spherical shell average concentration \bar{c}_i . Neglecting the interface contribution and considering each phase homogeneous, the free energy in the spherical shell state can be estimated directly via

$$F_{\text{mix}} = V^+ f^+ + (V_{\text{sys}} - V^+) f^-, \quad (34)$$

where the free energy density in each phase is $f^\pm = f(c_A^\pm, c_B^\pm)$ and V^+ is the total volume of the dense phase. With the parameters displayed in Table 6, this difference yields $F_{\text{mix}} = 2 \text{ nJ}$.

This free energy can be compared with the total activation free energy, defined as the energy of a B molecule times the number of excess B molecules at the spherical shell steady state

$$F_{\text{act}} = \Delta\omega(\bar{c}_B - c_B^0)V_{\text{sys}}, \quad (35)$$

where $c_B^0 = c_{\text{tot}}/[1 + \exp(\Delta\Omega)]$ is the B concentration in the homogeneous equilibrium state, i.e., without fuel present, and $\Delta\Omega$ is the activation free energy of a single A molecule, which is roughly $10 k_B T$ ¹³. As outlined in the main text, making use of the parameters in Table 6, we estimate $F_{\text{act}} \simeq 80 \text{ nJ}$.

Next, we estimate the number of particles that constantly get converted from the precursor

A into the product B , per unit time and volume,

$$n_{\text{tot}} = \frac{1}{V_{\text{sys}}} \int dV c_A k_{BA}, \quad (36)$$

which determines the total free energy turned over per time and volume

$$J_{\text{tot}} = \Delta\Omega n_{\text{tot}}. \quad (37)$$

Here, $\Delta\Omega$ denotes the activation energy supplied by fuel to the precursor to form a product. Using the parameters shown in Table 6, $c_F = 8.6$ mM, and $\Delta\Omega \simeq 10k_B T$, we obtain $n_{\text{tot}} = 4 \cdot 10^6 \text{ s}^{-1} \mu\text{m}^{-1}$ and $J_{\text{tot}} = 0.25$ W/L as outlined in the main text.

We can also estimate the free energy flux through the spherical shell interface. Specifically, we calculate the flux of product B through the interface where each product is activated by $\Delta\Omega$

$$J_{\text{int}} = \left[4\pi R_{\text{out}}^2 j_A^{\text{II}}(R_{\text{out}}) - 4\pi R_{\text{in}}^2 j_A^{\text{I}}(R_{\text{in}}) \right] \Delta\omega / V_{\text{sys}}. \quad (38)$$

Using the parameters shown in Table 6, and $\Delta\omega \sim 10k_B T$, this leads to an energy influx per unit time of $J_{\text{int}} = 0.198$ W/L. Comparing it to the total power J_{tot} , this leads to an efficiency $J_{\text{int}}/J_{\text{tot}}$ around 70%. In Sup. Fig. 2, we explored how J_{tot} and J_{shell} vary upon changes in the activation rate, induced by changes of the fuel concentration. Note that in our minimal model, the fuel enters implicitly in the activation rate. As expected, J_{tot} , which represents the total power needed to activate precursor A to product B to their respective values at the non-equilibrium steady state (see definition in Eq. (37)), varies linearly with the fuel concentration. On the other hand, the free energy transported to the spherical shell interface, J_{int} , scales sublinearly with fuel concentration. This is because the higher the fuel the more activation occurs inside, making the B particle flux at the interface less pronounced. As a consequence, the efficiency decreases as fuel concentration increases.

III. Supplementary tables

Total concentrations			Precursor			
Precursor [mM]	Product* [mM]	pSS [mM]	C _{in} [mM]	C _{out} [mM]	V _{coa} /V _{dilute} [vol%]	K _{partitioning} [C _{in} /C _{out}]
20	0	5	309 ± 323	18.2 ± 1.5 (91%)	0.57 ± 0.10	17 ± 19
9.5	0.5	5	782 ± 584	7.8 ± 0.9 (82%)	0.22 ± 0.04	101 ± 88
9	1	5	734 ± 229	6.1 ± 0.5 (67%)	0.40 ± 0.05	121 ± 49
8	2	5	655 ± 236	6.2 ± 0.3 (78%)	0.28 ± 0.05	106 ± 43
0	2	5	-	-	-	-

Table S1: Experimentally determined values for the partitioning of the precursor in passive droplets for the phase diagram.

Total concentrations			Product*			
Precursor [mM]	Product* [mM]	pSS [mM]	C _{in} [mM]	C _{out} [mM]	V _{coa} /V _{dilute} [vol%]	K _{partitioning} [C _{in} /C _{out}]
20	0	5	-	-	-	-
9.5	0.5	5	176 ± 48	0.11 ± 0.03 (23%)	0.22 ± 0.04	1545 ± 904
9	1	5	233 ± 35	0.07 ± 0.02 (7%)	0.40 ± 0.05	3360 ± 1645
8	2	5	692 ± 139	0.10 ± 0.0 (5%)	0.28 ± 0.05	7146 ± 3258
0	2	5	699 ± 434	0.78 ± 0.08 (39%)	0.18 ± 0.05	901 ± 653

Table S2: Experimentally determined values for the partitioning of the product* in passive droplets for the phase diagram.

Total concentrations			Fuel			
Precursor [mM]	Product* [mM]	pSS [mM]	C _{in} [mM]	C _{out} [mM]	V _{coa} /V _{dilute} [vol%]	K _{partitioning} [C _{in} /C _{out}]
0	2	5	14.4 ± 17.3	9.98 (99.8%)	0.10 ± 0.01	1.44 ± 1.73

Table S3: Experimentally determined values for the partitioning of the fuel in passive droplets.

Diffusivity	Spherical shell	Droplet
$D_{\text{precursor}} [\mu\text{m}^2/\text{s}]$	0.060 ± 0.010	0.042 ± 0.003
$D_{\text{product}}^* [\mu\text{m}^2/\text{s}]$	0.029 ± 0.008	0.032 ± 0.003

Table S4: Experimentally determined values for the diffusivities in the active droplet and the active spherical shell.

reaction constant	Value
k_0	$2.9 \cdot 10^{-4} \text{ s}^{-1}$
k_1	$1.7 \pm 0.08 \cdot 10^{-1} \text{ M}^{-1} \text{ s}^{-1}$
K	1.34 ± 1.0
k_2	$1.2 \pm 0.9 \cdot 10^{-2} \text{ s}^{-1}$

Table S5: Kinetic parameters determined by the kinetic model.

5. Liquid Spherical Shells are a Non-Equilibrium Steady State



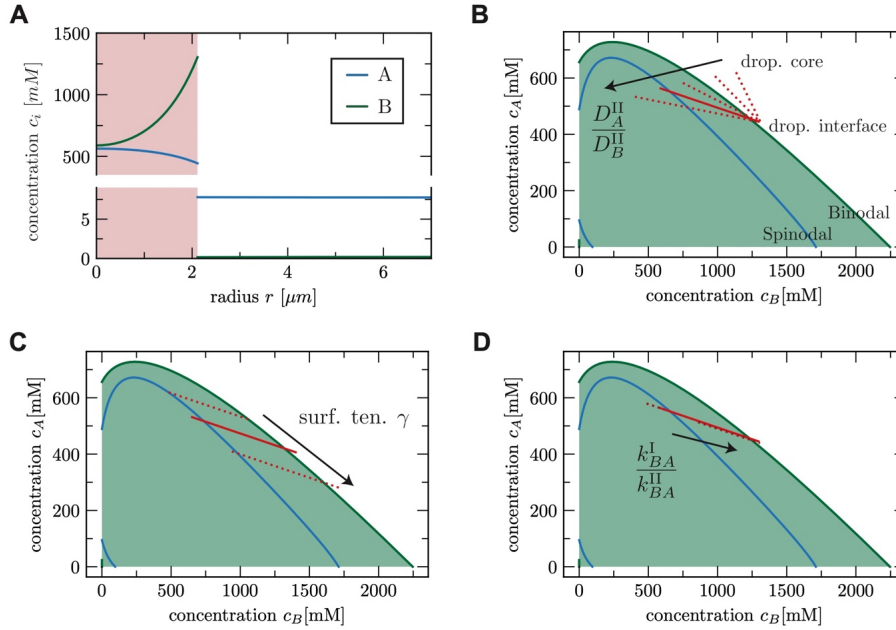
Quantity	Symbol	Value	Reference
Interaction parameter precursor - product	χ_{AB}	-0.18	SI (F)
Interaction parameter precursor - solvent	χ_{AS}	0.78	SI (F)
Interaction parameter product - solvent	χ_{BS}	1.28	SI (F)
Precursor relative molecular volume	r_A	35.1	SI (F)
Product relative molecular volume	r_B	19.4	SI (F)
Surface tension	γ	$75 \mu\text{N m}^{-1}$	SI (F)
Activation rate outside the drop	k_{BA}^{II}	$0.17 c_F \text{ M}^{-1} \text{ s}^{-1}$	SI (B) and Tab.5
Activation rate inside the drop	k_{BA}^{I}	$0.51 c_F \text{ M}^{-1} \text{ s}^{-1}$	SI (B) and Tab.5
Deactivation rate outside the drop	k_{AB}^{II}	0.012 s^{-1}	SI (B) and Tab.5
Deactivation rate inside the drop	k_{AB}^{I}	0.012 s^{-1}	SI (B) and Tab.5
Diffusion coefficient of <i>A</i> outside the drop	D_A^{II}	$300 \mu\text{m}^2 \text{ s}^{-1}$	¹⁴
Diffusion coefficient of <i>B</i> outside the drop	D_B^{II}	$300 \mu\text{m}^2 \text{ s}^{-1}$	¹⁴
Diffusion coefficient of <i>A</i> inside the drop	D_A^{I}	$0.04 \mu\text{m}^2 \text{ s}^{-1}$	Tab.4
Diffusion coefficient of <i>B</i> inside the drop	D_B^{I}	$0.0073 \mu\text{m}^2 \text{ s}^{-1}$	Tab.4
Activation rate outside the spherical shell	k_{BA}^{II}	$0.17 c_F \text{ M}^{-1} \text{ s}^{-1}$	SI (B) and Tab.5
Activation rate in the spherical shell shell	k_{BA}^{III}	$0.51 c_F \text{ M}^{-1} \text{ s}^{-1}$	SI (B) and Tab.5
Activation rate in the spherical shell core	k_{BA}^{I}	$0.17 c_F \text{ M}^{-1} \text{ s}^{-1}$	SSI (B) and Tab.5
Deactivation rate outside the spherical shell	k_{AB}^{II}	0.012 s^{-1}	SI (B) and Tab.5
Deactivation rate in the spherical shell shell	k_{AB}^{III}	0.012 s^{-1}	SI (B) and Tab.5
Deactivation rate in the spherical shell core	k_{AB}^{I}	0.012 s^{-1}	SI (B) and Tab.5
Diffusion coefficient of <i>A</i> outside the spherical shell	D_A^{II}	$300 \mu\text{m}^2 \text{ s}^{-1}$	¹⁴
Diffusion coefficient of <i>B</i> outside the spherical shell	D_B^{II}	$300 \mu\text{m}^2 \text{ s}^{-1}$	¹⁴
Diffusion coefficient of <i>A</i> in the spherical shell shell	D_A^{III}	$0.04 \mu\text{m}^2 \text{ s}^{-1}$	Tab.4
Diffusion coefficient of <i>B</i> inside spherical shell shell	D_B^{III}	$0.0073 \mu\text{m}^2 \text{ s}^{-1}$	Tab.4
Diffusion coefficient of <i>A</i> inside the spherical shell core	D_A^{I}	$300 \mu\text{m}^2 \text{ s}^{-1}$	¹⁴
Diffusion coefficient of <i>B</i> inside the spherical shell core	D_B^{I}	$300 \mu\text{m}^2 \text{ s}^{-1}$	¹⁴

Table S 6: Table with input parameters used in the numerical calculations.

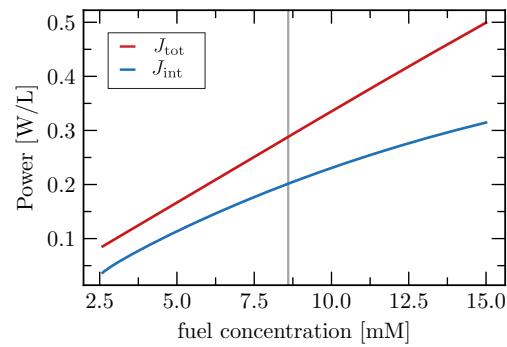
Figure	Quantity	Symbol	Value
Fig. 4 C and D	System radius	R_{sys}	35 μm
Fig. 4 C and D	Fuel concentration	c_{fuel}	8.6 mM
Fig. 4 E	System radius	R_{sys}	17.5 μm
Fig. 4 E	Fuel concentration	c_{fuel}	8.6 mM
Fig. 4 G	System radius	R_{sys}	25 μm
Fig. 4 G	Fuel concentration	c_{fuel}	10 mM
Fig. 4 H	System radius	R_{sys}	25 μm
Fig. 4 H	Fuel concentration	c_{fuel}	10 mM
Fig. 4 H	Dif. coef. of A in inside the shell	D_A^{III}	as indicated by $D_{\text{Precursor}}$
Fig. 4 H	Dif. coef. of B in inside the shell	D_B^{III}	$D_A^{\text{III}}/5.5$
Ext. Data Fig. 10 A-C	System radius	R_{sys}	25 μm
Ext. Data Fig. 10 B, C	Fuel concentration	c_{fuel}	8.6 mM
Sup. Fig. 1 A-D	System radius	R_{sys}	20 μm
Sup. Fig. 1 B	Ratio of dif. inside the drople	$\frac{D_A^{\text{II}}}{D_B^{\text{II}}}$	{1, 2, 4, 5.5, 10} (ind. by arrow)
Sup. Fig. 1 C	Surface tension	γ	{25 μN , 75 μN , 175 μN } (ind. by arrow)
Sup. Fig. 1 D	Ratio of act. rates	$\frac{k_{\text{BA}}^{\text{I}}}{k_{\text{BA}}^{\text{II}}}$	{0.1, 3, 10} (ind. by arrow)
Sup. Fig. 2	System radius	R_{sys}	35 μm

Table S 7: Table with input parameters used for specific figures.

IV. Supplementary Figures



Supplementary Figure 1. Influence of different parameter choices. **A** Concentration values of A and B as a function of the radial distance r from the droplet center (red shaded domain is the droplet inside). **B-D** Concentration profiles of the components A and B of the droplet domain (red shaded domain in A) in composition space (red line) in addition to the binodal line (green) and the spinodal line (blue). Red solid line corresponds to the kinetic parameters used in the main text (Tab. 6 and 7).



Supplementary Figure 2. Influence of fuel concentration on power turn over in the spherical shell state. The red curve represents the power per unit volume needed to constantly activate particles from state A to B, J_{tot} . We compare it to the free energy transported through the interface corresponding to activated B particles crossing the interface, J_{int} (blue curve). The vertical line corresponds to the fuel concentration value used for the estimates in the main text. In the shown fuel concentration range, the efficiency J_{int}/J_{tot} varies non monotonically between 46% and 70%.

V. Supplementary Movies

Supplementary movie 1. Spherical shell formation upon dissolution. *Confocal micrograph timelapse series of a solution of 22 mM precursor, 5 mM pSS in 200 mM MES at pH 5.3 with 0.1 μ M sulforhodamine B as a dye and fueled with 20 mM DIC. The active droplets grew and fused initially and big droplets formed spherical shells upon dissolution. Imaging was done in PVA-coated ibidi chambers.*

Supplementary movie 2. Dissolution without spherical shell formation. *Confocal micrograph timelapse series of a solution of 22 mM precursor, 5 mM pSS in 200 mM MES at pH 5.3 with 0.1 μ M sulforhodamine B as a dye and fueled with 10 mM DIC. The active droplets grew and fused initially but no spherical shells were formed upon dissolution. Imaging was done in PVA-coated ibidi chambers.*

Supplementary movie 3. Formation of a stable active droplet. *Confocal micrograph timelapse series of a solution of 10 mM precursor, 5 mM pSS in 200 mM MES at pH 5.3 with 0.1 μ M sulforhodamine B as a dye. To achieve a steady state, 0.5 M DIC was added to the oil phase. The active droplets grew and fused until they reached a stable size of $r < r_{\text{unstable}}$. The time-lapse series represents the maximum z-projection of a z-stack throughout one microreactor. Imaging was started 10 min after the addition of fuel.*

Supplementary movie 4. Stable active droplet. *Confocal micrograph timelapse series of a solution of 10 mM precursor, 5 mM pSS in 200 mM MES at pH 5.3 with 0.1 μ M sulforhodamine B as a dye. To achieve a steady state, 0.5 M DIC was added to the oil phase. Start of imaging was 2 h after the addition of fuel. A representative stable active droplet with $r < r_{\text{unstable}}$.*

Supplementary movie 5. Stable active shell. *Confocal micrograph timelapse series of a solution of 10 mM precursor, 5 mM pSS in 200 mM MES at pH 5.3 with 0.1 μ M sulforhodamine B as a dye. To achieve a steady state, 0.5 M DIC was added to the oil phase. Start of imaging was 3 h after the addition of fuel. A representative stable active shell with $r > r_{\text{unstable}}$.*

Supplementary movie 6. Transition of an active droplet into an active spherical shell. *Confocal micrograph timelapse series of a solution of 10 mM precursor, 5 mM pSS in 200 mM MES at pH 5.3 with 0.1 μ M sulforhodamine B as a dye. To achieve a steady state, 0.5 M DIC was added to the oil phase. An active droplet with a critical radius larger than r_{unstable} transitioned into an active spherical shell. Imaging was done in a microreactor. Imaging was started 1 h after the addition of fuel.*

VI. Supplementary References

- 1 Schnitter, F. & Boekhoven, J. A Method to Quench Carbodiimide-Fueled Self-Assembly. *ChemSystemsChem* **3** (2020). <https://doi.org:10.1002/syst.202000037>
- 2 Donau, C. *et al.* Active coacervate droplets as a model for membraneless organelles and protocells. *Nature Communications* **11**, 5167 (2020). <https://doi.org:10.1038/s41467-020-18815-9>
- 3 Spath, F. *et al.* Molecular Design of Chemically Fueled Peptide-Polyelectrolyte Coacervate-Based Assemblies. *Journal of the American Chemical Society* **143**, 4782-4789 (2021). <https://doi.org:10.1021/jacs.1c01148>
- 4 Jayalath, I. M., Wang, H., Mantel, G., Kariyawasam, L. S. & Hartley, C. S. Chemically Fueled Transient Geometry Changes in Diphenic Acids. *Organic Letters* **22**, 7567-7571 (2020). <https://doi.org:10.1021/acs.orglett.0c02757>
- 5 Donau, C., Spath, F., Stasi, M., Bergmann, A. M. & Boekhoven, J. Phase Transitions in Chemically Fueled, Multiphase Complex Coacervate Droplets. *Angewandte Chemie International Edition* **61**, e202211905 (2022). <https://doi.org:10.1002/anie.202211905>
- 6 Nott, T. J. *et al.* Phase transition of a disordered nuage protein generates environmentally responsive membraneless organelles. *Mol Cell* **57**, 936-947 (2015). <https://doi.org:10.1016/j.molcel.2015.01.013>
- 7 Flory, P. J. Thermodynamics of High Polymer Solutions. *The Journal of Chemical Physics* **10**, 51-61 (1942). <https://doi.org:10.1063/1.1723621>
- 8 Huggins, M. L. Thermodynamic Properties of Solutions of Long-Chain Compounds. *Transactions of the New York Academy of Sciences* **4**, 107-107 (1942). <https://doi.org:https://doi.org/10.1111/j.2164-0947.1942.tb00827.x>
- 9 Spruijt, E., Sprakel, J., Cohen Stuart, M. A. & van der Gucht, J. Interfacial tension between a complex coacervate phase and its coexisting aqueous phase. *Soft Matter* **6**, 172-178 (2010). <https://doi.org:10.1039/B911541B>
- 10 Brangwynne, C. P. *et al.* Germline P Granules Are Liquid Droplets That Localize by Controlled Dissolution/Condensation. *Science* **324**, 1729-1732 (2009). <https://doi.org:doi:10.1126/science.1172046>
- 11 Weber, C. A., Zwicker, D., Jülicher, F. & Lee, C. F. Physics of active emulsions. *Reports on Progress in Physics* **82**, 064601 (2019). <https://doi.org:10.1088/1361-6633/ab052b>
- 12 Bauermann, J., Weber, C. A. & Jülicher, F. Energy and Matter Supply for Active Droplets. *Annalen der Physik* **534**, 2200132 (2022). <https://doi.org:https://doi.org/10.1002/andp.202200132>
- 13 Higuchi, T., Ebersson, L. & McRae, J. D. Acid anhydride-free acid equilibria in water in some substituted succinic acid systems and their interaction with aniline. *Journal of the American Chemical Society* **89**, 3001-3004 (1967). <https://doi.org:10.1021/ja00988a036>
- 14 Miyamoto, S. & Shimono, K. Molecular Modeling to Estimate the Diffusion Coefficients of Drugs and Other Small Molecules. *Molecules* **25** (2020). <https://doi.org:10.3390/molecules25225340>

6. Oscillations in Active Emulsions

In the previous chapter, we described the formation of spherical shells as a dissipative structure when active droplets were continuously fueled. The active droplets fused and, once they reached a critical size, would be unstable, resulting in the transition to a spherical shell. The transition was attributed to reaction-diffusion gradients that result from the spatial separation of the activation and deactivation reaction of the droplets' building blocks. However, as shown in Figure 10, other behaviors like the control over the droplets' size have been described as well for externally maintained active droplets. In this chapter, I will explain how the size regulation of active droplets induced by reaction-diffusion gradients can lead to yet another dissipative phenomenon: An oscillatory behavior of droplet nucleation, growth, fusion and shrinkage. The project in the following chapter has not been published in a peer-reviewed journal and was conducted in collaboration with Judit Sastre.

6.1 Experimental Setup

The carbodiimide-fueled reaction cycle developed by Donau *et al.*⁵⁶ was used to prepare active droplets (Figure 11). These active droplets were continuously fueled using the experimental microsetup described in Chapter 5 (Figure 18). Briefly, the reaction solution containing the precursor (AcF(RG)₃D-OH) and the polyanion (pSS) are encapsulated into surfactant-stabilized water-in-oil droplets (microreactors). To achieve a non-equilibrium steady state within the microreactors, the fuel (*N,N'*-diisopropylcarbodiimide, DIC) is added to the surrounding oil phase. The fuel is chosen in a way that it has a high solubility within the oil phase but only a very limited solubility within the aqueous microreactors. The fuel that is consumed in the reaction cycle will be replenished by a diffusive influx at the interface as the excess fuel in the oil phase acts as a fuel reservoir (Figure 18B). Similarly, the waste preferably partitions and crystallizes in the oil phase.

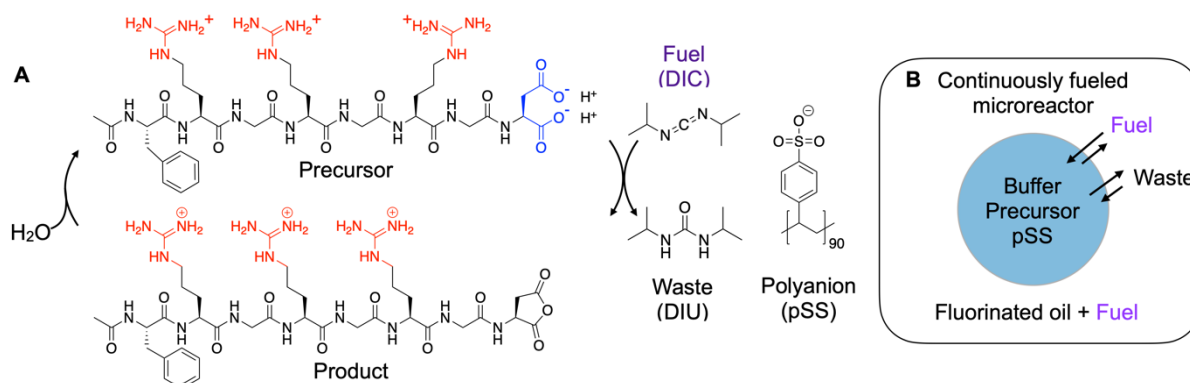


Figure 18: Continuous fueling. **A)** Schematic representation of the reaction cycle. **B)** Schematic representation of a continuously fueled microreactor.

6.2 Continuous Nucleation, Growth, Fusion, and Shrinkage of Active Droplets

To obtain large active droplets that transition into spherical shells as a dissipative structure, we used relatively long, 75 kDa, pSS. Instead, 17 kDa pSS did not result in the formation of only one droplet within each microreactor, but multiple droplets were always present. Interestingly, the presence of multiple droplets was not a consequence of less fusion. Instead, we observed the continuous nucleation and growth of new droplets (Figure 19A). These droplets predominantly nucleated in the upper half of the microreactors, and as they grew, they slowly sunk down until they eventually fused with other droplets at the bottom of the microreactor. After a brief absence of droplets in the upper half of the microreactors, new droplets nucleated, and the process was repeated continuously (Figure 19B). This fusion process did not result in one continuously growing droplet at the bottom of the microreactor. Instead, the central droplet shrunk significantly in size in between the fusion events, switching between fusion-induced growth and spontaneous shrinkage (Figure 19C-D). During this entire process, the total volume of all droplets in the microreactor stayed constant (Figure 19E), confirming that the system was in a steady state.

The continuous alternation of growth and shrinkage of the center droplet is reminiscent of oscillatory behavior. However, due to the randomness of the fusion events, no periodicity could be observed in the evolution of the center droplet's volume (Figure 19D). In contrast, in the upper half of the reactor, where droplets nucleated and grew, fusion played only a minor role. Here, the total volume revealed a periodic oscillatory behavior (Figure 19F). The shrinking of droplets at the bottom and the nucleation and growth of droplets in the upper half of the reactor occurred in an anti-cyclic fashion—whenever the total volume in the bottom half decreased, it increased in the upper half. Interestingly, there was no significant lag period but an almost immediate interchange of the droplet material (Figure 19F insert). These oscillations could be maintained for at least 7 h with only little fatigue in the amplitude of some of the repeating nucleation cycles (Figure 19G).

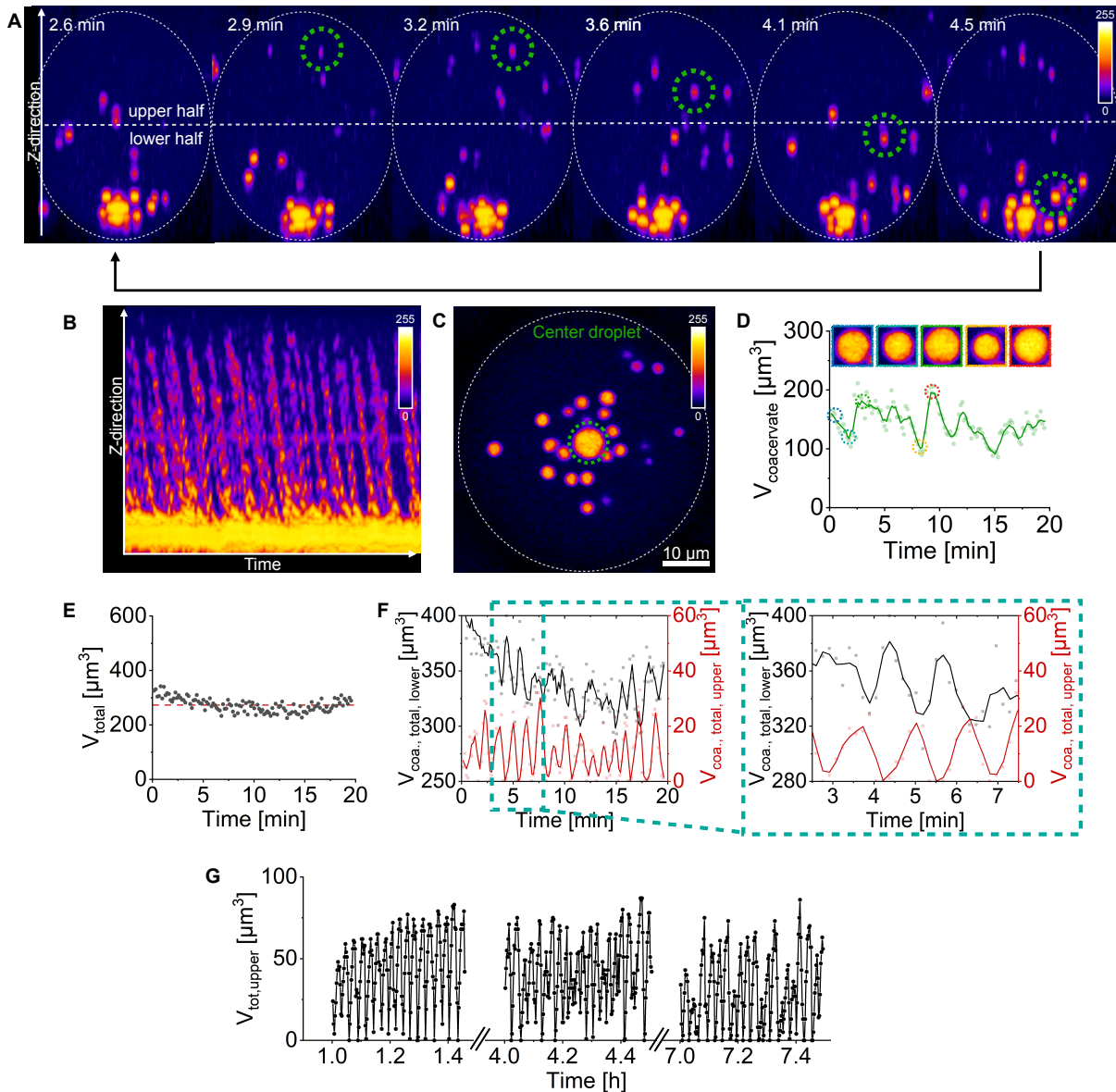


Figure 19: Continuous nucleation, growth, fusion, and shrinkage of droplets. Conditions were 10 mM precursor, 5 mM pSS in 200 mM MES pH 5.3 with 0.5 μM sulforhodamine B as the dye. 250 mM DIC was added to the oil phase to induce coacervation. **A)** Y-projections from the Z-stack time series show the nucleation and growth of new droplets in the upper half of the reactors. Upon growth, these droplets sink down and fuse at the bottom of the reactor, while new droplets nucleate in the upper half of the reactor. Grey dotted circles represent the periphery of the reactors, and green dotted circles mark a tracked droplet through the time series. **B)** Kymograph of a microreactor. **C)** Representative Z-projection showing the presence of multiple smaller and one larger center droplet. Grey dotted circles represent the periphery of the reactors. **D)** Volume evolution of the marked center droplet of **C**. Inserts show identically scaled images of the center droplet at the marked time points. **E)** Representative plot of the total volume of all coacervate-based droplets within one reactor. The Red dashed line represents the average total volume. **F)** The total volume evolution of coacervate-based droplets in the upper and lower half of the reactor from **A**. Turquoise dashed line marks the zoomed-in region. The insert highlights the anti-cyclic oscillation of the total volumes. **G)** Oscillations could be sustained for over 7 h. The shown oscillations were analyzed for three different reactors of the same size.

6.3 Oscillations Result from the Interplay of Size-Control and Fusion

The observed behavior of continuous nucleation, growth, fusion, and shrinkage of droplets is impossible for a system in equilibrium as such a system would strive towards the formation of a single droplet to minimize its interfacial surface tension. The continuous upkeep of an increased surface area due to the presence of multiple droplets is thermodynamically unfavored and needs a continuous supply of energy to be maintained. In Chapter 1, I introduced how chemical reactions can influence the behavior and properties of active droplets. Theoretical calculations predict that the size of externally maintained active droplets is controlled by the underlying reaction cycle.^{46,53} As has been shown in Chapter 5, the activation of the precursor occurs predominantly outside the droplets, and the deactivation of the product occurs predominantly inside the droplets. This spatial separation of the reactions leads to a flux of product from the dilute phase into the droplets (influx) that stabilizes their size, while the corresponding flux of deactivated precursor from the droplets to the dilute phase (efflux) induces a destabilizing effect on the droplet size (Figure 20A). These fluxes are dependent on the size of the droplets—the efflux of precursor scales with the volume of the droplet, while the influx of product scales with the surface area of the droplets. This difference in scaling of the fluxes results in an optimal size for all droplets in which both fluxes are balanced. Consequently, droplets smaller than their optimal size grow while droplets larger than this size shrink (Figure 20B). Theoretically, all droplets in the system described above should evolve to the same size, but fusion prevents this. As a result, droplets are continuously pushed away from their optimal size resulting in an increasing net efflux of droplet material the further away from its optimal size the droplet is. In the simplest case in which oscillations could be expected, fusion-driven growth leads to the incorporation of all droplet material into a single droplet that is larger than its optimal size, followed by a period of net efflux of precursor until the stable size of the droplet is restored (Figure 20C). However, under steady-state conditions, the total amount of product is conserved, and as a result, the shrinkage of one droplet leads to nucleation and growth of new droplets. We hypothesize that the central droplet induces a fuel gradient resulting in decreased fuel and product concentrations at the bottom of the microreactor and, reciprocally, higher concentrations of fuel and product towards the upper boundaries of the microreactors. These gradients lead to the preferential nucleation of droplets the furthest away from the center droplet, *i.e.*, the top of the microreactor. The recurrent presence of multiple droplets induces fusion-driven growth into one droplet, completing one oscillation of the system and enabling the following. Although multiple droplets are always present in the example in Figure 19, the described case can be observed for smaller containers. These show the fusion of all droplets into a single remaining droplet and the

6. Oscillations in Active Emulsions

consecutive nucleation of new droplets (Figure 20D). Additionally, the same anti-cyclic oscillation of the center droplet's and the newly nucleated droplet's volume is seen, further corroborating the explained mechanism.

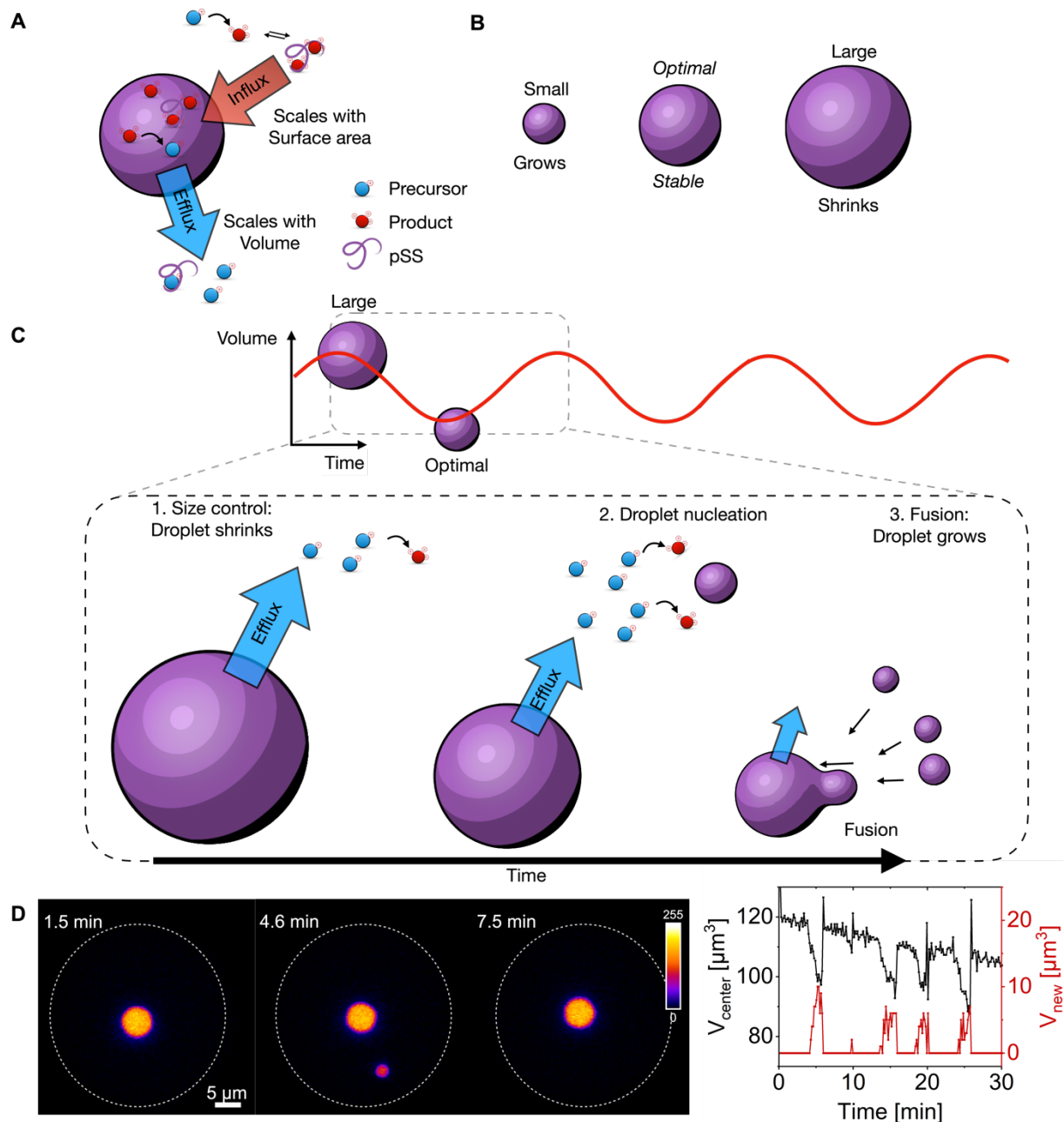


Figure 20: Interplay of size-control and fusion induces oscillations. **A)** A Schematic representation illustrating the activation and deactivation-dependent influx of product (red) and efflux of precursor (blue) for a coacervate-based droplet. **B)** The size-dependent behavior of coacervate-based droplets as a result of the different scaling of influx and efflux. **C)** A Schematic representation of the mechanism behind the oscillations. **D)** Representative images displaying droplet oscillations and the corresponding volume evolution of the center and newly nucleated droplets.

6.4 Control and Limitations of the Oscillations

Next, we determined which parameters affect the frequency of the oscillations and whether they can be tuned. We first examined how the total volume of droplets in the reactor affects the oscillations. The total volume of droplets can be easily tuned due to its linear scaling with the reactor volume. The Z-stack imaging of differently sized reactors revealed that an increasing reactor size resulted in increasingly more droplets whose presence in different Z-locations continuously oscillated. To characterize the frequency of the oscillations, the total volume of droplets in the upper half of each reactor was determined, and the resulting time evolution of the volume was analyzed by a fast Fourier transform (FFT) (Figure 21A and B). We observed no oscillations for reactors with a radius $< 17.5 \mu\text{m}$. Above that radius, the frequency rapidly increased until it leveled at a maximum frequency of $\sim 0.8 \text{ min}^{-1}$. A comparison of the total volume of all droplets within each reactor confirmed the linear scaling with the reactor size (Figure 21C). This plot revealed that a minimum droplet volume of $V_{\text{min}} > 67 \mu\text{m}^3$ was needed to observe oscillations. To confirm that oscillations depend on the droplet volume and not the reactor size, we conducted similar experiments in which the reactor size was constant, but the salt concentration controlled the total droplet volume in each reactor. As electrostatic interactions are one of the main driving forces for complex coacervation in this system, an increasing concentration of NaCl competes with droplet formation. Indeed, adding 0-200 mM NaCl decreased the total droplet volume by up to 10-fold (Figure 21D). The resulting decrease in the volume had the same effect on the oscillation frequency as seen in Figure 21B (Figure 21E), showing an almost identical V_{min} (Figure 21F) and confirming the droplet volume to be the determining factor for the presence of oscillations.

6. Oscillations in Active Emulsions

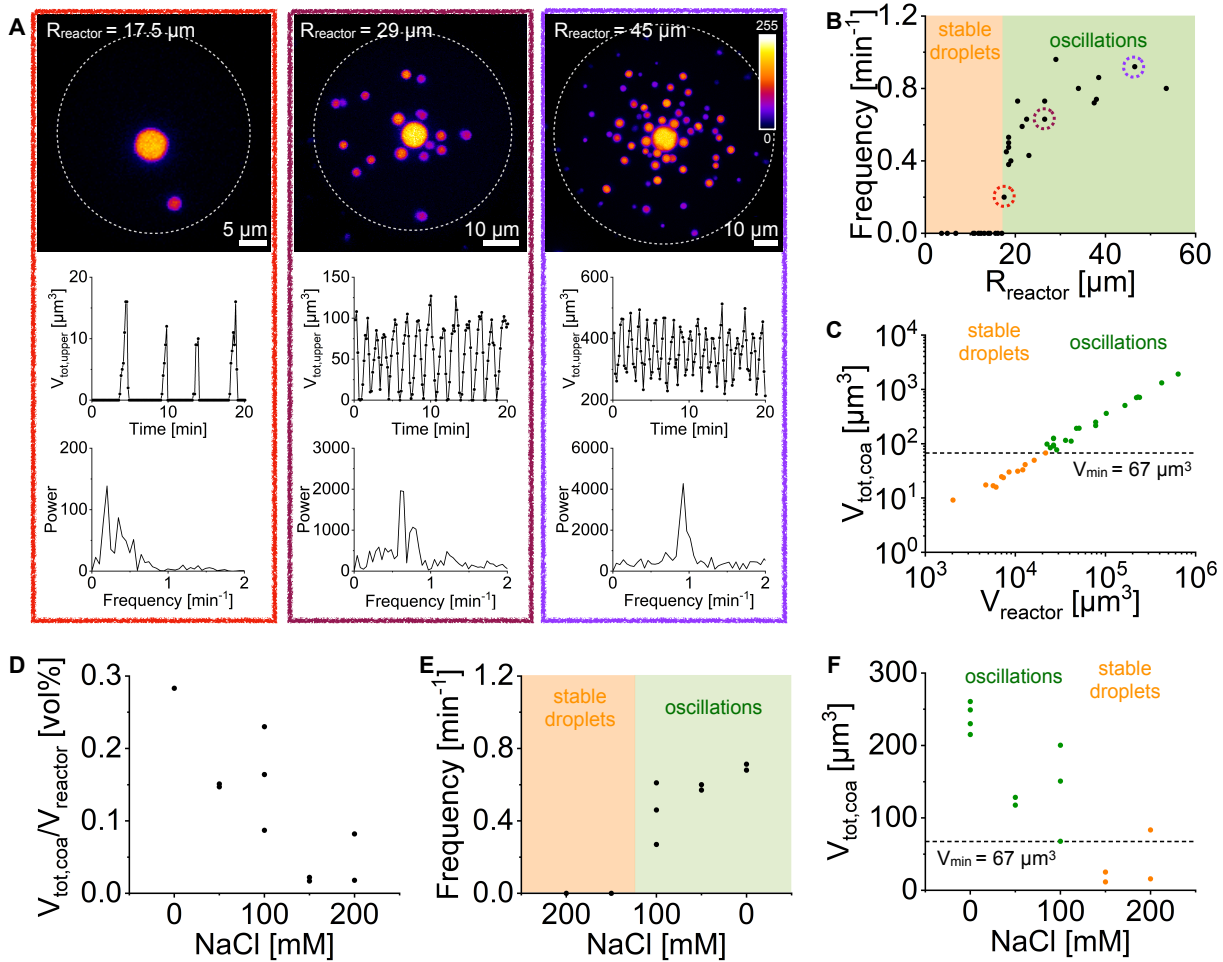


Figure 21: Influence of reactor size and total volume of droplets on oscillations. Conditions were 10 mM precursor, 5 mM pSS in 200 mM MES pH 5.3 with $0.5 \mu\text{M}$ sulforhodamine B as the dye. 250 mM DIC was added to the oil phase to induce coacervation. **A**) Representative Z-projections of differently sized reactors, the corresponding total volume evolution of coacervate-based droplets in the upper half of the reactors, and the FFT analysis of the oscillating volume evolution. **B**) The most prominent frequency obtained by FFT, as depicted in **A**, is plotted against the size of the corresponding reactor. **C**) The total volume of all droplets within each reactor is plotted against the reactor size, categorized into two groups: not oscillating reactors containing stable droplets (orange) and reactors containing oscillating droplets (green). The dashed line represents the minimum volume (V_{min}) of droplets in a reactor required to observe oscillations. **D**) Volume percentage of the total droplet volume in a container plotted against the added NaCl concentration. **E**) Frequency of the oscillations in dependence on the NaCl concentration. **F**) The total volume of all droplets within each reactor is plotted against the NaCl concentration, categorized into two groups: not oscillating reactors containing stable droplets (orange) and reactors containing oscillating droplets (green). The dashed line represents V_{min} of **C**.

Lastly, we investigated how the fuel steady-state level influences the system's oscillations. We observed no droplet formation for fuel concentrations of $c_{\text{fuel,oil}} \leq 20 \text{ mM}$ (Figure 22A). A $c_{\text{fuel,oil}} = 35 \text{ mM}$ led to the formation of stable droplets because insufficient phase-separated droplet material was induced to surpass V_{min} (Figure 22B). In line with previous observations, a further increase in $c_{\text{fuel,oil}}$ increased the total droplet volume, and beyond a $c_{\text{fuel,oil}} = 70 \text{ mM}$ oscillations were consistently observed until $c_{\text{fuel,oil}} = 1000 \text{ mM}$ (Figure 22A-C). Unlike the

6. Oscillations in Active Emulsions

experiments where we increased the reactor size, the oscillation frequency did not level after reaching a certain fuel concentration. Instead, it decreased again until barely any newly nucleating droplets were observed for $c_{\text{fuel, oil}} = 1000 \text{ mM}$ (Figure 22A and C). We hypothesize that at increasing fuel concentrations, fuel gradients in the dilute phase are diminished while most of the polyanion is recruited into the center droplet, preventing the nucleation of new droplets.

We next tested the effect of the polyanion concentration on the oscillations to verify that the depletion of polyanion in the dilute phase limited the nucleation of new droplets. For this, we increased the pSS concentration from 5 mM to 10 mM, and, indeed, we observed the nucleation of new droplets for 500 and 1000 mM (Figure 22D) with a recovery of the frequency to similar levels as for 250 mM DIC (Figure 22C).

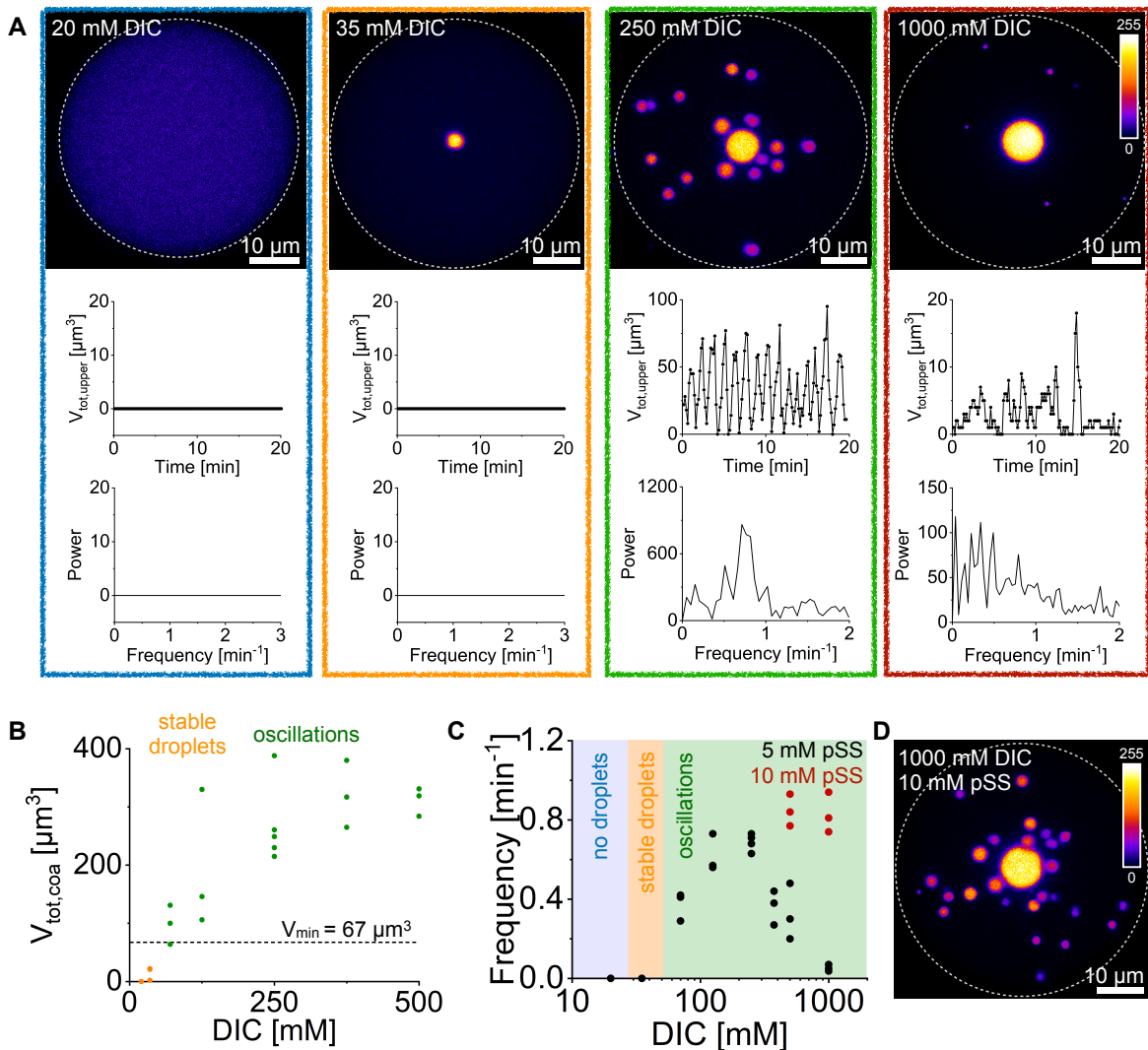


Figure 22: Influence of fuel concentration on oscillations. Conditions are 10 mM precursor, 5 mM pSS in 200 mM MES pH 5.3 with $0.5 \mu\text{M}$ sulforhodamine B as the dye. The indicated DIC concentration is added to the oil phase to induce coacervation. **A)** Representative Z-projections of similarly sized reactors fueled with different DIC concentrations in the oil phase, the corresponding total volume

6. Oscillations in Active Emulsions

evolution of coacervate-based droplets in the upper half of the reactors, and the FFT analysis of the oscillating volume evolution. **B)** The total volume of all droplets within each reactor is plotted against the DIC concentration used for fueling, categorized into two groups: not oscillating reactors containing stable droplets (orange) and reactors containing oscillating droplets (green). The dashed line represents V_{\min} of Figure 21C. **C)** Frequency of the oscillations in dependence on the DIC concentration. **D)** Representative Z-projection similar to the ones shown in **A**.

6.5 Conclusion

In Chapter 5, we observed the morphological transition from an unstable droplet into a stable spherical shell. The spherical shell is still active, but due to its regained stability, no further dynamics in the morphology can be observed. In this Chapter, the system is not allowed to reach a stable state resulting in oscillating cycles of nucleation, growth, fusion, and shrinkage of active droplets. The oscillations are driven by the shrinkage of unstable active droplets that are continuously maintained above their stable size through gravitationally induced fusion events.

We verified that the oscillations depend on the total volume of droplet material and demonstrated control over the oscillations by varying the reactor size, as well as adjusting salt and fuel concentration. These results demonstrate how active droplets can actively regulate their size and number. Similar mechanisms may play a role in the regulation of membraneless organelles in cells.

7. Synthesis and Characterization of Chemically Fueled Supramolecular Materials Driven by Carbodiimide-Based Fuels

Abstract.

In the previous Chapters, I focused on the analysis of active droplets as an example of dissipative structures. However, in nature, countless other structures, such as microtubules, are also driven away from equilibrium. Synthetic counterparts like chemically regulated fibers have been developed to understand and emulate the regulatory mechanisms behind these systems. Given the considerable differences in properties among these various systems, a diverse range of analytical methods is required to investigate their unique characteristics. This protocol describes the synthesis and characterization of chemically fueled supramolecular materials driven by carbodiimide-based fuels. We outline a general strategy for the analysis of their kinetics and their macroscopic to microscopic properties. We used a fiber- and a crystal-forming precursor as examples to emphasize the different requirements in the analysis.

This work has been published:

Title: Synthesis and characterization of chemically fueled supramolecular materials driven by carbodiimide-based fuels

Authors: Fabian Schnitter, Alexander M. Bergmann, Benjamin Winkeljann, Jennifer Rodon Fores, Oliver Lieleg, Job Boekhoven

First published: 30. June 2021

Journal: *Nat Protoc* **16**, 3901–3932 (2021)

Publisher: Springer Nature

DOI: 10.1002/anie.202203928

Reprinted with permission from Springer Nature. Copyright © 2021, the Authors, under exclusive licence to Springer Nature Limited

This section states the individual work of each author in the publication above. F.S. and A.M.B. contributed equally to this protocol. They designed and performed the experiments and wrote the manuscript. B.W. and J.R.F. carried out the experiments. J.B. designed experiments, outlined and wrote the manuscript, and supervised the project. O.L. designed the experiments.



Synthesis and characterization of chemically fueled supramolecular materials driven by carbodiimide-based fuels

Fabian Schnitter¹, Alexander M. Bergmann¹, Benjamin Winkeljann², Jennifer Rodon Fores¹, Oliver Lieleg² and Job Boekhoven^{1,3}✉

Many supramolecular materials in biological systems are driven to a nonequilibrium state by the irreversible consumption of high-energy molecules such as ATP or GTP. As a result, they exhibit unique dynamic properties such as a tunable lifetime, adaptivity or the ability to self-heal. In contrast, synthetic counterparts that exist in or close to equilibrium are controlled by thermodynamic parameters and therefore lack these dynamic properties. To mimic biological materials more closely, synthetic self-assembling systems have been developed that are driven out of equilibrium by chemical reactions. This protocol describes the synthesis and characterization of such an assembly, which is driven by carbodiimide fuels. Depending on the amount of chemical fuel added to the material, its lifetime can be tuned. In the first step, the protocol details the synthesis and purification of the peptide-based precursors for the fuel-driven assemblies by solid-phase peptide synthesis. Then, we explain how to analyze the kinetic response of the precursors to a carbodiimide-based chemical fuel by HPLC and kinetic models. Finally, we detail how to study the emerging assembly's macro- and microscopic properties by time-lapse photography, UV-visible spectroscopy, shear rheology, confocal laser scanning microscopy and electron microscopy. The procedure is described using the example of a colloid-forming precursor Fmoc-E-OH and a fiber-forming precursor Fmoc-AAD-OH to emphasize the differences in characterization depending on the type of assembly. The characterization of a precursor's transient assembly can be done within 5 d. The synthesis and purification of a peptide precursor requires 2 d of work.

Introduction

Supramolecular materials consist of molecular building blocks assembled into larger architectures by noncovalent interactions^{1,2}. In the past decades, the field has emerged and evolved into a discipline with design rules and a plethora of prominent examples³, such as liquid crystals^{4–6}, supramolecular polymers^{7–9}, or vehicles that can deliver pharmaceuticals^{10,11}.

Supramolecular materials are also present in biological systems; skin and bone are both examples of materials constructed using molecular self-assembly^{12–15}. A property of most natural supramolecular materials is that their building blocks are continuously recycled, which allows them to adapt to changing conditions or to repair themselves¹⁶. These properties are seldom seen in synthetic materials.

Synthetic supramolecular materials almost always exist in or close to equilibrium¹⁷. In contrast, living materials exist far out of equilibrium^{18,19}. To sustain biological materials out of equilibrium, these materials are continually dissipating energy, which is harvested from chemical reaction cycles that irreversibly consume high-energy molecules such as GTP or ATP^{20–22}. Owing to their constantly active nature, these materials are endowed with a higher degree of dynamics than synthetic (static) materials.

Inspired by this dynamic, energy-consuming form of self-assembly of molecules, the field of supramolecular materials has more recently focused on developing synthetic counterparts of biological supramolecular materials: so-called chemically fueled supramolecular materials^{23–31}. In such supramolecular materials, the self-assembly of molecules is regulated by a chemical reaction cycle (Fig. 1a,b). The chemical reaction cycle irreversibly consumes a high-energy reagent, called a chemical fuel, and thereby dissipates energy. Thus, in these systems, the formation of assemblies away from

¹Department of Chemistry, Technical University of Munich, Garching, Germany. ²Department of Mechanical Engineering and Munich School of Bioengineering, Technical University of Munich, Garching, Germany. ³Institute for Advanced Study, Technical University of Munich, Garching, Germany. ✉e-mail: job.boekhoven@tum.de

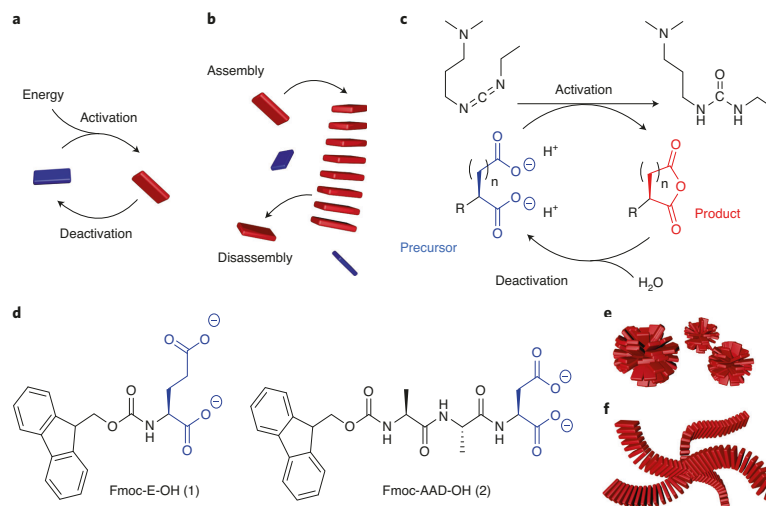
PROTOCOL
NATURE PROTOCOLS


Fig. 1 | In chemically fueled self-assembly, molecules are activated and deactivated for assembly by a chemical reaction cycle. **a**, An energy-driven chemical reaction activates a precursor molecule for self-assembly. A spontaneous deactivation reaction reverts the activated product to the precursor state. **b**, The result is a transient product that, in its finite lifetime, can take part in a dynamic assembly. **c**, In the chemical reaction cycle, a dicarboxylate precursor molecule is converted into an asymmetric anhydride product. The hydration of EDC fuels the activation reaction and generates the waste byproduct EDU (1-ethyl-3-(3-dimethylaminopropyl)urea). The hydrolysis reaction reverts the formed anhydride to the original precursor. **d**, The molecular structures of precursors that are used in this work. **e, f**, The resulting supramolecular structures are schematically shown as colloids (**e**) and hydrogel fibers (**f**).

Table 1 | Different precursors and the corresponding types of assembly when fueled with EDC

Type of assembly	Precursor
Colloids	Fmoc-D-OH ³⁹ , Fmoc-E-OH ⁴² , Fmoc-GD-OH ⁴⁶
Fibers	Fmoc-AAD-OH ³⁹ , Fmoc-AVD-OH ³⁹ , Fmoc-AAE-OH ³⁹ , Fmoc-AVE-OH ³⁹ , Ac-FIID-OH ⁴¹
Aggregates of nanoparticles	5-hexenoic acid coated SiNCs ⁴³ , 3-mercaptopropionic acid coated AuNPs ⁴⁴
Coacervate-based droplets	Ac-FRGRGRGD-OH ⁴⁷
Oil droplets	2-octen-1-ylsuccinic acid ⁴⁶ , 2-decen-1-ylsuccinic acid ⁴⁶ , valeric acid ⁴⁵ , caproic acid ⁴⁵

equilibrium is driven by a kinetic asymmetry in the energy consumption pathway^{32,33}. Examples are ubiquitous in biology (e.g., the GTP-fueled formation of microtubules), but only a few reactions have been tried synthetically. One approach is the use of biological fuel sources in chemical reaction cycles such as the phosphorylation and dephosphorylation with ATP or GTP^{28,34}. These systems are conceptually close to biology, but the requirement of specialized enzymes limits the versatility of these systems compared with more artificial approaches. Simpler synthetic systems allow a more in-depth study of individual mechanisms in otherwise complex biological systems. Artificial approaches of fuel-driven assemblies include methylation³⁵, thiol-thioester exchange³⁶ or redox chemistry as the activation reaction^{37,38}. Many of these systems require just one functional group and are more versatile compared with enzymatic reactions.

We recently introduced a carbodiimide-fueled reaction cycle that leads to dynamic assemblies^{39,40}. In several studies, we showed how the chemical reaction cycle could drive the formation of different types of assemblies depending on the type of precursor used (Table 1). We showed the formation of fibers^{39,41}, colloids⁴², aggregates of nanoparticles^{43,44}, oil droplets^{45,46} and coacervate-based droplets⁴⁷.

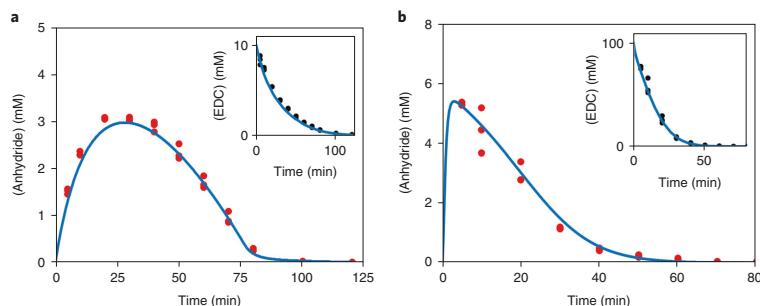


Fig. 2 | Kinetic analysis of the reaction cycle. a,b, The analysis was performed with precursor **1** in response to 10 mM EDC (**a**) and precursor **2** in response to 100 mM EDC (**b**). HPLC measures the concentration of anhydride and EDC (inset). The markers represent triplicate HPLC data, and the lines are predicted values from our kinetic model.

Due to the emerging material properties, a wide variety of different applications can be envisioned. For example, coacervate-based droplets serve as a model for membranellar organelles and protocells⁴⁷. The out-of-equilibrium formation of oil droplets from a set of primitive carboxylic acids exhibits self-selective behavior⁴⁵. Temporal control over aggregation of silicon nanocrystals shows potential as a platform for controlled uptake of nanoparticles into cells⁴³. Fuel-driven fiber formation can serve as a model to study cytoskeleton structures such as microtubulin and actin filaments⁴⁸. Moreover, other research groups are also starting to use this chemical reaction cycle^{49,50}.

Overview of the protocol

In this protocol, we use a chemical reaction cycle that transiently activates dicarboxylate precursors by converting them into their corresponding cyclic anhydrides at the expense of a carbodiimide-based condensing agent (Fig. 1c). In the activation reaction, the precursor reacts irreversibly with the 1-ethyl-3-(3-dimethylaminopropyl)carbodiimide (EDC or fuel) to yield its corresponding anhydride. In the deactivation reaction, the anhydride product reacts with water to yield the original precursor. Consequently, the precursor is activated into its temporary, anhydride state. The anhydride state is uncharged, whereas the precursor carries two anionic carboxylate groups. We use the loss of charges to induce self-assembly of the precursors (Fig. 1d). For example, if the precursor carries a relatively large hydrophobic group (e.g., Fmoc-E-OH (**1**)), it is soluble in its precursor state but assembles into colloids in the product state (vide infra)³⁹. We found that, when we add amino acids with a high propensity to form β -sheets in the precursor design, it is more likely to form anisotropic assemblies in its activated state. For example, in this protocol, we will show that Fmoc-AAD-OH (**2**) will form fibers when fueled with EDC.

We start the protocol by describing the synthesis and purification of the precursors. Precursor **1** is commercially available and used without further purification. Precursor **2** was synthesized using solid-phase peptide synthesis, purified by preparative HPLC, and finally freeze-dried to yield a fluffy, white powder on a 100 mg scale. Both precursors are dissolved in 2-morpholinoethanesulfonic acid (MES)-buffered water. The pH of the resulting solution is adjusted to 6.0.

In the next section of the procedure, we describe how to study the kinetics of the reaction cycle for the two precursors in the EDC-driven chemical reaction cycle. The cycle is initiated by adding the chemical fuel EDC to the precursor solutions. At predetermined intervals, we quench a sample of the experiment by adding benzylamine. Benzylamine freezes the reaction cycle in its current state by converting the reactive anhydride into the respective stable amide. Moreover, the addition of the quenching solution stops the activation reaction owing to an increase of the pH to 10. At this pH, EDC does not react with the carboxylic acids, and therefore, no more anhydride is formed. The quenched samples are studied by reversed-phase analytical HPLC. Using a nonpolar hydrocarbon stationary phase allows separation of the reaction cycle's components and determining the concentration of precursor, product and fuel (Fig. 2a,b).

We then explain how to use a kinetic model, written in MATLAB, to predict both the concentration of the components in the mixture and the reaction rates. This model is especially powerful for predicting for how long the anhydride product is present when adding different amounts of EDC.

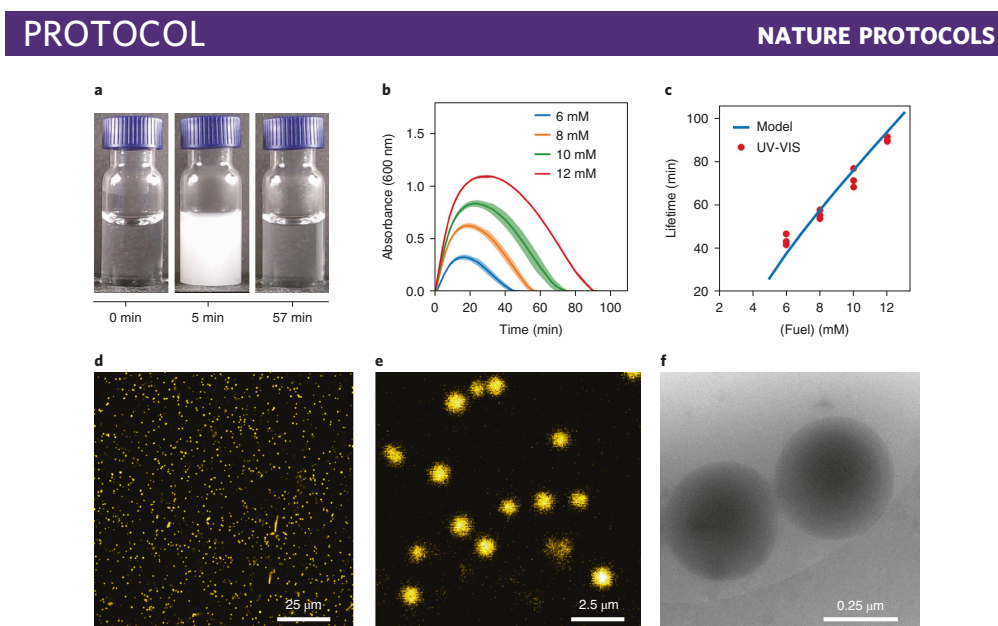


Fig. 3 | Material properties of 10 mM precursor 1 in response to fuel. **a**, Time-lapse photography shows the transient increase in turbidity in response to 10 mM EDC. **b**, The absorbance at 600 nm is a measure for turbidity of **1** in response to EDC's varying concentrations. The shaded area represents the deviation from triplicate data. **c**, The lifetime of the turbidity as a function of fuel added is determined from the data of **b** (markers) and the kinetic model (line). **d,e**, Fluorescence microscopy micrograph as recorded by confocal microscopy (**d**) and a magnification (**e**). **f**, Cryo-TEM microscopy micrograph.

In later experiments, the anhydride lifetime can be correlated to the material's lifetime. For example, we show that increasing the amount of fuel results in a longer presence of the anhydrides, which corresponds to a prolonged presence of the material properties.

The next stage of the procedure involves studying the dynamic material properties of the emerging dissipative supramolecular materials. We describe how to set up a webcam to record time-lapsed photographs of the fueled reaction cycle (Figs. 3a and 4a and Supplementary Video 1 and 2). This is a cheap way to get rapid, qualitative information about the evolution of material properties such as turbidity or the ability to form self-standing hydrogels. To better quantify the turbidity and the time course of its evolution, we use UV-visible (UV-VIS) spectroscopy and measure the optical density at 600 nm in a plate reader over time (Fig. 3b). If the reaction generates a hydrogel, we follow the time course using shear rheology (Fig. 4b). The quantitative information of the material properties' evolution can be correlated to the previously described kinetic model. We do so by determining a threshold concentration of the anhydride product. Above this threshold, the property of the materials (turbidity or the formation of an elastically dominated hydrogel) can be expected. We find that, for precursor **1**, the model can accurately predict the lifetime of the turbid solution, which we describe in the next section of the protocol (Fig. 3c). The correlation between the lifetime of the gels formed by **2** is also calculated (Fig. 4c).

In the final section of the procedure, we describe how to characterize the structure of the temporary assemblies by confocal microscopy using the hydrophobic dye Nile red (Figs. 3d,e and 4d,e) and by cryogenic transmission electron microscopy (cryo-TEM) (Figs. 3f and 4f).

Experimental design

In the following sections, we describe the peptide synthesis, the kinetic analysis of the reaction cycles and the observation of the emerging macro-, micro- and nanoscopic properties (Fig. 5).

Synthesis of precursors

Precursor **1** was commercially available and used without further purification. Precursor **2** was synthesized via solid-phase peptide synthesis (Fig. 6). Different methods for peptide synthesis have

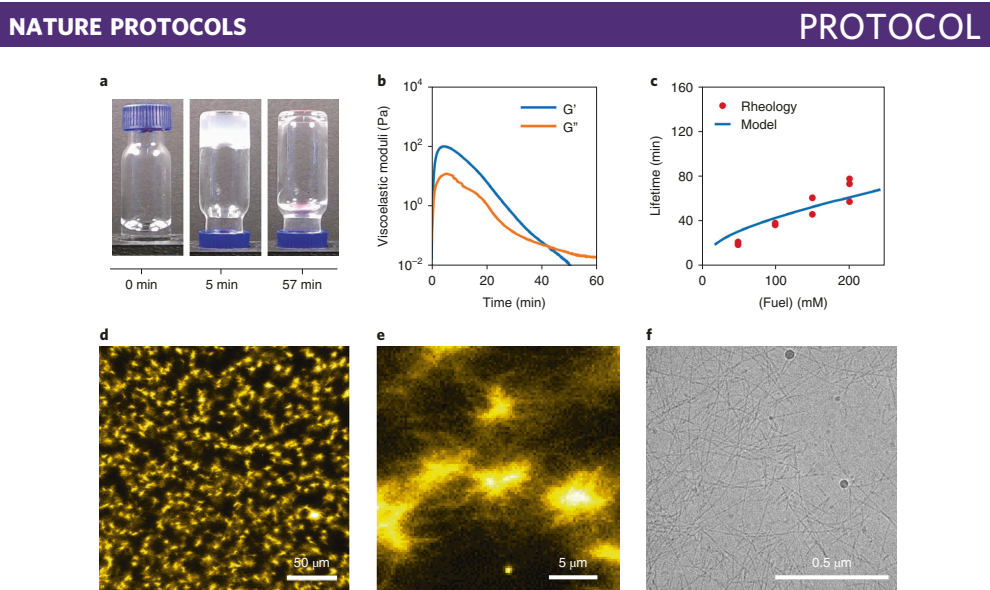


Fig. 4 | Material properties of precursor 2 in response to fuel. **a**, Time-lapse photography shows the formation of a transient hydrogel when fueling with 100 mM EDC. **b**, The viscoelastic response as represented by the storage (G') and loss modulus (G'') of the hydrogel formed when adding 100 mM EDC as a function of time as measured by shear rheology. **c**, The lifetime of the hydrogel as a function of concentration fuel added. The lifetime is measured by rheology (markers) and predicted by the model (line). **d, e**, Fluorescence microscopy micrograph as recorded by confocal microscopy (**d**) and a magnification (**e**) to show the nucleation sites. **f**, Cryo-TEM shows the formation of a fiber network.

been described in previous protocols. These methods range from a general procedure to the synthesis of more complex sequences^{51,52}, and approaches for simultaneous synthesis of different peptide sequences⁵³. In general, any Fmoc-based solid-phase peptide synthesis method is suitable for the synthesis of the peptide sequences listed in Table 1. A requirement is a free C-terminal carboxylic acid after cleavage from the resin. We thus used Wang resin, which was purchased preloaded with the first amino acid. The peptide was further reacted from the C to the N terminus by repeated deprotection and coupling steps. The resulting peptide is cleaved from the resin, the identified product peak is purified by preparative HPLC and the final product is characterized by analytical HPLC, electrospray ionization mass spectrometry (ESI-MS) and NMR. The synthesis can either be performed using a microwave-assisted automated peptide synthesizer or performed manually using a peptide synthesis vessel. The advantage of automated synthesis is that it takes only ~1 h to complete. However, the type of peptide synthesizer used limits the reaction scale (0.5 mmol, which is the equivalent of 122 mg Fmoc-AAD-OH (**2**) after purification). In contrast, the manual synthesis of **2** takes 5 h, but bigger scales can be obtained. Both techniques yield roughly equal amounts of the peptide product at a scale of 0.5 mmol. We recommend manual peptide synthesis if a peptide synthesizer is not available or when scales >0.5 mmol are synthesized.

Nile red assay

In carbodiimide driven self-assembly, the precursor's carboxylate groups react to form an anhydride group, which means that this section of the molecule becomes more hydrophobic. This transition often affects only a small domain of the overall precursor; therefore, the precursor itself needs to be quite hydrophobic for the modification to induce self-assembly. Thus, it is possible that the precursor might assemble without the addition of fuel, especially when the precursor is present at high concentrations. A fast method to test whether the precursor is unimolecularly dissolved is a Nile red assay. Nile red is a solvatochromic dye. Its solubility and quantum yield are low in polar solvents such as water, but are substantially higher in nonpolar environments. Additionally, the absorption and emission wavelength is blue-shifted in nonpolar environments^{54,55}. When structures like micelles are present in an aqueous solution, Nile red accumulates in the hydrophobic microenvironment, resulting in a high fluorescence intensity that is blue-shifted. Both the enhancement and shift in

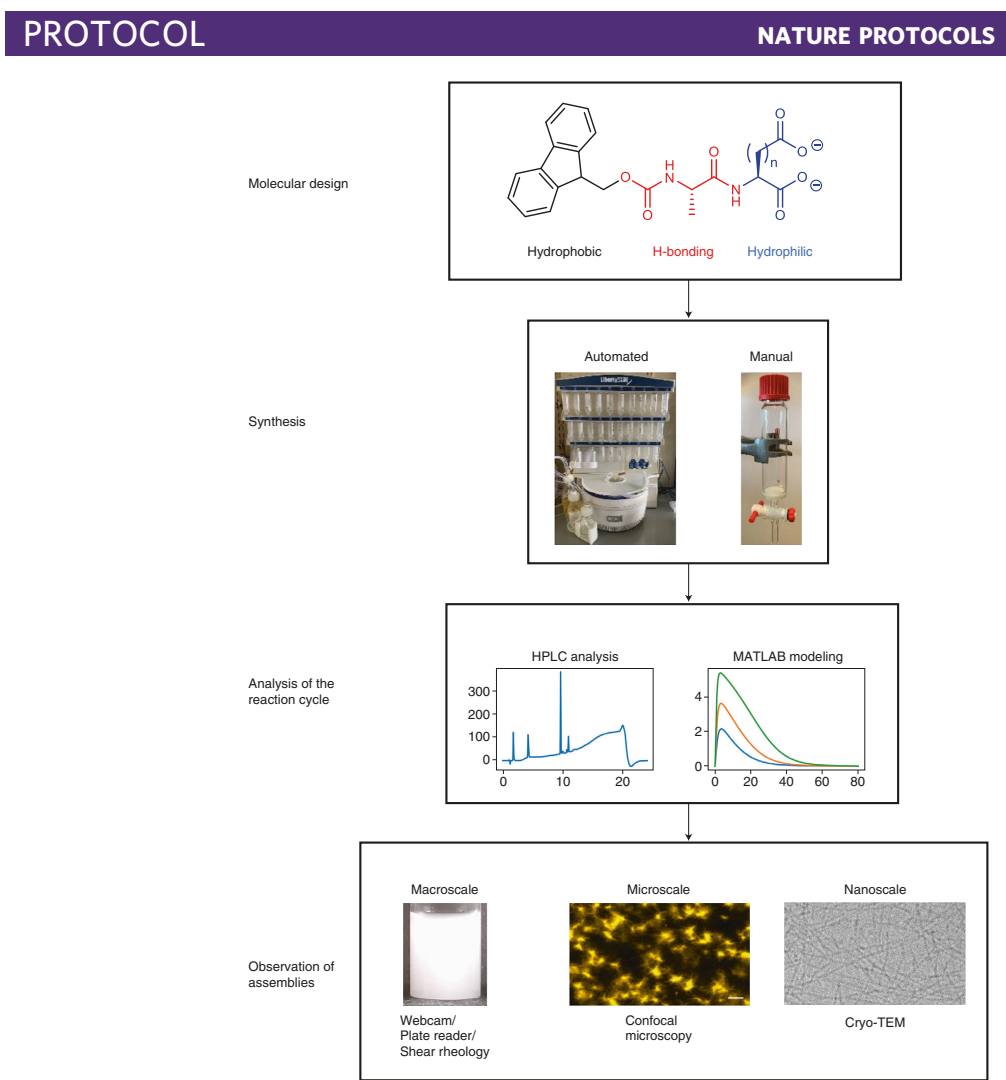


Fig. 5 | Overview of the experimental design. The precursor is designed by balancing attractive and repulsive interactions. While the charge repulsion of the inactivated precursor suppresses self-assembly, self-assembly occurs upon transformation into an anhydride. The peptide precursor is synthesized by applying manual or automated solid-phase peptide synthesis and purified by reversed-phase HPLC. Analytical HPLC measures the concentrations of fuel and product upon fuel addition. By fitting the experimental data to a computational model, the reaction cycle's rate constants are determined. Finally, the assemblies' lifetimes as well as their morphologies are analyzed on the macro-, micro- and nanoscopic scale.

fluorescence are used to identify the critical aggregation concentration. We measure the fluorescence intensity at 635 nm at an excitation wavelength of 550 nm for various concentrations of **1** and **2**. An increase in the fluorescence intensity indicates the presence of assemblies or aggregates in absence of the chemical fuel. As a final test to exclude preassembly, we record cryo-TEM micrographs of the applied reaction cycle's precursor stock solutions (Extended Data Fig. 1).

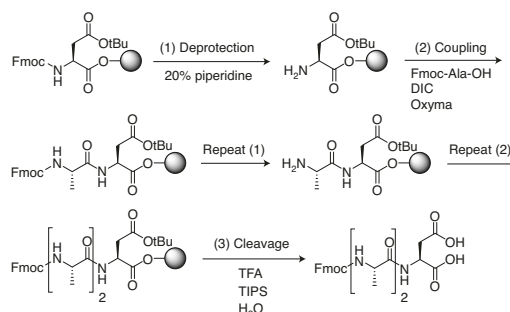


Fig. 6 | Reaction scheme of the proposed solid-phase peptide synthesis of 2. The solid support is Wang resin. Repeated Fmoc deprotection and coupling steps promote chain growth. The final product is obtained after cleavage from the resin and simultaneous removal of the protection groups.

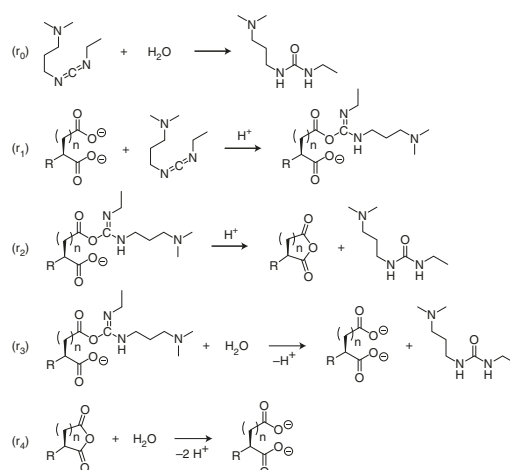


Fig. 7 | Reactions involved in the chemical reaction cycle. Reaction (r_0) shows the direct hydration of EDC in the reaction medium. The reaction (r_1) shows the activation as EDC is added to a carboxylate. The anhydride product formation is depicted by (r_2). A side reaction taking place is shown by (r_3), which is the activated precursor's direct hydrolysis. The deactivation reaction is described by (r_4) showing the anhydride hydrolysis reaction.

Analysis of kinetics by HPLC

The kinetics of the fuel-driven chemical reaction cycle for both precursors **1** and **2** are analyzed with analytical HPLC (Fig. 7). In these experiments, we measure the concentration of the carbodiimide-based fuel (EDC) and the anhydride product. The chemical reaction cycle is initiated by the addition of fuel to the precursor solution. At 7 min intervals, aliquots of the reaction mixture are added to a previously prepared benzylamine solution. The benzylamine solution quenches all reactions in the reaction cycle and converts the anhydride product into its corresponding amide⁵⁶. The quenched samples are stored and analyzed after the reaction cycle is completed by injection into the HPLC. The signals in the chromatograms corresponding to the benzylamide and EDC are integrated. A calibration curve is measured for both components to determine their corresponding concentrations in the experiment.

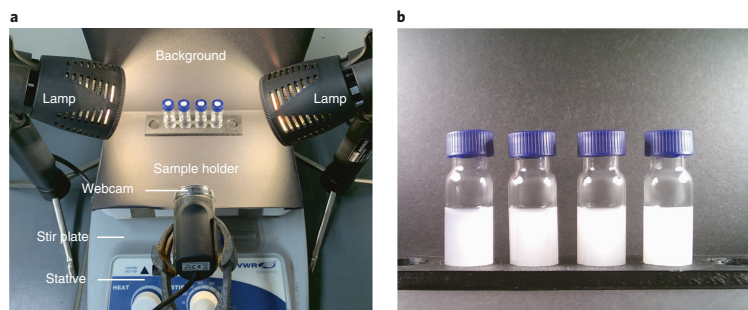
PROTOCOL
NATURE PROTOCOLS


Fig. 8 | Time-lapse photography setup. a,b, The experimental setup of a webcam experiment (a) and the webcam view 5 min into the reaction cycle of Fmoc-E-OH (1) with 6, 8, 10 and 12 mM EDC from left to right (small differences in the turbidity for highly turbid solutions cannot be observed with this technique) (b).

Using a kinetic model in MATLAB

We use the data from the kinetic experiments to fit rate constants for a kinetic model. This kinetic model describes five chemical reactions to predict the concentration of the reactants involved at every second in the experiment (r_0, \dots, r_4). The first reaction is the direct hydration of EDC (r_0). The second is the reaction of EDC with the precursor to yield O-acylisourea (r_1). The third reaction is the conversion of the O-acylisourea to the anhydride product (r_2). The other fate of the O-acylisourea is that it hydrolyzes to the precursor (r_3). Finally, the anhydride product hydrolyzes in the deactivation reaction (r_4). The rate constants of these reactions will be estimated by fitting the concentration profiles measured by HPLC. For example, k_0 can be estimated by fitting the EDC decay in the absence of precursor. Similarly, by fitting the EDC depletion curve in the presence of precursor, the rate constant for the reaction of the precursor with EDC (k_1) can be estimated.

Time-lapse photography

The materials we describe change their turbidity and viscoelastic properties during the reaction cycle; i.e., they transit from a solution to gel state and vice versa (Fig. 8). Changes in turbidity can be observed with the naked eye and can be monitored using a simple webcam setup without the need for laborious and time-consuming experiments. For example, for precursor 1, a fuel-induced, temporary increase in turbidity was observed (Fig. 3a, Fig. 12). The time for which the increased turbidity is present gives an estimation about the lifetime of the assemblies and can be further investigated by UV-VIS analysis. Similarly, precursor 2 shows a temporary increase in turbidity in response to fuel. An inverted tube test is used as an indication for a temporary transition from a solution to a gel state (Fig. 4a). However, this transition needs to be further characterized by rheology measurements as the inverted tube test can give false-positive results⁵⁷.

UV-VIS analysis to measure the evolution of the turbidity

For more accurate kinetic information, the evolution of the turbidity as a function of time can be recorded with a UV-VIS instrument or plate reader. We measure the absorbance at 600 nm as a measure for turbidity as the evolving particles scatter light. This experiment can be done using a plate reader or using cuvettes; the plate reader experiment allows multiple experiments to be performed simultaneously. For example, we can measure the evolution of five different initial concentrations of fuel in triplicate in a single experiment. We use these acquired data to determine the lifetime of the assemblies of precursor 1 in response to varying amounts of fuel. Comparison of the measured lifetimes with anhydride concentrations at these time points provides mechanistic information about the dissipative system such as solubility or kinetic trapping.

Rheology measurements

The viscoelastic properties of a gel can be determined in a quantitative manner using macrorheology. The material response σ^* to an induced oscillating deformation γ^* is mapped to describe such viscoelastic materials. The corresponding modulus $G^*(\omega)$ is a complex parameter and can be

separated into a real and an imaginary part. The real part $G'(\omega)$ describes the elastic response of a material, whereas the imaginary part $G''(\omega)$ describes its viscous properties:

$$\begin{aligned}G'(\omega) &= \frac{\sigma_0}{\gamma_0} \cos(\delta) \\G''(\omega) &= \frac{\sigma_0}{\gamma_0} \sin(\delta)\end{aligned}$$

Here, σ_0 and γ_0 denote the amplitude of the shear stress and the shear strain, respectively. The phase shift between the deformation of the material and its stress response is denoted with δ , dependent on the angular frequency ω of the stimulation. Dominance of the storage modulus ($G' > G''$) indicates the formation of a gel, whereas a dominance in the loss modulus ($G'' > G'$) indicates a liquid-like behavior of the material.

In addition to time-lapse imaging and turbidity measurements, which together can provide a time-resolved visualization of the gelling process, macrorheology can offer a quantitative assessment of the gel formation process, not only over time but also determining absolute mechanical values.

Analysis by confocal laser scanning fluorescence microscopy

Confocal laser scanning fluorescence microscopy is used to examine the dissipative supramolecular materials' evolution on the microscopic scale. As the self-assembling building blocks are not fluorescently labeled, a fluorescent dye incorporated into the assemblies is used. We use the hydrophobic dye Nile red as it is sufficiently hydrophobic to incorporate into our assemblies. Moreover, due to its solvatochromic shift and increased quantum yields between hydrophilic and hydrophobic environments, it is possible to selectively observe the assembled product resulting in a high signal-to-noise ratio in the micrographs⁵⁸. The sample is placed in a grease chamber on a glass microscope slide. The grease chamber offers an efficient method to prevent evaporation and flow of the sample throughout the experiments. In our experiments, confocal microscopy shows the formation of colloids for Fmoc-E-OH (1) (Fig. 3d,e) and the formation of entangled fibers for Fmoc-AAD-OH (2) (Fig. 4d,e).

Analysis by cryo-TEM

In our laboratory, we use cryo-TEM to study the assemblies on the nanometer scale, e.g., to determine the diameter of fibers. We prefer cryo-TEM to conventional TEM, because the cryofixation process prevents ice crystal formation and, therefore, preserves all structures in their native aqueous state. Immediate cryogenic freezing at specific times during the reaction cycle further ensures temporal integrity of the assemblies. For precursor 1 with fuel, colloids with a mean diameter of 300–400 nm were found (Fig. 3f), whereas precursor 2 showed the presence of long and entangled fibers with a uniform diameter of ~6 nm in response to fuel (Fig. 4f).

Limitations

This protocol is written for carboxylate precursor molecules, forming assemblies that include colloids and hydrogel-fiber networks. In our experience with chemically fueled assemblies, we found that the emerging materials' dynamic properties are highly dependent on the amino acid sequence of the precursor. For example, this protocol describes the formation of transient hydrogels formed by Fmoc-AAD-OH (2). We found that changing the amino acid sequence to Fmoc-AVD-OH resulted in solutions that would convert into a hydrogel upon fuel application. However, these hydrogels would remain kinetically trapped and would not revert to their initial solutions state³⁹.

We have also found that the reaction cycle is highly pH-dependent. The EDC activation reaction is most active at acidic pH⁵⁹, but the closer the pH is to the pK_a of the carboxylic acids, the higher is the degree of protonation. Upon protonation of the carboxylic acids, self-assembly of the precursor can be induced without the need of anhydride formation. In contrast, increasing the pH from 6.0 to 7.0 would be sufficient to decrease the yield of anhydride sufficiently that no hydrogel is formed for Fmoc-AAD-OH (2)³⁹.

Finally, the design of our experimental protocol aims at anhydride-based assemblies. Minor parts such as the quenching method or the kinetic model are tailored to this specific system. The major part, however, focuses on the study of the dynamic material's properties. These techniques are independent of a specific chemical functionality. As a result, e.g., the described webcam setup can be applied to other reported forms of out-of-equilibrium systems to screen initial conditions. In general, the protocol instructions can be adapted to dynamic materials that possess the required physical properties of the applied technique. Limitations like the ability to scatter light or the incorporation of a hydrophobic dye are mentioned in the procedures part of this protocol.

Materials

Reagents

! CAUTION Chemical reagents are potentially harmful. Apply the appropriate safety procedures. Wear gloves, a laboratory coat and safety glasses. Take care to appropriately dispose of all chemicals used.

- MES hydrate, 99.5% (Sigma-Aldrich, cat. no. M8250)
- NaOH (Sigma-Aldrich, cat. no. S5881-1KG) **! CAUTION** Sodium hydroxide is highly corrosive and can cause severe skin and eye damage. Wear the appropriate protective equipment when handling this reagent.
- HCl (Sigma-Aldrich, cat. no. 320331-500ML) **! CAUTION** Hydrogen chloride is highly corrosive and can cause severe skin and eye damage. Inhalation might lead to respiratory damage. Wear the appropriate protective equipment, and use a fume hood when handling this reagent.
- Fmoc-E-OH (Alfa Aesar, cat. no. H62936)
- EDC (Sigma-Aldrich, cat. no. 03450-5G) **! CAUTION** *N*-(3-dimethylaminopropyl)-*N'*-ethylcarbodiimide hydrochloride has acute oral (category 4) and skin (category 3) toxicity and can cause severe skin and eye damage. Wear the appropriate protective equipment, and use a fume hood when handling this reagent.
- Benzylamine (Sigma-Aldrich, cat. no. 77869-25ML) **! CAUTION** Benzylamine has acute oral (category 4) and skin (category 4) toxicity and can cause severe skin damage. Wear the appropriate protective equipment, and use a fume hood when handling this reagent.
- Acetonitrile, HPLC grade (Sigma-Aldrich, cat. no. 34851-2.5L) **! CAUTION** Acetonitrile is highly flammable, has respiratory (category 4), skin (category 4) and oral (category 4) toxicity and can cause severe eye irritation. Wear the appropriate protective equipment, and use a fume hood when handling this reagent.
- Dimethylformamide (DMF), for peptide synthesis (Sigma-Aldrich, cat. no. 1003972500) **! CAUTION** DMF is flammable and has reproductive (category 1), respiratory (category 4) and skin (category 4) toxicity. Wear the appropriate protective equipment, and use a fume hood when handling this reagent.
- Diisopropylcarbodiimide (DIC; Sigma-Aldrich, cat. no. D125407-25G) **! CAUTION** DIC has acute respiratory (category 2) toxicity and can cause severe eye damage. Wear the appropriate protective equipment, and use a fume hood when handling this reagent.
- Piperidine (Sigma-Aldrich, cat. no. 104094-100ML) **! CAUTION** Piperidine has acute oral (category 4), skin (category 3) and respiratory (category 3) toxicity and can cause severe skin and eye damage. Wear the appropriate protective equipment, and use a fume hood when handling this reagent.
- Oxyma Pure (Sigma-Aldrich, cat. no. 8510860100)
- Fmoc-L-Ala-OH (Sigma-Aldrich, cat. no. 531480-100G)
- Fmoc-L-Asp(OtBu)-Wang resin, loading 0.6–1.0 mmol/g, 100–200 mesh (Iris Biotech, cat. no. WAA11305.0005)
- 4-Dimethylaminopyridine, ReagentPlus (Sigma-Aldrich, cat. no. 107700-25G) **! CAUTION** 4-Dimethylaminopyridine has acute oral (category 2) and skin (category 3) toxicity and can cause skin and eye damage. Wear the appropriate protective equipment, and use a fume hood when handling this reagent.
- Dichloromethane (DCM), HPLC grade (Sigma-Aldrich, cat. no. 34856-1L) **! CAUTION** DCM can cause skin and eye damage and is suspected to be carcinogenic. Wear the appropriate protective equipment, and use a fume hood when handling this reagent.
- Triisopropylsilane (TIPS; Sigma-Aldrich, cat. no. 233781-50G) **! CAUTION** TIPS is flammable.
- Diethyl ether, anhydrous (Sigma-Aldrich, cat. no. 346136-1L) **! CAUTION** Diethyl ether has acute oral (category 4) toxicity and is highly flammable. Wear the appropriate protective equipment, and use a fume hood when handling this reagent.
- Trifluoroacetic acid (TFA, Sigma-Aldrich, cat. no. T6508-500ML) **! CAUTION** TFA has respiratory (category 4) toxicity. It is highly corrosive (category 1) and can cause severe skin and eye damage. It is hazardous to aquatic environments, with long-lasting effects. Wear the appropriate protective equipment, and use a fume hood when handling this reagent.
- Dry ice **! CAUTION** Dry ice is a deep-cold solid and can cause cold burns. Wear cryogenic gloves, and work in a ventilated room. Wear the appropriate protective equipment, and use a fume hood when handling this reagent.
- Liquid nitrogen **! CAUTION** Liquid nitrogen is a deep-cold liquid and can cause cold burns. Wear cryogenic gloves, and work in a ventilated room. Wear the appropriate protective equipment, and work in a fume hood.

- Liquid ethane **!CAUTION** Liquid ethane is a deep-cold liquid and can cause cold burns. Wear cryogenic gloves, and work in a ventilated room. Ethane is highly flammable. Wear appropriate protective equipment, and work in a fume hood.
- Potassium cyanide (KCN), BioUltra (Sigma-Aldrich, cat. no. 60178-25G) **!CAUTION** KCN has acute oral (category 2), skin (category 1) and respiratory (category 2) toxicity. It is hazardous to aquatic environments, with long-lasting effects. Wear appropriate protective equipment, and work in a fume hood. Do not dispose in acidic aqueous waste to prevent the formation of volatile hydrogen cyanide.
- Pyridine, anhydrous (Sigma-Aldrich, cat. no. 270970-100ML) **!CAUTION** Pyridine has acute oral (category 4), skin (category 4) and respiratory (category 4) toxicity. It is flammable and can cause eye damage. Wear appropriate protective equipment, and work in a fume hood.
- Ninhydrin, ACS grade (Sigma-Aldrich, cat. no. 151173-25G) **!CAUTION** Ninhydrin has acute oral (category 4) toxicity and can cause skin and eye irritations. Wear appropriate protective equipment, and work in a fume hood.
- N-butanol (Sigma-Aldrich, cat. no. B7906-500ML) **!CAUTION** N-butanol is flammable. It has acute oral toxicity (category 4) and can cause skin and severe eye damage. Wear appropriate protective equipment, and work in a fume hood.
- Phenol (Sigma-Aldrich, cat. no. P1037-100G) **!CAUTION** Phenol has acute oral (category 3), skin (category 3) and respiratory (category 3) toxicity. It can cause severe skin and eye damage. It shows germ cell mutagenicity, and it is hazardous to aquatic environments, with long-lasting effects. Wear appropriate protective equipment, and work in a fume hood.

Equipment

General equipment

- High-resolution balance (with a minimum resolution of 0.1 mg, VWR, cat. no. 611-2265)
- Glass bottles (250 ml, Schott, cat. no. 21 801 365)
- Magnetic stir bar and magnetic stirrer (VWR, cat. no. 444-0614)
- Volumetric flasks (250 ml, 50 ml, 5 ml, 2 ml, 1 ml, VWR)
- Conical centrifuge tube (50 ml, 15 ml, Carl Roth, cat. no. N462.1)
- Microcentrifuge tube (1.7 ml, Carl Roth, cat. no. 4182.1)
- Funnel (VWR, cat. no. 221-0175)
- Single-channel pipettes (1 ml to 0.5 μ l) and corresponding tips and wide bore tips (Eppendorf Research plus, cat. no. 3120000046)
- Glass HPLC vials (1.7 ml, Carl Roth, cat. no. XC64.1)
- Countdown timer (VWR, cat. no. 609-0226)
- Round-bottom flask (100 ml, VWR, cat. no. 201-1326)
- Glass sample vials with snap caps (5 ml, VWR, cat. no. MANA70271)
- Vortex mixer (IKA Vortex 2 8000, VWR, IKA A25000258)
- Liquid nitrogen dewar (VWR, cat. no. 478-4411)
- High-precision tweezers for microscopy (VWR, cat. no. 232-0143)

Peptide synthesis

- 50 ml peptide synthesis vessel for solid-phase peptide synthesis with a medium frit porosity (FengTecEx, cat. no. P120050M)
- Freezer (-30 °C)
- Flask shaker. For this study, we used the Stuart SF1 Flask Shaker (Sigma-Aldrich, cat. no. Z675245-1EA)
- Pressured nitrogen or air

Automated peptide synthesis

- For the automated synthesis, a microwave-assisted automated peptide synthesizer with a reaction vessel suitable for 20 ml batches is needed. For this study, we used a CEM Liberty Blue automated peptide synthesizer equipped with a Discovery Bio microwave module

Peptide purification

- Rotary evaporator. We used the Hei-VAP Core (VWR, 531-1111)
- Preparative HPLC setup capable of detecting and separating peptides. For this study, we used an Ultimate 3000 (Dionex/Thermo Fisher Scientific, cat. no. IQLAAAGABHFAPBMBFB) HPLC system with a Hypersil Gold, reversed-phase C_{18} column (particle size: 5 μ m, length: 250 mm, ID: 20 mm;

Thermo Fisher Scientific, cat. no. 25005-259270A) and an automated fraction collector (Thermo Fisher Scientific, cat. no. VF-F11-A-01)

- ESI-MS setup to detect peptides with an m/z value of 500. For this study, we used an LCQ Fleet Ion Trap Mass Spectrometer (Thermo Fisher Scientific) with an electrospray ionization source
- NMR setup to measure $^1\text{H-NMR}$ at 400 MHz. For this study, we used a Bruker AVNeo 400. Chemical shifts are reported as δ -values in ppm relative to the deuterated solvent peak: $(\text{CD}_3)_2\text{SO}$ (δH : 2.05). MestReNova is used to analyze the spectra
- Lyophilizer to dry the peptides. The lyophilizer should hold 50 ml conical centrifuge tubes. In this study, we used a Christ Freeze Dryer Alpha 2-4 LDplus (VWR, cat. no. 535-3157)

Nile red assay

- Fluorescence spectrometer. We used a Jasco (Jasco FP-8300) spectrofluorometer with external temperature control (Jasco MCB-100)
- Quartz cuvette (10 mm path length, Hellma, cat. no. HL100-10-40)

Kinetic measurements

- An analytical HPLC setup is used for separation and detection of the various compounds in the reaction cycle. The setup also determines the purity of the synthesized peptides. For this study, we used a Vanquish Duo (Thermo Fisher Scientific, cat. no. VF-S02-A-02) HPLC system with a Hypersil Gold, reversed-phase C_{18} column (particle size: 3 μm , length: 100 mm, ID: 2.1 mm, Thermo Fisher Scientific, cat. no. 25003-102130)

Webcam-based experiments

- Webcam with manual focus connected to a computer. For this study, we used a full HD 1080p 12.0 megapixel webcam. To record the time-lapse series, we used the software Webcam Time-lapse from TNL Enterprises
- Magnetic stirrer and lifting ramp (VWR, cat. no. 444-0614)
- Retort stand with a clamp to hold the camera
- USB-powered LED lights
- Carton box to adjust light conditions
- Double-sided sticky tape
- Paper/cardboard

UV-VIS measurements

- Quartz cuvette (1 mm path length, Hellma, cat. no. HL100-1-40)
- UV-VIS spectrophotometer to perform turbidity measurements. For this study, we used Multiskan Go Microplate Spectrophotometer (Thermo Fisher Scientific)

Rheology based experiments

- Research-grade macrorheometer with torque resolution in the sub-micro-Newton range, an appropriate detection limit of the angular deflection and a temperature control unit. Here we used an MCR302 (Anton Paar, Graz, Austria). P-PTD200/Air (Anton Paar, Graz, Austria) and PP25 (Anton Paar, Graz, Austria) were used as bottom plate and measuring head, respectively
- Plate/plate measuring setup with a minimum diameter of the measuring head of 25 mm
- Humidity trap

Confocal microscopy

- Confocal microscope capable of exciting and detecting Nile red stained samples. For this study, we used a Leica TCS SP8 Lightning Confocal Microscope equipped with a 552 nm continuous wave laser (solid-state laser 20 mW), an HC PL APO CS2 63 \times water immersion objective, and a hybrid detector (HyD).
- High-vacuum silicon grease (Carl Roth, cat. no. 0855.1)
- 5 ml disposable syringe (Carl Roth, cat. no. 0057.1)
- Glass microscope coverslips (thickness 1, 24 \times 60 mm, Carl Roth, cat. no. H878.2)
- Glass microscope coverslips (thickness 1, \varnothing 12 mm, Carl Roth, cat. no. P231.1)

Cryo-TEM microscopy

- Transmission electron microscope suitable for cryogenic samples. For this study, we used a Tecnai spirit, FEI/Thermo Fisher Scientific
- C-Flat 2/2 Cryo-EM Grid-Copper (400 grid mesh, 20 nm carbon thickness, ScienceServices, cat. no. ECFT-224C-50)
- Cryo-TEM grid box
- Paraffin film (VWR, cat. no. 291-0057)
- Microscope slide (thickness 1 mm, 76 × 26 mm, Carl Roth, cat. no. H869.1)
- EMS Glow discharger K100X
- A controlled environment vitrification system to prepare cryogenic samples for TEM. In this study, we used an FEI Vitrobot Mark IV (Thermo Fisher Scientific)
- Cryo-transfer-specimen holder (Gatan)

Software

- The processing of the recorded data from both confocal and cryo-TEM microscopy was done using ImageJ in combination with the Fiji distribution

Reagent setup

Preparation of reagents and stock solutions

For the preparation of the stock solutions, deionized water was used. We obtained the water from a Millipore Milli-Q laboratory water system.

200 mM MES pH 6.0

For the preparation of 250 ml MES buffer at 200 mM, dissolve 9.76 g MES hydrate in ~200 ml of water in a glass bottle equipped with a stir bar. After dissolution, transfer the bottle to a calibrated pH meter, and adjust the pH to 6.0 by titration with NaOH and HCl stock solutions. Pour the buffer solution into a 250 ml volumetric flask, and fill it up to the water calibration line. The pH should not have been changed by dilution, but it is worth a second control with the pH meter. The resulting buffer can be stored for weeks, but the pH should be checked occasionally. When a color change is observed, the buffer should be renewed. ▲ **CRITICAL** Take care of the temperature dependency of the pH, and use the temperature sensor while adjusting.

10 mM precursor stock solution of Fmoc-E-OH (1) for HPLC calibration

For the HPLC calibration of precursor **1**, we prepare a 1 ml solution in 200 mM MES with 10 mM of precursor **1**. Therefore, 3.7 mg of **1** is weighed in a 1 ml volumetric flask, and 200 mM MES pH 6.0 is added to the calibration line. There is no need to adjust the pH. ▲ **CRITICAL** Use buffered water instead of pure water to increase the solubility of **1**.

10 mM precursor stock solutions of Fmoc-E-OH (1) and Fmoc-AAD-OH (2) for kinetic analyses

The preparation of 5 ml stock solutions is sufficient to conduct the experiments described below. Weigh in 18.5 mg of precursor **1** in a 15 ml conical centrifuge tube. Similarly, 24.9 mg of **2** is weighed in a 15 ml conical centrifuge tube. Dissolve the solid in slightly less than 5 ml 200 mM MES pH 6.0. Then, transfer the solutions to a pH meter, and adjust the pH to 6.0 by titration with NaOH and HCl stock solutions. After pouring the solution into a 5 ml volumetric flask, add 200 mM MES pH 6 buffer solution up to the calibration line. The precursor stock solutions can be stored in conical centrifuge tubes for weeks in a refrigerator. ▲ **CRITICAL** The peptide synthesis typically yields low amounts of product. When doing kinetic experiments, the results can change for varying synthesis batches due to differing impurities. Therefore, better repeat the synthesis and combine the batches for the precursor stock solution preparation.

2.0 M EDC stock solution

We prepare 100 µL of a 2.0 M EDC stock solution by weighing in 38.3 mg of EDC in a 1.7 ml microcentrifuge tube. The solid is dissolved by adding 61.4 mg of water to yield a final volume of 100 µL. The water is added to the microcentrifuge tube and should be equal to the mass of 100 µL water, which is 99.7 mg. ▲ **CRITICAL** EDC reacts with water, albeit slowly. The EDC solutions should be prepared fresh right before the experiment.

PROTOCOL
NATURE PROTOCOLS
22 mM benzylamine stock solution in acetonitrile/H₂O (6%/94%)

A 22 mM benzylamine stock is prepared by weighing in 117.9 mg in a 50 ml volumetric flask. Dissolve the benzylamine by adding 3 ml acetonitrile. Finally, add water to a final volume of 50 ml. The stock solution can be stored in conical centrifuge tubes in the refrigerator for ~1 week. **▲ CRITICAL** Benzylamine reacts with air carbon dioxide, forming carbamic acid (white crusts around the bottleneck).

2.5 mM Nile red stock solution

A 2.5 mM Nile red stock solution is prepared by weighing in 7.96 mg of Nile red and subsequent dissolution in 10 ml of methanol. The stock solution can be stored for several weeks in a refrigerator when adequately sealed with parafilm.

Procedure
Synthesis of precursor Fmoc-AAD-OH (2)

1 The following describes the 0.5 mmol scale synthesis of **2** using (A) an automated peptide synthesizer or (B) manually using a peptide synthesis vessel. The yield and purity are equivalent.

(A) Automated solid-phase peptide synthesis

(i) **Preparation of amino acid solutions** (steps i–iii; Timing 1 h) In separate 50 ml centrifugal tubes, weigh in Fmoc-Ala-OH, Oxyma, DIC and piperidine. Afterwards, add DMF to dissolve the reagents. Find the required amounts for a 0.5 mmol batch of Fmoc-AAD-OH (**1**) in the table below.

▲ CRITICAL STEP For calculation, a dead volume in the peptide synthesizer tubing of 4 ml has been considered. When too little reagent solution is used, it may cause an error during the automated peptide synthesis.

! CAUTION DIC is flammable and highly toxic. Wear gloves and protective gear, and use a fume hood while working with DIC.

! CAUTION DMF is flammable and has suspected reproductive toxicity. Wear gloves and protective gear and use a fume hood while working DMF.

! CAUTION Piperidine has acute oral, skin and respiratory toxicity and can cause skin and eye damage. Wear appropriate protective equipment, and use a fume hood.

Compound	Concentration	Total volume	Amount
Fmoc-Ala-OH	0.20 M	44 ml	2.7 g
Oxyma	1.0 M	15 ml	2.1 g
DIC	0.50 M	20 ml	1.6 ml
Piperidine	20 vol%	60 ml	12 ml

(ii) For the solid support, weigh Fmoc-Asp(OtBu)-Wang resin (773 mg, 0.68 mmol/g, 1 eq.) in a 15 ml centrifugal tube to yield a total loading of 0.5 mmol.

▲ CRITICAL STEP Make sure to use resins with a mesh size recommended for the used peptide synthesizer. Using the wrong mesh size can damage the machine.

(iii) Add 10 ml of DMF to the resin, vortex it and allow it to swell for 10 min.

■ PAUSE POINT The prepared stock solutions can be stored for up to 1 week at room temperature (RT, 25 °C).

(iv) **Automated peptide coupling** (iv–vi, Timing 1 h) Mount the prepared stock solutions on the Liberty Blue peptide synthesizer at their respective positions, and add the resin to the reaction vessel.

(v) Empty the waste container, fill up the DMF solvent container and open the supply line for the peptide synthesizer's inert gas.

(vi) Switch on the peptide synthesizer, and start the synthesis protocol for Fmoc-AAD-OH (**2**). The coupling protocol we are using includes double deprotection and double coupling for each addition of amino acid. We list the procedures for deprotection, coupling and washing performed by the peptide synthesizer in the table below.

Step	Procedure	Action
1	Deprotection	(1) Add 10 ml piperidine (20% in DMF) (2) Run microwave at 205 W for 30 s (max temp. of 80 °C) (3) Run microwave at 50 W for 65 s (max temp. of 90 °C) (4) Drain reaction vessel
2	Wash	(1) Add 5 ml solvent (2) Drain reaction vessel
3	Deprotection	
4	Wash (3×)	
5	Coupling	(1) Add 10 ml of the amino acid (2) Add 4 ml DIC (3) Add 2 ml Oxyrna (4) Run microwave at 220 W for 35 s (max temp. of 85 °C) (5) Run microwave at 50 W for 120 s (max temp. of 90 °C) (6) Drain reaction vessel
6	Wash	
7	Coupling	
8	Wash (2×)	

? TROUBLESHOOTING

- (vii) **Workup** (vii–viii, Timing 30 min) After finishing all the steps, add 5 ml DMF to the reaction vessel. Carefully shake the reaction vessel to suspend the resin, and pour the DMF together with the resin in a peptide vessel. Repeat this step two times.
- (viii) Filter off the DMF, and wash the resin three times with DCM. Use pressured air to speed up the filtration and to dry the resin.

! CAUTION DCM is flammable and suspected to be carcinogenic. Wear gloves and protective gear, and use a fume hood while working with DCM.

■ PAUSE POINT The resin can be stored for up to 1 month in the freezer at –20 °C.

(B) Manual solid-phase peptide synthesis

▲ CRITICAL The peptide synthesis (from step v) is explained for Fmoc-AAD-OH (2) but can be performed in a similar way for other sequences.

- (i) **Preparation of stock solutions for the Kaiser test** (steps i–iii, Timing 30 min) Dissolve 16.5 mg KCN in 25 ml water. Dilute 1 ml of this aqueous KCN solution with 49 ml of pyridine.

! CAUTION KCN is highly toxic. Wear gloves and protective gear, and use a fume hood while working with KCN. Highly toxic hydrogen cyanide forms when acidifying the solution.

! CAUTION Pyridine is flammable and toxic. Wear gloves and protective gear, and use a fume hood while working with pyridine.

- (ii) Dissolve 1 g of ninhydrin in 20 ml of n-butanol.

! CAUTION Ninhydrin is toxic and can cause skin and eye irritations. Wear appropriate protective equipment, and use a fume hood.

- (iii) Dissolve 40 g of phenol in 20 ml of n-butanol.

! CAUTION Phenol is toxic and can cause severe skin and eye damage. It shows germ cell mutagenicity, and it is hazardous to aquatic environments, with long-lasting effects. Wear appropriate protective equipment, and use a fume hood.

■ PAUSE POINT The stock solutions for the Kaiser test can be stored for up to 1 month at RT.

- (iv) **Stock solutions for the peptide coupling reactions** (step iv, Timing 30 min) Weigh in Fmoc-Ala-OH, Oxyrna, DIC and piperidine in a 50 ml conical centrifuge tube each, and dissolve them in DMF by the help of vortexing. Find the corresponding amounts for the synthesis of 0.5 mmol Fmoc-AAD-OH (2) in the table below.

Compound	Concentration	Total volume	Amount
Fmoc-Ala-OH	0.20 M	33 ml	2.1 g
Oxyrna	1.0 M	10 ml	2.1 g
DIC	0.50 M	15 ml	1.6 ml
Piperidine	20 vol%	50 ml	12 ml

PROTOCOL

NATURE PROTOCOLS

- (v) **Peptide coupling reactions** (steps v–xvii, Timing 5 h) Add Fmoc-Asp(OtBu)-Wang resin (773 mg, 0.68 mmol/g loading, 1 eq.) with a total loading of 0.5 mmol into a 50 ml peptide vessel, and swell the resin in 20 ml DMF for 20 min. Use the shaker to accelerate the swelling.
- (vi) Remove the solution by filtration through the frit with the assistance of a nitrogen gas flow.
- (vii) To remove the Fmoc protection group, add 10 ml of 20 vol% piperidine to the resin and shake it for 15 min.
 - ▲ **CRITICAL STEP** Do not let it react for more than 20 min to avoid epimerization of the last amino acid.
- (viii) Remove the solution by filtration through the frit with the assistance of a nitrogen gas flow.
- (ix) Wash the resin with 5 ml DMF three times.
- (x) To perform the Kaiser test as a reaction control, transfer a small number of resin beads (less than 20 beads is sufficient) into a 5 ml glass sample vial.
- (xi) Add one drop of the KCN, ninhydrin and phenol solutions (prepared in steps i–iii).
- (xii) Carefully heat the tube to 100 °C for a few seconds with a heat gun. A blue coloration of the beads and the solution indicates a successful deprotection.
 - ? **TROUBLESHOOTING**
- (xiii) For the coupling of the next amino acid, add 10 ml of the 0.2 M Fmoc-Ala-OH solution (5 eq.), 2 ml of the 1.0 M Oxyma solution (5 eq.) and 4 ml of the 0.5 M DIC solution (5 eq.) to a 50 ml conical centrifuge tube, and mix the solutions. Add the solution to the resin in the peptide vessel, and agitate it for 1 h at RT.
- (xiv) Remove the solution by filtration through the frit with the assistance of a nitrogen gas flow.
- (xv) Wash the resin with 5 ml DMF three times.
- (xvi) Confirm the successful coupling with the Kaiser test (steps x–xii). The absence of a blue coloration of the beads and solution indicates a complete coupling.
 - ? **TROUBLESHOOTING**
- (xvii) Repeat steps vii–xvi for the deprotection and the coupling of the second Fmoc-Ala-OH amino acid.
 - **PAUSE POINT** The resin can be stored for up to 1 month in the freezer at –20 °C.

Microcleavage as reaction control ● Timing 2 h

▲ **CRITICAL** We perform microcleavage after completing the synthesis to check the quality of the product. However, it can also be performed at any step during the synthesis to test if unexpected errors occurred.

- 2 Take a small amount of the resin (one spatula tip), and transfer it into a peptide vessel. Add 0.95 ml of TFA, 0.025 ml of TIPS and 0.025 ml of water.
 - ! **CAUTION** TFA is toxic and highly corrosive. Wear gloves and protective gear, and use a fume hood while working with TFA.
- 3 Agitate the peptide vessel for 1 h at RT.
- 4 Collect the deprotection solution in a 25 ml round-bottom flask by filtering it through the frit with a nitrogen gas flow assistance. Wash the resin once with DCM.
- 5 Remove the DCM under reduced pressure (850 mbar at 40 °C). Remove the TFA by coevaporation with 5 ml of diethyl ether under reduced pressure. Start to remove diethyl ether at 850 mbar and 40 °C until no more condensate is observed. Reduce the pressure slowly to 40 mbar, and wait for 15 min. Repeat the coevaporation procedure (roughly three times) until almost no liquid is left.
- 6 Add 1 ml of a water:acetonitrile 60:40 vol/vol mixture, and dissolve the residue.
- 7 Filter the residue with a syringe filter, and dispense the filtrate in an HPLC vial.
- 8 Analyze the presence and purity of the peptide by HPLC and ESI-MS. Perform an analytical HPLC run, and detect the compounds at 254 nm. At this wavelength, the Fmoc group dominates the absorption of the peptide. The number of signals and their proportion offer a first estimation about the product purity (Fig. 9). ESI-MS analysis qualitatively confirms the successful synthesis. An analytical dataset is listed in Step 21.
 - ? **TROUBLESHOOTING**

Peptide deprotection and cleavage from the resin ● Timing 3 h

- 9 To deprotect and cleave the peptide off the resin, we use a solution of TFA. Add 9.5 ml of TFA, 0.25 ml of TIPS and 0.25 ml of water to a 15 ml conical centrifuge tube and shake the solution.
- 10 Add the cleavage solution to the resin in the peptide vessel, and close the vessel with the corresponding cap. Shake the peptide vessel for 1 h.

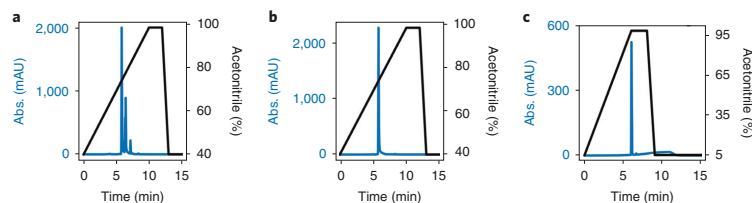


Fig. 9 | HPLC chromatograms of precursor Fmoc-AAD-OH (2) after purification detected at 254 nm and the applied pump gradient. a, The preparative HPLC chromatogram shows a synthesis approach yielding several side products, most likely caused by an old piperidine stock solution. **b,** A preparative HPLC chromatogram of a successful synthesis with only one observed product peak with high intensity. **c,** Analytical HPLC chromatogram to estimate the product purity. The peptide's purity is given by the proportion of the product integral compared with the combined integrals of all signals detected (product and impurities). The purity is determined to be 98% in the example shown.

- 11 Collect the deprotection solution in a 100 ml round-bottom flask by filtering it through the peptide vessel's frit with the assistance of a nitrogen gas flow. Wash the resin three times with DCM, and combine it with the deprotection solution.
- 12 Remove DCM and TFA as described in Step 5.
 - ▲ **CRITICAL STEP** Use a dry ice cooling trap to prevent damage of the vacuum pump due to corrosion by TFA.
 - ▲ **CRITICAL STEP** Do not store the peptide in concentrated TFA to prevent decomposition.

Preparative HPLC purification ● Timing 6 h

▲ **CRITICAL** The preferred method to purify the peptide is by reversed-phase HPLC with C_{18} as a stationary phase. We detect the compounds formed by absorption at 220 and 254 nm. The absorption at 254 nm is characteristic for the Fmoc-protected peptides and makes it easy to distinguish them from other side products. Detection at 220 nm gives an overview of further reaction products. Fractions are collected depending on the absorption at 254 nm with a start and end threshold of 15 mAU. As eluent, we used a mixture of water with 0.1 vol.% TFA and acetonitrile with 0.1 vol.% TFA. The eluents are degassed in a sonication bath for 30 min prior to use. A linear gradient of 40% acetonitrile to 98% acetonitrile over 10 min was applied at a flow rate of 20 ml/min, resulting in the successful separation of all reaction products (Fig. 9a,b). If the separation is not sufficient, the gradient can be prolonged to 20 or 30 min. The high acetonitrile content was maintained for 2 min to elute all compounds completely, and afterwards the starting condition was reset within 1 min. A final equilibration of 2 min resulted in a total runtime of 15 min per injection.

- 13 Dissolve the residual solution in 20 ml of a water:acetonitrile 60:40 vol/vol solution. Filter the solution with a polytetrafluoroethylene syringe filter (pore size 0.45 μ m).
 - ▲ **CRITICAL STEP** Different filters may be used, but make sure the filter material is resistant to acetonitrile.
- 14 Perform the first purification by using only 0.5 ml of the reaction solution. Check whether the separation is sufficient to collect individual peaks and whether the detector is not saturated.
 - ▲ **CRITICAL STEP** A saturation of the detector can indicate a saturation of the stationary column phase, resulting in lower separation efficiency.
- 15 Analyze the peaks with the highest intensity at 254 nm by ESI-MS to verify the product peak.
- 16 For the subsequent runs, the amount of injected peptide solution can be gradually increased to reduce the total number of injections required. However, ensure that the peaks for the product do not start to overlap. Typically, 2–3 ml are injected, but the injection volume depends on the product concentration and the number of impurities. To reduce the collected fractions of unwanted side products with a low absorption at 254 nm, the threshold for peak collection at 254 nm can be increased. If the absorbance of side products is similarly high as the product peak, the collection can be done depending on the retention time instead of the absorbance.
- 17 According to the absorbance, combine all fractions that contain exclusively the product peak in a round-bottom flask. Additionally, combine in a separate round-bottom flask all fractions that partially contain the product peak. These fractions can be combined with the main product after analysis if they are of equal purity.

PROTOCOL
NATURE PROTOCOLS

- 18 Remove the acetonitrile of the combined solutions under reduced pressure.
- 19 Transfer the remaining water solutions to 50 ml conical centrifuge tubes, and freeze them in liquid nitrogen.
- ! CAUTION** Skin contact with liquid nitrogen leads to cold burn. Wear cryo gloves, safety glasses and a laboratory coat.
- ? TROUBLESHOOTING**
- 20 Lyophilize the samples (2–3 d).
- 21 Perform analytical HPLC, ESI-MS (positive mode) and ¹H NMR analysis. Check that the product has the following analytical data before continuing with the procedure.
- ¹H-NMR (400 MHz, DMSO-d₆): δ/ppm 8.10 (d, *J* = 8.0 Hz, 1H), 7.99 (d, *J* = 7.6 Hz, 1H), 7.90 (d, *J* = 7.6 Hz, 2H), 7.73 (t, *J* = 7.2 Hz, 2H), 7.52 (d, *J* = 7.7 Hz, 1H), 7.42 (t, *J* = 7.4 Hz, 2H), 7.34 (t, *J* = 7.4 Hz, 2H), 4.57–4.48 (m, 1H), 4.27 (td, *J* = 17.8, 6.9 Hz, 4H), 4.06 (d, *J* = 7.1 Hz, 1H), 2.72–2.55 (m, 2H), 1.28–1.17 (m, 6H).
- ESI-MS: Fmoc-AAD-OH *m/z* calc.: 498.18 [M + H]⁺, 520.17 [M + Na]⁺, 536.14 [M + K]⁺, found: 487.93 [M + H]⁺, 520.27 [M + Na]⁺, 536.07 [M + K]⁺.
- Analytical HPLC: gradient of acetonitrile:water (vol:vol) from 5:95 to 98:2 within 6 min and detection at 220 and 254 nm. Fmoc-AAD-OH (**2**) retention time 6.0 min.
- 22 The purity of the synthesized peptide can be estimated by integrating the signals in an analytical HPLC chromatogram (Fig. 9c). We typically obtain precursor **2** with a yield of 50% (122 mg) and a purity of 98% as a solid white powder.

Nile red assay

- ▲ CRITICAL** For most precursors in dynamic self-assembly, there will be a concentration at which supramolecular structures will form directly from the precursor state. The critical aggregation concentration, which is determined by a Nile red assay⁶⁰, marks the upper limit at which concentration the precursor should be applied in the later-described fueling experiments ● **Timing** 2 h
- 23 Prepare 15 mM stock solutions of Fmoc-E-OH (**1**) and/or Fmoc-AAD-OH (**2**) by weighing in 11.1 mg and 14.9 mg of **1** and **2**, respectively. Transfer the compounds to a 2 ml volumetric flask, and dissolve them with 0.2 M MES pH 6.0.
- ▲ CRITICAL STEP** There is no need to adjust the pH since the fluorescence is unaffected by pH between 4.5 and 8.5⁵⁴.
- 24 Set up a dilution row (from 15 mM to 2.5 mM) by mixing the stock solution with 0.2 M MES pH 6.0 inside microcentrifuge tubes. A final volume of 200 μl works well.
- 25 Prepare the 2.5 mM Nile red solution as described in 'Reagent setup'.
- 26 Add 0.4 μl of the Nile red solution to each centrifuge tube, and incubate the probe for 30 min in dark.
- ▲ CRITICAL STEP** The dye should be added at low concentrations (<10 μM); higher concentrations may result in aggregation or self-quenching effects.
- 27 Transfer the solution to a quartz cuvette, and measure the fluorescence intensities at 635 nm when exciting the probes at 550 nm.
- 28 Plot the measured intensities against the applied precursor concentrations (Fig. 10a,b).

Kinetic analysis by HPLC

- ▲ CRITICAL** For the kinetic analysis, we require calibration values for the applied precursor molecules and the chemical fuel. Both precursors Fmoc-E-OH (**1**) and Fmoc-AAD-OH (**2**) bear the large Fmoc-protecting group with a characteristic absorption at 254 nm. Since no other functional groups contribute substantially to the absorption, we use the calibration of **1** as a measure for **2** and the corresponding benzyl amides. The chemical fuel EDC is calibrated at 220 nm ● **Timing** Steps 29–34, 2 h; Step 35, 15 h automated HPLC measurement time

Setup and calibration

- 29 Create an HPLC method by defining the flowrate, pump gradient and detection wavelength. In our study, we used relatively short columns with a length of 100 mm. Thus, we applied a relatively low flow rate of 0.4 ml/min. We used the eluent 0.1% TFA in acetonitrile mixed with 0.1% TFA in water. The starting mixture was 2% acetonitrile, whose content increases up to 98% within 14 min. The high acetonitrile content was maintained for 3 min to elute all compounds completely, and afterwards the starting condition was reset within 1 min. Finally, the column was equilibrated for

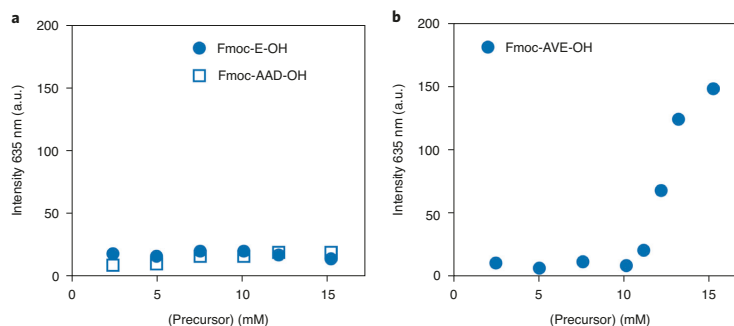


Fig. 10 | Nile red fluorescence intensity at 635 nm against concentration of the precursor. The intensity of the solvatochromic dye serves as an indication for self-assembly. **a**, No increase in fluorescence intensity of Nile Red is observed for concentrations <15 mM concerning precursor **1** and **2**. **b**, An example of a positive result of the Nile red assay. A sharp increase of the fluorescence intensity >10 mM of the more hydrophobic precursor Fmoc-AVE-OH indicates the formation of assemblies without EDC.

6 min at the original 2% acetonitrile in water. The detection was set to 220 nm and 254 nm at a data collection rate of 2.0 Hz.

▲ CRITICAL STEP TFA was added to the acetonitrile and water to improve the resolution as partial deprotonation of carboxylic groups is prevented at low pH.

- Prepare in triplicate 1 ml stock solutions of **1** in 0.2 M MES pH 6 as described above. Create a dilution series starting from 10 mM and diluting down at 2 mM (10 mM, 8 mM, 6 mM ... 0 mM). Typically, we prepare sample volumes of 100 μ l in total. The resulting samples are further diluted 1:10 by the addition of 900 μ l buffer.

▲ CRITICAL STEP The 1:10 dilution allows for higher injection volumes and removes the need for HPLC vial inserts, improving data quality.

- Prepare 2.0 M EDC stock solutions in triplicate, as described above.

? TROUBLESHOOTING

- Dilute the 2.0 M EDC stock to a final concentration of 100 mM by adding 285 μ l water to 15 μ l of 2.0 M EDC.

- Set up a dilution row in triplicate as described in Step 30, starting from 100 mM and pipetting 20 mM intervals.

▲ CRITICAL STEP Prepare the EDC dilution row last, and use water instead of buffer to minimize hydrolysis.

- Transfer the HPLC vials into the autosampler chamber.

- Create an injection sequence at the HPLC. Apply the method created in Step 29. Consider that EDC reacts slowly with water and should thus be analyzed first. We used an injection volume of 1 μ l. However, the injection volume can be increased depending on the sensitivity of the HPLC detector. Start the sequence.

▲ CRITICAL STEP The retention of the EDC is low on C₁₈ columns. Start the gradient with a low percentage of acetonitrile (2%) to separate the EDC signal from the injection peak. If separation fails, the usage of longer columns increases the retention time.

▲ CRITICAL STEP When changing the solvent composition at the HPLC for the first injection, make sure to equilibrate the column with the new composition for around ten column volumes. At the applied settings, an equilibration time of 6 min is required.

? TROUBLESHOOTING

- Integrate the peaks in each chromatogram for the peaks of EDC and **1**. Import the data in a data processing software. The mean area in mAU \times min is plotted together with the standard deviation against the concentration injected (Fig. 11a,b). Then, the calibration value is calculated by the slope of the linear regression.

? TROUBLESHOOTING

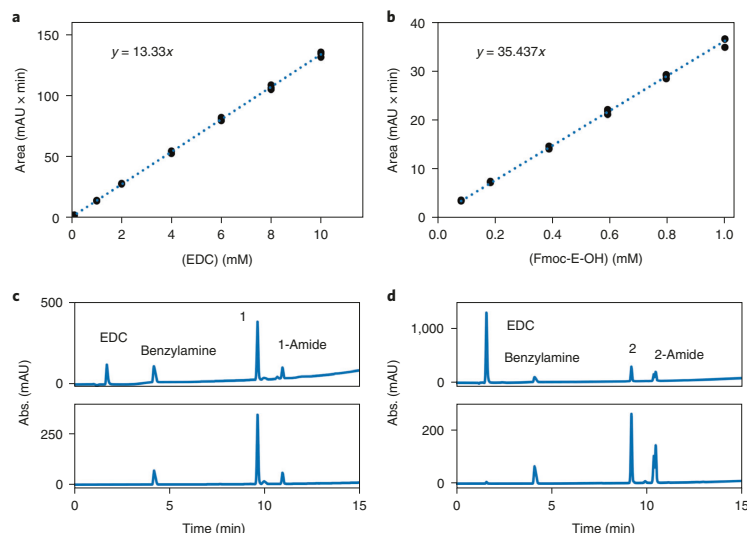
PROTOCOL
NATURE PROTOCOLS


Fig. 11 | Calibration curves. **a, b.** The curves shown are of EDC (**a**) and precursor Fmoc-E-OH (**1**) (**b**) as measured at 254 nm. The markers represent HPLC data of injecting several concentrations in triplicate. The dotted line shows the linear regression of the experimental data and provides the calibration value given by the line equation. **c, d.** The chromatograms show the quenched reaction cycle of Fmoc-E-OH (**1**) (**c**) and Fmoc-AAD-OH (**2**) (**d**). The upper boxes show the retention profiles as detected at 220 nm, whereas the boxes below show the profiles recorded at 254 nm.

Kinetic analysis of the reaction cycle

▲ **CRITICAL** After the calibration values have been obtained, a kinetic analysis of the reaction cycle is started. The evolution of the reaction cycle's components is monitored for 120 min

● **Timing** Steps 37–44, 6 h; Step 45, 12 h automated HPLC measurement time

37 Prepare the benzylamine, EDC and corresponding precursor solution as described in 'Reagent setup'.

? **TROUBLESHOOTING**

38 For each datapoint in the time series, pipette 450 μ l of the benzylamine solution in an HPLC vial.

▲ **CRITICAL STEP** Close each vial after pipetting to prevent evaporation of the solvent.

39 Prepare three HPLC vials for the actual reaction cycle by adding 995 μ l of the Fmoc-E-OH (**1**) stock solution to each vial. For Fmoc-AAD-OH (**2**), 950 μ l of the stock solution should be added.

40 Start the reaction cycle by adding 5 μ l of the 2.0 M EDC stock solution to the first vial containing **1** (50 μ l of the 2.0 M EDC to precursor **2**), and start the timer. Fuel the remaining two vials with a delay of 20 s.

▲ **CRITICAL STEP** Be aware of adequate mixing of the EDC and precursor solution by pipetting the solution up and down.

▲ **CRITICAL STEP** The dilution factor of the precursor solution should not exceed 5% when EDC is added; otherwise, the precursor concentration differs too much from the applied concentration.

41 Quench the reaction cycle at the planned time points. Start with the first vial activated by removing 50 μ l of the reaction mixture, and add it to a vial with the quenching solution prepared in Step 38. Mix the solution by pipetting it up and down, which aids the dissolution of the assemblies. Quench the remaining two samples of the triplicate datapoint, which were started with a delay of 20 s and 40 s.

▲ **CRITICAL STEP** To accurately determine the anhydride concentration by means of the formed amide, the transformation should be complete and should outcompete the hydrolysis reaction. As a test, dissolve a definite amount of synthesized anhydride in acetonitrile and dilute with the quenching solution. Inject the sample into the HPLC right after dilution. The measured amide should equal the anhydride weighed in, and no acid signal should appear in the chromatogram.

? **TROUBLESHOOTING**

- 42 Store the quenched samples at 4–8 °C.
▲ **CRITICAL STEP** Do not store the samples longer than 12 h; at longer time periods, the Fmoc deprotection reaction will start to affect the reliability of the measurements (Extended Data Fig. 2a,b)⁵⁶.
- 43 Repeat Steps 41 and 42 for the remaining samples at the planned time intervals until the cycle is finished.
? **TROUBLESHOOTING**
- 44 Program the HPLC injection sequence as described in Step 29. Set the injection volume to 1 μ l. Additionally, set the autosampler temperature to 8 °C to reduce side reactions.
- 45 Transfer the samples to the HPLC autosampler, and start the analysis sequence programmed in the step before. This step takes 7 h; this timing is mainly dependent on the components' retention time on the HPLC column.
- 46 The obtained chromatograms show four peaks corresponding to the EDC, the benzylamine, the precursor **1** or **2**, and their corresponding benzylamide (Fig. 11c,d). Over time, the EDC peak decreases, the precursor peak initially decreases but then returns to its original level, and the benzylamide follows the opposite trend.
▲ **CRITICAL STEP** To align the signals correctly, compare the retention times with the previously performed calibration experiments. In addition to that, the signals should be collected after detection and analyzed by ESI-MS.
? **TROUBLESHOOTING**
- 47 Calculate the area under the EDC and amide signals (at 220 nm and 254 nm, respectively) by integration.
- 48 Convert the values of the area into concentration by applying the corresponding calibration factors.
▲ **CRITICAL STEP** Determine the concentration of anhydride during the reaction cycle by calculating the concentration of the corresponding amide.
▲ **CRITICAL STEP** The dilution factor when adding the quenching solution must be considered to obtain the concentrations during the reaction cycle. Regarding the described 1:10 dilution, a multiplication by a factor of 10 is required.
- 49 Plot the EDC and anhydride concentration against the time the reaction cycle was quenched (Fig. 2).

Using a kinetic model in MATLAB

- ▲ **CRITICAL** We use a kinetic model written in MATLAB to predict the concentrations in the reaction cycle throughout our experiments. A download link for the model is provided in the supplementary information. The rate constants are determined by fitting the experimental concentration curves of EDC and anhydride obtained from HPLC measurements. The relevant reactions are the hydration of EDC (k_0), the second-order activation reaction (k_1), the transformation into a cyclic anhydride (k_2), the hydrolysis of the O-acylisourea intermediate (k_3) and, finally, the hydrolysis of the anhydride (k_4) ● **Timing 2 h**
- 50 Create a new folder, and rename it 'Model'.
 - 51 Create a folder within 'Model', and name it 'Data'.
 - 52 Open a basic text editor, and create and save the experimental datasets obtained by HPLC as comma-separated text files (.dat). For each kinetic experiment, three files should be created, i.e., time.dat, anhydride.dat and edc.dat. Each of these files should contain the data in a row with the datapoints separated by commas. The units of the data should be in min for time and mM for concentration. It is important that each file contains the same number of data points. Exemplary files can be downloaded from GitHub.
 - 53 Download our MATLAB script 'kinetic_model.m' from the supporting, and save it in the 'Model' folder.
 - 54 The main script 'kinetic_model' contains variables (lines 6–17) that are varied depending on the reaction conditions and the different precursors used. Set the time variable 't' to the time frame of the experiment in minutes.
 - 55 Set the variable 'Acid' and 'Fuel' to the precursor and fuel concentration in mM used in the experiment.
 - 56 Assign the reaction rate constant ' k_0 ' to the value 0.0000135 for reactions in 0.2 M MES buffer pH 6.0³⁹.
 - 57 Set the 'feedback' variable to 1 or 0, depending on whether self-protection of the assemblies is expected or not. We showed that anhydrides that form colloids, such as Fmoc-E-OH (**1**), protect the anhydride from hydrolysis by water⁴². Only the fraction anhydride in solution hydrolyzes. The fraction that remains in solution is defined as the variable 'solubility' and has to be set as well.

PROTOCOL
NATURE PROTOCOLS

For the anhydride of Fmoc-E (1) in 200 mM MES, that value is 0.4 mM. In the calculations, the model switches from pseudo first-order hydrolyses of the anhydride to zero-order hydrolysis when the concentration anhydride reaches a value above the solubility. The feedback variable is set to 0 for hydrogel-forming precursors such as Fmoc-AAD-OH (2).

- 58 Start the fitting process by finding the best fit for the decay of the EDC concentration. This concentration is only affected by the direct hydration (k_0) and the reaction with precursor (k_1). The direct hydration was entered in the Step 56. The decay curve can thus be fitted by varying k_1 . For our dataset, k_1 for precursor 1 was set at 0.037 and for precursor 2 at 0.11.
- 59 Fit the evolution of the anhydride by varying the rate constants k_2 , k_3 and k_4 . k_2 is the first-order conversion of the O-acylurea to the anhydride. Because we cannot detect the O-acylisourea, we know that k_2 has to be higher than k_1 . Therefore, we describe k_2 as a factor of k_1 (in the case of Fmoc-E (1) and Fmoc-AAD (2) $4 \times k_1$). Similarly, we set the second-order k_3 as a factor of k_1 (in the case of Fmoc-E (1), $0.01 \times k_1$ and Fmoc-AAD (2) $2 \times k_1$). k_4 is the anhydride hydrolysis and is set to 0.0048 for Fmoc-E (1) and 0.009 for Fmoc-AAD (2).

Time-lapse photography ● Timing Steps 60–65, 30 min; Steps 66–70, 1.5 h measurement time

- 60 Put an elevated flat surface like a magnetic stirrer or a lifting platform on the laboratory bench as a sample holder. Ensure that the surface is level.
- ▲ **CRITICAL STEP** Set the webcam up in an air-conditioned room with a constant temperature to avoid nonreproducible results due to, e.g., temperature changes during day and night.
- 61 Behind the sample holder, install a black sheet of paper glued to a flat piece of cardboard.
- ▲ **CRITICAL STEP** Other colors are possible, but a black background gives the best contrast for the turbid solutions.
- 62 Stick a strip of double-sided sticky tape to the flat and leveled sample holder, ~1 cm in front of the background (Fig. 8b). The sticky tape will prevent the samples from falling or moving during the time lapse. Alternatively, use a stand to place the samples.
- 63 Install the retort stand in front of the sample holder. Use a clamp to hold the webcam in place. Adjust the webcam to get a focused image with centered samples. Alternatively, use a tripod for the webcam.
- 64 Prepare the samples.
- For Fmoc-E-OH (1), use four 1.7 ml HPLC vials, and pipette 1 ml of the 10 mM stock solution of 1 into it.
 - For Fmoc-AAD-OH (2), take a 1.7 ml HPLC vial, and pipette 400 μ l of the 10 mM Fmoc-AAD-OH (2) stock solution into it.
- ▲ **CRITICAL STEP** Do not use smaller vials for hydrogel-forming precursors like 2. The increased wall-surface area to volume may lead to false-positive results in the inverted tube test because of increasing capillary forces.
- 65 Position the samples, and adjust the lighting, background and webcam by checking the quality of the shots.
- 66 Start the imaging with the time-lapse software, and save the images with a time stamp. We recommend a time interval of 1 min between image acquisitions.
- ▲ **CRITICAL STEP** After 5 min, check the focus of the webcam and readjust it if necessary. The focus can drift as the camera is warming up during image acquisition.
- 67 Start the reaction cycle by the addition of EDC.
- (A) For Fmoc-E-OH (1), add EDC to the samples according to the table below. Mix the samples by pipetting the solution up and down five times. Close the vials.

[EDC]	6.0 mM	8.0 mM	10 mM	12 mM
2 M EDC stock	3.0 μ l	4.0 μ l	5.0 μ l	6.0 μ l

- (B) For Fmoc-AAD-OH (2), add 20 μ l of a 2.0 M EDC stock solution to the sample to get a final concentration of 100 mM EDC. Mix the sample by pipetting the solution up and down five times. Close the vials. After 5 min, invert the vial on its cap for the inverted tube test.
- 68 Place a large cardboard box over the entire setup to avoid changes in the illumination conditions, e.g., due to sunset or reflections.

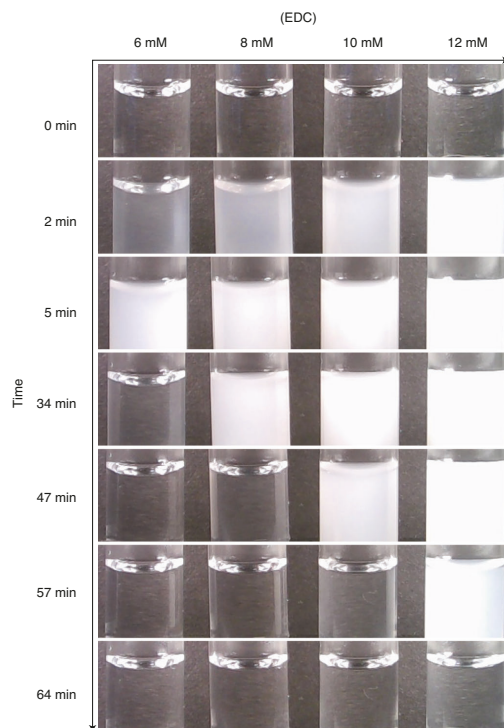


Fig. 12 | Time-lapse series of photographs shows the activation of 10 mM Fmoc-E-OH (1) with several amounts of EDC. An increase in fuel concentration results in a longer persistence of the assemblies. We show the photographs directly after the addition of fuel (0 min) and 2 min and 5 min after fuel addition. From there on, we show the timepoints after a sample has reached transparency (34, 47, 57 and 64 min).

- 69 After the reaction cycle is completed, determine the assemblies' lifetime for each fuel concentration according to the time the turbidity is depleted.
- 70 Present the data as photographs, indicating the amounts of fuel added and the timepoints when taking the image (Figs. 3a, 4a and 12).

UV-VIS measurement

▲ CRITICAL In UV-VIS spectroscopy, it is important that the absorption values are not much higher than one absorbance unit. At high concentrations, the response of the instrument is nonlinear, because insufficient light reaches the detector. Given Lambert-Beer's law, the extinction can be tuned by the path length of the light penetrating the sample. For precursor Fmoc-E-OH (1), a 1 mm quartz cuvette gave good results ● **Timing** Steps 71–73, 1 h; Steps 74–75, 2 h measurement time

- 71 A kinetic loop is programmed by the plate reader software, recording the absorbance of light at 600 nm at predetermined times. We estimate the length of the experiment by webcam experiments done beforehand. In the described experiment, we measured the absorbance every 30 s for 100 min.
- 72 A baseline is recorded, which is subtracted from the later fueled samples. Load the cuvette with 300 μ l of the Fmoc-E-OH (1) stock solution, and monitor the baseline for \sim 10 min.
- 73 Then, prepare a 1.7 ml microcentrifuge tube with 300 μ l of the Fmoc-E-OH (1) stock solution, and start the reaction cycle by adding 1.5 μ l of the 2.0 M EDC stock solution. After mixing thoroughly, transfer the reaction mixture into the quartz cuvette and load the plate

reader's chamber. Start the measurement, and continue recording until the absorption reached its starting value.

▲ CRITICAL STEP The choice of the sample container can influence the data quality (Extended Data Fig. 3a,b).

- 74 Repeat Step 73 for various EDC concentrations by changing the volume of the EDC stock solution added.
- 75 Subtract the calculated mean baseline value from the obtained absorbance values. Then, plot the absorbance over time (Fig. 3b).

? TROUBLESHOOTING

Correlation with the kinetic model

▲ CRITICAL For a better understanding of the self-assembly process, we correlated the turbidity to the anhydride concentrations obtained by the kinetic model.

- 76 We used a threshold value of 0.01 absorbance units to define when assemblies were present or not. We determined when the solution passed through this threshold to determine when the assemblies had dissolved and plotted these timepoints against the amount EDC added (Fig. 3c).
- 77 Using the kinetic model, we calculated the concentrations of anhydride product when the assemblies had dissolved. This concentration was considered the solubility and was determined for several amounts of EDC added.
- 78 Determine the time point when the anhydride concentration passes below its solubility using the kinetic model for various EDC concentrations. The results are added to the graph drawn in Step 76 (Fig. 3c).

Rheological characterization

▲ CRITICAL We conduct rheological measurements to determine the time-dependent viscoelastic properties of the precursor **2** in response to EDC. A research-grade shear rheometer was used, applying a plate/plate measuring setup ● **Timing** Steps 79–84, 30 min; Step 85, 1 h measurement time

- 79 Make sure the device is heated up, i.e., switch the rheometer 'ON' at least 30 min before conducting the experiments.
- 80 Mount the bottom plate, and insert the measuring head into the device. Install a humidity trap, and switch on the temperature control (here, $T = 25\text{ °C}$) to allow for equilibration.
- 81 Initialize the setup by performing the following preset calibration protocols in the correct order, and check for success by running a blank.
- (1) Set zero gap (determines the distance between the bottom plate and measuring head)
 - (2) Motor adjustment (ensures the angular deflection is determined correctly)
 - (3) Determine inertia of the measuring head
- 82 Prepare a measuring protocol for oscillatory shear measurements. Set the measuring gap to $d = 300\text{ }\mu\text{m}$. The oscillating frequency should be fixed to a value of 1 Hz and the shear deformation to $\gamma = 1\%$ as, at those values, linear material response can be expected

▲ CRITICAL Always measure with the same gap size to allow for comparison.

? TROUBLESHOOTING

- 83 Start the measurement by lowering the measuring head to an appropriate loading position. As the measurements will record a dynamic material, data recording should start immediately after sample addition to not lose information in the beginning. Consequently, the ideal loading position should be as low as possible while still allowing to load the sample into the measuring gap. We here found 30 mm to be suitable for this purpose.
- 84 Quickly mix the 10 mM precursor stock solution of **2** with the 2.0 M EDC fuel in a 20:1 (vol:vol) ratio by using a pipette and transferring 150 μl of the mixture into the measuring gap. Immediately afterward, lower the head to the measuring position, close the humidity trap to avoid evaporation, and start the measurement.

▲ CRITICAL STEP As the initial gel formation happens very quickly, the transfer to the measuring system should be as fast as possible. Otherwise, mechanical shear during the pipetting process and when lowering the measuring head to the measuring position might already damage the supramolecular structure, thus falsifying the obtained results. First, it is recommended to fill the highly concentrated EDC solution into a microcentrifuge tube, then add the precursor solution that automatically mixes both components and, finally, pipette the mixture without further homogenization into the measuring gap.

- 85 Record data for a time span of 60 min at a data acquisition frequency of 1 Hz.
86 Plot the viscoelastic moduli against time (Fig. 4b).

Compare rheology lifetime with anhydride concentrations

▲ **CRITICAL** We compare the lifetimes derived from the rheology experiment to the anhydride concentrations obtained from the kinetic experiment.

- 87 Determine the timepoint of the storage modulus falling below the loss modulus, indicating a gel-to-sol transition. Regarding the activation of **2** with 100 mM fuel, this transition occurs at 42 min.
88 With the kinetic model, calculate the anhydride concentration at 42 min when fueled with 100 mM EDC. When falling below this anhydride concentration (0.45 mM), the end of the lifetime is expected.
89 Redo the calculation for several fuel concentrations, and note the anhydride concentration's timepoints falling below 0.45 mM.
90 Plot the lifetime against the applied fuel concentration of the experimental values together with the calculated ones (Fig. 4c).

Analysis by confocal laser scanning fluorescence microscopy

Sample preparation ● Timing 10 min

- 91 Take a 2 ml syringe, and fill it with vacuum grease by removing the plunger.
92 Cut the upper 4 mm of a 200 μ l pipette tip, and mount it on the syringe.
93 Take a rectangular glass microscope cover slide, and draw a greased circle with a diameter of 5 mm onto it (Fig. 13a).
94 Take 200 μ l of the 10 mM peptide stock solution of Fmoc-E-OH (**1**) or Fmoc-AAD-OH (**2**), and pipette them into a 1.7 ml centrifuge tube each.
95 Add 0.2 μ l of a 2 mM Nile red stock to the samples, resulting in a concentration of 2 μ M in the sample.
96 Start the reaction cycle.
(A) Fmoc-E-OH (**1**)
(i) Add 1 μ l of a 2.0 M EDC stock to the precursor solution, resulting in 10 mM concentration, and mix with a 200 μ l pipette five times.
(ii) Pipette 20 μ l of the reaction solution into the grease chamber (Fig. 13b).
(B) Fmoc-AAD-OH (**2**)
(i) Pipette 1 μ l of a 2.0 M EDC stock into the grease chamber (Fig. 13b).
(ii) Add 20 μ l of the precursor solution of **2** on top of the EDC, and mix it with the pipette five times.
▲ **CRITICAL STEP** For hydrogel-forming precursors like Fmoc-AAD-OH (**2**), transferring the activated reaction mixture from a microcentrifuge tube to the microscope glass slide causes shear stress upon the built fiber network. The fiber network's damage can be avoided by adding the respective amount of EDC onto the glass slide first and then adding the peptide solution (Fig. 13e,f).
97 Seal the grease chamber with a small cover slide (Fig. 13c).
98 Gently press down the cover slide with a tweezer to remove air bubbles (Fig. 13d).
▲ **CRITICAL STEP** Prevent applying too much pressure. Otherwise, the sample will break through the grease and spill on the glass slide.

Imaging of the samples ● Timing 10 min

- 99 Excite the samples with a 552 nm laser or similar, and image them at 580–700 nm. Use a 63 \times objective and a HyD to image the samples.
100 Set the imaging parameters depending on the mobility of the samples. The following examples can be used as guidelines:
(A) Since the fibers formed by **2** in response to EDC are quite static, a slow scan speed and line averaging results in a good resolution. Use a scan speed of 10–100 \times , a line average of 4–16 and a pinhole size of 1 AU. For the image size in pixels, consider the ideal Nyquist sampling frequency according to the microscope setup used.
▲ **CRITICAL STEP** Do not image the assemblies that are close to the glass surfaces. Possible interactions with the surface lead to results that are not representative.
(B) The colloids formed by **1** in response to EDC move rapidly because of Brownian motion, and therefore, a quicker scan speed and lower line averages result in better-resolved images. Use a

PROTOCOL

NATURE PROTOCOLS

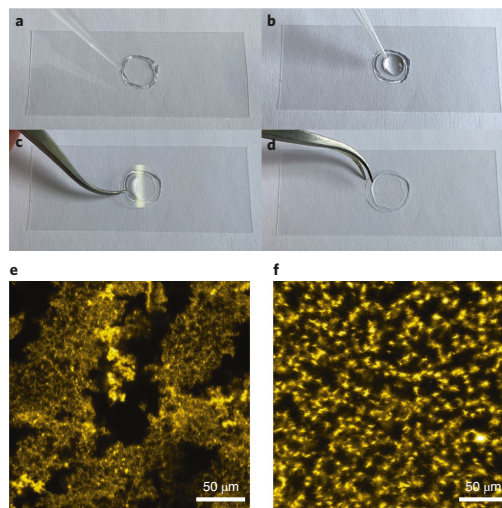


Fig. 13 | Preparation of a microscope glass slide with a grease chamber for microscope imaging. **a**, Preparation of a grease ring on a microscope slide by using a grease-filled syringe. **b**, Pipetting the sample into the grease ring. **c,d**, Closing the grease chamber with a cover slide. **e**, The micrographs show the effect of sample deposition. Confocal microscope micrographs of 10 mM Fmoc-AAD-OH (**2**) fueled with 100 mM EDC. We added EDC to a separate vial together with the precursor. Directly afterwards, the mixture was pipetted on the microscope slide. Shear forces of the pipetting after activation destroy the fibers. As a result, the fibers agglomerate and are not homogeneously distributed over the glass slide. **f**, The EDC was put on the microscope slide first, and the precursor is added on top of the EDC. This sample preparation prevents the rupture of peptide fibers and results in a homogeneous fiber network.

scan speed of 100–600×, no line averaging and a pinhole size of 1 AU. For the image size in pixel, consider the ideal Nyquist sampling frequency according to the microscope setup used.

▲ **CRITICAL STEP** Do not image the assemblies that are close to the glass surfaces. Possible interactions with the surface lead to results that are not representative.

101 Save the images in LIF format, and analyze them with Fiji-ImageJ.

102 Present the micrographs' relevant parts together with scale bars (Figs. 3d,e and 4d,e).

Analysis by cryo-TEM

Sample preparation ● Timing 2 h

103 Prepare two 50 µl samples, each of 10 mM Fmoc-E-OH (**1**) and Fmoc-AAD-OH (**2**) in a 1.7 ml centrifuge tube.

104 Set the Vitrobot temperature to 23 °C and the relative humidity to 100%. Set the automated blotting procedure to 30 s waiting time, 2.5 s blot time and –1 blot force.

105 Wrap paraffin film around a microscope slide, and put two Cu grids (2 µm hole size, 2 µm spacing, 400 mesh) for each sample and one additional as a backup on the paraffin film with the carbon side facing upwards. The paraffin film holds the grids in place during plasma cleaning and makes it easier to remove the microscope slide's grids.

106 Position the microscope slide in a plasma cleaner, and plasma treat the grids for 1.5 min at a 50 mA voltage and a pressure of 3×10^{-2} mBar. This step will hydrophilize the grids.

107 Cool the ethane pot with liquid nitrogen, and slowly fill in the gaseous ethane until the ethane pot is filled up with liquid ethane.

▲ **CRITICAL STEP** Use a low ethane flow to prevent it from spilling and freezing in the liquid nitrogen. Frozen ethane might impact the quality of the blotted grids during the transfer into the grid box.

! **CAUTION** Skin contact with liquid ethane leads to cold burn. Wear a face shield, a laboratory coat and gloves.

108 Insert the grid box in the liquid nitrogen of the ethane pot.

109 Start the reaction cycle by adding EDC to the precursor solution. At predetermined time points, take away the sample and process it in the Vitrobot. Blot at least two grids for each sample.

(A) **Fmoc-AAD-OH (2)**

(i) To a sample of 50 μ l of 10 mM Fmoc-AAD-OH (2), add 2.5 μ l of 1.0 M EDC to get a concentration of 50 mM of EDC.

▲ CRITICAL STEP The EDC concentration and waiting time are essential to obtain acceptable cryo-TEM images. These parameters determine how many assemblies will be present. If the assemblies' density is too high, the thickness of the sampled ice will increase, which hampers imaging. If the concentration of assemblies is too low, no assemblies might be present during imaging.

(ii) Take a grid with the Vitrobot tweezers, attach them to the Vitrobot and bring the ethane pot into the lifted plunge freezing position.

? **TROUBLESHOOTING**

(iii) After 2 min, shake the sample thoroughly, thereby breaking the gel, and pipette 5 μ l of the reaction solution on the grid's hydrophilized carbon side.

? **TROUBLESHOOTING**

(B) **Fmoc-E-OH (1)**

(i) Add 1 μ l of 0.5 M EDC to a 50 μ l 10 mM Fmoc-E-OH (1) sample to yield a concentration of 10 mM of EDC.

(ii) Take a grid with the Vitrobot tweezers, attach them to the Vitrobot and bring the ethane pot into the lifted plunge freezing position.

? **TROUBLESHOOTING**

(iii) After 1 min, shake the sample gently and take 5 μ l of the reaction solution and pipette it on the grid's hydrophilized carbon side.

? **TROUBLESHOOTING**

110 Blot the grid by starting the automated blotting procedure on the Vitrobot.

111 Transfer the copper grid in a grid holder, and store the holder in liquid nitrogen.

■ **PAUSE POINT** Samples can be stored in liquid nitrogen for up to 1 week.

Imaging of the samples ● Timing 30 min

112 Transfer the grid into a cryo-transfer-specimen holder precooled with liquid nitrogen to maintain the specimen temperature at -170 °C or below during the imaging process.

113 Insert the holder into the TEM.

114 Search for holes with assemblies and a proper ice thickness. A good hole can be recognized by a good contrast and visible borders.

115 Acquire bright-field images in low-dose mode at a magnification of 21,000 \times , and vary the exposure time between 1 and 2 s depending on the intensity.

▲ CRITICAL STEP Image at least three different holes in three different squares distributed over the grid to ensure that the images are representative for the sample.

? **TROUBLESHOOTING**

116 Save images in MRC format, and analyze them with Fiji-ImageJ.

117 Present the micrographs with scale bars (Figs. 3f and 4f).

Troubleshooting

Troubleshooting advice can be found in Table 2.

Step	Problem	Possible reason	Solution
1A(vi)	Peptide synthesizer has stopped the synthesis because of an error	Full waste container; pressure drop due to leakage	Empty the waste container; check the reagent bottles and the reaction vessel for any leakage of gas or liquid; drain the reaction vessel, and wash the resin with 5 ml DMF; swell the resin for 10 min in DMF if the synthesis was stopped for >30 min; restart the synthesis from the step when it stopped
1B(xii)	No coloration	Unsuccessful deprotection	Repeat Step 1B(vii-xii)

Table continued

PROTOCOL
NATURE PROTOCOLS
Table 2 (continued)

Step	Problem	Possible reason	Solution
1B(xvi)	Blue coloration	Incomplete coupling	Repeat Step 1B(xiii-xvi)
8	Peptide mass not found in mass spectrum; HPLC chromatogram shows many signals	Required peptide was not synthesized or at low purity; often encountered with old stock solutions of piperidine	Prepare a fresh piperidine stock solution
19	Low rate of lyophilization	Huge sample volume (low surface-to-volume ratio)	Split up the total volume into several smaller ones
31	How to check resulting volume	Volumetric flask is not available	The end volume can be tested by aspiration of the solution with pipettes: after aspiration, test the volume by turning the volume-adjusting knob
35	Saturation of the absorption signal	Too much probe was injected	Dilute the samples; decrease the injection volume; change to higher wavelengths
36	Calibration value has changed over time	The intensity of the light source and the sensitivity of the detector decrease over time	Repeat Steps 30-36, and determine new calibration values
37	Precursors do not dissolve	Solubility of Fmoc-protected precursors is low in aqueous buffer	Sonicate the samples; adjusting the pH to basic conditions increases the solubility of acid precursors
41	Assemblies do not dissolve	The acetonitrile content is not sufficient to dissolve the assemblies instantly	Increasing the acetonitrile content in the quenching solution increases the solubility of the assemblies when the quenching solution is added; the drawback is the decrease in EDC retention time when analyzing the samples by HPLC
	Homogeneous pipetting fails	Hydrogel precursors like 2 form stiff fibers	Vortex the HPLC vial for 5 s; use wide bore pipette tips
43	Insufficient pipetting time	The proposed method saves time as triplicate data are obtained within the time of one reaction cycle, but a routine in fast pipetting is required	Increase the time intervals between the triplicate samples; start only one reaction cycle
46	The EDC signal is not resolved from the injection peak	The EDC retention on C18 columns is low; the retention is further decreased when the injected probe contains acetonitrile; the added acetonitrile causes big injection signals	Start the pump gradient with low acetonitrile content (2%); prepare the quenching solution with a resulting acetonitrile concentration <5% in the quenched samples; lower the flow rate; use longer columns
	The signal areas have changed	The HPLC method created in Step 29 has been changed	Apply the same methods regarding the calibration and the kinetic measurement; changes in, e.g., the flow rate can affect the signal area ⁶¹
75	Saturation of the UV-VIS signal	High probe concentration	Try cuvettes with different path lengths
82	Nonlinear material response	Deformation of $\gamma = 1\%$ already too high	Perform a torque-controlled measurement: the torque should be selected as small as possible ($M = 0.5-1$ mNm). The drawback is a slightly lower signal-to-noise ratio
109A/B (ii)	Not enough time to attach the tweezers between starting the reaction cycle and the sampling time point		Attach the tweezers and lift the ethane pot before starting the reaction cycle. This still needs to be done quite quickly; the longer the ethane pot remains in the lifted position, the more likely it is that the ethane freezes, which might reduce the quality of the blotted grid
109A/B (iii)	Liquid ethane freezes during the waiting time	The ethane pot is too long in the lifted waiting position, or the ethane pot is filled with too much liquid nitrogen	Reduce the amount of liquid nitrogen in the ethane pot to prevent spillage into the liquid ethane while it is in the lifted waiting position; try to minimize the time the ethane pot is in the lifted waiting position
115	Not possible to properly focus on the sample, because the ice on the grid is too thick	Often apparent for hydrogel-forming precursors like 2 at high anhydride concentrations	Reduce the concentration of assemblies formed in the sample by reducing the EDC concentration; freeze the samples at an earlier time point in the cycle

Timing

Step 1A, automated solid-phase peptide synthesis: 2.5 h
 Step 1B, manual solid-phase peptide synthesis: 6 h
 Steps 2-8, microcleavage as reaction control: 2 h
 Steps 9-12, peptide deprotection and cleavage from the resin: 3 h
 Steps 13-22, preparative HPLC purification: 6 h

Steps 23–28, Nile red assay: 2 h
Steps 29–36, calibration: 17 h
Steps 37–49, kinetic analysis by HPLC: 18 h
Steps 50–59, using a kinetic model in MATLAB: 2 h
Steps 60–70, time-lapse photography: 2 h
Steps 71–78, UV-VIS measurement: 3 h
Steps 79–90, rheological characterization: 1.5 h
Steps 91–102, analysis by confocal laser scanning fluorescence microscopy: 20 min
Steps 103–117, analysis by cryo-TEM: 2.5 h

Anticipated results

We have referred to analytical data and figures at the ‘Procedure’ steps where it is required in order to know whether to proceed to the next step.

The synthesis of **2** can be monitored by cleaving and analyzing small fractions from the solid support (Steps 2–8). Figure 9 compares results from two experiments that yielded different amounts of side products. An increased appearance of side products can be referred to the quality of the piperidine stock solution, which should be exchanged occasionally. Additionally, the composition of the crude product provides information on the subsequent purification steps regarding the pump gradient or injection volumes (see Steps 14–17).

The Nile red assay (Fig. 10) is used to determine the concentrations at which the precursors can be applied in the later fueling experiments. The concentration of the reaction cycles’ products can be determined by HPLC using calibration curves prepared as described in Steps 29–36 (Fig. 11a,b). The concentration ranges will depend on which precursors are applied and which HPLC setup is used. A typical HPLC chromatogram that can be expected applying this protocol is shown in Fig. 11c,d. To correctly align the reaction cycle’s components, all signals must be resolved. Therefore, often an adaption of the pump gradient described in Step 29 is helpful.

The webcam experiment provides valuable information about what further experiments can be conducted. Whereas transient turbid solutions indicate the presence of dynamic assemblies, a differentiation between, e.g., colloids and hydrogels can be made by inverting the vials (Step 67B). Samples with a transient turbidity should be further analyzed by UV-VIS measurements. For hydrogel-forming precursors, rheology is a suitable follow-up technique. In UV-VIS experiments, the physical properties of the assemblies dictate the choice of the sample container (Extended Data Fig. 3a,b). Before the screening of several EDC concentrations (Step 74), several containers should be tested. Figure 13e,f shows how incorrect sample preparation effects the assemblies’ structures during confocal laser scanning fluorescence microscopy. Depending on the nature of the precursor, the guidelines provided in either Step 96A or 96B should be considered as a correct way of sample preparation.

Reporting Summary

Further information on research design is available in the Nature Research Reporting Summary linked to this article.

Data availability

The authors declare that all the data supporting the findings of this study are available within the article, the source data files and the Supplementary Information files. Source data are provided with this paper.

Software availability

The MATLAB code used in this protocol together with an exemplary dataset is provided at https://github.com/BoekhovenLab/Nature_protocols. Source data are provided with this paper.

References

1. Stupp, S. I. et al. Supramolecular materials: self-organized nanostructures. *Science* **276**, 384–389 (1997).
2. Amabilino, D. B., Smith, D. K. & Steed, J. W. Supramolecular materials. *Chem. Soc. Rev.* **46**, 2404–2420 (2017).
3. Zhou, J., Li, J., Du, X. & Xu, B. Supramolecular biofunctional materials. *Biomaterials* **129**, 1–27 (2017).
4. Kato, T., Uchida, J., Ichikawa, T. & Soberats, B. Functional liquid-crystalline polymers and supramolecular liquid crystals. *Polym. J.* **50**, 149–166 (2017).

5. Hegmann, T., Qi, H. & Marx, V. M. Nanoparticles in liquid crystals: synthesis, self-assembly, defect formation and potential applications. *J. Inorg. Organomet. Polym. Mater.* **17**, 483–508 (2007).
6. Greaves, T. L. & Drummond, C. J. Ionic liquids as amphiphile self-assembly media. *Chem. Soc. Rev.* **37**, 1709–1726 (2008).
7. de Greef, T. F. & Meijer, E. W. Materials science: supramolecular polymers. *Nature* **453**, 171–173 (2008).
8. Aida, T., Meijer, E. W. & Stupp, S. I. Functional supramolecular polymers. *Science* **335**, 813–817 (2012).
9. Weingarten, A. S. et al. Self-assembling hydrogel scaffolds for photocatalytic hydrogen production. *Nat. Chem.* **6**, 964–970 (2014).
10. Grimaldi, N. et al. Lipid-based nanovesicles for nanomedicine. *Chem. Soc. Rev.* **45**, 6520–6545 (2016).
11. Webber, M. J. & Langer, R. Drug delivery by supramolecular design. *Chem. Soc. Rev.* **46**, 6600–6620 (2017).
12. Kadler, K. E., Holmes, D. F., Trotter, J. A. & Chapman, J. A. Collagen fibril formation. *Biochem. J.* **316**, 1–11 (1996).
13. Zhu, J. & Kaufman, L. J. Collagen I self-assembly: revealing the developing structures that generate turbidity. *Biophys. J.* **106**, 1822–1831 (2014).
14. Prockop, D. J. & Kivirikko, K. I. Collagens: molecular biology, diseases, and potentials for therapy. *Annu. Rev. Biochem.* **64**, 403–434 (1995).
15. Zhao, B., Hu, H., Mandal, S. K. & Haddon, R. C. A bone mimic based on the self-assembly of hydroxyapatite on chemically functionalized single-walled carbon nanotubes. *Chem. Mater.* **17**, 3235–3241 (2005).
16. Amendola, V. & Meneghetti, M. Self-healing at the nanoscale. *Nanoscale* **1**, 74–88 (2009).
17. Tantakitti, F. et al. Energy landscapes and functions of supramolecular systems. *Nat. Mater.* **15**, 469–476 (2016).
18. Lancia, F., Ryabchun, A. & Katsonis, N. Life-like motion driven by artificial molecular machines. *Nat. Rev. Chem.* **3**, 536–551 (2019).
19. Needleman, D. & Dogic, Z. Active matter at the interface between materials science and cell biology. *Nat. Rev. Mater.* **2** (2017).
20. Korn, E., Carlier, M. & Pantaloni, D. Actin polymerization and ATP hydrolysis. *Science* **238**, 638–644 (1987).
21. Desai, A. & Mitchison, T. J. Microtubule polymerization dynamics. *Annu. Rev. Cell Dev. Biol.* **13**, 83–117 (1997).
22. Kohler, S., Schaller, V. & Bausch, A. R. Structure formation in active networks. *Nat. Mater.* **10**, 462–468 (2011).
23. Boekhoven, J. et al. Dissipative self-assembly of a molecular gelator by using a chemical fuel. *Angew. Chem. Int. Ed. Engl.* **49**, 4825–4828 (2010).
24. Boekhoven, J., Hendriksen, W. E., Koper, G. J., Elkema, R. & van Esch, J. H. Transient assembly of active materials fueled by a chemical reaction. *Science* **349**, 1075–1079 (2015).
25. van Esch, J. H., Klajn, R. & Otto, S. Chemical systems out of equilibrium. *Chem. Soc. Rev.* **46**, 5474–5475 (2017).
26. Saha, B., Chatterjee, A., Reja, A. & Das, D. Condensates of short peptides and ATP for the temporal regulation of cytochrome c activity. *Chem. Commun.* **55**, 14194–14197 (2019).
27. Post, E. A. J. & Fletcher, S. P. Dissipative self-assembly, competition and inhibition in a self-reproducing protocell model. *Chem. Sci.* **11**, 9434–9442 (2020).
28. Deng, J. & Walther, A. Pathway complexity in fuel-driven DNA nanostructures with autonomous reconfiguration of multiple dynamic steady states. *J. Am. Chem. Soc.* **142**, 685–689 (2020).
29. Cardona, M. A. & Prins, L. J. ATP-fuelled self-assembly to regulate chemical reactivity in the time domain. *Chem. Sci.* **11**, 1518–1522 (2020).
30. Hossain, M. M., Atkinson, J. L. & Hartley, C. S. Dissipative assembly of macrocycles comprising multiple transient bonds. *Angew. Chem. Int. Ed. Engl.* **59**, 13807–13813 (2020).
31. Bal, S., Ghosh, C., Ghosh, T., Vijayaraghavan, R. K. & Das, D. Non-equilibrium polymerization of cross-beta amyloid peptides for temporal control of electronic properties. *Angew. Chem. Int. Ed. Engl.* **59**, 13506–13510 (2020).
32. Ragazzon, G. & Prins, L. J. Energy consumption in chemical fuel-driven self-assembly. *Nat. Nanotechnol.* **13**, 882–889 (2018).
33. Astumian, R. D. Kinetic asymmetry allows macromolecular catalysts to drive an information ratchet. *Nat. Commun.* **10**, 3837 (2019).
34. Maiti, S., Fortunati, I., Ferrante, C., Scrimin, P. & Prins, L. J. Dissipative self-assembly of vesicular nanoreactors. *Nat. Chem.* **8**, 725–731 (2016).
35. van Ravensteijn, B. G. P., Hendriksen, W. E., Elkema, R., van Esch, J. H. & Kegel, W. K. Fuel-mediated transient clustering of colloidal building blocks. *J. Am. Chem. Soc.* **139**, 9763–9766 (2017).
36. Dambeniaks, A. K., Vu, P. H. Q. & Fyles, T. M. Dissipative assembly of a membrane transport system. *Chem. Sci.* **5**, 3396–3403 (2014).
37. Ogden, W. A. & Guan, Z. Redox chemical-fueled dissipative self-assembly of active materials. *ChemSystemsChem* <https://doi.org/10.1002/syst.201900030> (2019).
38. Leira-Iglesias, J., Sorrenti, A., Sato, A., Dunne, P. A. & Hermans, T. M. Supramolecular pathway selection of perylenediimides mediated by chemical fuels. *Chem. Commun.* **52**, 9009–9012 (2016).
39. Tena-Solsona, M. et al. Non-equilibrium dissipative supramolecular materials with a tunable lifetime. *Nat. Commun.* **8**, 15895 (2017).
40. Kariyawasam, L. S. & Hartley, C. S. Dissipative assembly of aqueous carboxylic acid anhydrides fueled by carbodiimides. *J. Am. Chem. Soc.* **139**, 11949–11955 (2017).

41. Dai, K. et al. Regulating chemically fueled peptide assemblies by molecular design. *J. Am. Chem. Soc.* **142**, 14142–14149 (2020).
42. Riess, B. et al. Dissipative assemblies that inhibit their deactivation. *Soft Matter* **14**, 4852–4859 (2018).
43. Grotsch, R. K. et al. Dissipative self-assembly of photoluminescent silicon nanocrystals. *Angew. Chem. Int. Ed. Engl.* **57**, 14608–14612 (2018).
44. Grotsch, R. K. et al. Pathway dependence in the fuel-driven dissipative self-assembly of nanoparticles. *J. Am. Chem. Soc.* **141**, 9872–9878 (2019).
45. Tena-Solsona, M., Wanzke, C., Riess, B., Bausch, A. R. & Boekhoven, J. Self-selection of dissipative assemblies driven by primitive chemical reaction networks. *Nat. Commun.* **9**, 2044 (2018).
46. Wanzke, C., Tena-Solsona, M., Rieß, B., Tebcharani, L. & Boekhoven, J. Active droplets in a hydrogel release drugs with a constant and tunable rate. *Mater. Horiz.* **7**, 1397–1403 (2020).
47. Donau, C. et al. Active coacervate droplets as a model for membraneless organelles and protocells. *Nat. Commun.* **11**, 5167 (2020).
48. Kriebisch, B. A. K. et al. Reciprocal coupling in chemically fueled assembly: a reaction cycle regulates self-assembly and vice versa. *J. Am. Chem. Soc.* **142**, 20837–20844 (2020).
49. Panja, S., Dietrich, B. & Adams, D. J. Chemically fuelled self-regulating gel-to-gel transition. *ChemSystemsChem* <https://doi.org/10.1002/syst.201900038> (2019).
50. Bal, S., Das, K., Ahmed, S. & Das, D. Chemically fueled dissipative self-assembly that exploits cooperative catalysis. *Angew. Chem. Int. Ed. Engl.* **58**, 244–247 (2019).
51. Coin, I., Beyermann, M. & Bienert, M. Solid-phase peptide synthesis: from standard procedures to the synthesis of difficult sequences. *Nat. Protoc.* **2**, 3247–3256 (2007).
52. Chung, B. K. W., White, C. J. & Yudin, A. K. Solid-phase synthesis, cyclization, and site-specific functionalization of aziridine-containing tetrapeptides. *Nat. Protoc.* **12**, 1277–1287 (2017).
53. Murray, J. K. & Gellman, S. H. Parallel synthesis of peptide libraries using microwave irradiation. *Nat. Protoc.* **2**, 624–631 (2007).
54. Sackett, D. L. & Wolff, J. Nile red as a polarity-sensitive fluorescent probe of hydrophobic protein surfaces. *Anal. Biochem.* **167**, 228–234 (1987).
55. Stuart, M. C. A., van de Pas, J. C. & Engberts, J. B. F. N. The use of Nile Red to monitor the aggregation behavior in ternary surfactant-water-organic solvent systems. *J. Phys. Org. Chem.* **18**, 929–934 (2005).
56. Schnitter, F. & Boekhoven, J. A method to quench carbodiimide-fueled self-assembly. *ChemSystemsChem* <https://doi.org/10.1002/syst.202000037> (2020).
57. Draper, E. R. & Adams, D. J. Low-molecular-weight gels: the state of the art. *Chem* **3**, 390–410 (2017).
58. Greenspan, P., Mayer, E. P. & Fowler, S. D. Nile red: a selective fluorescent stain for intracellular lipid droplets. *J. Cell Biol.* **100**, 965–973 (1985).
59. Nakajima, N. & Ikada, Y. Mechanism of amide formation by carbodiimide for bioconjugation in aqueous media. *Bioconjug. Chem.* **6**, 123–130 (1995).
60. Goodling, K., Johnson, K., Lefkowitz, L. & Williams, B. W. The modern student laboratory: luminescent characterization of sodium dodecyl sulfate micellar solution properties. *J. Chem. Educ.* **71**, A8 (1994).
61. Brown, P. R. Effect of flow rates and the slope of the linear concentration gradient on peak areas in high pressure liquid chromatography. *J. Chromatogr. A* **57**, 383–390 (1971).

Acknowledgements

This research was conducted within the Max Planck School Matter to Life supported by the German Federal Ministry of Education and Research (BMBF) in collaboration with the Max Planck Society. J.B., F.S., A.M.B., B.W. and O.L. acknowledge funding by the Deutsche Forschungsgemeinschaft (DFG, German Research Foundation) – SFB-863 – Project ID 111166240 (Project B11) and funding by the European Research Council (ERC starting grant 852187). J.R.F. acknowledges the Deutsche Forschungsgemeinschaft for project 411722921. Cryo-TEM measurements were performed using infrastructure contributed by the Dietz Lab and the TUM EM Core Facility. We acknowledge the technical support provided by F. Kohler.

Author contributions

F.S. and A.M.B. contributed equally to this protocol. They designed and performed the experiments and wrote the manuscript. B.W. and J.R.F. carried out the experiments. J.B. designed experiments, outlined and wrote the manuscript, and supervised the project. O.L. designed the experiments.

Competing interests

The authors declare no competing interests.

Additional information

Extended data is available for this paper at <https://doi.org/10.1038/s41596-021-00563-9>.

Supplementary information The online version contains supplementary material available at <https://doi.org/10.1038/s41596-021-00563-9>.

Correspondence and requests for materials should be addressed to J.B.

Peer review information *Nature Protocols* thanks Dibyendu Das and the other, anonymous reviewer(s) for their contribution to the peer review of this work.

Reprints and permissions information is available at www.nature.com/reprints.

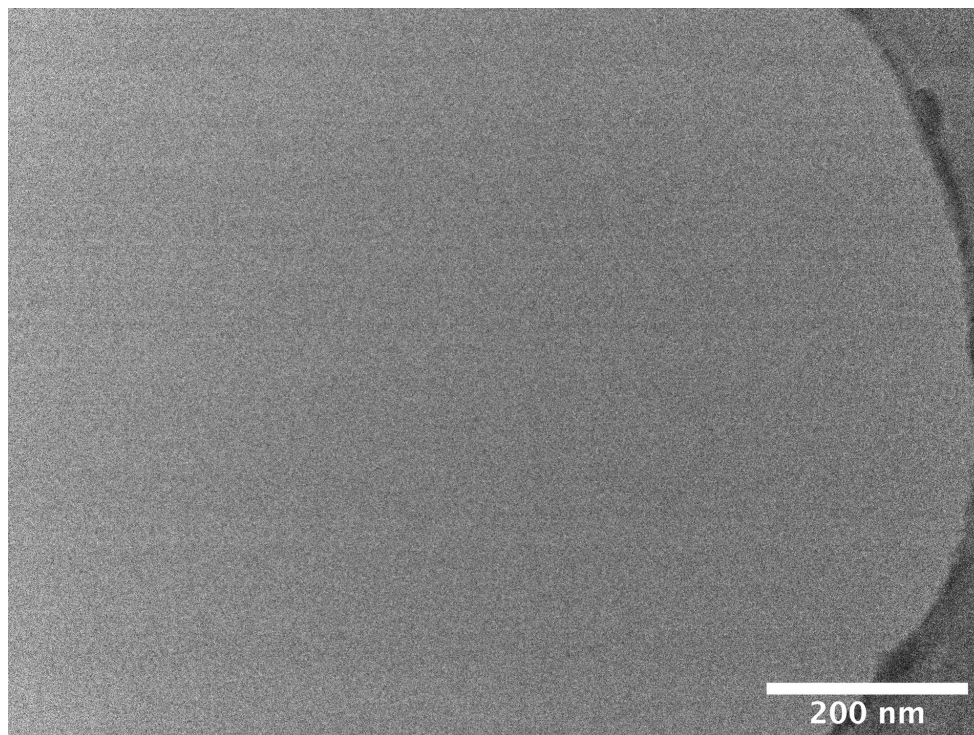
Publisher's note Springer Nature remains neutral with regard to jurisdictional claims in published maps and institutional affiliations.

Received: 23 October 2020; Accepted: 26 April 2021;
Published online: 30 June 2021

Related links

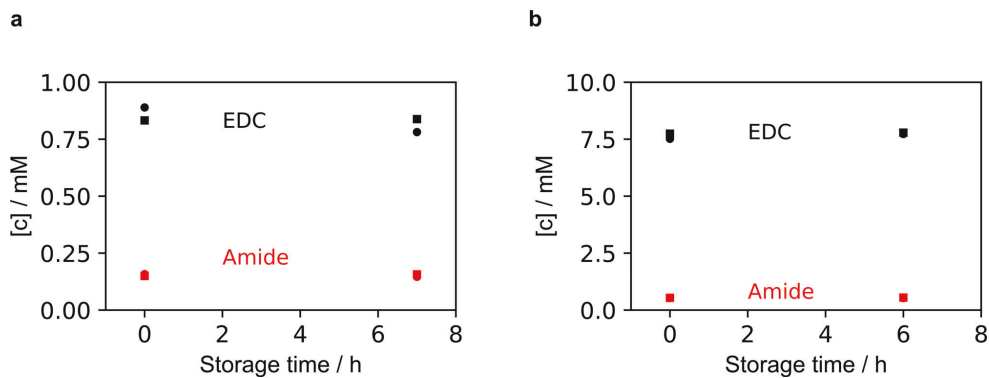
Key references using this protocol

Tena-Solsona, M. et al. *Nat. Commun.* **8**, 15895 (2017): <https://doi.org/10.1038/ncomms15895>
Schnitter, F. & Boekhoven, J. *ChemSystemsChem* **3**, e2000037 (2021): <https://doi.org/10.1002/syst.202000037>
Donau, C. et al. *Nat. Commun.* **11**, 5157 (2020): <https://doi.org/10.1038/s41467-020-18815-9>
Dai, K. et al. *J. Am. Chem. Soc.* **142**, 33 (2020): <https://doi.org/10.1021/jacs.0c04203>
Kriebisch, B. A. K. et al. *J. Am. Chem. Soc.* **142**, 49 (2020): <https://doi.org/10.1021/jacs.0c10486>



Extended Data Fig. 1 | Cryo-TEM microscope micrograph. The control micrograph of a 10 mM precursor **2** stock solution excludes preassembly of the inactivated precursor in the absence of EDC fuel.

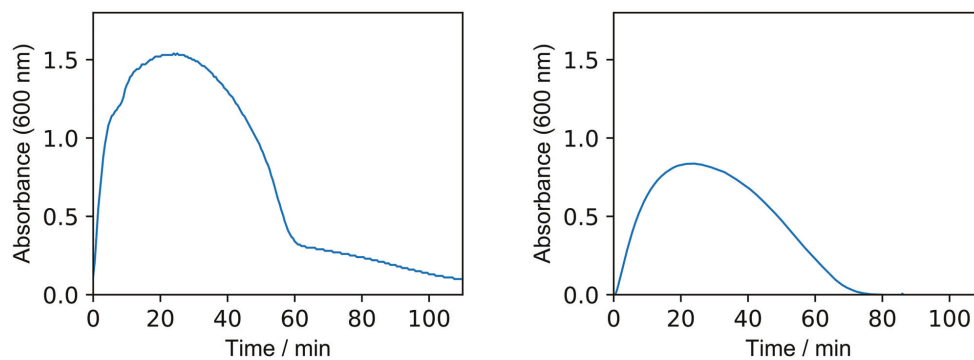
PROTOCOL NATURE PROTOCOLS



Extended Data Fig. 2 | EDC hydrolysis and Fmoc deprotection kinetics. a,b. The addition of the quenching solution freezes the reaction cycle of Fmoc-E-OH (**1**) (a) and Fmoc-AAD-OH (**2**) (b). In the timescale of the HPLC analysis, the degradation of EDC and Fmoc deprotection does not falsify the concentration determination.

NATURE PROTOCOLS

PROTOCOL



Extended Data Fig. 3 | The absorbance of light as a measure for turbidity. **a**, Usage of different sample containers affects the measurement quality as sedimentation in a 96-well plate wrongly extends the system's lifetime. **b**, Regarding colloids formed by **1**, a cuvette is a better choice as sample container.

8. Conclusion and Outlook

Dissipative structures are ubiquitous in living organisms. These structures are regulated by catalytical reaction cycles and rely on continuous energy consumption to be maintained away from equilibrium. Coupling the formation of structures to catalytic reaction cycles gives spatiotemporal control, enabling quick responses to external stimuli as well as the recycling of building blocks. However, the non-equilibrium nature of these structures also endorses them with dynamic properties, which are impossible for static structures in thermodynamic equilibrium.

This thesis aimed to shed light on the dynamic properties arising from coupling liquid-liquid phase separation to a catalytical reaction cycle. We chose chemically regulated complex coacervates as an active droplet system that also serves as a model system for regulating membraneless organelles. We used droplet-based microfluidics to encapsulate these active droplets into microreactors and study their behavior on the collective and individual levels. Driving this system by the addition of batches of fuel emphasized the role of fuel concentration in dictating active droplet formation and properties and revealed that active droplets grow through fusion, decay simultaneously and that their shrinkage rate scales with their volume. However, these behaviors are primarily influenced by either the activation or deactivation reaction rather than arising from their simultaneous interplay.

To overcome this issue, we continuously fueled the microreactors through the continuous diffusive addition of fuel to maintain the active droplet system in a non-equilibrium steady state. We observed that active droplets can undergo a morphological transition into spherical shells of liquid droplet material as well as oscillating cycles of nucleation, growth, and shrinkage. Under equilibrium conditions, both of these dynamic behaviors would be impossible due to an increase in the surface area. However, under non-equilibrium steady-state conditions, they are consequences of reaction-diffusion gradients, demonstrating the capability of chemical gradients to regulate the morphology and behavior of active droplets.

In conclusion, this work unraveled the dynamic behaviors of chemically fueled active emulsions. We envision that similar mechanisms are involved in the regulation of membraneless organelles, controlling their morphology, size, and number.

Further complex dynamic behaviors, such as self-division of active droplets, have also been predicted but were not yet observed for the current system. Potential ways to discover further dynamic behaviors are the introduction of interchanging steady-state fuel concentrations, feeding of the microreactors with additional droplet building blocks, or the introduction of additional feedback on the droplet morphology. For example, feedback could be achieved through orthogonal assemblies that locally alter the properties of droplets or promote certain

droplet shapes, such as the elongation of droplets. The introduction of such additional complexity in the system could favor the self-division of droplets instead of their transition into spherical shells or their oscillatory behavior to reduce their surface area-to-volume ratio.

Furthermore, the spatial oscillation of active droplets could be envisioned as a molecular transport system to control the location and concentration of partitioning molecules. In the present state, the accumulation of partitioning molecules oscillates with the presence of droplets and is, therefore, shuttled one-dimensionally between the upper and lower parts of the reactors. However, more complex patterns can be envisioned for fluctuating or inhomogeneously distributed fuel concentrations as well as different reactor shapes. For example, molecules could be locally concentrated along a fuel gradient and spatially repositioned through fluctuating fuel sources. By changing the shape of a reactor from a spherical droplet to a flat disk, gravitationally induced fusion processes could be stopped, and two-dimensional stable droplet patterns could be expected.

Altogether, we predict this work to be a stepping stone in unraveling further dynamic behaviors in chemically fueled emulsions and self-assembling systems in general.

9. Materials and Methods

In this Chapter, the used materials and methods for Chapter 6 are described. The materials and methods for Chapters 4,5 and 7 are included in the reprinted publications.

Materials

Polystyrene sulfonate (pSS, 17 kDa), sulforhodamine B and 4-morpholineethanesulfonic acid (MES) buffer, were purchased from Sigma-Aldrich and used without any further purification unless indicated otherwise. Peptides Ac-F(RG)₃D-OH and Ac-F(RG)₃N-NH₂ were purchased from CASLO Aps. Peptides NBD-G(RG)₃N-NH₂ and NBD-G(RG)₃D-OH were synthesized using a published procedure.⁷⁷ 2 w% 008-Fluorosurfactant in Novec 7500 was purchased from RAN Biotechnologies. Novec 7500 was purchased by lolitec.

Standard sample preparation

Stock solutions of Ac-F(RG)₃D-OH (precursor, 300 mM), pSS (41 mM, according to monomer units, 7.6 mg ml⁻¹), and MES (650 mM) were prepared by dissolving the respective amount of each component in MQ water and adjusting the pH to 5.3. Stock solutions for Ac-F(RG)₃N-NH₂ (product*), and the fluorescent dye were also prepared in MQ water but without pH adjustment. All stocks were filtrated with a syringe filter (PTFE, 0.2 μm pore size). To continuously fuel active droplets, a solution (5 μL) containing precursor and pSS in 200 mM MES at pH 5.3 was mixed with perfluorinated oil (Novec 7500, 50 μL) containing the fluorosurfactant and 0.020-1.0 M DIC. For passive droplets that are not fueled, pSS was added to a solution containing precursor and product* in 200 mM MES at pH 5.3, and the solution was mixed with a pipette.

Method to continuously fuel active droplets

Surfactant-stabilized water in oil droplets was produced using 1 % 008-FluoroSurfactant in 3M HFE7500 as the oil phase. To form microreactors of varying size, 5 μL of a solution containing 10 mM precursor and 5 mM pSS in 200 mM MES at pH 5.3 were added to 50 μL of the oil phase in a 200 μL Eppendorf tube. Active droplets: For the preparation of active droplets, fuel was added to the oil phase before adding the sample containing the precursor and pSS. Snipping of the centrifugal tube resulted in the formation of microreactors with a random size distribution. The microreactors were imaged at the confocal microscope in untreated observation chambers⁷⁸ consisting of a 24 mm x 60 mm glass cover slide and a 16 mm x 16 mm glass cover slide that were separated by two slices of double-sided sticky tape and sealed with two-component glue.

Passive droplets: For the preparation of passive droplets, coacervation is induced right before

9. Materials and Methods

the encapsulation into the microreactors by adding pSS as the last component. The microreactors were sealed and imaged in untreated observation chambers.

Confocal fluorescence microscopy

A Stellaris 5 confocal microscope (Leica) with a 63x oil immersion objective (1.2 NA) was used to analyze the coacervates in the microfluidic reactors (microreactors). Sulforhodamine B was added to track the coacervates via fluorescence if not indicated otherwise, and the dye was excited at 552 nm and imaged at 565-700 nm with a HyD detector. The pinhole was set to 1 Airy unit. To analyze the coacervate-based droplets, z-stack time series of the entire microreactor were imaged with 4 μm steps in between images.

Kymograph

The kymograph was generated using ImageJ (Fiji). Therefore, a Z-stack time series was converted into an interpolated 3D projection along the Y-axis. The kymograph was obtained along a vertical line with a width of 400 pixels using the plugin KymographBuilder.

Analysis of droplets and oscillations

Images were analyzed with ImageJ (Fiji). The Z-stack time series obtained by confocal microscopy were converted into maximum Z-projections, and bleach correction and a Gaussian blur were applied. Images were binarized using the Otsu thresholding algorithm and applying the watershed function to separate overlapping droplets. Subsequently, the images were analyzed with the analyze particle plugin in ImageJ. The droplet volumes were calculated assuming a spherical shape. To analyze the upper half of a microreactor, the same procedure was used, but a maximum z-projection was only generated of the upper half of the z-stack. For data sets with periods of no total droplet volume measured, a rolling average was applied to improve the signal in the frequency domain. The frequencies of oscillations were obtained by subtracting the mean and using FFT. FFT calculations were performed in OriginLab.

10. Further Publications

A list of all publications I contributed to, that have not been reprinted above, is given in the following sections.

Publications

- [1] Kun Dai, Jennifer Rodon Fores, Caren Wanzke, Benjamin Winkeljann, Alexander M. Bergmann, Oliver Lieleg, Job Boekhoven, Regulating Chemically Fueled Peptide Assemblies by Molecular Design. *J. Am. Chem. Soc.* **2020**, 142, 33, 14142–14149.
- [2] Brigitte A.K. Kriebisch, Alexander Jussupow, Alexander M. Bergmann, Fabian Kohler, Hendrik Dietz, Ville R.I. Kaila, Job Boekhoven, Reciprocal Coupling in Chemically Fueled Assembly: A Reaction Cycle Regulates Self-Assembly and Vice Versa. *J. Am. Chem. Soc.* **2020**, 142, 49, 20837–20844.
- [3] Kun Dai, Marta Tena-Solsona, Jennifer Rodon Fores, Alexander M. Bergmann, Job Boekhoven, Morphological transitions in chemically fueled self-assembly. *Nanoscale* **2021**, 13, 19864-19869.
- [4] Fabian Späth, Carsten Donau, Alexander M. Bergmann, Moritz Kränzlein, Christopher V Synatschke, Bernhard Rieger, Job Boekhoven, Molecular Design of Chemically Fueled Peptide–Polyelectrolyte Coacervate-Based Assemblies. *J. Am. Chem. Soc.* **2021**, 143, 12, 4782–4789.
- [5] Christine M.E. Kriebisch, Alexander M. Bergmann, Job Boekhoven, Fuel-Driven Dynamic Combinatorial Libraries. *J. Am. Chem. Soc.* **2021**, 143, 20, 7719–7725.
- [6] Michaela A. Würbser, Patrick S. Schwarz, Jonas Heckel, Alexander M. Bergmann, Andreas Walther, Job Boekhoven, Chemically Fueled Block Copolymer Self-Assembly into Transient Nanoreactors. *ChemSystemsChem* **2021**, 3, e2100015.
- [7] Jennifer Rodon-Fores, Michaela A. Würbser, Martin Kretschmer, Benedikt Rieß, Alexander M. Bergmann, Oliver Lieleg, Job Boekhoven, A chemically fueled supramolecular glue for self-healing gels. *Chem. Sci.* **2022**, 13, 11411-11421.
- [8] Carsten Donau, Fabian Späth, Michele Stasi, Alexander M. Bergmann, Job Boekhoven, Phase Transitions in Chemically Fueled, Multiphase Complex Coacervate Droplets. *Angew. Chem. Int. Ed.* **2022**, 61, e202211905.
- [9] Brigitte A.K. Kriebisch, Christine M.E. Kriebisch, Alexander M. Bergmann, Caren Wanzke, Marta Tena-Solsona, Job Boekhoven, Tuning the Kinetic Trapping in Chemically Fueled Self-Assembly. *ChemSystemsChem* **2023**, 5, e202200035.

10. Further Publications

- [10] Xiaoyao Chen, Brigitte A.K. Kriebisch, Alexander Bergmann, Job Boekhoven, Design rules for reciprocal coupling in chemically fueled assembly. *Chem. Sci.* **2023**, Accepted Manuscript.
- [11] Xiaoyao Chen, Michele Stasi, Jennifer Rodon-Fores, Paula F. Großmann, Alexander M. Bergmann, Kun Dai, Marta Tena-Solsona, Bernhard Rieger, Job Boekhoven, A Carbodiimide-Fueled Reaction Cycle That Forms Transient 5(4H)-Oxazolones. *J. Am. Chem. Soc.* **2023**, 145, 12, 6880–6887.
- [12] Fabian Späth, Anton S. Maier, Michele Stasi, Alexander M. Bergmann, Kerstin Halama, Monika Wenisch, Bernhard Rieger, Job Boekhoven, The Role of Chemically Innocent Polyanions in Active, Chemically Fueled Complex Coacervates. *Angew. Chem. Int. Ed.* **2023**, e202309318.

11. Acknowledgments

First of all, I want to thank Prof. Job Boekhoven not only for the opportunity to conduct this Ph.D. thesis in his group, but also for all his time, effort, enthusiasm and optimism he has dedicated to all the projects we pursued together. You had always a good suggestion to solve any occurring problems and no obstacle in the way seemed too big to overcome.

A special thanks goes to Patrick without whom I might have never attended the lecture about supramolecular chemistry nor joined the BoekhovenLab for an internship.

Furthermore, I want to thank the rest of the first generation, as I like to call them. Raphael, Benno, Caren, Schnitti, and Marta, you quickly integrated everyone joining the group and with the atmosphere you created, the lab never felt like work.

Another big thank you goes to Carsten, with whom it was a pleasure to work together on projects and who was always my first contact for questions about droplets. With your work, you did not only lay the foundation for my thesis, but without your support, I would have been lost multiple times. Beating you during chess breaks also helped to keep the motivation high, even though it seems the tides have turned.

I further want to thank my collaborators. Thank you, Kerstin and Kevin, for inviting me to Heidelberg to introduce me to microfluidics and for your continuous support through the years on any upcoming problem associated with it. Thank you, Christoph, Giacomo, and Jonathan, for your patience in the countless and sometimes seemingly endless discussions on spherical shells. It was a pleasure to work with you, and I hope we will, at some point, manage to finally grab a beer together and celebrate the successful end of our shared project.

I also want to thank everyone who started their journey in the BoekhovenLab with and after me for their scientific as well as emotional support. I want to thank Michi for making sure I always had a delicious lunch and a safe day in the lab. I want to thank Kun and Xiaoyao for introducing me to the Chinese culture and, especially, to hot pot. I want to thank Simone, Monika, and Anna-Lena for continuing the lunch break tradition at 11 a.m. I want to thank Spabi for his cakes, even though I have to redirect that to Christian towards the end. I want to thank Michele for the coffee that got me started every single day in the lab. I want to thank Laura and Judit for fighting endlessly to keep our labs clean. I want to thank Brigitte and Christine for helping out everywhere at the same time. I want to thank Oleksii for everything heavy that needed to be carried. I want to thank Jennifer for distracting us with the cutest lab dog. I want

11. Acknowledgments



to thank Hector for trying to introduce me to the world of Python. I want to thank Pablo for taking over projects I didn't have time to continue.

A huge thanks goes to Julia for supporting me this entire time whenever I got home exhausted and for pushing me to finally finish this thesis.

I further want to thank my parents for their support over all these years. Without them, I would not be where I am today.

12. References

1. Whitesides, G.M. & Grzybowski, B. Self-Assembly at All Scales. *Science* **295**, 2418-2421 (2002).
2. Schrodinger, E. *What is Life?: With Mind and Matter and Autobiographical Sketches*, (Cambridge University Press, 2012).
3. Luisi, P.L. About Various Definitions of Life. *Origins of life and evolution of the biosphere* **28**, 613-622 (1998).
4. Yewdall, N.A., Mason, A.F. & van Hest, J.C.M. The hallmarks of living systems: towards creating artificial cells. *Interface Focus* **8**, 20180023 (2018).
5. Scaruffi, P. *Thinking about Thought - Life*, (CreateSpace Independent Publishing Platform, 2014).
6. Walsh, C.T., Tu, B.P. & Tang, Y. Eight Kinetically Stable but Thermodynamically Activated Molecules that Power Cell Metabolism. *Chemical Reviews* **118**, 1460-1494 (2018).
7. Milo, R. & Phillips, R. *Cell biology by the numbers*, (Garland Science, 2015).
8. Westheimer, F.H. Why Nature Chose Phosphates. *Science* **235**, 1173-1178 (1987).
9. Kiani, F.A. & Fischer, S. Comparing the catalytic strategy of ATP hydrolysis in biomolecular motors. *Physical Chemistry Chemical Physics* **18**, 20219-20233 (2016).
10. Litwack, G. Chapter 11 - Protein Biosynthesis. in *Human Biochemistry (Second Edition)* (ed. Litwack, G.) 357-375 (Academic Press, Boston, 2022).
11. Knowles, J.R. Enzyme-Catalyzed Phosphoryl Transfer Reactions. *Annual Review of Biochemistry* **49**, 877-919 (1980).
12. Rajas, F., Gautier-Stein, A. & Mithieux, G. Glucose-6 Phosphate, A Central Hub for Liver Carbohydrate Metabolism. *Metabolites* **9**(2019).
13. Das, K., Gabrielli, L. & Prins, L.J. Chemically Fueled Self-Assembly in Biology and Chemistry. *Angewandte Chemie International Edition* **60**, 20120-20143 (2021).
14. Albert, B. et al. *Molecular Biology of the Cell*, New York: Garland Publish. Inc., pp34, 787-815 (1994).
15. Sweeney, H.L. & Holzbaur, E.L.F. Motor Proteins. *Cold Spring Harb Perspect Biol* **10**(2018).
16. Korn, E.D., Carlier, M.-F. & Pantaloni, D. Actin Polymerization and ATP Hydrolysis. *Science* **238**, 638-644 (1987).
17. Ragazzon, G. & Prins, L.J. Energy consumption in chemical fuel-driven self-assembly. *Nature Nanotechnology* **13**, 882-889 (2018).
18. Squire, J. Special Issue: The Actin-Myosin Interaction in Muscle: Background and Overview. *International Journal of Molecular Sciences* **20**, 5715 (2019).
19. Sugi, H. et al. Direct demonstration of the cross-bridge recovery stroke in muscle thick filaments in aqueous solution by using the hydration chamber. *Proceedings of the National Academy of Sciences* **105**, 17396-17401 (2008).
20. Banani, S.F., Lee, H.O., Hyman, A.A. & Rosen, M.K. Biomolecular condensates: organizers of cellular biochemistry. *Nature Reviews Molecular Cell Biology* **18**, 285-298 (2017).

12. References

21. Lyon, A.S., Peeples, W.B. & Rosen, M.K. A framework for understanding the functions of biomolecular condensates across scales. *Nature Reviews Molecular Cell Biology* **22**, 215-235 (2021).
22. Kedersha, N. & Anderson, P. Mammalian Stress Granules and Processing Bodies. in *Methods in Enzymology*, Vol. 431 61-81 (Academic Press, 2007).
23. Protter, D.S.W. & Parker, R. Principles and Properties of Stress Granules. *Trends in Cell Biology* **26**, 668-679 (2016).
24. Anderson, P. & Kedersha, N. Stress granules. *Current Biology* **19**, R397-R398 (2009).
25. Kedersha, N. et al. Evidence That Ternary Complex (eIF2-GTP-tRNAⁱ Met)-Deficient Preinitiation Complexes Are Core Constituents of Mammalian Stress Granules. *Molecular Biology of the Cell* **13**, 195-210 (2002).
26. McEwen, E. et al. Heme-regulated Inhibitor Kinase-mediated Phosphorylation of Eukaryotic Translation Initiation Factor 2 Inhibits Translation, Induces Stress Granule Formation, and Mediates Survival upon Arsenite Exposure *. *Journal of Biological Chemistry* **280**, 16925-16933 (2005).
27. Söding, J., Zwicker, D., Sohrabi-Jahromi, S., Boehning, M. & Kirschbaum, J. Mechanisms for Active Regulation of Biomolecular Condensates. *Trends in Cell Biology* **30**, 4-14 (2020).
28. Wurtz, J.D. & Lee, C.F. Stress granule formation via ATP depletion-triggered phase separation. *New Journal of Physics* **20**, 045008 (2018).
29. Wang, J.T. et al. Regulation of RNA granule dynamics by phosphorylation of serine-rich, intrinsically disordered proteins in *C. elegans*. *Elife* **3**, e04591 (2014).
30. Alberti, S. & Hyman, A.A. Biomolecular condensates at the nexus of cellular stress, protein aggregation disease and ageing. *Nature Reviews Molecular Cell Biology* **22**, 196-213 (2021).
31. Patel, A. et al. A Liquid-to-Solid Phase Transition of the ALS Protein FUS Accelerated by Disease Mutation. *Cell* **162**, 1066-1077 (2015).
32. Conicella, A.E., Zerze, G.H., Mittal, J. & Fawzi, N.L. ALS Mutations Disrupt Phase Separation Mediated by alpha-Helical Structure in the TDP-43 Low-Complexity C-Terminal Domain. *Structure* **24**, 1537-49 (2016).
33. Alberti, S. & Dormann, D. Liquid-Liquid Phase Separation in Disease. *Annual Review of Genetics* **53**, 171-194 (2019).
34. Linsenmeier, M. et al. Dynamic arrest and aging of biomolecular condensates are modulated by low-complexity domains, RNA and biochemical activity. *Nature Communications* **13**, 3030 (2022).
35. Hondele, M. et al. DEAD-box ATPases are global regulators of phase-separated organelles. *Nature* **573**, 144-148 (2019).
36. Hondele, M., Heinrich, S., De Los Rios, P. & Weis, K. Membraneless organelles: phasing out of equilibrium. *Emerging Topics in Life Sciences* **4**, 343-354 (2020).
37. Kirschbaum, J. & Zwicker, D. Controlling biomolecular condensates via chemical reactions. *Journal of The Royal Society Interface* **18**, 20210255 (2021).
38. Mattia, E. & Otto, S. Supramolecular systems chemistry. *Nature Nanotechnology* **10**, 111-119 (2015).
39. Rieß, B., Grötsch, R.K. & Boekhoven, J. The Design of Dissipative Molecular Assemblies Driven by Chemical Reaction Cycles. *Chem* **6**, 552-578 (2020).

12. References

40. Boekhoven, J., Hendriksen, W.E., Koper, G.J.M., Eelkema, R. & van Esch, J.H. Transient assembly of active materials fueled by a chemical reaction. *Science* **349**, 1075-1079 (2015).
41. Morrow, S.M., Colomer, I. & Fletcher, S.P. A chemically fuelled self-replicator. *Nature Communications* **10**, 1011 (2019).
42. Singh, N., Formon, G.J.M., De Piccoli, S. & Hermans, T.M. Devising Synthetic Reaction Cycles for Dissipative Nonequilibrium Self-Assembly. *Advanced Materials* **32**, 1906834 (2020).
43. Ashkenasy, G., Hermans, T.M., Otto, S. & Taylor, A.F. Systems chemistry. *Chemical Society Reviews* **46**, 2543-2554 (2017).
44. Schwarz, P.S., Tena-Solsona, M., Dai, K. & Boekhoven, J. Carbodiimide-fueled catalytic reaction cycles to regulate supramolecular processes. *Chemical Communications* **58**, 1284-1297 (2022).
45. Kriebisch, B.A.K. et al. Tuning the Kinetic Trapping in Chemically Fueled Self-Assembly**. *ChemSystemsChem* **5**, e202200035 (2023).
46. Zwicker, D. The intertwined physics of active chemical reactions and phase separation. *Current Opinion in Colloid & Interface Science* **61**, 101606 (2022).
47. Weber, C.A., Zwicker, D., Jülicher, F. & Lee, C.F. Physics of active emulsions. *Reports on Progress in Physics* **82**, 064601 (2019).
48. Zwicker, D., Hyman, A.A. & Jülicher, F. Suppression of Ostwald ripening in active emulsions. *Physical Review E* **92**, 012317 (2015).
49. Zwicker, D., Seyboldt, R., Weber, C.A., Hyman, A.A. & Jülicher, F. Growth and division of active droplets provides a model for protocells. *Nature Physics* **13**, 408-413 (2017).
50. Popkin, G. The physics of life. *Nature* **529**, 16-18 (2016).
51. Tena-Solsona, M. et al. Accelerated Ripening in Chemically Fueled Emulsions**. *ChemSystemsChem* **3**, e2000034 (2021).
52. Donau, C. & Boekhoven, J. The chemistry of chemically fueled droplets. *Trends in Chemistry* **5**, 45-60 (2023).
53. Weber, C.A., Zwicker, D., Jülicher, F. & Lee, C.F. Physics of active emulsions. *Rep Prog Phys* **82**, 064601 (2019).
54. Rai, A.K., Chen, J.-X., Selbach, M. & Pelkmans, L. Kinase-controlled phase transition of membraneless organelles in mitosis. *Nature* **559**, 211-216 (2018).
55. Liu, J. et al. Cell cycle-dependent localization of the CDK2-cyclin E complex in Cajal (coiled) bodies. *Journal of Cell Science* **113**, 1543-1552 (2000).
56. Donau, C. et al. Active coacervate droplets as a model for membraneless organelles and protocells. *Nature Communications* **11**, 5167 (2020).
57. Gucht, J.v.d., Spruijt, E., Lemmers, M. & Cohen Stuart, M.A. Polyelectrolyte complexes: Bulk phases and colloidal systems. *Journal of Colloid and Interface Science* **361**, 407-422 (2011).
58. Veis, A. A review of the early development of the thermodynamics of the complex coacervation phase separation. *Advances in Colloid and Interface Science* **167**, 2-11 (2011).
59. Fu, J. & Schlenoff, J.B. Driving Forces for Oppositely Charged Polyion Association in Aqueous Solutions: Enthalpic, Entropic, but Not Electrostatic. *Journal of the American Chemical Society* **138**, 980-990 (2016).
60. Yewdall, N.A., André, A.A.M., Lu, T. & Spruijt, E. Coacervates as models of membraneless organelles. *Current Opinion in Colloid & Interface Science* **52**, 101416 (2021).

12. References

61. Liu, Y., Momani, B., Winter, H.H. & Perry, S.L. Rheological characterization of liquid-to-solid transitions in bulk polyelectrolyte complexes. *Soft Matter* **13**, 7332-7340 (2017).
62. Stasi, M. et al. Regulating DNA-Hybridization Using a Chemically Fueled Reaction Cycle. *Journal of the American Chemical Society* **144**, 21939-21947 (2022).
63. Rodon-Fores, J. et al. A chemically fueled supramolecular glue for self-healing gels. *Chemical Science* **13**, 11411-11421 (2022).
64. Borsley, S., Leigh, D.A. & Roberts, B.M.W. A Doubly Kinetically-Gated Information Ratchet Autonomously Driven by Carbodiimide Hydration. *Journal of the American Chemical Society* **143**, 4414-4420 (2021).
65. Sorrenti, A., Leira-Iglesias, J., Sato, A. & Hermans, T.M. Non-equilibrium steady states in supramolecular polymerization. *Nature Communications* **8**, 15899 (2017).
66. Howlett, M.G., Engwerda, A.H.J., Scanes, R.J.H. & Fletcher, S.P. An autonomously oscillating supramolecular self-replicator. *Nature Chemistry* **14**, 805-810 (2022).
67. Maiti, S., Fortunati, I., Ferrante, C., Scrimin, P. & Prins, L.J. Dissipative self-assembly of vesicular nanoreactors. *Nature Chemistry* **8**, 725-731 (2016).
68. Dhiman, S., Jain, A. & George, S.J. Transient Helicity: Fuel-Driven Temporal Control over Conformational Switching in a Supramolecular Polymer. *Angewandte Chemie International Edition* **56**, 1329-1333 (2017).
69. Schnitter, F., Rieß, B., Jandl, C. & Boekhoven, J. Memory, switches, and an OR-port through bistability in chemically fueled crystals. *Nature Communications* **13**, 2816 (2022).
70. Linsenmeier, M. et al. Dynamics of Synthetic Membraneless Organelles in Microfluidic Droplets. *Angew Chem Int Ed Engl* **58**, 14489-14494 (2019).
71. Berry, J., Weber, S.C., Vaidya, N., Haataja, M. & Brangwynne, C.P. RNA transcription modulates phase transition-driven nuclear body assembly. *Proceedings of the National Academy of Sciences* **112**, E5237-E5245 (2015).
72. Linsenmeier, M., Kopp, M.R.G., Stavrakis, S., de Mello, A. & Arosio, P. Analysis of biomolecular condensates and protein phase separation with microfluidic technology. *Biochim Biophys Acta Mol Cell Res* **1868**, 118823 (2021).
73. Love, C. et al. Reversible pH-Responsive Coacervate Formation in Lipid Vesicles Activates Dormant Enzymatic Reactions. *Angew Chem Int Ed Engl* **59**, 5950-5957 (2020).
74. Deshpande, S. et al. Spatiotemporal control of coacervate formation within liposomes. *Nature Communications* **10**(2019).
75. Cochereau, R., Renard, D., Nous, C. & Boire, A. Semi-permeable vesicles produced by microfluidics to tune the phase behaviour of encapsulated macromolecules. *J Colloid Interface Sci* **580**, 709-719 (2020).
76. Last, M.G.F., Deshpande, S. & Dekker, C. pH-Controlled Coacervate–Membrane Interactions within Liposomes. *ACS Nano* **14**, 4487-4498 (2020).
77. Spath, F. et al. Molecular Design of Chemically Fueled Peptide-Polyelectrolyte Coacervate-Based Assemblies. *Journal of the American Chemical Society* **143**, 4782-4789 (2021).

78. Hofmann, T.W., Hänselmann, S., Janiesch, J.-W., Rademacher, A. & Böhm, C.H.J. Applying microdroplets as sensors for label-free detection of chemical reactions. *Lab on a Chip* **12**, 916-922 (2012).